Design, Synthesis, and Structure of Lithium Ion Conducting Materials for All-Solid-State Batteries

by

Kavish Kaup

A thesis
presented to the University of Waterloo
in fulfillment of the
thesis requirement for the degree of
Doctor of Philosophy
in
Chemical Engineering (Nanotechnology)

Waterloo, Ontario, Canada, 2021

Examining Committee Membership

The following served on the Examining Committee for this thesis. The decision of the Examining Committee is by majority vote.

External Examiner:	Jeff Sakamoto Associate Professor Dept. of Mechanical Engineering, University of Michigan
Supervisor:	Linda Nazar Professor Dept. of Chemistry, University of Waterloo
Internal Member:	Michael Pope Associate Professor Dept. of Chemical Engineering, University of Waterloo
Internal-External Member:	Holger Kleinke Professor Dept. of Chemistry, University of Waterloo
Internal-External Member:	Rodney Smith Assistant Professor Dept. of Chemistry, University of Waterloo

Author's Declaration

I hereby declare that I am the sole author of this thesis. This is a true copy of the thesis, including any required final revisions, as accepted by my examiners.

I understand that my thesis may be made electronically available to the public.

Abstract

Energy storage plays a pivotal role in enabling intermittent renewable energy sources, electrified transportation, and portable electronics. The rapidly growing energy demand in these sectors requires improvement to the commercial lithium-ion systems. All-solid-state batteries are candidates for next-generation batteries because of their potential to be paired with a lithium metal anode, which leads to significant energy density gains. Furthermore, solid electrolytes can dramatically improve the safety and longevity of battery technologies by replacing the flammable liquid organic electrolytes that are typically used. This thesis broadly focuses on two types of solid electrolytes: thiophosphates and thioborates.

Chapters 3 and 4 focus on thiophosphate type solid electrolytes. In **chapter 3**, an *in-situ* variable temperature neutron powder diffraction study on Li_3PS_4 was conducted to elucidate the crystal frameworks and lithium substructures of its respective polymorphs ($\gamma \rightarrow \beta \rightarrow \alpha$). The lithium diffusion pathways of both the bulk β and α polymorphs are evaluated using the maximum entropy method and bond valence site energy calculations, revealing that the structure of α-Li_3PS_4 favors facile 3D conduction. Building on these concepts, **chapter 4** focuses on the experimental elucidation of lithium ion conductors in the $Li_{1+2x}Zn_{1-x}PS_4$ solid solution. Using neutron and synchrotron X-ray powder diffraction, their crystalline structures are resolved to show the nature of likely pathways for lithium ion conduction and this is correlated with the improved ion conductivity upon increasing the lithium concentration and inducing Li/Zn site disorder.

In **chapter 5**, new quaternary lithium oxythioborosilicate glasses (termed 'LIBOSS') were synthesized that exhibit high ion conductivity up to 2×10^{-3} S·cm^{-1}. Superionic conductivity can be achieved despite relatively high oxygen:sulfur ratios of more than 1:2, which also greatly reduces H_2S evolution upon exposure to air. Stripping/plating onto lithium metal results in very low polarization at a current density of 0.1 mA·cm^{-2} over repeated cycling. Evaluation of the optimal glass composition as an electrolyte in an all-solid-state battery shows it exhibits excellent cycling stability and maintains near theoretical

capacity for over 130 cycles at room temperature with Coulombic efficiency close to 99.9%, opening up new avenues of exploration for these quaternary compositions.

In **chapter 6**, a new class of lithium thioborate halides is reported. These materials adopt a so-called supertetrahedral adamantanoid structure that houses mobile lithium ions and halide anions within interconnected 3D structural channels. Investigation of the $Li_{7.5}B_{10}S_{18}X_{1.5}$ (X = Cl, Br, and I) structures using single-crystal XRD, neutron powder diffraction, and neutron PDF reveals significant lithium and halide anion disorder. These new superadamantanoid materials exhibit high ionic conductivities up to 1.4×10^{-3} S·cm^{-1}. In **chapter 7**, a new fast-ion conducting lithium thioborate halide, $Li_6B_7S_{13}I$ is presented. $Li_6B_7S_{13}I$ exhibits a perovskite topology and an argyrodite-like lithium substructure that leads to superionic conduction with a theoretical Li-ion conductivity of 5.2×10^{-3} S·cm^{-1}. Combined single-crystal XRD, neutron powder diffraction, and AIMD simulations elucidate the Li^+ ion conduction pathways through three-dimensional intra and inter-cage connections, and Li-ion site disorder, which are all essential for high lithium mobility.

Acknowledgements

First and foremost, I would first like to express my sincere gratitude to my supervisor, Professor Linda F. Nazar, for her guidance and support during my doctoral studies. Her willingness and eagerness to discuss research on short notice every time I knocked on her office door has been extremely invaluable to drive my projects forward. I've enjoyed our impromptu and fruitful scientific discussions over the years. I would like to thank my internal committee members: Professors Holger Kleinke, Rodney Smith, and Michael Pope. I have learned a lot from each of them during my time here at Waterloo, in the form of both courses and useful research discussions. I would also like to thank Professor Jeff Sakamoto, for his time as the external examiner in my committee.

I thank all my past and present fellow lab mates for the stimulating discussions, for the late nights working together before deadlines, for all the fun we have had, and for their friendship. I would especially like to mention Dr. Fabien Lalère, Dr. Kern-Ho Park, Abhinandan Shyamsunder, Se Young Kim, Erika Ramos, Laidong Zhou, and Ivan Kochetkov, who I have had the pleasure of working closely with. Thank you to CY Kwok and Lauren Blanc who were my go-to when I urgently needed high-quality SEM images. A big thank you to our lab manager, Andrew Kacheff, who helps keeps our lab running and with whom I've spent countless hours repairing gloveboxes, diffractometers, and many other instruments. I would like to extend my appreciation towards Dr. Jalil Assoud in the Chemistry department for his help with the single-crystal diffraction in this thesis, as well as our discussions on crystallography, solid-state chemistry, and much more. I'd also like to acknowledge the machine and electronic shop who consistently brought my design ideas to life: thank you Harmen, Mike, Andrew, Peter, Hiruy, Kruno, and Zhenwen.

Last but not the least, I would like to thank my family: my parents, my sister, and my aunt for supporting me throughout my PhD and life in general.

Dedication

In loving memory of my grandparents. To my grandmother who unfortunately never got to see this adventure and my grandfather who missed its end.

Table of Contents

List of Figures

List of Tables

List of Abbreviations

ADP Atomic Displacement Parameter 47, 54, 67, 144, 146

AIMD Ab-initio Molecular Dynamics v, 19, 45, 47, 64, 66, 67, 70, 137, 144, 146, 155, 156, 167

ASSB All-Solid-State Battery 6, 7, 11, 18, 118, 138

BVEL Bond Valence Energy Landscape xv, 62, 63, 65, 66, 68, 70

BVSE Bond Valence Site Energy xv, 62–70, 72, 164

DFT Density Functional Theory 19, 42, 44, 45, 47, 167

DSC Differential Scanning Calorimetry xiv, 35–37

EDX Energy-Dispersive X-ray Spectroscopy xvi, xvii, xxii, 94, 96, 124–128, 140

EELS Electron Energy Loss Spectroscopy xvi, 88, 94, 96

EIS Electrochemical Impedance Spectroscopy xvii, 75, 81, 93, 108, 119–121, 135, 136, 155, 167

LATP $Li_{1+x}Al_xTi_{2-x}(PO_4)_3$ 12

LGPS $Li_{10}GeP_2S_{12}$ 13, 74

LIB Lithium-Ion Battery 2–5, 7

LIBOSS Li_2S – B_2S_3 – SiO_2 – LiI xvii, xxi, 90, 93, 94, 101, 103, 108–112, 114, 166

LiPON Lithium Phosphorous Oxynitride 14, 89, 107

LISICON Lithium Superionic Conductor 13

LLTO $Li_{0.5-3x}La_{0.5+x}TiO_3$ 12

LLZO $Li_7La_3Zr_2O_{12}$ 12, 14, 89, 108

LZPS $Li_{1+2x}Zn_{1-x}PS_4$ 74, 75, 80–82, 85

MAS Magic Angle Spinning xi, xvii, 32, 34, 35, 88, 90, 102, 104, 107, 116, 165

MEM Maximum Entropy Method xv, 54, 62–69, 72, 164

NASICON Natrium (Sodium) Super Ionic Conductor 12

NMR Nuclear Magnetic Resonance xi, xvii, 32–34, 47, 63, 88, 90, 92, 102–107, 116, 118, 129, 165

NPD Neutron Powder Diffraction xv, xviii, xxi, xxii, 27, 28, 48–51, 53, 55, 119, 125–130, 132, 150, 164–166

PDF Pair Distribution Function v, xiv, xviii, xxii, 29–31, 107, 117, 119, 125, 129–132, 135, 166

SEM Scanning Electron Microscope xvi, xvii, 82, 83, 94, 96, 124–127, 136, 140

STEM Scanning Transmission Electron Microscope xvi, 88, 94, 96

THF Tetrahydrofuran 47, 49, 50, 71

TOF Time-of-Flight xviii, 28, 31, 76, 86, 150

VASP Vienna Ab initio Simulation Package 41, 160, 162

XRD X-Ray Diffraction v, xv, xvi, xxi, xxii, 24, 47–49, 55, 71, 75, 76, 78, 80, 84, 86, 92–94, 99, 106, 107, 113, 117, 119, 122–125, 127, 137, 139, 140, 144, 150, 165, 166

Chapter 1

Introduction

Batteries have changed the global energy landscape by allowing us to easily store, transport, and use electricity on demand whenever and wherever we want. In our world today, energy storage solutions have enabled the emergence of portable electronic devices, electric vehicles, and renewable energy sources such as solar and wind. These energy storage systems could not have been possible without the development of novel advanced materials and their chemistries. While significant progress has been made, a monumental global effort is taking place to improve these technologies further. This is in part due to rapidly increasing energy demands that stem from a variety of causes, such as the proliferation of electronic devices to the growing electric vehicle industry. Electric vehicles are extremely important from both an environmental and economical perspective as the automotive industry transitions from gasoline powered vehicles to electric. On a broader scale, energy storage can improve the reliability of intermittent renewable energy sources such as solar and wind to be used as part of the grid-based supply system. Batteries can provide electricity during off-peak production times when energy cannot be generated. As energy demand increases and the effects of climate change become more severe, the need for new and improved energy storage systems becomes crucial.

1.1 Lithium-Ion Batteries (LIBs)

LIBs were developed on the basis of intercalation reactions, where ions are able to move into and reside in a solid host. Looking at the intercalation of lithium ions into metal disulfides, Whittingham[1] developed the first rechargeable lithium battery in 1976 at then Exxon Corporation, using a TiS_2 cathode, a lithium metal anode, and an organic liquid electrolyte. This exciting discovery spurred interest into many other intercalation materials. Although this system was promising, the use of a sulfide based cathode limited the cell voltage to less than 2.5 V, which in turn limits the energy density. Additionally, the use of a pure lithium-metal anode leads to dendrite growth and ultimately short-circuiting that when paired with an organic electrolyte presents a fire hazard. The low voltage problem was addressed by the discovery of higher voltage (4 V) oxide based cathodes. Notably, the lithium layered oxide $LiCoO_2$, developed by Goodenough *et al.*[2] at the University of Oxford, was fundamental in enabling the commercialization of LIBs. $LiCoO_2$ exhibits good structural stability along with high electrical and lithium-ion conductivity, which allows it to be quickly charged and discharged. The cell architecture and assembly is also simplified since a metallic lithium anode is no longer required because Li^+ is already contained within the structure of the cathode material. Lithium-free anodes can then be paired with $LiCoO_2$. Yoshino *et al.* in 1987 at the Asahi Kasei Corporation in Japan did exactly that by studying $LiCoO_2$ paired with various carbon based anodes.[3] While there were many notable milestones on each aspect of the battery, these three discoveries are the foundation for the modern LIB. Sony Corporation in 1991 commercialized the LIB with a $LiCoO_2$ cathode and graphite anode. Prof. Stanley Whittingham, Dr. Akira Yoshino, and Prof. John B. Goodenough were awarded the 2019 Nobel Prize in Chemistry for the development of the lithium-ion battery.

In general, a battery is composed of a positive electrode (e.g. $LiCoO_2$), a negative electrode (e.g graphite) and an organic electrolyte with a Li salt (e.g. $LiPF_6$ in ethylene carbonate or dimethyl carbonate). An insulating and electrolyte permeable separator is

used to avoid physical contact between the two electrodes. A schematic of a typical LIB during charge and discharge is shown in **Figure 1.1**.

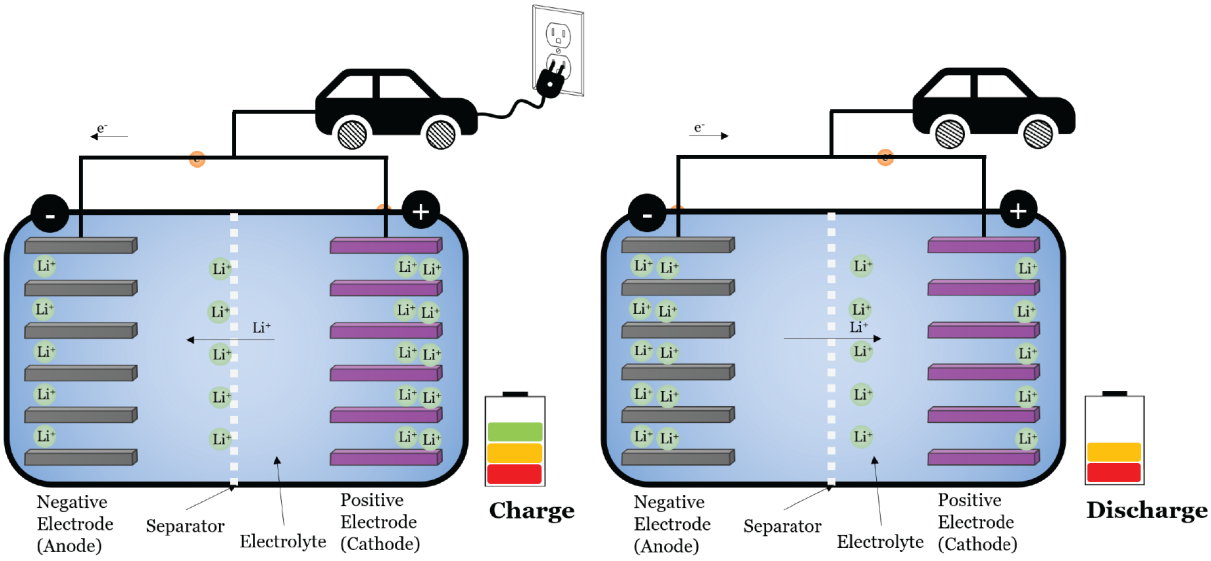

Figure 1.1: Schematic illustration of a typical lithium-ion battery during charge and discharge consisting of a layered $LiCoO_2$ positive electrode and a graphite negative electrode.

Starting from the fully discharged state, a battery must be charged by an external power source, which applies a voltage that forces electrons to move from the positive to the negative electrode through the external circuit. This loss of electrons results in the oxidation of the positive electrode (e.g. Co^{3+} to Co^{4+} in $Li_{1-x}CoO_2$) during charge while Li^+ deintercalates from the structure to compensate the charge. The Li-ions migrate through the electrolyte and intercalate into the porous negative electrode (i.e. graphite layers). This process is driven until a certain potential or time is reached where the structure of the electrode is stable and no adverse effects take place in the cell. Once the cell reaches that potential it is considered charged and the energy is stored. The equations for charge in each electrode are given by:

$$\text{Positive Electrode: } LiCoO_2 \rightarrow Li_{1-x}CoO_2 + xLi^+ + xe^- \tag{1.1}$$

$$\text{Negative Electrode: } C_6 + xLi^+ + xe^- \rightarrow Li_xC_6 \tag{1.2}$$

The reverse process takes place spontaneously due to the higher chemical potential of the positive electrode than the negative, which allows the battery to be used as an energy source. During the discharge process, lithium ions move from the negative to the positive electrode through the electrolyte. In the $LiCoO_2$ positive electrode, the transition metal is reduced from Co^{4+} to Co^{3+}. The equations for discharge are given by:

$$\text{Positive Electrode: } Li_{1-x}CoO_2 + xLi^+ + xe^- \rightarrow LiCoO_2 \tag{1.3}$$

$$\text{Negative Electrode: } Li_xC_6 \rightarrow C_6 + xLi^+ + xe^- \tag{1.4}$$

Although $LiCoO_2$ has been a good positive electrode material for LIBs it has some limitations with respect to energy density. Only half the lithium can be removed from the structure without compromising structural stability, providing a practical specific capacity of 140 mAh/g (theoretical capacity is 274 mAh/g). Charging further to higher voltage results in removal of lattice oxygen, which collapses the structure and ultimately leads to capacity fading and safety concerns. Furthermore, the high price and toxicity of cobalt Has prompted both academia and industry to consider alternative cathode materials.

This has lead to substitution of Co for other transition metals and has given rise to the "NCM" or "NCA" series of materials, which is quickly becoming the electric vehicle industry standard for cathode materials. These layered lithium Ni-Co-Mn oxide (NCM) and lithium Ni-Co-Al oxide (NCA) are widely used in commercial cells due to their high specific capacities (>150 mAh/g), good cycle stability, and enhanced thermal stability.[4] Furthermore, the ratios between the transition metals can be tuned, where Ni-rich compositions are favoured due to the reduction in Co content and increase in capacity, which in turn increases the energy density of the battery.[5]

1.2 All-Solid-State Batteries (ASSBs)

1.2.1 Motivation for ASSBs

It has become apparent that energy demand is out-pacing the theoretical limits of the LIB. As manufactures attempt to squeeze more energy density out of the battery by pushing its limits we have seen severe safety hazards such as battery fires and explosions become more common. The Li-ion battery is limited by its Li^+ intercalation chemistry and is approaching the theoretical energy density limits, assuming a graphitic anode and transition metal oxide cathode. In the case of electric vehicles, the energy density needs to be increased from the current 260 W·h/kg to the targeted 500 to 700 W·h/kg to achieve long driving ranges of more than 500 km.[6] There are two main ways of increasing the theoretical energy density; change the positive electrode or change the negative electrode material. A lot of work has focused on developing higher capacity and high voltage cathodes to improve the energy density or by developing batteries based on conversion chemistries such as Li-S and Li-O_2.[7] Irrespective of the cathode chemistry, the greatest theoretical increase in energy density always comes from changing the anode to pure lithium metal (**Figure 1.2**).[8] Achieving a commercially viable battery using a lithium metal anode is considered the "holy grail" of batteries. It's important to note, for a lithium metal battery to truly provide high practical energy densities, the Li foil needs to be extremely thin (a few microns). Alternatively, an "anodeless" configuration is the best case, where the Li anode is formed upon charging the assembled battery.

Lithium metal is one of the best choices as a negative electrode material for a battery because of its light weight (6.941 g/mol) and low redox potential (-3.04 V vs. standard hydrogen electrode (SHE)). Using a lithium metal anode could nearly double the energy density to 500 W·h/kg.[9] Unfortunately, a lithium metal anode comes with safety concerns due to the unstable chemistry at the Li metal-electrolyte interface. Fire hazards are a concern due to lithium's tendency to form dendrites in liquid organic electrolytes, which

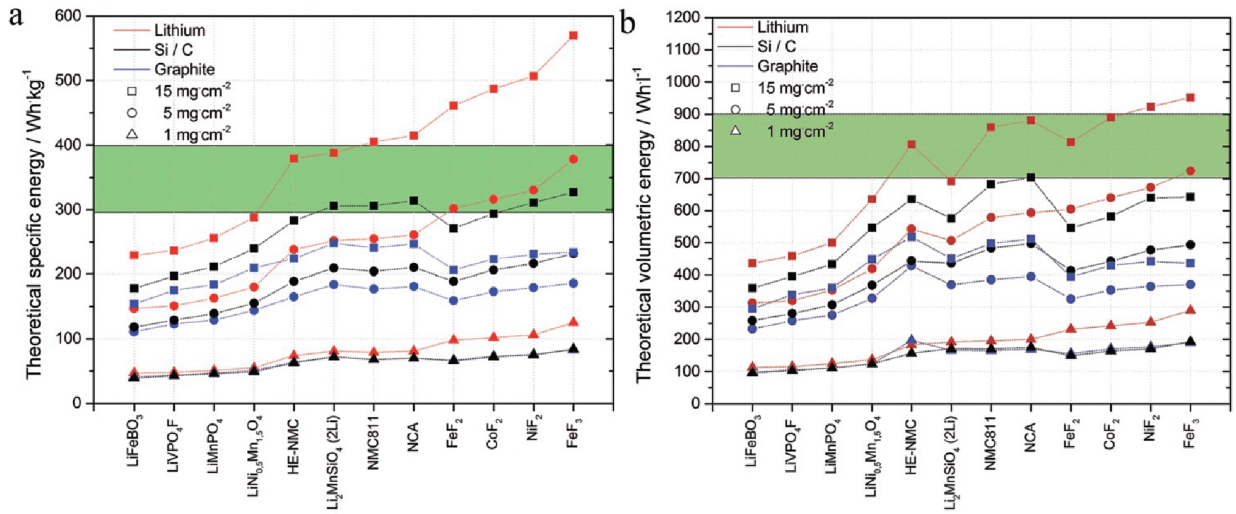

Figure 1.2: (a) Gravimetric energy density for selected cathode materials (at different loadings) in full cell configuration with metallic lithium (red lines), graphite (blue lines) and silicon (black lines) as anode. Green bands: targets at cell's level. (b) Corresponding volumetric energy density. Calculations based on the theoretical energy density values of the corresponding electrodes, using the materials stoichiometry and molecular weight, considering full range of Li. Reproduced with permission from The Royal Society of Chemistry.[8]

on its own are flammable and toxic liquids. These dendrites grow upon cycling and short-circuits the cell, which ultimately cause thermal runaway and explosions. Furthermore, the unstable interface chemistry results in the formation of a solid electrolyte interphase (SEI) which increases the interfacial resistance, lowers the Coulombic efficiency, and depletes the electrolyte. This results in rapidly deteriorating performance accompanied by the extreme safety concerns of fire and explosion hazards due to the highly flammable organic electrolyte component.

The most promising strategy to combat this problem is the use of inorganic solid electrolytes to enable ASSBs. A solid electrolyte may be a viable alternative to prevent the incompatibility between the lithium anode and liquid electrolyte. Flammability issues would no longer be of concern in Li-ion systems as inorganic solids replace the flammable organic liquids and a lithium anode can be used to achieve a high-energy density as dendrites are inhibited by the mechanical strength of the solid. In addition to improved safety, there are

several other advantages of ASSBs. LIBs have a limited operating temperature range, where at low temperature the ionic conductivity of the liquid electrolyte is reduced such that performance declines significantly, and at elevated tempeatures ($\geq$ 60°C) the reactivity of liquid electrolytes accelerates decomposition and deterioration of cell performance.[10] Solid electrolytes, on the other hand, can operate over a wider temperature range from -30 to 100°C.

1.2.2 Overview of ASSBs

Solid-state batteries and solid ion conductors have a long history that dates back to even before the development of liquid-based LIB. In the 1960s, the discovery of the sodium beta-alumina solid electrolyte led to the development of a commercial high-temperature Na-S battery by the Ford Motor Company, although they used molten cathodes, precluding a true all-solid-state approach.[11] In the 1970s, fully all-solid-state cells were reported with a Li metal anode and TiS_2 cathode using solid electrolytes of lithium nitride,[12] lithium phosphates,[13] and poly(ethylene oxide) (PEO) polymers.[14] The discovery of lithium phosphorus oxynitride (LiPON) in the 1980s prompted the development of thin-film solid-state batteries.[15] While a tremendous amount of research on ion conductors and solid-state batteries has been conducted, unsatisfactory performance of ASSBs and commercialization of the LIB drove the focus away from solid-state batteries, leaving a nearly 20 year gap before the resurgence of interest that has occurred in the last decade.[16]

All-solid-state batteries follow the same working principles as a typical rechargeable battery and consist of a solid anode (negative electrode), cathode (positive electrode) and electrolyte. The battery can use an intercalation or conversion type positive electrode, a lithium negative electrode and a solid electrolyte that acts as a separator to block electrical contact but allows the flow of lithium ions. A schematic of a typical solid-state battery is shown in **Figure 1.3**.

A key difference between a traditional battery and a solid-state battery is the cathode preparation – the cathode composite requires solid electrolyte material mixed in to achieve

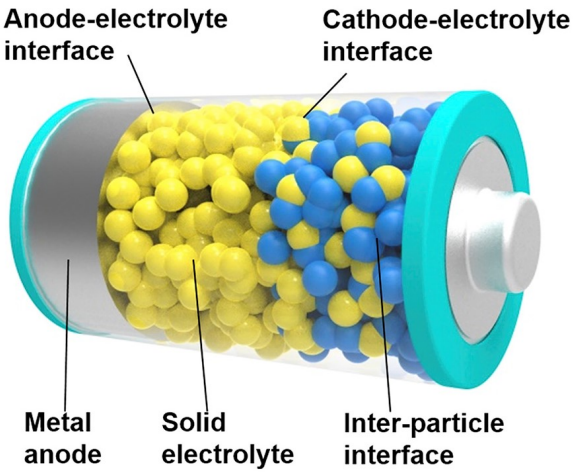

Figure 1.3: Schematic illustration of an all-solid-state battery and the different interfaces within the cell. Reproduced with permission from Elsevier.[17]

sufficient ionic conductivity (i.e. an ionic conduit is required). The cathodes for solid-state cells are typically a composite that contains active material (e.g. $LiCoO_2$ for lithium ion batteries), an ionic conductor (solid electrolyte) and sometimes an electronic conductor (typically a carbon additive to provide electronic percolation). Most solid-state batteries in laboratory-scale settings report using an anode composed of a double layer foil of lithium and indium. This ensures that the highly reactive nature of lithium will play less of a role in degrading the solid electrolyte material since no stable electrolyte currently exists, although the goal is to eventually pair a pure lithium metal anode with a compatible solid electrolyte material.

1.2.3 Challenges of ASSBs

While solid-state batteries bring about improved energy density and safety, there are still many challenges to overcome owing to the higher resistances compared to that of liquid cells at ambient temperature and due to the typically lower ionic conductivities of solid electrolytes. Although solid-state cells can have longer lifetimes as they are not as sensitive to shocks, leaks, and extreme temperatures, they experience additional stresses at each solid-solid interface, which negatively affects performance and cell life.

The biggest challenges solid-state batteries face are the high interfacial resistances. There are a significant amount of interfaces to consider, and each have their own effects. A visual illustration that provides an overview of all the types of interfaces are shown in **Figure 1.4**.

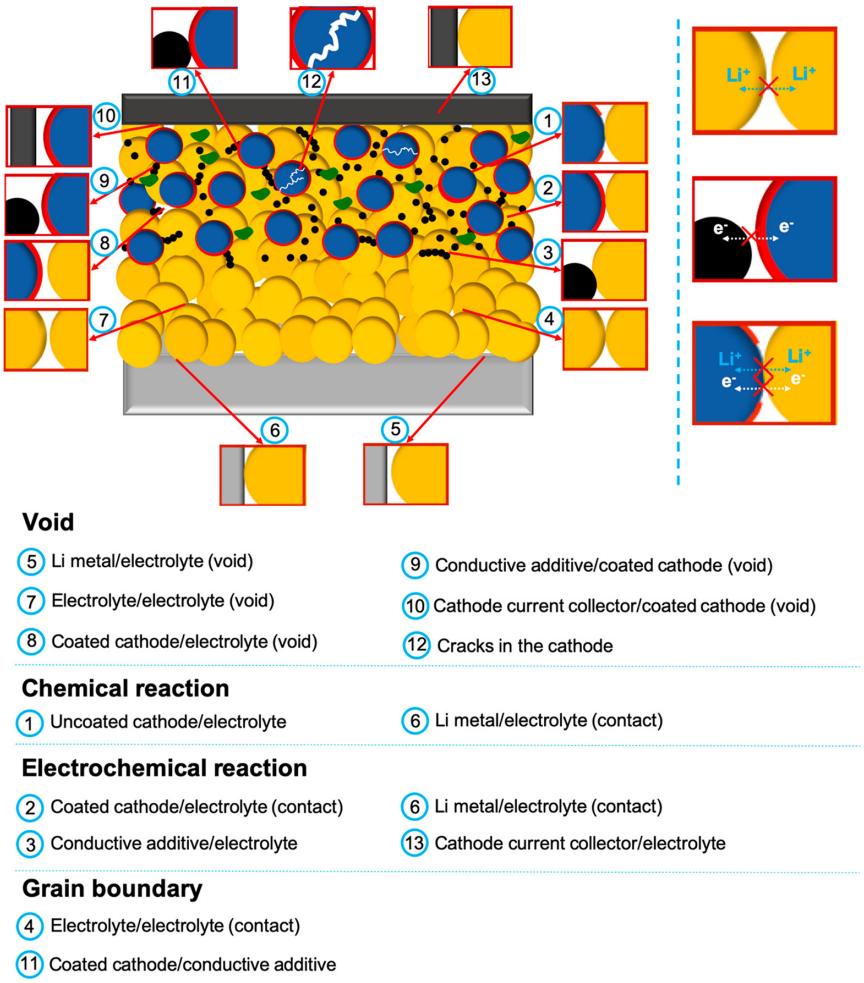

Figure 1.4: Schematic illustration of interfacial phenomena that can arise in ASSBs. Reprinted with permission from American Chemical Society.[18]

The two interfaces that are of the most concern are the Li-metal/solid electrolyte and solid electrolyte/cathode interface. At the positive electrode, there are three main considerations:

1. Chemical Stability: The interface between the solid electrolyte material and cathode

active material should ideally remain unchanged during fabrication and storage over the operating temperature range. A cathode electrolyte interphase (CEI) between the two components will likely form because of the chemical potential difference between the two materials, leading to a spontaneous reaction. This can lead to a highly insulating layer or can undergo continuous decomposition that leads to cell failure.

2. Electrochemical Stability: During the charge/discharge process the materials will be subjected to a wide potential window. The electrolytes can be oxidized at high voltage and reduced at low voltages if they are in contact with an electronic conductor in the composite, which can lead to the formation of passivating and inactive interphases.

3. Mechanical Stability: The active material and solid electrolyte may face external or internal stresses, which can lead to contact loss (void formation), particle cracking or pulverization. This may stem from volume change of the cathode material upon cycling, which would mechanically deform the electrode/electrolyte interface.

At a lithium metal negative electrode, we not only have to consider the interface, but also how the solid electrolyte separator layer is processed (i.e. defects in the separator). In general, there are two main considerations at the negative electrode:

1. Thermodynamic and Kinetic Stability: Li metal will reduce almost anything it comes in contact with and the reaction products that form an interface layer may not be ionically conductive. These thermodynamic considerations alone are not sufficient to understand the interface. The thickness of the interphase formed will increase the cell resistance, so kinetic considerations are important. Since thermodynamic stability of a solid electrolyte with lithium metal is unlikely, the solid electrolyte interphase (SEI) formed between the two components must be kinetically stable.

2. Mechanical Stability: The solid electrolyte separator must be processed in such a way that it is free from interparticle voids or defects. The presence of voids and

defects would not only hinder Li-ion diffusion but can induce dendritic growth of Li metal through the separator. Defects on the separator surface may also lead to nonuniform lithium plating, which prevents high-rate capability and increases dendrite penetration.

1.2.4 Current Approaches Towards ASSBs

To combat some of these interface issues, researchers have used hybrid solid/liquid electrolytes. Specifically in the cathode where it is necessary to obtain sufficient contact between the cathode and solid electrolyte particles, a small amount of liquid or gel electrolyte is used to reduce the interface resistance and improve mechanical contact.[19] This is sometimes referred to as a "quasi" solid-state battery.

An alternative method is to use thin coating layers to extend the stability window of the materials or to apply a multiple solid electrolyte approach to mitigate the various interface issues. A ductile and high-voltage stable solid electrolyte could be used in the composite positive electrode to prevent any detrimental interface reactions. Then, the separator solid electrolyte can be a material of any choice, ideally one that is easily processable and is a very fast lithium-ion conductor to reduce the Ohmic drop across the cell. Finally, a thin secondary separating solid electrolyte layer that is kinetically stable with Li metal can be used as an artificial interphase to protect any detrimental side reactions at the negative electrode. The challenge is these layers would also need to be compatible with each other.

1.3 Solid Electrolytes

An ideal electrolyte is an electronic insulator to prevent self-discharge, a fast ion conductor to quickly transport Li^+ between the electrodes, and electrochemically stable in the operating voltage range of the battery. Inorganic solid electrolytes are typically good electronic insulators due to the predominant ionic bonding present in these materials. However, despite the potential of ASSBs, a solid electrolyte material that achieves a high lithium ion

conductivity coupled with good chemical and electrochemical stability has not yet been found.

Solid electrolytes can generally be classified as polymeric or inorganic. While each type has their unique advantages and disadvantages, the focus here will be on inorganic solid electrolytes, due to their typically higher ionic conductivity at room temperature. The inorganic solid electrolytes can be further divided by their structures or chemical compositions. The inorganic materials can be broadly categorized as a halide, nitride, oxide, or sulfide depending on the anion family. Finally, the materials can be crystalline or glassy (amorphous) where most commonly they are crystalline in nature. The two most studied classes of solid electrolytes are sulfides and oxides.

1.3.1 Crystalline Electrolytes

From the oxide electrolytes, crystalline phosphates with a NASICON (NAtrium Super Ionic CONductor) structure exhibit good ionic conductivity approaching 10^{-3} S·cm^{-1} (e.g. $Li_{1+x}Al_xTi_{2-x}(PO_4)_3$ - LATP).[20] Perovskite type oxide electrolytes such as $Li_{0.5-3x}La_{0.5+x}TiO_3$ (LLTO) exhibit very high bulk ionic conductivity (10^{-3} S·cm^{-1}), but are limited by a much lower total ionic conductivity due to large grain boundary resistances that decreases the overall conductivity by up to two orders of magnitude.[21] Unfortunately, these electrolytes have very poor stability against lithium metal anodes due to Ti^{4+} being easily reduced. Garnet type oxide electrolytes such as $Li_7La_3Zr_2O_{12}$ (LLZO) has garnered a lot of attention because of its high ionic conductivity ($3x10^{-4}$ S·cm^{-1}) and excellent chemical stability against lithium.[22] The garnet electrolytes typically require a mechanical or chemical surface processing step due to build up of an insulating Li_2CO_3 layer that forms upon moisture exposure and increases the interfacial resistance.[23] Oxides in general also require high processing temperatures to form a densified pellet, which is also required to minimize the grain boundary resistances and achieve good ion conductivity. This makes the processing of these materials into a battery challenging.

Sulfide electrolytes in comparison are extremely ductile, allowing for simple cold-pressing

at room temperature. Some thio-LISICON (thio-Li Super Ionic Conductor) structures exhibit very high ionic conductivities that exceed 10^{-3} S·cm^{-1}. For reference, liquid electrolytes typically have an ionic conductivity of 10^{-2} S·cm^{-1}. Some examples are $Li_{10}GeP_2S_{12}$ (LGPS)[24] and the metastable phase $Li_7P_3S_{11}$,[25] which both exhibit an ionic conductivity up to 10^{-2} S·cm^{-1}. The compound $Li_{9.54}Si_{1.74}P_{1.44}S_{11.7}Cl_{0.3}$, which has the same structure as LGPS, is the fastest lithium ion conductor at room temperature with a total ionic conductivity of 2.5×10^{-2} S·cm^{-1}.[26] The argyrodite family (e.g. Li_6PS_5X where X = Cl, Br, I) are equally fast ion conductors with conductivity up to 10^{-3} to 10^{-2} S·cm^{-1}.[27,28] The downside of sulfides are the poor chemical stability with moisture in the atmosphere, which forms H_2S, requiring them to be handled in an inert atmosphere or dry room. These sulfides also suffer from poor electrochemical stability, especially at high voltage due to the oxidation of the S^{-2} anion at around 2.4 V vs Li/Li$^+$.[29] An overview of the various crystalline lithium (and sodium) ion conductors are shown in **Figure 1.5**. It's apparent that the fastest ion conductors are overwhelmingly thiophosphate-based (P-S) electrolytes.

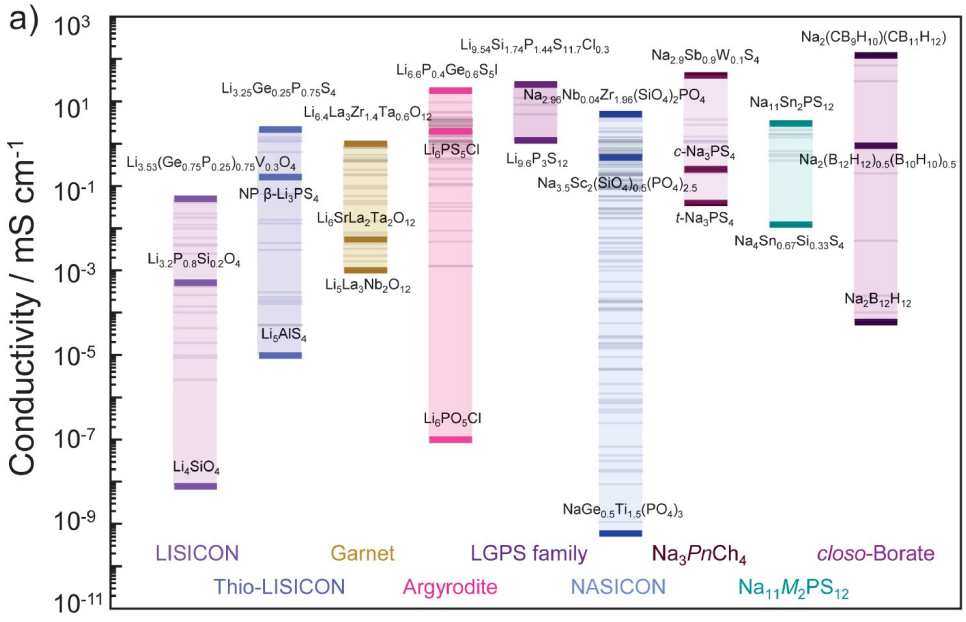

Figure 1.5: Overview of ionic conductivities for various classes of solid electrolytes. Certain compositions are highlighted, whereas grey lines indicate all found transport properties within the list of references. Reproduced with permission from IOP Publishing.[30]

1.3.2 Glass Electrolytes

In general, glasses have unique properties because of their lack of long-range order. Glasses do not exhibit a periodic arrangement of atoms and are thus amorphous. This leads to isotropic conduction that doesn't suffer from grain boundaries, which typically impede charge transport. Additionally, no grain boundaries means monolithic films of the glass material can be easily processed. However, despite the lack of grain boundaries, most glasses have poor ionic conductivity, especially in oxide-based systems. Furthermore, studying the structure of amorphous materials is incredibly challenging due to the lack of periodicity. There are a limited number of techniques that can characterize the local structure and thus the structure of glasses and its effect on ion transport is not well understood in comparison to its crystalline counterparts.

Some examples of glass electrolytes are lithium ortho-oxosalts that exhibit conductivities of 10^{-6} S·cm^{-1}.[31] The most well-known amorphous electrolyte might be LiPON (Lithium Phosphorous Oxynitride), which has the same order of magnitude in ionic conductivity and therefore is limited for use only in thin-film type batteries.[32] Sulfide glasses with mixtures such as Li_2S-GeS_2, Li_2S-P_2S_5, Li_2S-B_2S_3, and Li_2S-SiS_2 exhibit ionic conductivities of over 10^{-4} S·cm^{-1}.[33] Many studies also incorporate lithium halide salts into the sulfide glasses to further increase the ionic conductivity.

Glasses may also be able to address the mechanical criterion when pairing an electrolyte with lithium metal. Because thin, dense, and defect free films can be processed, dendrite formation and penetration through the separator might be mitigated by mechanical means. While dendrite growth has been observed in grain boundaries of polycrystalline materials such as LLZO, studies on defect-free regions of amorphous thiophosphate pellets have shown lithium deposition without any dendrite formation for current densities up to 5 mA·cm^{-2}.[34] A defect free amorphous film that does not contain grain boundaries and has minimal or carefully controlled surface defects may be a suitable method to mitigate dendrite penetration.

1.4 Design Considerations for Solid Electrolytes

1.4.1 Effect of Synthesis

The synthesis method has been shown to influence the structure of the material and thus the ion transport within it. Most solid electrolyte materials are synthesized by a solid-state route, mechanical alloying (ball milling), or solution synthesis. Ball milling has been shown to impact the local and average structure in thiophosphate materials such as Na_3PS_4.[35,36] Generally speaking, solid-state or ball-milled synthesized samples tend to be higher in ion conductivity than solution synthesized materials (**Figure 1.6**). The effect of solution

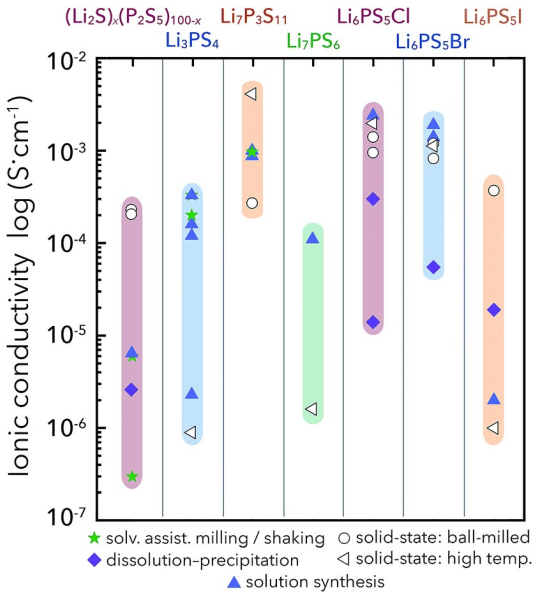

Figure 1.6: Overview of ionic conductivities for thiophosphate solid electrolytes obtained by various synthesis methods. Reproduced with permission from The Royal Society of Chemistry.[37]

synthesis is still unclear, however, it is suspected that solvent may be incorporated into the structure. Depending on the synthesis method, the ionic conductivity can vary by several orders of magnitude , which indicates that even subtle structural differences have a strong influence on conductivity, underlining the importance of studying the structure to better understand its effect on ion transport.[30,37]

1.4.2 Influence of Lattice Dynamics

It is typically assumed that a softer (i.e. more polarizable) anion sublattice leads to increased alkali ion mobility due to the weaker coulombic interactions between the cation and anion. Experimental studies on the "softness" of the lattice confirmed this by studying the material's Debye frequency[38] or phonon band center[39] (i.e. the average vibrational frequency) and correlating it to the ion conductivity. It was found that for many cases, a softer lattice does lower the activation energy barrier for transport but simultaneously decreases the prefactor for ionic motion.

This can be understood from the equation of the prefactor (1.5) and conductivity (1.6):

$$\sigma_o = \frac{zn(Ze)^2}{k_B T} exp\left(\frac{\Delta S_m}{k_B}\right) a_o^2 \nu_o \tag{1.5}$$

where z is the geometric factor for the structure (dimensionality of conduction pathways), n is the density of mobile charge carriers, Ze is the charge of the ions, k_B is the Boltzmann constant, T is the tempeature, ΔS_m is the entropy of migration, a_o is the jump distance, and ν_o is the jump frequency.

$$\sigma_{ion} = \sigma_o \cdot exp\left(-\frac{\Delta H_m}{k_B T}\right) \tag{1.6}$$

where ΔH_m is the enthalpy of migration and often generalized as the activation energy E_a.

When the lattice softness increases, it results in weaker interatomic forces, which results in larger atomic displacements of the mobile atoms and decreases the activation energy barrier for migration. This also decreases the prefactor because the increased displacement and softer lattice simultaneously lowers the jump frequency and the entropy of migration. The entropy of migration is affected by the changing vibrations of the sublattice. The decreasing prefactor that accompanies the decrease in activation energy is known as the Meyer-Neldel rule.[40] While the slope of this relationship may be related to the average phonon energies,[41] the exact origin of this relationship and the influence of the entropy of migration is not well understood.

1.4.3 Concerted Migration and Frustrated Energy Landscapes

The energy landscape of the structure ultimately dictates the ion mobility. Ideally, the structure should lead to a flatter landscape with a lower activation barrier for ionic motion. However, the origin for some of these observed flatter energy landscapes is not well understood. Theoretical work has suggested that self-correlation between mobile ions cause concerted migration of multiple ions with low energy barriers instead of the classical isolated ion hopping in solids.[42] Unfortunately, this has not yet been experimentally proven.

Alternatively, a flattened energy landscape can be described by the frustrated energy landscape concept. A frustrated energy landscape can occur by structural, chemical, and dynamic frustration (i.e. anion vibrational/rotational dynamics). Structural frustration is described by the disorder of the mobile ion over many available crystallographic sites (i.e. no lattice site preference). Chemical frustration arises from local vs average structural distortions in a material, which modifies the shape of the energy landscape at the saddle points and introduces anharmonicity into the energy wells. Dynamic frustration can also introduce distortions in the local energy landscape that stems from anion vibrational/rotational dynamics. The three different types are schematically shown in **Figure 1.7A-C**.

1.4.4 Inductive Effects

Recently, it was shown that chemical bonding interactions can be modulated to promote Li-ion diffusion.[43] The solid solution $Li_{10}Ge_{1-x}Sn_xP_2S_{12}$ was studied. Replacing GeS_4 anions with larger SnS_4 should widen the diffusion channels and lower the activation barrier. However, due to the inductive effect, the expected trend with respect to volume does not occur. The electronegativity of the central cation (M) changes the M-S bonding interactions. By putting more of the less electronegative element Sn, the Sn-S bonding is weaker (more polar) than the Ge-S bond, and the charge density on the Sn bonded S^{2-} increases. This charge redistribution strengthens the bonding of nearby Li^+ ions to the S^{2-} anion framework (Figure 1.7D), which increases the activation energy barrier and lowers ion conductivity.

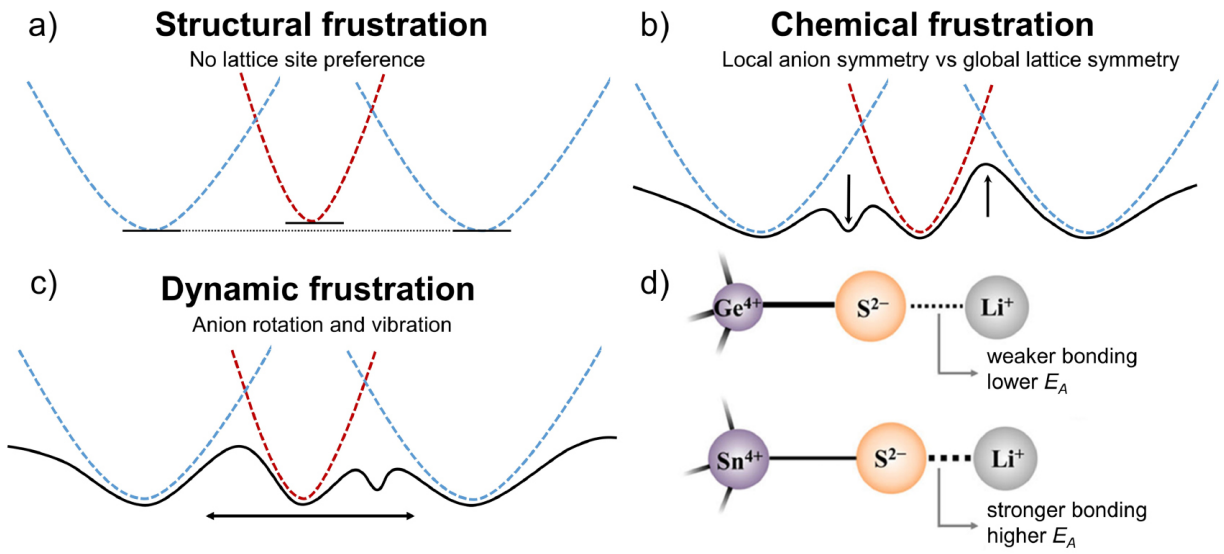

Figure 1.7: Possible frustrations that lead to flattened energy landscapes: (a) structural frustration, (b) chemical frustration, (c) dynamic frustration. (D) Schematic of inductive effects influencing ionic transport. Reproduced with permission from IOP Publishing.[30]

1.5 Thesis Objectives and Overview

It is abundantly clear that the development of new solid electrolytes will ultimately shape whether the ASSB becomes a commercial success; starting from the inherent properties of the material itself, to processing/preparation of the separating electrolyte layer, how it is mixed into the cathode, and what interphases form on each electrode. Thus, the question arises - is there one solid electrolyte to rule them all? Most likely, the best solution will involve multiple different electrolytes. No matter what approach is taken towards achieving ASSBs, more fast-ion conducting solid electrolytes must be developed that can tackle each or multiple of these issues at once. In order to discover new superionic conductors, a better understanding of the materials structures and the fundamental properties that govern ion conduction is also required.

Building a fundamental atomic scale understanding of these materials and what drives superionic conduction in them can assist in optimizing known materials or may serve as a guideline for discovering new ones. Moreover, since properties such as electrochemical

stability and mechanical stability are inherent to the materials structure, this knowledge can help develop new electrolytes to tackle some of the aforementioned interface problems.

This thesis focuses on two general goals of 1) the design and synthesis of new lithium ion conductors and 2) a deep understanding of the atomic structure and the properties that govern fast ionic diffusion in solid electrolyte materials. Both experimental and computational methods are utilized to explore the bulk electrolyte properties such as ion transport. Experimental techniques such as X-ray and neutron diffraction are invaluable to better understand the inherent structure and how it affects transport and stability. Density functional theory (DFT) calculations and *ab-initio* molecular dynamics (AIMD) simulations can also provide a microscopic viewpoint on thermodynamic stability, favorable kinetics, and atomic interactions at an interface.

Chapter 2 The background and theory for the experimental synthesis and characterization techniques that are employed for the studies in this thesis are described in detail.

Chapter 3 An *in-situ* neutron powder diffraction study is presented on Li_3PS_4, the archetype of the thiophosphate family of solid electrolytes. The phase transitions, the structure of the three polymorphs, and their corresponding lithium substructures are elucidated in detail.

Chapter 4 A new thiophosphate lithium-ion conductor, $Li_{1+2x}Zn_{1-x}PS_4$ was synthesized for the first time following computational predictions of exceptionally high lithium-ion conductivity. The effect of lithium interstitials and Li/Zn site disorder on ion conduction in this material was studied.

Chapter 5 Amorphous ion conductors are relatively unexplored in comparison to crystalline materials. Quaternary glass systems of Li_2S-B_2S_3-SiO_2-LiI were explored and new lithium oxythioborosilicate superionic glasses are presented. These glasses have the highest oxygen:sulfur ratios and the fastest lithium ion

conductivity of any known oxysulfide glass. Simultaneously, the higher oxygen content improves the moisture stability.

Chapter 6 A different class of solid electrolytes are explored that have intriguing properties similar to thiophosphates. New fast-ion conducting crystalline thioborate halides, $Li_{7.5}B_{10}S_{18}X_{1.5}$ (X = Cl, Br, I), were discovered that exhibit a superadamantanoid framework with massive channels of "glassy" or disordered Li cation and halide anions.

Chapter 7 The first thioboracite material was discovered by a quasi solid-state conversion process of a superadamantanoid phase. $Li_6B_7S_{13}I$ exhibits a perovskite topology and argyrodite-like lithium substructure that leads to high ionic conductivity. The fast lithium transport through the material is studied by combining computational and experimental techniques. The importance of controlling the grain boundary resistance is also highlighted.

Chapter 8 A summary of the advances made through the studies presented in this thesis and an outlook on future directions in the field of solid electrolytes and solid-state batteries.

Chapter 2

Characterization Methods and Techniques

2.1 Synthesis Techniques

2.1.1 Solid-state Synthesis

For preparation of solid electrolytes, exact stoichiometric quantities and pure starting materials need to be used. Solid-state reactions can be performed by flame, furnace, heated filament, ball mill, or microwave. In a typical solid-state reaction, an alkali or alkaline-earth metal compound with the desired anion is reacted with a metal halide, oxide, or sulfide. While there are many different types of solid-state synthesis routes, they will not be described here, as the synthesis of the materials described in this thesis primarily use the conventional method.

A conventional solid-state synthesis is one of the most widely used methods and is simply composed of mixing powders together and heating in a furnace for prolonged periods of time. Although the reactants are mixed well on a particle scale, the reaction itself is slow because the reactants are inhomogeneous on an atomic scale. High temperature heating,

long heating times, and repeated grinding and heating steps may be required to achieve complete reaction.

In general, a typical synthesis has several steps with the following considerations:

1. Select and weigh out starting materials in accurate stoichiometries
    - Starting materials with high purity and sufficient reactivity must be chosen.
    - For air and moisture sensitive reagents, purity becomes an important factor, and are stored and handled in a glovebox filled with inert gas to mitigate this issue.
2. Mix and pelletize
    - Precursors are ground in an agate mortar and pestle to achieve sufficient mixing. Sometimes liquid or gas phase transport may be used to bring atoms of different elements together to achieve mixing on the atomic scale.
    - The mixed reactants are pelletized to achieve close particle to particle contact, which can facilitate the reaction.
3. Heat
    - For annealing, factors such as heating rate, heating time, atmosphere, and crucible container all need to be considered.
    - The mixture cannot be heated under air if atmospheric sensitivity of the desired product is of concern. An inert atmosphere such as argon must be used, or the sample must be sealed under vacuum.
    - A container that does not react with the sample must be selected. Quartz tubes, alumina crucibles, or graphite/glassy carbon crucibles are commonly used.
    - The heating temperature is selected to avoid any volatilization of one or more of the reactants, while still being high enough to allow for reactions on a suitable timescale (several hours or days).

4. Grind and analyze products

    - Samples are typically analyzed by X-ray diffraction to confirm if the reaction is completed and no remaining unreacted precursors are present.

5. Repeat steps 2-4 if reaction is incomplete

2.1.2 Quenching

Thermodynamically stable solid solutions tend to exhibit a change in their solubility limits with a change in temperature, and thus cooling rate can be important to stabilize the solid solution at room temperature without any precipitation of secondary phases. High-temperature crystal phases can sometimes be metastable, making it difficult to synthesize by simple heating and cooling. In order to synthesize such materials at room temperature, they must be stabilized by rapid cooling, otherwise precipitation of secondary phases may occur. Most commonly this is done by quenching.

Glasses (i.e. amorphous materials), by definition, are always metastable. Melt quenching is the most common technique of glass making. Precursors are mixed together, heated up to high temperature (typically $\geq$700°) to form a melt, and then quenched (rapidly cooled) using an ice bath, liquid nitrogen, or a cooled plate. The quenched materials are sometimes annealed to remove internal stresses from the glass.

2.1.3 Mechanochemical Synthesis (Ball Milling)

Mechanical mixing techniques such as ball milling is extremely useful to intimately mix reactants on a level that cannot be achieved by simply grinding reactants in a mortar. A mixture of reactants is placed inside a rotating vessel with a number of balls. The balls and vessels can be made of a hard material such as agate, zirconia, or silicon nitride. The container is then spun for some period of time, typically in the range of hours or in some cases days. The constant impact between the balls and powder reduce the average particle size of the reactants while simultaneously producing an intimate mixture. Sometimes milling

is facilitated by the use of a liquid media, which is removed at the end of the milling process. Many factors such as speed, milling time, and size of the balls and jars need to be considered and have a major impact on the mixing of the reactants.

High-energy milling is achieved in planetary ball mills, which operate at very high speeds. Rather than using high-temperature, reactions can be carried out by aggressively grinding together reagents. It is still unclear exactly how solids react upon mechanochemical synthesis. In general, precursors are reduced to nanometer size particles with mechanically induced crystal defects. Despite no heating being applied, local heating with high temperatures occurs as the mechanical energy from ball to particle impact is transferred to heat. This local heating and reduced particle size speeds up inter-particle diffusion rates and formation of products. This is especially useful for targetting metastable materials that contain some compositional inhomogeniety, structural disorder, and high vacancy concentration.[44] Given the possible structural differences from mechanochemical synthesis, it is likely that properties may also differ.

2.2 Materials Characterization

2.2.1 Powder X-Ray Diffraction (XRD)

Powder XRD is a common technique to analyze crystal structures and is widely used for phase identification of crystalline materials. In 1912, Max von Laue discovered X-ray radiation can be diffracted by crystals as their wavelength is on the same order of magnitude as the interatomic spacing of crystal structures. When an incident beam of monochromatic X-rays interacts with the target material, the atoms from within the sample scatter X-rays. For materials with a crystalline structure, these scattered X-rays undergo constructive and destructive interference in what is called diffraction. Bragg's Law in Equation 2.1 describes the diffraction of X-rays:

$$n\lambda = 2d\sin\theta \tag{2.1}$$

This law relates the incoming parallel X-ray beams of wavelength λ to the diffraction angle formed θ and the lattice spacing of the crystalline sample d; the integer n refers to the order of diffraction and is typically unity. When Bragg's law is satisfied, the X-ray beams scattered from successive planes in the crystal (**Figure 2.1**) travel distances that differ by exactly one wavelength (for $n = 1$). These scattered X-rays interact constructively to form the diffracted beam.

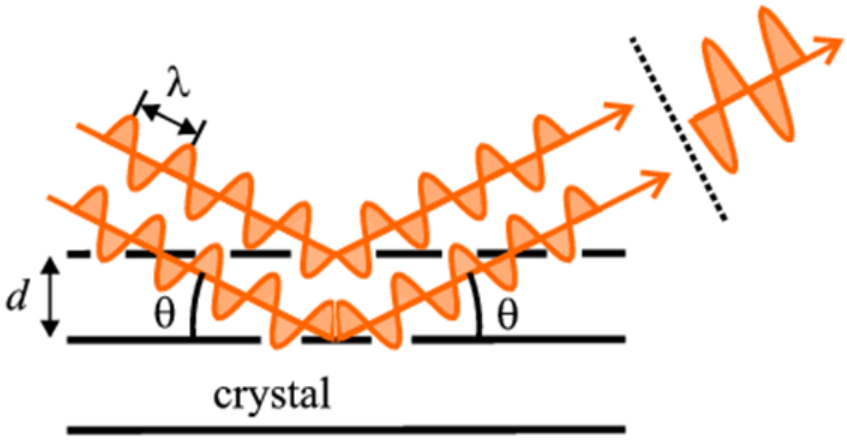

Figure 2.1: Schematic illustration of Bragg's Law.[45]

The diffracted X-rays are then detected, processed, and counted by a detector. By scanning through a range of 2θ angles we can account for all possible diffraction directions due to the random orientation of the powder material. The directions of the various diffracted waves depend on the size and shape of the unit cell of the material. The intensities depend on the type of atoms and their arrangement in the crystal structure.

Because X-rays are scattered by the electron clouds around the atomic nucleus, the intensity of the diffracted beam correlates to the number and position of electrons (i.e. the specific atoms). The structure factor can be used to calculate the intensity and is given by:

$$F_{hkl} = \sum_{n} f_n \exp[2\pi i(hx + ky + lz)] \tag{2.2}$$

where (hkl) are the Miller indices of the plane, (x, y, z) are the coordinates of the atom, f

is the atomic scattering factor that depends on the type of atom and scattering angle, and is sum over all atoms (n) in the cell.

The intensity of a specific reflection is then determined by the square of its structure factor. In practice, there are several specimen (particle shape, size, etc.) and instrumental factors that have an influence on the intensity. For simplicity, they are denoted as A here:

$$I_{hkl} = AF_{hkl}^2 \tag{2.3}$$

The most common method of measurement is using a flat-plate diffractometer, which makes use of reflection geometry (also referred to as Bragg-Brentano geometry). The X-ray source can be fixed and the sample and detector is rotated by θ and 2θ, respectively. Alternatively the sample is fixed and the source and detector move by -θ and θ, respectively. While flat sample holders are very easy to prepare, they may lead to preferential orientation effects, depending on the crystal shape. In general, it is not necessary to rotate powder samples because tiny crystals are randomly distributed and oriented through the powder. However, for certain crystals shapes (e.g. plate or rod shaped crystals), preferential orientation may occur where all the crystals are oriented in the same direction when packed, thus skewing the diffracted pattern intensities.

Alternatively, transmission geometry can be used, which is also known as Debye-Scherrer geometry. Samples are loaded into a capillary rather than packed in a flat stage, and the source and detector move by -θ and θ, respectively. This has the advantage of being able to run air-sensitive materials, since capillaries can be easily sealed under inert atmosphere to prevent exposure to the air. Furthermore the capillary is aligned and spun, removing any preferential orientation effects typically seen with a flat-plate diffractometer. The disadvantage is sample preparation is more time consuming, and diffracted intensities are generally weaker in transmission geometry, making data collection times longer.

2.2.2 Neutron Powder Diffraction (NPD)

Neutrons are diffracted by crystals in a similar manner as X-rays, and can also be equipped for single-crystal or powder diffraction. However, neutron powder diffraction (NPD) can give additional information regarding magnetic structure and greater contrast between some elements in the periodic table.

The scattering properties of an atom is determined by the interaction of the neutron spin (spin one-half) with the spin state of the nucleus of the atom. The spin-spin interaction can lead to coherent scattering or incoherent scattering. Coherent scattering is used in powder diffraction, leading to patterns similar to X-rays, which can be used for structure refinement using the Rietveld method. Incoherent scattering can be used for other types of analysis, but simply adds to the background noise for the purpose of neutron powder diffraction. Alternatively, neutrons can be absorbed by the nucleus of an atom. It's also possible for the spin of the neutron to interact with the spin of any unpaired electrons of an atom, which leads to magnetic scattering.

For neutron diffraction, the structure factor is given using the exact same equation as that for X-rays (Equation 2.2), except that the X-ray scattering factor, f, is replaced with the neutron scattering length, b. These two differ quite significantly because X-ray diffraction is due to the scattering by electrons of an atom, while neutron diffraction is due to scattering from the nucleus of an atom. While the X-ray scattering factor has a form factor that decreases with scattering angle, the neutron scattering factor is independent of scattering angle, 2θ. This means NPD patterns have no drop in intensity at smaller d spacings, unlike its X-ray counterpart. Thus, more precise atomic displacement parameters can be determined from neutron powder diffraction.

Additionally, b does not vary in a systematic way that f does. Thus, heavy elements that scatter well with X-rays may not necessarily scatter well with neutrons, or vice-versa. For example, natural Li scatters X-rays very weakly (f = 3 e^-/atom), but has a negative neutron scattering length (b = -1.90 fm), which provides invaluable elemental contrast in

the NPD patterns for detection of Li in a crystal structure. Note that this is for Li in its natural abundance, the isotopes of a given element have different scattering lengths. These differences between the two techniques allow neutron diffraction to provide complementary information when elements in a structure are difficult to distinguish by X-rays alone. For example, light X-ray scatterers as previously mentioned or distinguishing between two elements next to each other on the periodic table due to their similar X-ray scattering lengths.

Intense beams of neutrons are generated by either a nuclear reactor or a pulsed spallation source. These two methods differ quite significantly. Since neutron beamlines at the Spallation Neutron Source (SNS) at Oak Ridge National Lab (ORNL) were used for the studies described in this thesis, only pulsed spallation sources using the time-of-flight (TOF) method will be discussed in detail below.

The de Broglie equation relates the wavelength of a neutron, λ, to its momentum, mv:

$$\lambda = \frac{h}{mv} \tag{2.4}$$

where h is Planck's constant (6.626×10^{-34} J·s) and m is the mass of the neutron (1.675×10^{-27} kg). By measuring the time a neutron takes to move over a fixed path length we can find its velocity, and consequently its wavelength. This is known as the time-of-flight (TOF) method. Combining the de Broglie equation (Equation 2.4) with the Bragg equation (Equation 2.1) gives:

$$\lambda = \frac{ht}{mL} = 2d\sin\theta \tag{2.5}$$

where t is the TOF and L is the path length. Thus, if the start time of the neutron is fixed, only the arrival time at the end of the path length (i.e. the detector) needs to be measured. At the reactor source, a constant flux of neutrons is time sliced by a mechanical chopper.

Pulsed neutron sources use a supply of charged heavy particles, such as H^- ions, which are accelerated in a linear accelerator (called a Linac). Electrons are then stripped off to produce a proton beam, which is then further accelerated in a ring to higher energy

(accumulator ring). The beam is then diverted to collide into a heavy-metal target, resulting in spallation; the metal nucleus is destroyed into a few smaller nuclei plus several neutrons. These high energies correspond to high-temperatures, which produce epi-thermal (very hot) neutrons, as opposed to neutrons from a reactor source, which are called thermal neutrons. A moderator is then used to slow the neutrons down on their way to the instruments (i.e. the beamlines). A three-dimensional rendering of how the SNS facility is set up at ORNL is shown in **Figure 2.2**.

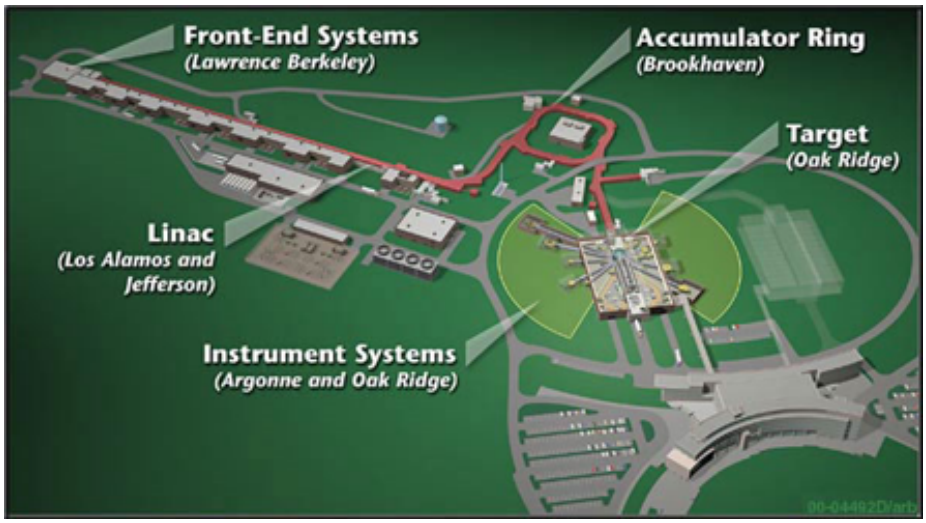

Figure 2.2: Three-dimensional rendering of the Spallation Neutron Source facility at Oak Ridge National Laborartory. Some components of the facility were developed in partnership by other US national labs and are labelled accordingly. Image courtesy of Oak Ridge National Laboratory, U.S. Dept. of Energy.[46]

2.2.3 Pair Distribution Function (PDF) Analysis

Pair distribution function (PDF) analysis is used to determine structural information of disordered materials by utilizing all the information in the powder diffraction pattern. It is commonly used in amorphous or nano-materials, where disorder is dominant or long-range order does not exist. The Bragg scattering and the diffuse scattering in the measured pattern are both used in the analysis. Thus, this technique is sometimes referred to as total scattering analysis since it provides information on both long range ordering and local

structure. Long-range order is deduced from the Bragg peaks while short range order such as local distortion can be deduced from the broad underlying features in the diffractogram. The structure is then described by the atomic pair distribution function, which can be used to describe the local structure.

The pair distribution function describes the probability of finding a correlation at a specific distance in real space (i.e. two atoms bonded at a certain distance), which is illustrated in **Figure 2.3**. It is determined from the Fourier transform of the total coherent scattering function $S(Q)$ and is defined as:

$$G(r) = \frac{2}{\pi} \int_{Q_{min}}^{Q_{max}} Q[S(Q) - 1] sin(Qr) dQ \tag{2.6}$$

$S(Q)$ is obtained from the scattering intensity/total scattering cross section. Because the underlying diffuse scattering is crucial for the analysis, extremely good signal to noise is required with minimal background contribution from the measurement setup. Factors that affect the background such as the sample environment and container, incoherent scattering, absorption, and fluorescence all need to be taken into account. Thus, $S(Q)$ is corrected for these various factors and normalized by the incident flux, number of atoms, and square of the scattering length (neutrons)/atomic form factors (X-rays).

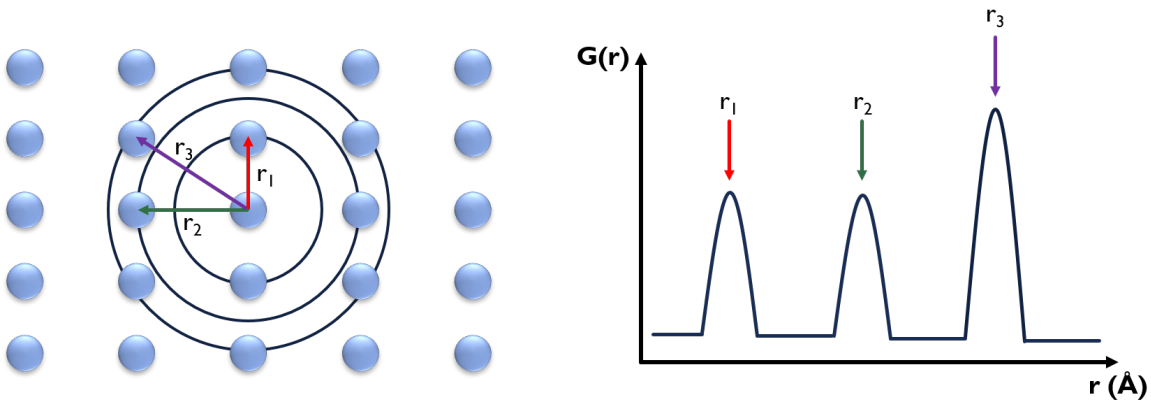

Figure 2.3: PDF construction from the atomic interaction between the center atom and first, second, and third nearest neighbours.

PDF analysis requires measurement up to a high Q-range, which means large diffraction angles and short wavelength (high energy radiation) are required. These types of measurements are usually performed at a synchrotron for high quality and high energy X-ray beams or at a TOF neutron diffractometer where high Q measurement are possible. Recently, there has been some progress in PDF measurements on laboratory X-ray diffractometers, although the data quality is still quite limited in comparison to measurements on a synchrotron or neutron TOF diffractometer.

Simple inspection of the PDF can provide lots of insight. The PDF is presented in real-space and is a straightforward representation of the atomic structure. The observed distances describe bond lengths between atomic pairs while the peak widths can be used to identify thermal motions and static disorder. The integrated intensity also contains information about the coordination number of the atoms. For detailed analysis, small box or large box modeling can be performed to fit the PDF and precisely determine the structure of the disordered materials in question. Small box modeling utilizes a crystal structure and can be considered a "real space Rietveld refinement", where parameters and constraints can be used to fit a model to the PDF pattern. The disadvantage is it may be difficult to find solutions to highly distorted systems. Large box modeling with thousands of atoms utilizes less constraints and can be very useful to explore such structures (e.g. amorphous materials), however, it is extremely difficult due to the possibility of overfitting or degenerate solutions.

2.2.4 Raman Spectroscopy

Raman spectroscopy provides information regarding vibrational and rotational modes in a system, thus providing spectral lines that are inherent to specific groups of atoms within a structure. These molecular vibrations can be used for sample or structural identification. Monochromatic light from a laser is shone on a sample where photons will either undergo elastic scattering (Rayleigh scattering) or interact with the material and undergo inelastic scattering (Stokes-Raman scattering). The inelastically scattered photons causes a shift in the frequency equivalent to the vibration frequency of the molecules, which is then detected

and used to generate the Raman spectra. The elastically scattered photons are filtered out.

Raman scattering can be thought of as a two-photon process. Electrons have different vibration levels with specific energy differences. When an electron absorbs energy from an incident photon, it rises to a virtual energy state. The electron then falls back to a lower energy level by losing some energy. Rayleigh scattering is when the electron fall back to its initial energy level by emitting a photon (energy lost equals energy of incident photon). Sometimes electrons can fall back to a different energy level (energy lost does not equal energy of incident photon) and the emitted photon has a different frequency (ν_s) than the incident photon (ν_i). This is known as Raman scattering. Raman scattering can be separated into Stokes lines ($\nu_s < \nu_i$) when the electron absorbs energy or anti-Stokes lines ($\nu_s > \nu_i$) when the electron releases energy.

A Raman spectrum contains a number of peaks that have some intensity and position of the Raman scattered light that corresponds to a specific bond vibration such as individual bonds (e.g. C-C, C=C, C-H, etc.) or groups of bonds such as ring breathing modes, polymer chain vibrations, or lattice modes. The spectra can be used as a chemical fingerprint to identify chemical structures and phases. In some systems, Raman mapping is possible to look at distribution of phases or variation within a sample.

2.2.5 Solid-state Nuclear Magnetic Resonance (NMR)

High-resolution NMR of solids has been implemented for many different types of experiments. For glasses, solid-state NMR is particularly useful to study their structures as the lack of long-range order prevents the use of typical diffraction techniques. In this section, the background theory will focus on the interactions in the solid state and the Magic Angle Spinning (MAS) technique, since this was the NMR technique used in this thesis.

NMR spectroscopy for solutions is extremely powerful to investigate the chemical structure by studying the chemical shifts, couplings, and relative intensities of the resonances in their spectra. NMR spectra in solids by comparison are not so well defined, typically

showing broad features. In high-resolution NMR experiments, the goal is to manipulate the spin systems to remove or average the characteristic solid-state interactions in order to simplify the spectrum to a point where chemical information can be inferred from the spectrum for structural investigations. In the solid state, the different interactions that can occur for a nuclear spin are dependent on the orientation of the nuclear spin vector to the magnetic field, where the random distribution of possible orientations gives rise to significant spectral broadening. The different interactions that can occur are briefly described below.

- Zeeman Interaction: Results from the interaction of the magnetic moment of the nucleus μ_N with the applied static magnetic field H_o. It causes the initial splitting of the energy levels of the nucleus, and determines the observed frequency of a particular nucleus for a given magnetic field and strength, and the detection sensitivity of that nucleus.

- Dipolar Interaction: Results from the interaction between two like or unlike spins. In a single crystal, this would lead to separated peaks that depend on the gyromagnetic ratio of the nuclei (γ), the distance between the two nuclei (r), and the angle (θ) between the the internuclear vector and the magnetic field. For a polycrystalline material, the interactions must be averaged over all angles of θ due to the random distribution of crystallites and thus internuclear vector orientations. These two factors lead to severe field-independent broadening of the spectrum.

- Chemical Shift Interaction: The chemical shift in NMR provides information about the local structure surrounding the nucleus. It is caused by the electrons surrounding the nucleus, which modifies the applied magnetic field experienced by the nucleus. This slightly changes the difference between the energy levels on the order of Hz (in comparison to the Zeeman interactions that are on the order of MHz). Averaging over all possible random orientations in a polycrystalline sample produces a field-dependent broadening.

- Spin-spin Coupling: The interaction between two nuclear spins from the indirect electron-coupled spin-spin interaction. This is also called scalar coupling (electron coupled). Interactions are mediated through bonds rather than space like in dipole interactions. This term is small in most cases but may be important for studying chemical structures. These interactions are important for spin ½ nuclei, while for nuclei with spin >½, quadrupolar interactions must also be considered.

- Quadrupolar Interactions: A quadrupole can be represented as two dipoles. Within the nucleus of an atom, the charge can be distributed symmetrically (spin ½) or asymmetrically (spin >½). Nuclei with spin I>½ (quadrupolar nuclei) exhibit a quadrupolar moment, which arises from the interaction between the nuclear spin and a non-spherically symmetric electric field gradient at the nucleus, resulting in extensive peak broadening.

In solution NMR spectra, fast rotational and translational motion of molecules average the interactions. This leads to dipolar and quadrupolar interactions not being observed, while isotropic chemical shifts and spin-spin couplings can be used for structural determination. For obtaining high-resolution solid-state spectra, experimental procedures must be implemented to remove the dipolar interaction and produce isotropic average values like in solution.

Chemical Shift Anisotropy: Magic Angle Spinning (MAS) Technique

Chemical shift anisotropy is a major interaction for spin ½ nuclei. The chemical shift interaction has an orientational dependence, which for a powder sample means there can be severe asymmetric broadening. An asymmetric local electronic environment surrounding the nucleus causes these peak shapes. In single crystals, this contains useful information of the three-dimensional chemical shielding, and can be related to the coordination environment and detailed nature of the bonding of the nucleus.

Using the magic angle spinning (MAS) technique, the anisotropic spectrum can be averaged to the isotropic value. The sample is spun around an axis inclined at angle θ

to the magnetic field axis at a frequency comparable to the frequency spread of the shift anisotropy (typically on the order of tens of kHz). Effectively, the experiment modifies the shift anisotropy by a factor of $3cos^2\theta - 1$. If $\theta = 54.74°$ (the "magic-angle"), this term becomes zero, leaving only the isotropic chemical shift. This setting also removes the dipolar interactions. If the sample is spun fast enough at a rate equal to the size of the chemical shift anisotropy, a single isotropic average peak will be observed. Spinning at slower rates will yield a spectrum with an isotropic peak plus spinning side bands separated by spinning frequency.

MAS at High Magnetic Field

There is often an advantage of carrying out MAS experiments on inorganic systems at high field strengths. For spin ½ nuclei there can be substantial improvement in resolution partly due to the high quality superconducting solenoid magnets used. Also, dipolar and quadrupolar interactions will be minimized at high magnetic fields, while the chemical shift dispersion is maximized.

Quadrupolar nuclei with non integral spins such as ^{11}B or ^{27}Al also have advantages when working at high magnetic fields. For example, the line shape for a nucleus with spin ⅜ is mainly distorted and shifted due to the second-order quadrupole interaction, which is inversely dependent on the magnetic field. Thus, undesired shifts and line shape distortions are minimized at high magnetic fields.

2.2.6 Differential Scanning Calorimetry (DSC)

Differential scanning calorimetry (DSC) measures the energy absorbed (endotherm) or produced (exotherm) from a material as a function of time or temperature. DSC can be used to provide information on a materials melting, crystallization, glass transition, degree of crystallinity, crystallization kinetics, purity, and oxidative stability. Basically, any process involving an energy change can be studied. The system is usually purged with inert gas during the measurement.

In a DSC instrument, the sample and reference, with identical pans, are placed on individual thermally conducting bases. A thermocouples is attached to each base. There are two types of DSC based on their method of operation: power compensation and heat-flux. In a power compensation DSC, electrical energy provided to the heaters below the pans is measured and adjusted to maintain the two pans at the same temperature. The focus of this section will be on a heat-flux DSC, since that was the type of instrument used for the DSC measurements described in this thesis.

Typically the reference is an empty pan and the sample is loaded into an identical pan. To remove the effects of the instrument, the heat flow from an empty reference pan is compared and subtracted from the heat flow from the sample. The heat flow of the sample is determined by measuring the difference in temperature between the two pans (ΔT) during the heating program. The heat flow (q) can be found by dividing ΔT by the resistance of the thermoelectric disk (R) connected to the base of the pans. This equation can be further modified by applying correction terms to account for differences between the sample and reference resistances and heating rates.

Interpreting the DSC Curve

DSC alone can provide a lot of thermal information on a material but it is especially powerful when combined with additional techniques such as Thermogravimetric Analysis (TGA) to measure mass loss or Gas Chromatography-Mass Spectrometry (GC-MS) to evaluate off-gassing. A flow chart in **Figure 2.4** outlines the general interpretation of DSC curves and provides a guideline for identify different processes.

Baselines are complicated and not easy to establish. There is typically some initial variation of the baseline that comes from mismatch of thermal properties between the sample and reference or from the instrument bases. After a thermal event, there may be some deviation in the baseline in comparison to before the event if the thermal properties of the the sample at the elevated temperature differs from the thermal properties of the low-temperature state. Abrupt changes in slope or position of the baselines are usually

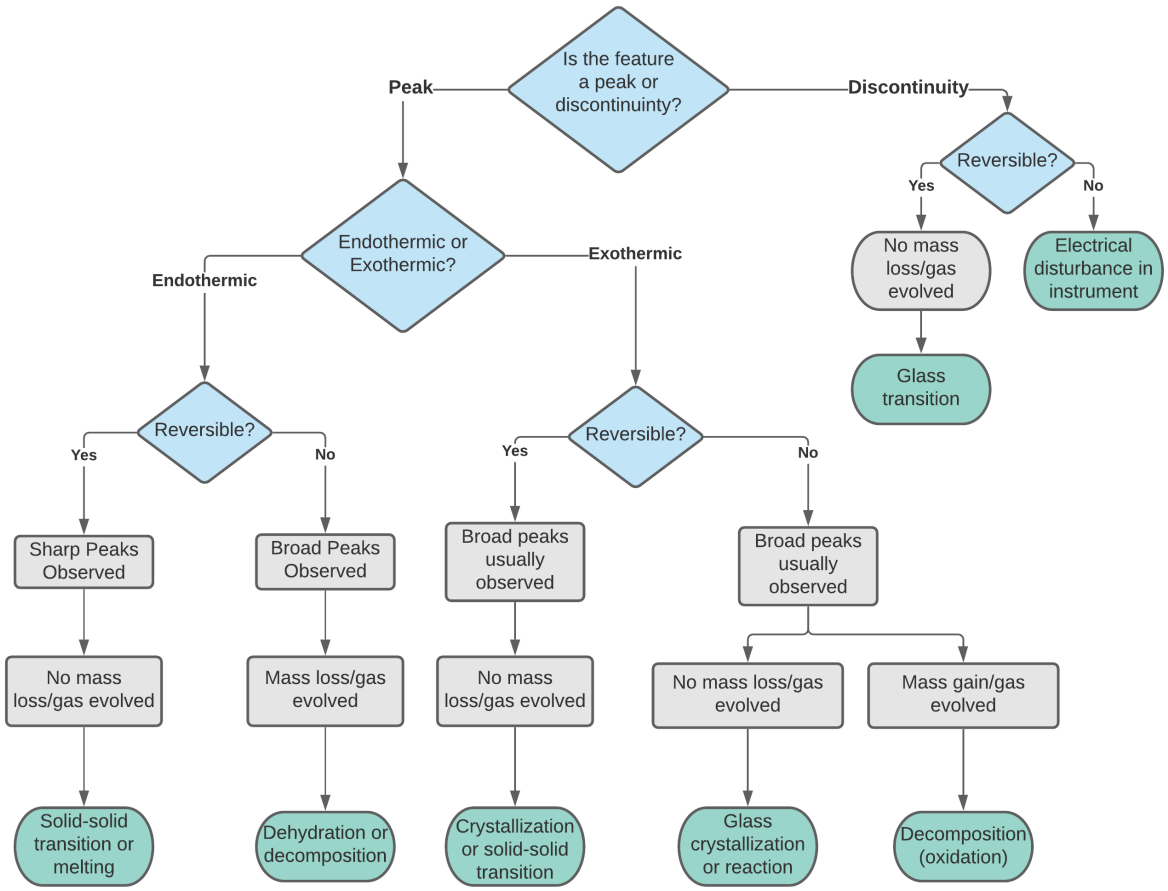

Figure 2.4: Flow chart outlining interpretation of DSC curves.

interpreted as second order transitions such as the glass transition temperature, where the enthalpy change (ΔH) is zero but there is a change in the heat capacity.

Endothermic and exothermic peaks are easier to identify. A sharp endothermic peak is typically indicative of melting and is characterized by its onset position because the peak apex (T_{max}) is dependent on heating rate or sample size. For impure substances, the endotherms are broad and it is possible to estimate the impurity content from a detailed shape analysis. Some exothermic processes are not always reversible, in contrast to melting and many solid-solid phase transitions. DSC can also provide quantitative information on the processes. For example, the enthalpy change (ΔH) can be determined by the peak area

in both exothermic or endothermic peaks. By heating and cooling the sample, it is possible to determine if a process is reversible or not.

Heating and cooling rates have a strongly influence on the signal quality as well. Transitions such as evaporation, crystallization, melting, and decomposition are kinetic events. Faster heating rates shift these peaks to higher temperature because the total heat flow increases linearly with heating rate due to the heat capacity of the sample. Thus, increasing the heating rate increases sensitivity, while decreasing the scanning rate increases resolution.

2.3 Electrochemical Techniques

2.3.1 Solid-State Cell Configuration and Assembly

The positive electrodes are commonly prepared by hand mixing the cathode active material and solid electrolyte. A solid electrolyte separator layer is first compressed, and then the composite of the positive electrode is compressed on top of the solid electrolyte. The other side of the solid electrolyte is interfaced with a lithium-indium alloy as the negative electrode.

2.3.2 Cyclic Voltammetry

Cyclic voltammetry (CV) is commonly used to investigate the reduction and oxidation processes of a material where current is measured as a function of the applied potential. The potential is first changed negatively, starting from a greater potential and ending at a lower potential. The potential extrema is called the switching potential, and is the point where the voltage is sufficient to have caused an oxidation or reduction of the material being analyzed. The reverse scan occurs after, where the potential scans positively and reverts the oxidation or reduction process.

A cyclic voltammogram is obtained by measuring the current and shows the redox reactions occurring in the cell. From the area and the width of the peaks, information about

the amount of material involved and the kinetics in the reactions can be inferred. However, this information will be used qualitatively in comparison to the quantitative data drawn from the galvanostatic cycling

2.3.3 Galvanostatic Cycling

This is the standard technique used to charge and discharge a battery. A potential window is defined and a constant current is applied to discharge the battery and then reversed to charge it again. The performance of a battery is determined as a function of its charge and discharge conditions: a given rate, within a given potential range. The cycling rate (C-rate) is usually expressed as C/h, where h is the number of hours it takes to be fully charged/discharged. For example, 1C is 1 hour to fully charge or discharge the cell, while C/10 would be 10 hours for a full charge or discharge.

One typically considers the specific capacity of the electrode material per weight (mA·h/g for example). Long-term performance is evaluated by the retained specific capacity values as a function of cycle numbers. Adjusting the cycling rate by increasing the current applied can also provide useful information regarding the performance behaviour.

Galvanostatic cycling will result in a charge/discharge voltage profile, as a function of specific capacity. A minimum voltage difference between charge and discharge is ideal to maximize energy efficiency, as it is indicative of good performance. The following parameters are typically calculated and evaluated after performing the galvanostatic cycling:

- Potential and Cell Voltage - the free energy of the half reaction ΔG is given by Equation 2.7, where n is the number of electrons involved in the reaction, F is Faraday's constant, and E^o is the standard reduction potential. The cell voltage is given by the difference of the standard reduction potential for the half cell at the positive electrode minus the negative electrode ($E_{cell} = E^o_+ - E^o_-$).

$$\Delta G = -nFE_{cell} \tag{2.7}$$

- Specific Capacity (mA·h/g) – as described in Equation 2.8, is defined by the amount of charge in milliamp-hours stored per mass of electrode for one full discharge/charge (capacity divided by the mass of active material)

$$\text{Specific Capacity} = \frac{\text{Capacity (mA·h)}}{\text{Mass of Active Material (g)}} \tag{2.8}$$

- Energy Density (W·h/kg) – battery energy in watt-hours per unit mass (product of capacity and voltage per mass)

- Capacity Retention –the ability of the cell to achieve a reversible specific capacity over a defined number of cycles (usually expressed as a fraction or percentage of the first cycle)

- Cycle Life – the number of discharge-charge cycles the battery can experience before it fails to meet specific performance criteria (typically 80% of specific capacity)

- Coulombic Efficiency – ratio of the discharge specific capacity to the charge specific capacity of the same cycle, compared over many cycles

2.3.4 Electrochemical Impedance Spectroscopy (EIS)

Electrochemical impedance is determined by applying an AC potential to a cell while measuring the current in the cell. The electrolyte material is pressed into a pellet and placed in a cell between two metal blocking electrodes. Typically, a sinusoidal potential is applied producing a response as an AC current signal. The excitation signal is sufficiently small to ensure the cell's current response is pseudo-linear. In linear systems, the current response to a sinusoidal potential will be shifted in phase. The impedance is expressed as a real and complex number. The data is plotted as a Nyquist plot, with the real part on the x-axis and the imaginary part on the y-axis. Another popular representation is the Bode plot where the impedance is plotted with log frequency on the x-axis and the absolute values of the impedance as well as the phase shift on the y-axis.

For impedance measurements on solid electrolytes, the Nyquist plot is composed of one or more semicircles in the high frequency range, corresponding to bulk resistance and capacitance, and the grain boundary resistance. After the semicircle, at low frequencies, a straight line is seen that correlates to the overall resistance of the material. This straight line is a result of diffusion that creates an impedance called a Warburg impedance. At lower frequencies, reactants have longer diffusion distances, thus increasing the Warburg-impedance.[47]

First, the pellet surface area (SA) in contact with the electrode, and pellet thickness (t) is measured. Once the resistance (R) is calculated, either by fitting the Nyquist plot to a corresponding circuit, or by extrapolating the linear part to the intersection with the x-axis, the ionic conductivity (σ) can be calculated using Equation 2.9:

$$\sigma = \frac{t}{R \times SA} \tag{2.9}$$

2.4 Computational Techniques

First principles calculations are widely used in studying the fundamental properties of materials. These simulations, based on the fundamental quantum physics of interaction between atoms, can be used to study the physical and chemical properties of materials to develop valuable understanding and insights as well as assist in the interpretation of experimental observations. The computational techniques carried out in this thesis were performed using the VASP software.[48]

2.4.1 Density Functional Theory (DFT)

To find the ground state of a collection of atoms we must solve the many-body Shrödinger equation:

$$\widehat{H}\psi = E\psi \tag{2.10}$$

This describes our system of atoms that are composed of a nuclei and electrons. E is

the energy of the system and $\widehat{H}$ is the Hamiltonian, which is an energy operator (kinetic and Coulombic interaction terms) applied to the wavefunction ψ. Solving the equation is extremely complicated due to the significant number of interactions between nuclei and electrons. To simplify this we apply the **Born-Oppenheimer approximation**, which decouples the dynamics of the nuclei and electrons by treating the nuclei as fixed. The time electrons need to find the ground state is significantly faster than the rate the nuclei can move and it can be considered that the electrons only see the external potentials of a static nuclei. Thus, ψ is decoupled into a nuclei and electron wavefunction and we can focus on solving the ground state of the electrons for a fixed set of atomic positions.

For solids and systems with many atoms, solving the electron wavefunction is still a challenge because of the large number of electrons. To simplify this further we can consider the electron density, which can be observed or measured. This reduces the problem from 3N dimensions to the 3 spatial dimensions of the electron density. Then, we can consider the electron as a point charge in a field with all the other electrons, which simplifies the many-electron problem to many single-electron problems:

$$\psi(r_1, r_2, r_3 ... r_N) = \psi_1(r_1) * \psi_2(r_2) * \psi_3(r_3) * ... * \psi_N(r_N) \tag{2.11}$$

Using the individual electron wave functions, the electron density can be defined as:

$$\rho(r) = 2 \sum_i \psi_i^*(\mathbf{r}) \psi_i(\mathbf{r}) \tag{2.12}$$

At the heart of DFT are the **Hohenberg-Kohn theorems**, which states that ground state energy is a unique functional of the electron density (i.e. E = E[$\rho(r)$]). Thus, the electron density is all that is required to define the ground state energy and the electron density that minimizes the energy of the overall functional is the true ground state electron density. In other words, the ground state density can be found by minimizing the energy functional.

The energy functional can be divided into two parts - one that is known and one that

is unknown:

$$E(\psi_i) = E_{known}(\psi_i) + E_{xc}(\psi_i) \tag{2.13}$$

The known part is composed of the kinetic energy term and the potential energy terms that come from the Coulombic interactions. The unknown part is the exchange-correlation functional (E_{xc}) that takes care of the quantum mechanical interactions between electrons. Unfortunately, this is not known and needs to be approximated. The simplest exchange-correlation functionals are the local density approximation (LDA), which is based on local electron density, and the generalized-gradient approximation (GGA), which accounts for the gradient of the electron density.

To obtain the ground state in practice we can use the **Kohn-Sham approach**. First, we consider a set of single-electron wavefunctions in a non-interacting system. The interactions are implicity accounted for in these potentials:

$$[-\frac{\hbar}{2m}\nabla^2 + V_{ext}(\mathbf{r}) + V_H(\mathbf{r}) + V_{xc}(\mathbf{r})]\psi(\mathbf{r}) = \epsilon_i(\mathbf{r})\psi_i \tag{2.14}$$

where the ∇^2 operator on the wavefunction ψ gives the independent particle kinetic energy, (V_{ext}) is the external potential acting on the electrons due to the nuclei, V_H is the Hartree (or Coulomb) potential that describes the electron interacting with the electron density, and V_{xc} is the approximated exchange-correlation potential that describes the interactions among electrons.

We start with some trial or initial guess for the electron density and utilize a self-consistency scheme. Using the trial density we can solve the set of Kohn-Sham equations (one equation for each electron). Then, the obtained set of wavefunctions can be used to recalculate the electron densities using **Equation 2.12**. This obtained electron density is compared to the inputted density, and if it has converged to an acceptable degree of tolerance, self-consistency is achieved and the ground state is found. If it has not converged, the obtained electron density is used as the new initial density and looped through until it

is converged.

Plane-wave DFT is typically used in periodic systems. In a crystal, there is a periodic arrangement of atoms that has a periodic potential. In general, free electrons are represented by a plane wave. Using Bloch's theorem, the electrons in a periodic potential can be considered as Bloch waves (i.e. perturbed free electrons) to give the electron wave function in the crystal:

$$\psi_{n\mathbf{k}}(\mathbf{r}) = e^{i\mathbf{k}\cdot\mathbf{r}} u_{n\mathbf{k}}(\mathbf{r}) = e^{i\mathbf{k}\cdot\mathbf{r}} \sum_{G} c_{\mathbf{k}} e^{i\mathbf{G}\cdot\mathbf{r}} \tag{2.15}$$

where $\mathbf{k}$ is the plane waves modulated by some periodic potential $u_{n\mathbf{k}}(\mathbf{r})$ within the lattice and is expanded as a sum of plane waves in reciprocal space given by the reciprocal lattice vectors $\mathbf{G}$. Numerically, a cutoff energy needs to be defined in practice to truncate the infinite expansion. The plane wave vectors span the reciprocal space and integration of the plane-wave basis functions occurs over the 1st Brillouin zone. Thus, in practice an appropriate number of k-points must be selected to sample the Brillouin Zone. Both the energy cutoff and k-point density need to be carefully chosen to ensure convergence in the DFT calculation while simultaneously keeping the computational cost low.

Finally, chemical bonding and other properties of the material are typically determined from the interaction of the valence electrons. To simplify and make the calculations more computationally feasible, the core electrons are "frozen" and the electron density of the core is represented as a smoothed density in a pseudopotential. This is typically pre-calculated and provided in libraries with the DFT software.

2.4.2 *Ab-initio* Molecular Dynamics (AIMD)

Molecular dynamics simulations are used to study the motion of atoms or molecules (i.e. the time-dependent behaviour of a system). Interaction between atoms and molecules in a system are simulated over a specific time period that allows us to study a dynamic picture of the system. At each discrete step, atoms and molecules are moved along trajectories that follow Newtonian dynamics. The forces acting on the particles and the potential energy of

the system can be determined using empirical interatomic potentials or quantum mechanical formulism. The former is referred to as classic molecular dynamics (MD) and the latter is known as *ab-initio* molecular dynamics (AIMD). For studying solid electrolytes, AIMD is more suitable than classical MD because of the limited accuracy of empirical potentials. Many approximations are made to develop these empirical potentials and may need to be re-developed from material to material. AIMD utilizes quantum mechanical methods such as DFT to evaluate the interatomic potentials. The tradeoff is AIMD is much more computationally expensive than classical MD.

From classical physics, a particle at position $\mathbf{r_o}$ and velocity $\mathbf{v_o}$ that feels a force $\mathbf{F}$ over a time t is moved to a new position $\mathbf{r}$(t):

$$\mathbf{r}(t) = \mathbf{r}_o + (\mathbf{v}_o(t) + \frac{1}{2}\mathbf{a}t^2)) \tag{2.16}$$

where $\mathbf{a}$ is the acceleration (which equals $\mathbf{F}$/m) and is assumed constant over the time interval t. However, in reality $\mathbf{a}$ is not constant, so this is considered an approximation. A smaller timestep would lead to a better approximation but longer computation time, so an appropriate timestep must be chosen carefully. The force $\mathbf{F}$ that acts on a particle comes from the derivative of the potential energy for the ions in the system, which is in part determined from the electron interactions solved by DFT.

A molecular dynamics simulation cam be run in a microcanonical ensemble (NVE) where the temperature is not controlled, or a canonincal ensemble (NVT), where the temperature is controlled by a thermostat. The choice of ensemble depends on the properties that are to be studied. For an NVT ensemble, thermostat algorithms can be used to control the temperature of the simulation since temperature is related to particle velocities. One such algorithm that is commonly used is the Nose-Hoover thermostat, which employs a "heat bath" as an additional variable and introduces a variable called a friction coefficient that is used to slow down or accelerate particles until the temperature reaches the desired value.

Chapter 3

Impact of the Li substructure on the diffusion pathways in α and β-Li_3PS_4: an *in-situ* high temperature neutron diffraction study

This section is reproduced in part with permission from the Royal Society of Chemistry: Kavish Kaup, Laidong Zhou, Ashfia Huq, and Linda F. Nazar, *Journal of Materials Chemistry A*, **2020**, 8, 12446-12456 (DOI: 10.1039/D0TA02805C)

* Laidong Zhou synthesized the $Li_{3.25}Si_{0.25}P_{0.75}S_4$ material.

* Dr. Ashfia Huq provided guidance for the in-situ neutron diffraction measurements at Oak Ridge National Lab.

3.1 Introduction

Among all the sulfidic electrolytes, Li_3PS_4 is prominent for its excellent (quasi)stability with lithium metal, ease of processability, and the decent ion conductivity of the β-polymorph.[49] Li_3PS_4 is considered the archetype of the thiophosphate solid electrolyte family today, and has been the subject, or launching point, of many experimental and computational studies.[50–52] It exists as three polymorphs: γ, β, and α. The bulk γ phase exhibits extremely low room temperature ionic conductivity - around 3×10^{-7} S·cm^{-1} - while at higher temperatures the γ phase transforms into the more conductive β phase, followed by conversion to the α-phase. The β phase can be stabilized at room temperature as a nanoporous form (via solution synthesis in THF) that exhibits a higher ion conductivity, on the order of 10^{-4} S·cm^{-1}.[53] Other solution-based syntheses have given similarly positive results,[37,54–57] and the ionic conductivity of these materials may still be improved by engineering the grain boundaries, an important area of research in fast-ion conducting materials.[58–60] It has also recently been shown that a "β-like" phase can be stabilized at room temperature via silicon substitution on the phosphorus site, increasing the conductivity up to 10^{-3} S·cm^{-1}.[61]

Numerous experimental studies on the parent Li_3PS_4 structures and their derivatives have used techniques such as X-ray Diffraction (XRD) and Nuclear Magnetic Resonance (NMR)[51,62] in conjunction with *ab initio* molecular dynamics (AIMD) and Density Functional Theory (DFT) calculations[50,63–68] to develop an understanding of the relationship between structure and properties. Homma *et al.* studied the phase transitions and structures of the polymorphs using synchrotron XRD.[69,70] However, lithium scatters poorly by X-rays owing to its low electron density and can result in ambiguity for the lithium siting, occupancies, and atomic displacement parameters (ADPs). To solve this issue, neutron diffraction is used to resolve lithium ions in a crystal structure, but because such studies have not been applied to the bulk β and α-Li_3PS_4, their structures remain incomplete. The structure of β-Li_3PS_4 was apparently solved by single crystal X-ray methods at 25°C,[71] but some degree of (Si + Li) substitution for P was clearly accidentally responsible for its

stabilization at this temperature,[61] since below 200°C, only the γ phase exists even with quenching. More significantly, the Li sublattice of the α-phase has never been resolved; early XRD studies were able to identify only one lithium site in the unit cell.[69,70] No complete experimental structure of α-Li_3PS_4 exists to date. As recent calculations have predicted that the α-phase may have true superionic conductivity - up to 8×10^{-2} S·cm^{-1} if it could be stabilized at room temperature[72] - it is of keen interest to determine the Li substructure in this lattice, and understand the Li-transport pathways. Such knowledge may be helpful to envisage if (and how) stabilization of α-Li_3PS_4 under ambient conditions could be possible.

In this work, *in-situ*, variable temperature, high resolution neutron powder diffraction (NPD) studies are performed on several Li_3PS_4 related materials - bulk Li_3PS_4, nanoporous β-Li_3PS_4, and Si-substituted Li_3PS_4 - to elucidate the structural differences of each composition that lead to fast-ion conductivity (summarized in **Figure 3.1**).

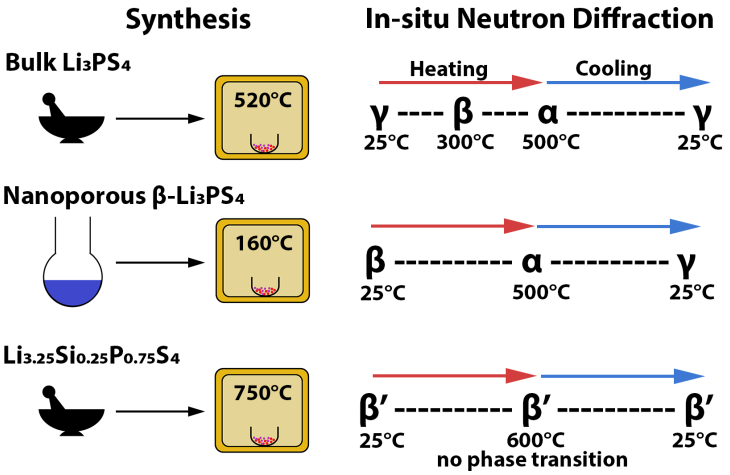

Figure 3.1: Overview of the synthesis procedure and results of the *in-situ* variable temperature neutron powder diffraction for bulk Li_3PS_4, nanoporous β-Li_3PS_4, and Si-substituted Li_3PS_4 ($Li_{3.25}Si_{0.25}P_{0.75}S_4$).

Using high-temperature NPD data, the structure of the α phase is solved for the first time and compared to its γ and β polymorphs. Second, while Li-ion transport is essentially similar in bulk β-Li_3PS_4 and its nanoporous β-form (which was examined previously by neutron diffraction),[63,66] the nanoporous material is shown here to be strongly affected by

the incorporation of a hydrogen-containing amorphous component which is not released from the structure until highly elevated temperatures. This may be the underlying cause of the fast-ion conductivity and good stability witnessed in numerous studies.[57,73–75] Furthermore, while Si substitution of P in Li_3PS_4 stabilizes a β-like phase (referred to as β') at room temperature via entropic effects, it was found here that, intriguingly, this composition does not exhibit a phase transition to the α-polymorph on heating even up to 600°C. Thus, the β'-$Li_{3.25}Si_{0.25}P_{0.75}S_4$ phase is stable on cooling back to room temperature. The rationale behind the suppression of the phase transition is presented.

3.2 Results

3.2.1 Phase transitions: $\gamma \rightarrow \beta \rightarrow \alpha$

Bulk γ-Li_3PS_4 was synthesized and examined by variable temperature NPD (on POWGEN, Oak Ridge National Lab) to monitor the phase transitions as a function of temperature. In good accord with previous studies on the phase transitions of Li_3PS_4,[69] the in-situ neutron studies (**Figure 3.2**A) show that the γ to β phase transition begins at 250°C and is complete at 300°C, while the β to α phase transition begins at 450°C and is complete at 475°C. The latter gradual transition between 450°C to 500°C is more clearly illustrated in a contour format in Figure 3.2B. Upon cooling, Li_3PS_4 directly transforms back to the thermodynamically stable γ phase, entirely skipping the β phase (**Figure 3.3**). While the structure of the γ phase has been previously reported based on powder XRD and is not relevant to this study, since it has never been solved from NPD those refinement details are provided in **Appendix A** for the sake of comprehensiveness (**Figure A.1** and **Table A.1**).

3.2.2 Nanoporous β-Li_3PS_4: stabilization by amorphous H-components up to 400°C

Nanoporous β-Li_3PS_4 was synthesized in THF following the procedure reported by Liu et al.[53] As described, the THF complex was then annealed for 16 hours at 160°C under

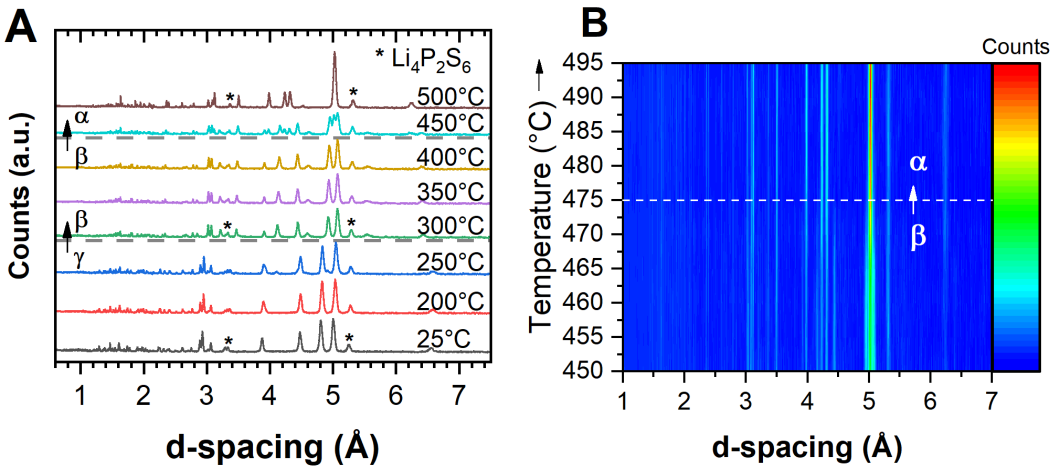

Figure 3.2: A) *In-situ* variable temperature neutron powder diffraction from 25°C to 500°C showing the evolution of γ-Li_3PS_4 to the β and α phases. B) Contour plot of diffraction patterns upon heating showing phase transition from the β to the α phase.

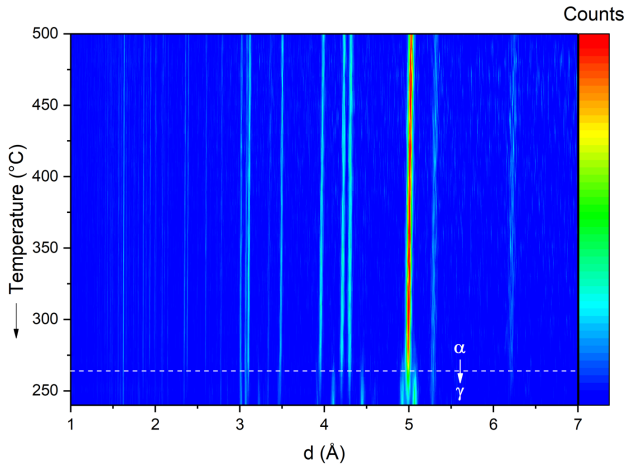

Figure 3.3: Contour plot upon cooling showing the phase transition from α directly to the γ phase occurs around 260°C.

vacuum to remove THF from the structure. **Figure 3.4** shows NPD patterns of the 160°C annealed nanoporous β-Li_3PS_4 measured at 50°C, 300°C, 350°C, and 400°C. The pattern at 50°C shows a significant background contribution indicative of the presence of hydrogen. The scattering length of the hydrogen nucleus has a large inelastic component, which results in a high continuous background that masks the intensity of the Bragg peaks from the coherent scattering component. Since the only possible source of hydrogen is THF, residual

solvent or solvent decomposition products clearly remain in the β-Li_3PS_4 material after annealing, although their correlation to the good ionic conductivity of the β-phase is unclear at present. The hydrogen-containing component can only be completely removed from the structure at about 400°C - as monitored by the background contribution (see Figure 3.4) - a temperature beyond what is typically used to synthesize nanoporous β-Li_3PS_4 (i.e. 160°C).

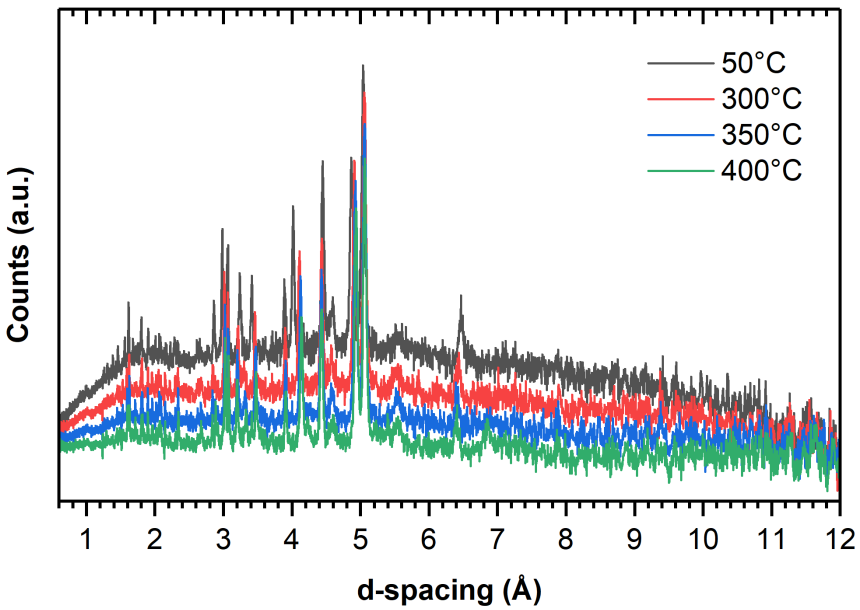

Figure 3.4: Variable-temperature NPD patterns of nanoporous β-Li_3PS_4. High background originates from incoherent scattering of hydrogen, indicating presence of a hydrogen containing component.

Inspection of the nanoporous and bulk diffraction patterns show no major differences except for the degree of crystallinity (bulk is better crystallized than nanoporous). The observed reflections are the same and both patterns are indexed to the *Pnma* space group. A contraction in the a lattice parameter for the nanoporous phase occurs when heating from 50 to 350°C (from a = 12.960 to 12.820 Å) as presented in **Figure 3.5**. However, b and c increase resulting in the lattice volumes of both phases to be nearly identical at 350°C, differing by approximately 4 $Å^3$. The same trend in the lattice parameters was observed for bulk Li_3PS_4 (see discussion section). Subsequent cooling of the material heated at 400°C to

room temperature results in transformation directly back to the γ phase. Thus, it is likely that residual solvent decomposition products trapped in the material on the nanoporous surfaces stabilize the β-phase at room temperature by helping to maintain the high surface area of the material.[53]

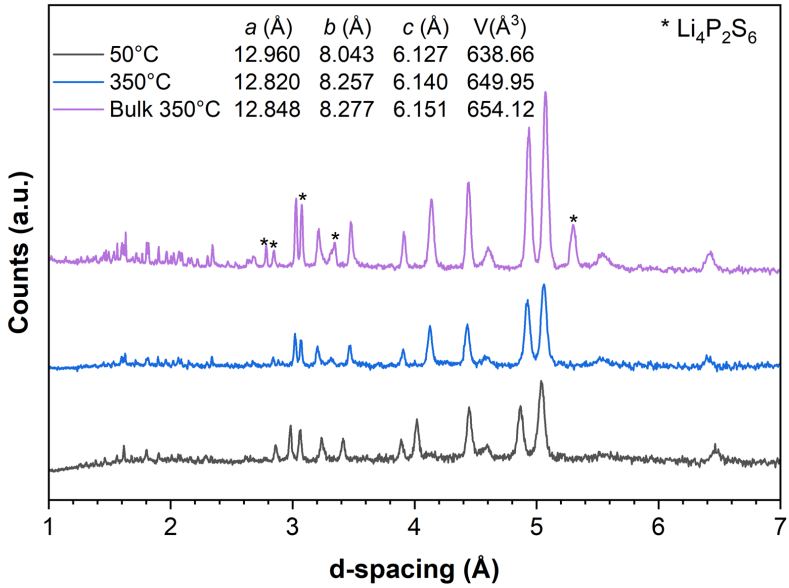

Figure 3.5: Neutron powder diffraction patterns of nanoporous β-Li_3PS_4 at 50°C and 350°C, compared with bulk β-Li_3PS_4 at 350°C. The lattice parameters were refined from Pawley fits of each diffraction pattern.

3.2.3 Bulk β-Li_3PS_4

The structure of bulk β-Li_3PS_4 was refined in the space group *Pnma* using a model that is quite similar to that from previous studies on bulk β-Li_3PS_4,[69] and nanoporous β-Li_3PS_4,[63,66] with the notable difference here being the identification of the splitting of the Li1 and Li2 sites (Wyckoff position 8d→(8d + 8d) and 4b→8d as seen in **Figure 3.6A**).

A comparison between the nanoporous and bulk β-Li_3PS_4 is summarized in **Table 3.1** and the full details of the fit and refined structure can be found in Appendix A, **Figure A.2** and **Table A.2**. A Fourier difference map revealed negative density for Li1 and Li2 that could either be accounted for (in each case) by one site with a massive anisotropic atomic

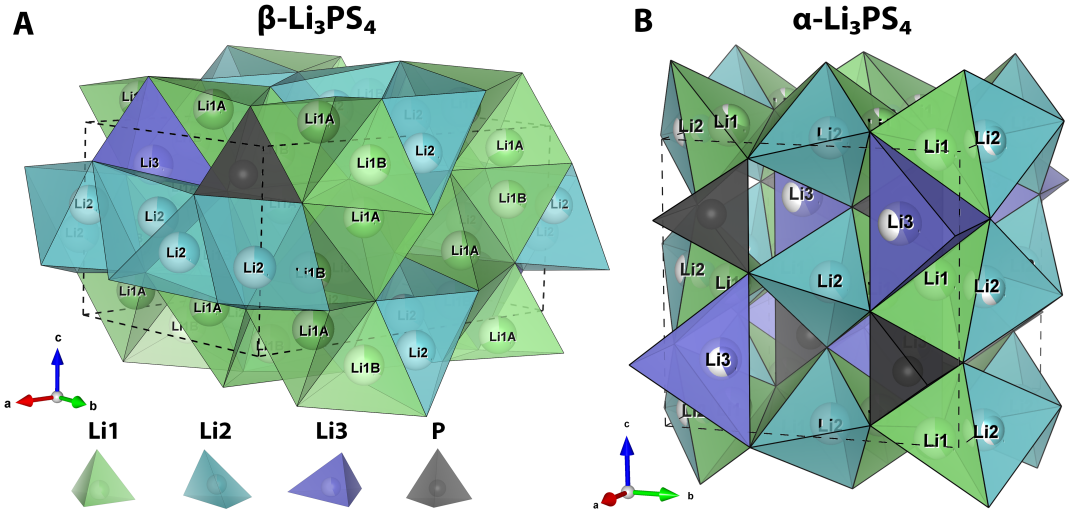

Figure 3.6: Crystal structures of A) β-Li_3PS_4 and B) α-Li_3PS_4. Sulfur atoms are omitted for clarity.

Table 3.1: Comparison of the refined structure between nanoporous β-Li_3PS_4 (Stöffler et al.)[66] and bulk β-Li_3PS_4 (this work). Both structures are refined from NPD data.

		Nanoporous β-Li_3PS_4 (Stöffler et al.)			**Bulk β-Li_3PS_4 (This work)**		
Measurement Temperature		25°C			350°C		
Space Group		*Pnma* (62)			*Pnma* (62)		
Lattice Parameters (Å)	*a*	12.993			12.848		
	b	8.0458			8.277		
	c	6.1377			6.151		
Atom		Site	Occ.	(x, y, z)	Site	Occ	(x, y, z)
Li1(A)		8d	1	(0.318, 0.017, 0.139)	8d	0.666	(0.849, 0.032, 0.104)
Li1(B)		-	-	-	8d	0.334	(0.841, 0.996, 0.371)
Li2		4b	0.66	(0, 0, ½)	8d	0.356	(0.009, 0.045, 0.582)
Li3		4c	0.34	(0.442, ¼, 0.55)	4c	0.288	(0.916, ¼, 0.804)
P1		4c	1	(0.088, ¼, 0.167)	4c	1	(0.088, ¼, 0.177)
S1		8d	1	(0.155, 0.0402, 0.267)	8d	1	(0.155, 0.048, 0.298)
S2		4c	1	(0.941, ¼, 0.254)	4c	1	(0.936, ¼, 0.254)
S3		4c	1	(0.101, ¼, 0.801)	4c	1	(0.105, ¼, 0.846)

displacement parameter, or two distinct sites. The latter provided a much better Rietveld fit. The site splitting may stem from the diffraction measurement being conducted at an elevated temperature (350°C), which leads to increased disordering of the lithium in

the structure. In the case of Li1, the Li1 8d site is refined as split sites Li1A and Li1B (tetrahedrally coordinated), separated by a relatively long distance of 1.75 Å, whereas the sites are split by 1.28 Å in the case of Li2 (coordinated with 5 sulfur atoms after splitting, but can be described as octahedrally coordinated for simplicity). Due to the high amount of disorder, (β-Li_3PS_4 has a lithium ion conductivity of nearly 10^{-2} S·cm^{-1} at 350°C)[69] the atomic displacement parameters of identical elements were constrained to be the same. This study pinpoints the lithium distribution, whereas previous reports used either X-ray diffraction to attempt to define Li positions/occupancies in the bulk β-Li_3PS_4 phase at elevated temperatures[69,70] or neutron diffraction to analyze the nanoporous β phase at room temperature.[63,66] While the high background contribution in the latter study could lead to inaccuracies with regard to lithium occupancy or ADPs as discussed above, their reconstruction of the lithium pathways using MEM and bond-valence showed similar results to what is determined here for the bulk variant; namely β-Li_3PS_4 exhibits a quasi-two-dimensional pathway on the *ac* plane with a discontinuous pathway along the *b*-direction as discussed below.

3.2.4 Crystal Structure of α-Li_3PS_4

The structure of α-Li_3PS_4 was previously reported in the space group *Pbcn* based on synchrotron X-ray powder diffraction data by Homma et al.[69,70] Unfortunately, the structural information was incomplete, as only one lithium position (8 out of 12 lithium per unit cell) was located, with errors on the atomic displacement parameter (ADP) almost as large as the value itself (more than 60% error on the ADP).[70] Nonetheless, computational studies based on this model were conducted to discern the lithium ion diffusion mechanism.[72] Using NPD data, refinement of the structure in the *Pbcn* space group was attempted to fully resolve the Li sites. However, closer inspection of the fit and structure revealed inaccuracies. For example, all the observed reflections in the measured pattern obey a systematic absence of $h + k = 2n + 1$, which indicates the crystal system is *C*-centered, and not primitive. There are also no (102), (121), and (211) reflections, which are expected for a primitive *Pbcn*

space group. The missing symmetry and correct space group (*Cmcm*) was identified using the ADDSYM function within PLATON.[76] Full profile and Rietveld fits confirm that the space group is *Cmcm* - a supergroup of *Pnma* (the space group of β-Li_3PS_4) - as outlined below. A comparison between the α-Li_3PS_4 structure solved in the *Pbcn* and *Cmcm* space group is provided in **Table 3.2**. Thus, the transformation from β to α is accompanied by a slight increase in symmetry from *Pnma* to its supergroup *Cmcm*. The lattice parameters of β-Li_3PS_4 are a = 12.8483 Å, b = 8.2772 Å, and c = 6.1512; the α-phase approaches cubic symmetry with lattice parameters a = 8.6435 Å, b = 9.0462 Å, and c = 8.4779 Å.

Table 3.2: Comparison of the refined structure for α-Li_3PS_4 between the synchrotron powder XRD study by Homma et. al[69,70] and the NPD study in this work.

		α-Li_3PS_4 (Homma et al.)			α-Li_3PS_4 (This work)		
Measurement Temperature		538°C			500°C		
Space Group		*Pbcn* (60)			*Cmcm* (63)		
Lattice Parameters (Å)	*a*	8.603			8.644		
	b	8.997			9.046		
	c	8.439			8.478		
Atom		Site	Occ.	(x, y, z)	Site	Occ	(x, y, z)
Li1		8d	1	(0.738, 0.591, 0.065)	16	0.42	(0.724, 0.353, 0.528)
Li2					8e	0.40	(0.714, 0, 0)
Li3					4c	0.43	(0, 0.196, ¼)
P1		4c	1	(0, 0.827, ¼)	4c	1	(0, 0.831, ¼)
S1		8d	1	(0.307, 0.453, 0.251)	8g	1	(0.304, 0.456, ¼)
S2		8d	1	(0.006, 0.294, 0.549)	8f	1	(0, 0.295, 0.554)

To resolve the structure of α-Li_3PS_4 from the NPD pattern collected at 500°C, the tetrahedral PS_4^{3-} framework was first refined in *Cmcm*, and the lithium positions were revealed using a Fourier difference map. Since lithium is highly visible to neutrons due to its negative scattering length, the lithium positions are distinguished by their negative intensities. This revealed an extremely disordered arrangement of Li^+ ions distributed over three sites in the Wyckoff positions 16h, 8e, and 4c as shown in Figure 3.6B. Owing to the high degree of Li disorder due to the fast ion motion, the three sites were constrained to have the same atomic displacement parameters. The structure is built of primarily edge-sharing

LiS_4 tetrahedra, but the Li2 site shares a face with the neighbouring Li1 tetrahedra. The sites were also split (8e site into 16h, and 4c double split into 16h) in an attempt to further improve the goodness-of-fit (GOF), but this was not successful (GOF of 2.35 vs. 2.38). Thus, the simpler non-split model is used hereafter. The resulting fit and refined crystallographic data using the preferred non-split site model is summarized in **Figure 3.7** and **Table 3.3** with corresponding bond lengths in **Table 3.4**. A comparison of the α structure in its split vs. non-split configurations is given in **Figure A.3** and the results from the split site model are also provided in Appendix A (**Figure A.4**, **Table A.3**, and **Table A.4**). A detailed description of the lithium ion pathways is given below in the discussion section.

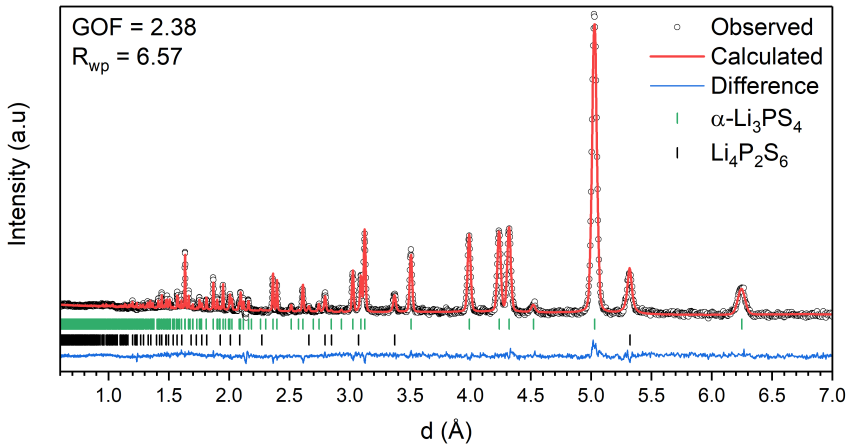

Figure 3.7: Rietveld refinement of α-Li_3PS_4 using TOF neutron powder diffraction data measured at 500°C (contains 9 wt.% $Li_4P_4S_4$ impurity).

3.2.5 Phase stability and structure of Si-substituted Li_3PS_4

Previous reports demonstrated that substitution of silicon into the phosphorus site of Li_3PS_4 results in stabilization of a β-like polymorph (space group *Pnma*), with optimal conductivity found for the composition $Li_{3.25}Si_{0.25}P_{0.75}S_4$.[61] It exhibits a similar orthorhombic structure (space group *Pnma*) to that of β-Li_3PS_4 at room temperature but with site splitting of the Li1 (Wyckoff position 8d), Li2 (4b), and Li3 (4c) sites. This splitting dramatically alters the energy barriers of the lithium diffusion pathways by frustrating the energy landscape,

Table 3.3: Crystallographic data of α-Li_3PS_4 obtained from Rietveld refinement of neutron powder diffraction at 500°C. Unit cell: orthorhombic *Cmcm* (63). a = 8.6435(5) Å, b = 9.0462(5) Å, c = 8.4779(5) Å, V = 662.90(7) Å^3, Z = 4

Label	**Wyck. Pos.**	**x**	**y**	**z**	**Occ.**	**B_{iso} (Å^2)**
Li1	16h	0.724(2)	0.353(3)	0.528(2)	0.415(19)	10.7(8)
Li2	8e	0.714(4)	0	0	0.40(2)	10.7(8)
Li3	4c	0	0.196(5)	0.25	0.43(3)	10.7(8)
P	4c	0	0.8306(5)	0.25	1	4.12(15)
S1	8g	0.3042(8)	0.4560(7)	0.25	1	5.98(15)
S2	8f	0	0.2949(7)	0.5537(8)	1	5.98(15)

Table 3.4: Interatomic distances in α-Li_3PS_4 obtained from Rietveld refinement (using non-split site model) of neutron powder diffraction at 500°C.

Center Atom	**Second Atom**	**Interatomic Distance (Å)**
Li1	S2	2.45(2) x 2
	S1	2.55(2)
	S1	2.57(2)
Li2	S1	2.293(12) x 2
	S2	2.66(3) x 2
Li3	S2	2.727(16) x 2
	S1	2.75(4) x 2
P	S2	2.015(7) x 2
	S1	2.037(7) x 2
Li1	Li2	1.45(3)
	Li1	1.97(3)
	Li3	2.73(2)

leading to enhanced lithium ion diffusion as previously reported.[61] Variable temperature NPD from room temperature to 600°C reveals the effect that Si substitution has on the β to α phase transition (**Figure 3.8**).

The fit and Rietveld refinement results are presented in **Figure A.5** and **Table A.5** and are consistent with previous reports.[61] The phase transition to the α-phase is completely suppressed (Figure 3.8), indicating that the Si-substituted phase is significantly more stable than the non-substituted β or α phases. In order to understand why this is the case, the structures of bulk β-Li_3PS_4, α-Li_3PS_4, and $Li_{3.25}Si_{0.25}P_{0.75}S_4$ are compared in detail below.

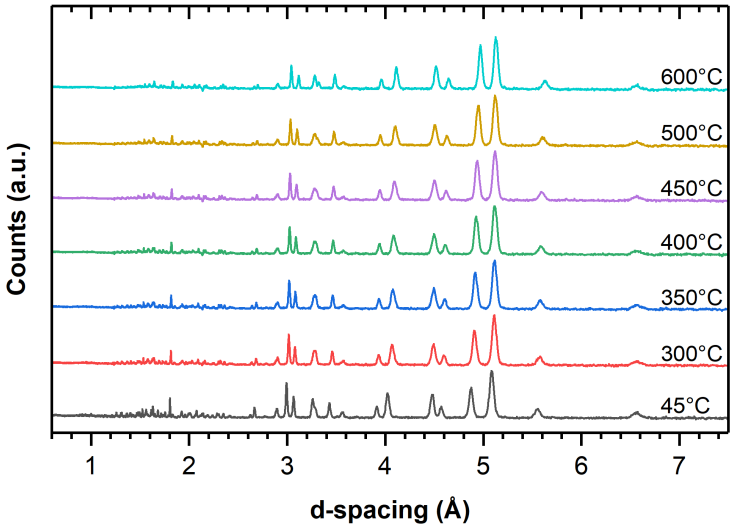

Figure 3.8: High-temperature neutron powder diffraction of $Li_{3.25}Si_{0.25}P_{0.75}S_4$, showing the suppression of the phase transformation to the α polymorph by Si-substitution.

3.3 Discussion

3.3.1 Structural Comparison

The structures of the three polymorphs ($\gamma \rightarrow \beta \rightarrow \alpha$) are compared in **Figure 3.9**. In the room temperature γ phase ($Pmn2_1$) - viewing the structure along [001] - the framework exhibits an ordered polyhedral motif where each PS_4 unit has its apex facing up (Figure 3.9A). In contrast, in the higher temperature β phase - viewing the structure down [001] - every PS_4 anion along [100] alternates between facing up and down (Figure 3.9B). It has been suggested that the zig-zag PS_4 arrangements in the β-phase create lithium positions both in octahedral (LiS_6) and tetrahedral (LiS_4) sites (compared to tetrahedral alone in the γ-phase), giving rise to a change in the energy landscape which makes the Li-ions more mobile.[69,70] The difference in the anion motifs in the two polymorphs parallels that in their oxide counterpart (Li_3PO_4), an isotype that exhibits a similar phase transition process from β ($Pmn2_1$) to γ ($Pnma$) at 500°C (note the opposite terminology in phase nomenclature).[77,78] The room temperature β-Li_3PO_4 ($Pmn2_1$) is comprised of PO_4 tetrahedra all

facing the same direction, analogous to γ-Li_3PS_4($Pmn2_1$). The intermediate temperature phase, γ-Li_3PO_4, exhibits alternating PO_4 tetrahedra, as observed for β-Li_3PS_4. At 1170°C, γ-Li_3PO_4 undergoes a transition γ to α, where α is an unknown space group and structure.

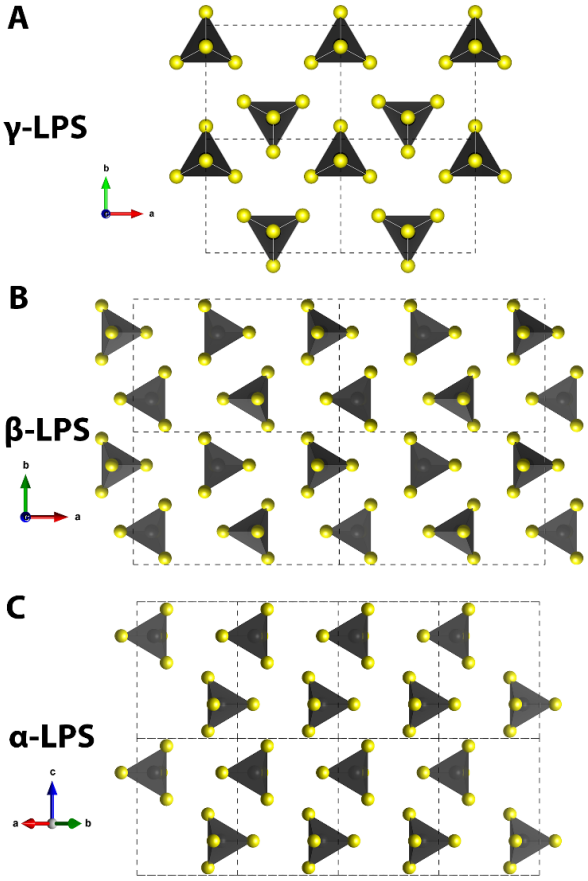

Figure 3.9: Arrangement of PS_4 tetrahedra in A) γ-Li_3PS_4, B) β-Li_3PS_4, and C) α-Li_3PS_4.

In Li_3PS_4, upon increasing the temperature between 400-450°C, β-Li_3PS_4 ($Pnma$) transforms into the higher symmetry α-Li_3PS_4 ($Cmcm$) phase. Along with the unit cell approaching a more cubic-like symmetry as a result of this transition, the inherent PS_4 tetrahedral framework is altered. The view of α-Li_3PS_4 along the [110] directions shows that the PS_4 tetrahedra that run along [001] are aligned facing up or down and alternate their orientation (Figure 3.9C). Previous studies have proposed that the α-phase allows for the most random distribution of lithium throughout the possible interstitial positions in the structure[69,70] (i.e. cation sublattice melting due to high mobility), which leads to the high level of ionic

conduction that has been predicted computationally. Note the calculations were carried out in the *Pbcn* space group, rather than the *Cmcm* space group presented here, although the conclusion is likely valid as discussed below.[72]

It was also predicted that a bcc S-sublattice leads to direct Li hopping between adjacent tetrahedral sites, invoking fast Li-ion conduction.[79] That study, using pymatgen,[80] suggested that the S-sublattice of β-Li_3PS_4 was bcc but with a large lattice length deviation. Using the refined structures for β and α-Li_3PS_4, their sulfur sublattices were analyzed, but with a different polyhedral template matching algorithm.[81] There is a distinct difference in the two arrangements. The S-sublattice of β-Li_3PS_4 is 100% hcp, in accord with results using the same polyhedral template-matching algorithm,[72] while α-Li_3PS_4 is composed of sulfur that exists as 75% in a bcc sublattice, and 25% in hcp. This finding is in accord with calculations of the α-phase that predict extremely fast ion conduction with a low activation energy.[72] In the α-structure, Li^+ occupies tetrahedral sites in close proximity to each other that leads to favorable intersite migration. Nevertheless, the polyhedral framework of β'-$Li_{3.25}Si_{0.25}P_{0.75}S_4$, which is similar to β-Li_3PS_4, also exhibits a 100% hcp S-sublattice, and yet still achieves fast-ion conduction $>1\times10^{-3}$ S·cm^{-1}. It can be surmised that while a bcc S-sublattice may lead to particularly high fast-ion mobility, good conductivity properties can also be achieved through other means, such as extensive Li-ion disorder and population of intermediate-energy sites that leads to correlated ion motion. Furthermore, while bulk β-Li_3PS_4 and β'-$Li_{3.25}Si_{0.25}P_{0.75}S_4$ structures are identical in terms of their PS_4 framework, there is a notable difference in their unit cell volumes. The latter are plotted against temperature for all of the polymorphs and $Li_{3.25}Si_{0.25}P_{0.75}S_4$ in **Figure 3.10** (change in lattice parameters are shown in **Figure 3.11**). Si-substituted Li_3PS_4 maintains a larger unit cell volume than its β and α counterparts (by at least 6 Å^3), owing to the larger ionic radius of Si^{4+} (0.26 Å) compared to P^{5+} (0.17 Å), and increased Li fraction that expands the lattice. Since the unit cell volume of the Si-substituted material is larger than the undoped α-phase, conversion to the α polymorph on heating is not possible. Hence, $Li_{3.25}Si_{0.25}P_{0.75}S_4$ is more stable and the phase transition to α at high temperature is suppressed.

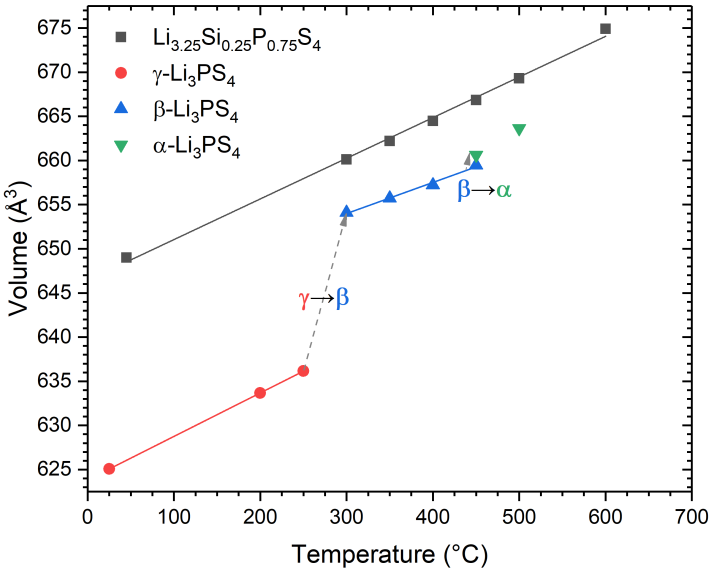

Figure 3.10: Unit cell volumes of γ, β, α, and β'-$Li_{3.25}Si_{0.25}P_{0.75}S_4$ with increasing temperature. Unit cell volume of the γ phase is multiplied by 2 in order to match the number of formula units of the other polymorphs.

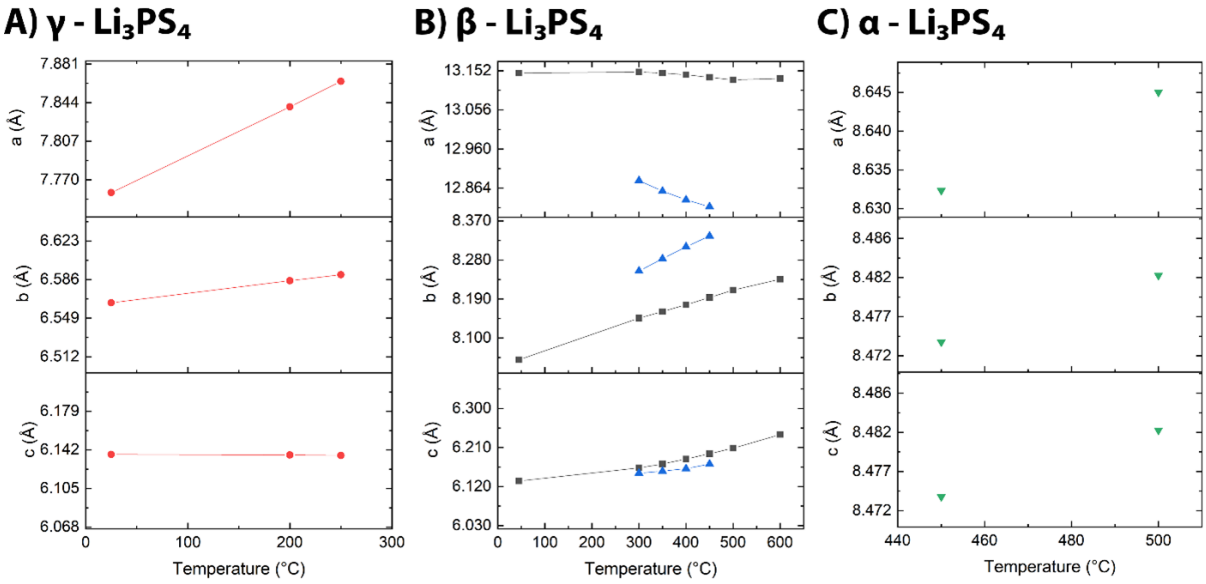

Figure 3.11: Lattice parameters with increasing temperature of A) bulk γ-LPS (red), B), bulk β-LPS (blue) and β'-$Li_{3.25}Si_{0.25}P_{0.75}S_4$ (black), and C) bulk α-Li_3PS_4 (green).

3.3.2 Comparison of Li Diffusion Pathways

Analysis of the lithium diffusion pathways was conducted by looking at the negative components of the nuclear density maps, since lithium has a negative neutron scattering length (b_{Li} = -1.9 fm). The nuclear density map was constructed by applying the maximum entropy method (MEM) to the experimental structure factors extracted from Rietveld refinement of the neutron diffraction data. MEM can provide more accurate electron and nuclear density maps than Fourier analysis, which is prone to termination effects. A detailed examination of the diffusion pathways of $Li_{3.25}Si_{0.25}P_{0.75}S_4$ can be found in previous studies, and is not repeated here.[61]

As described above, the β and α-Li_3PS_4 structures are related by symmetry due to their subgroup-supergroup relation. In the transformation from the β ($Pnma$) to the α ($Cmcm$) phase, the a-axis becomes the b-axis (and is multiplied by $1/\sqrt{2}$); the b-axis becomes the c-axis; and the c-axis becomes the a-axis (multiplied by $\sqrt{2}$). The comparisons hereafter are carried out with these transformations taken into consideration. The results from the MEM maps were fully corroborated with Bond-Valence Site Energy (BVSE) maps derived from the SoftBV program developed by S. Adams.[82] The BVSE method can reliably model pathways for mobile Li^+ as regions of low bond valence site energy, using only the crystal structure as an input.[82] In this approach, lithium ion site energies are calculated for a dense grid of points with a resolution of 0.1 Å using the transferable Morse-type softBV force field. Such calculations have been used to study a wide variety of ion conductors and show good agreement with experimental investigations, although the absolute values are generally higher than experimental. Calculation of the Bond Valence Energy Landscape (BVEL) corresponding to the visual presentation in the BVSE maps are performed for the β and α-Li_3PS_4 polymorph (note that owing to the accuracy of softBV, the overall activation energy may differ from the experimental value, but it still provides an approximate assessment of the relative height of the barriers).[82] Discussion of these pathways is provided in the next section.

Lithium-ion conduction in bulk β-Li_3PS_4

The crystallographic study here on bulk β-Li_3PS_4 shows the Li1 (tetrahedral) and Li2 (octahedral) positions are both split into two distinct sites, which reflects the disorder in the structure at the elevated measurement temperature (350°C). MEM and BVSE maps reveal that Li-ion transport is primarily within the *ac* plane (i.e., Li2-Li2-Li1B-Li1A-i3-Li1A, **Figure 3.12A**, cyan arrows) and consists of migration between these two sites and an interstitial site, i3 (distorted octahedral with bond lengths 2.64-2.73 Å; Wyck. pos. 4a), to give an overall activation energy (E_a) of 0.36 eV as measured from the BVEL (**Figure 3.13A**, cyan line). This value is effectively the same as that calculated for β-Li_3PS_4 from molecular dynamics studies (0.35 eV),[65] and as experimentally measured for nanoporous β-Li_3PS_4 (0.36 eV),[53,66] a material which was also shown to exhibit lithium ion conduction predominantly in the *ac* plane via a Li1-Li2-Li1 connection.[66] Although not explicitly identified by the authors, the presence of an interstitial site between Li1 to Li1 is evident in their "differential bond valence" map of the material,[66] which is indicated here as i3 for bulk β-Li_3PS_4. Although the experimentally determined activation energy for Li-ion transport (E_a) for bulk β-Li_3PS_4 between 300-400°C is reported to be two-fold lower (0.16 eV),[69] this likely reflects the difficulty of carrying out EIS measurements at greatly elevated temperatures where impedance from the wire connections is anticipated to play a dominant role. While BVEL can overestimate activation energies, other measurements of E_a for the β-phase, as determined from ^{7}Li NMR studies that favour local motion, also are around 0.36 eV, ranging between 0.24 eV (nanoporous β-Li_3PS_4)[66] and 0.40 eV (ball-milled material).[83] Furthermore, the predicted room temperature conductivity for the β-phase was extrapolated from a plot of log σ vs $1/T$ measurements carried between 300-400°C, with a measured slope corresponding to an E_a of 0.16 eV. This extrapolated value of 8.9×10^{-7} S·cm^{-1} corresponds to a diffusion coefficient on the order of 7×10^{-12} cm^2/s based on the Nernst-Einstein equation that relates the diffusion coefficient and conductivity:

$$\sigma = \frac{N\,(Ze)^2\,D}{k_B T}$$

(where N is the number density of the mobile ions and in this case is taken as N_{Li} = 2×10^{28} m^{-3} from previous studies on β-Li_3PS_4,[66] Z is the ionic charge, e is the elementary electron charge, D is the diffusion coefficient of the mobile species, σ is the ionic conductivity of the mobile species, k_B is the Boltzmann constant, and T is the temperature). That diffusion coefficient is unreasonably low in light of the AIMD simulations that determine a diffusion coefficient on the order of 10^{-8} cm^2/s to 10^{-9} cm^2/s at room temperature.[50,65]

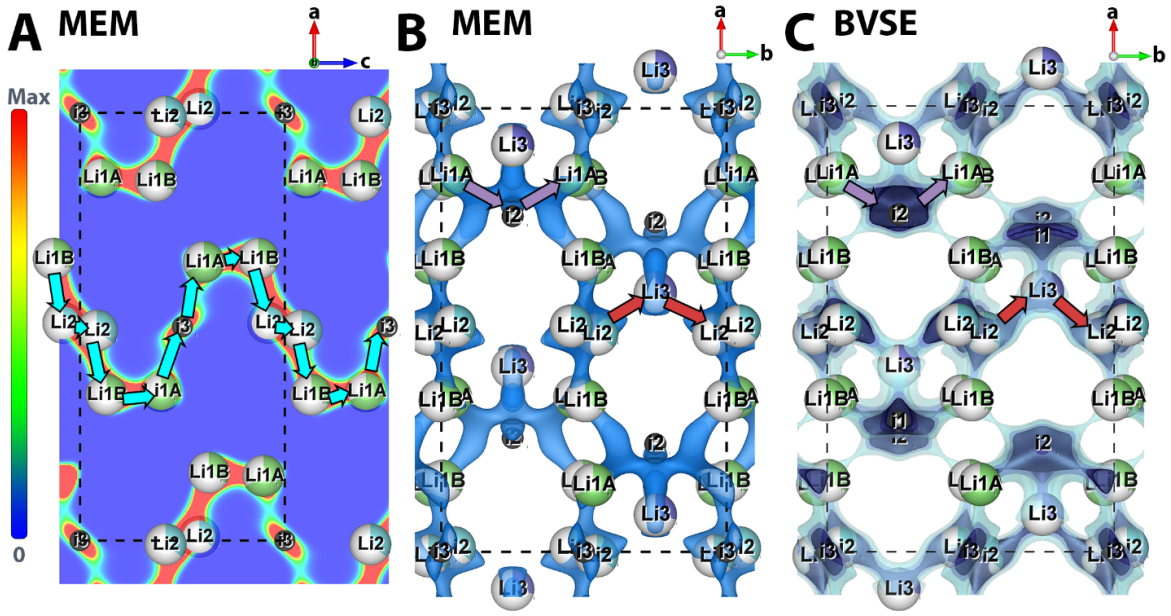

Figure 3.12: MEM maps (isosurface of -0.01 fm/Å^3) of β-Li_3PS_4 shown in A) 2D format viewing the *ac* plane, B) 3D format viewing the *ab* plane, and C) 3D BVSE map of the *ab* plane. Cyan arrows indicate the pathway along the *ac* plane. Purple and red arrows indicate paths connecting parallel *ac* planes.

In β-Li_3PS_4, lithium ion diffusion along the *b*-direction can take place along two potential pathways, where Li3 or an interstitial site i2, primarily act as connections between parallel *ac* planes shown in Figure 3.12B,C to establish quasi-3D migration. The Li3 site acts as a connection point between the Li2 sites in adjacent *ac* planes (Li2 Li3 Li2, Figure 3.12B,C, red arrows), with an energy barrier of 0.255 eV (Figure 3.13A, red line); the density is more apparent in the BVSE map than the MEM map. This Li2-Li3-Li2 path resembles the pathway identified in previous neutron MEM studies on nanoporous β-Li_3PS_4, which was

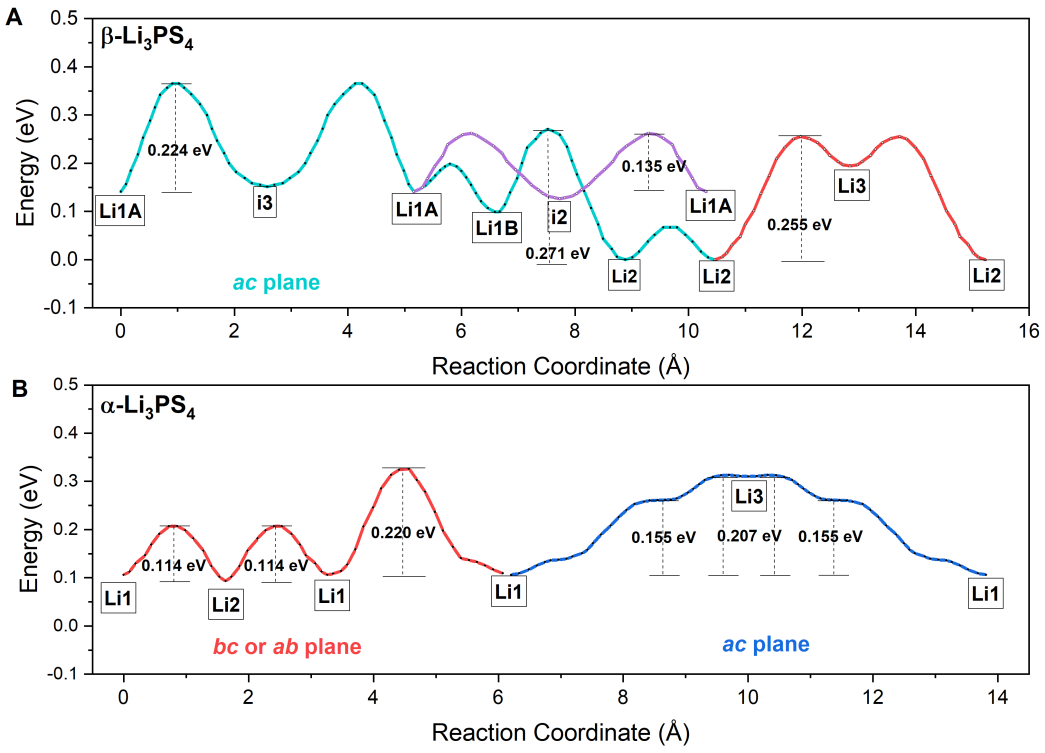

Figure 3.13: Bond-valence energy landscapes (BVEL) indicating the reaction pathways and energy barriers of transport calculated from BVSE maps for A) bulk β-Li_3PS_4 and B) bulk α-Li_3PS_4. Coloured lines correspond to the coloured arrows in Figure 3.12.

shown to connect adjacent *ac*-planes via the Li3 site.[66] An alternative lower energy path with an energy barrier of 0.135 eV (Figure 3.13A, purple line) links adjacent *ac* planes, as seen here in both the MEM and BVSE maps of bulk β-Li_3PS_4. In this case, Li^+ can migrate between the Li1A sites in adjacent *ac* planes via an interstitial site (i2), which facilitates Li^+ diffusion along the *b*-direction (Li1A-i2-Li1A, Figure 3.12B,C, purple arrows).

Lithium-ion conduction in α-Li_3PS_4

MEM maps of the α-phase reveal linear Li^+ diffusion pathways along the *b*-axis that are connected by the Li3 site in the *ac* plane, observed in the 3D nuclear distribution in **Figure 3.14A**. Compression of the *b*-axis by $1/\sqrt{2}$ (relative to the *a*-axis of the β-phase) causes a narrowing of the distance between the atoms along *b*. This forces the Li3 and Li1

site in the α-phase to reside on the same plane (Figure 3.14, blue arrows), separated by a distance of 2.76 Å, and allows for facile diffusion in the *ac* plane of the α-phase with a low energy barrier of 0.207 eV (Figure 3.13B, blue line). The Li1 ions also form part of a chain along the *b*-axis (Li1-Li2-Li1-Li1 pathway) that becomes the dominant pathway in α-Li_3PS_4, which can be seen in the *ab* and *bc* planes (Figure 3.14B,C, red arrows). Note that two adjacent Li1 sites are edge-sharing, and thus the Li1-Li1 hop must occur through an interstitial site that connects the two tetrahedral faces. BVEL did not detect an interstitial site in this location, however, both the MEM and BVSE maps show very weak density in the space between the edge-sharing Li1-Li1 tetrahedra (see **Figure 3.15**).

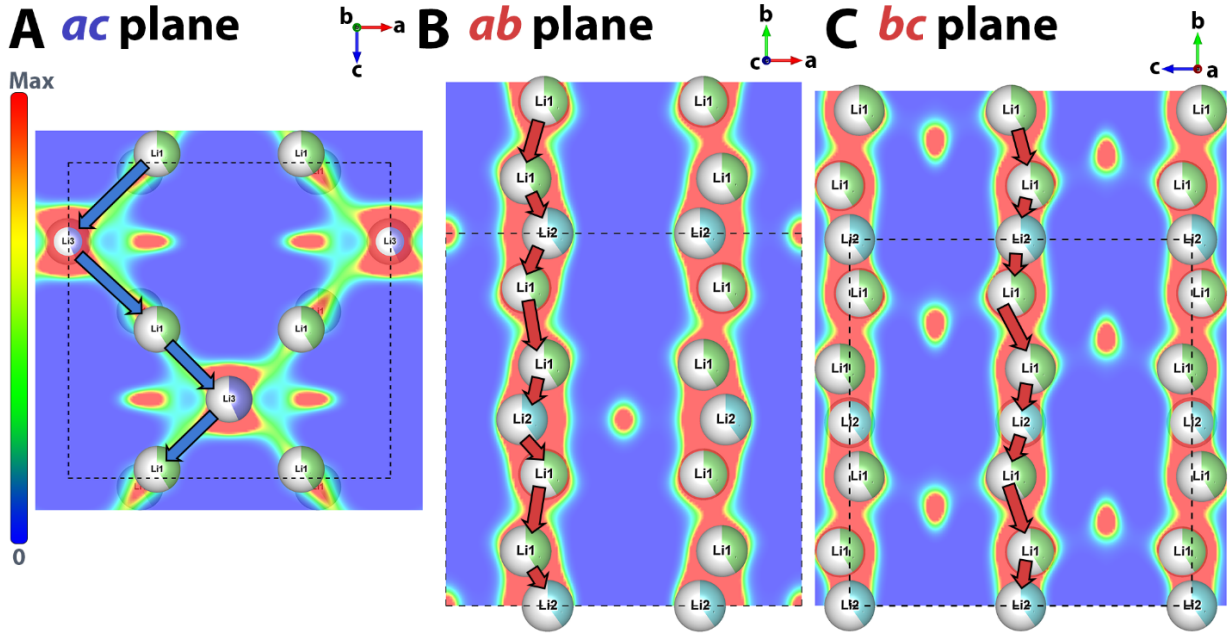

Figure 3.14: 2D MEM (isosurface of -0.01 fm/Å^3) maps of α-Li_3PS_4 illustrating the Li^+ diffusion pathways in the A) *ac* plane, B) *ab* plane, and C) *bc* plane. Li1 is represented by green atoms, Li2 by cyan atoms, Li3 by purple atoms, and interstitial sites by black atoms.

A low energy barrier of 0.22 eV along this path (Figure 3.13B, red line) is determined. Importantly, the channels along *b* are connected by the Li3 site (in the *ac* plane) to enable 3D diffusion with an overall activation energy of about 0.22 eV (Figure 3.13B, red line). This is in agreement with AIMD calculations of α-Li_3PS_4 that predict an overall activation energy

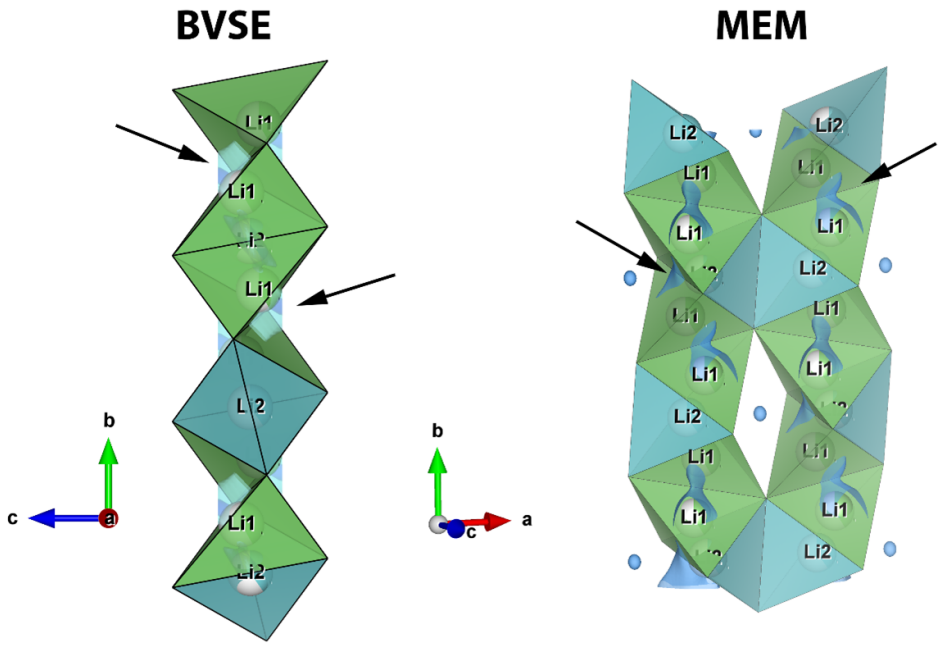

Figure 3.15: BVSE and MEM map (isosurface of -0.01 fm/ Å^3) of α-Li_3PS_4 showing the linear Li^+ diffusion pathways along the b-axis. Black arrows are pointing to the density from the maps that indicate an interstitial site that connects adjacent Li1 sites.

of 0.18 eV, with an ionic conductivity of 8×10^{-2} S·cm^{-1} at room temperature.[72] Furthermore, visualization of the 3D nuclear densities from MEM for α-Li_3PS_4 (**Figure 3.16A**) closely matches the Li-ion probability density distribution from the reported AIMD calculations,[72] despite the latter being carried out in the lower symmetry *Pbcn* space group.

The Li-Li distances from the refined structure in this study are much shorter than those predicted from the AIMD study, which all are in the range of 2.46-2.81 Å.[72] The refined α-Li_3PS_4 structure in *Cmcm* exhibits a Li1-Li2 distance of 1.45 Å, a Li1-Li1 distance of 1.97 Å, and a Li1-Li3 distance of 2.73 Å. The shorter Li-Li distances are due to the high degree of Li delocalization over the sites (i.e. a large ADP value of 10.7 Å^2 was determined from Rietveld refinement), which may explain the high lithium mobility observed by molecular dynamics. The short Li-Li distances may be responsible for concerted ion migration as Li site energies are pushed up due to the repulsion of the Li atoms in close proximity. *Ab initio* modeling has pointed out that Li ions in high-energy sites can activate concerted migration with a

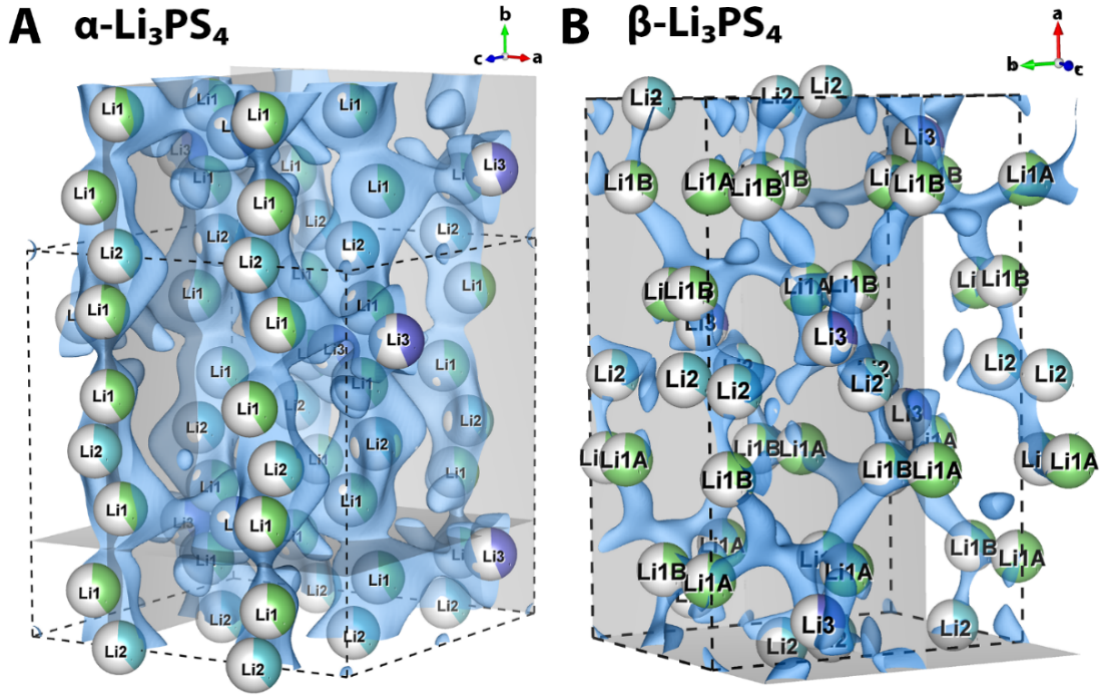

Figure 3.16: 3D MEM (isosurface of -0.01 fm/Å^3) maps illustrating the Li^+ diffusion pathways in A) of α-Li_3PS_4 at 500°C and B) β-Li_3PS_4 at 350°C

lowered migration energy barrier,[42] which was previously observed in the $Li_{3.25}Si_{0.25}P_{0.75}S_4$ material using BVEL.[61] Note that the short distances alone are not the reason for fast-ion conduction, as the energy landscape will dictate the long-range lithium-ion transport. Short bond-distances are also prevalent in β-Li_3PS_4, yet long range transport is more favourable in α-Li_3PS_4 due to the energy landscape of the structure, as described above.

In short, in the α-structure, diffusion is extremely facile along channels in the b-axis, and also predominates in the interconnected ac planes to result in 3D ion diffusion with a low activation energy barrier. In the bulk β structure, the transport pathways are more limited. They are dominant in the ac plane, making the material essentially a 2D conductor, but each plane is weakly linked together (in a non-continuous fashion) by sites along the b-direction. This agrees well with other MEM and BVSE analysis on nanoporous β-Li_3PS_4.[61,66] There is no experimental measurement for the activation energy of α-Li_3PS_4 to date due to the aforementioned difficulty of measurement at the extremely high temperature range necessary

to perform the experiment (≥475°C), but from the previously reported MD calculations, the α-phase has an extremely high extrapolated "room temperature" lithium ion conductivity of 8×10^{-2} S·cm^{-1}. Regarding diffusivity, the diffusion prefactor D_o:

$$D_o = f a_o^2 \, \nu_o \, e^{\frac{-\Delta S}{k_B}}$$

plays a major role, where D_o is composed of a correlation factor f accounting for the fact that successive ion jumps can be related to one another, the jump distance a_o, the jump frequency ν_o, the Boltzmann constant k_B, and the sum of migration (ΔS_m) and defect formation (ΔS_f) entropies, ΔS. The influence of activation energy and prefactor is reflected in the MEM maps, where the difference in Li nuclear density distribution for α vs. β is quite striking (Figure 3.16). Making allowances for the higher temperature of data collection (500°C vs 350°C), lithium ions are nonetheless clearly much more delocalized in the α phase, implying a difference in diffusivity that is likely indirectly reflected in the doubling of the atomic displacement factor (from 5.4 to 10.7 Å^2 , see Table 3.3 and Table A.2). The prefactor has been shown to strongly affect the ionic conductivity of many fast-ion conducting solid electrolytes, which is also influenced by the dynamics of the host lattice.[84] Considering that the anion framework for both structures should have the same polarizability and the jump distances between the two structures are similar, polyhedral anion rotation may also play a role here as it has been shown to couple to, and facilitate long range cation mobility.[85] Anion rotation would affect the phonon properties of the material which is directly related to the entropy of migration, and that, in turn, governs the prefactor, D_o.

3.4 Conclusions

Variable-temperature in-situ neutron powder diffraction studies of the intermediate and high-temperature β and α polymorphs of bulk-Li_3PS_4, nanoporous β-Li_3PS_4, and $Li_{3.25}Si_{0.25}P_{0.75}S_4$ - coupled with Rietveld refinement, and MEM and BVSE analysis to study the lithium diffusion pathways - elucidate important structure-property relationships in these related

materials. The high symmetry α-Li_3PS_4 phase (space group *Cmcm*) in its stability regime ($\geq$475°C), exhibits highly delocalized Li-ion siting/distribution over three sites in the lattice, and shorter Li-Li distances than were reported in previous studies based on a computed structure. Furthermore, such proximate Li-Li sites result in high Li-site energies based on the BVEL map due to Li-Li repulsion, and may be responsible for correlated ion motion. Recent *ab initio* modelling shows mobile Li ions occupying high-energy sites can activate concerted migration with a reduced migration energy barrier.[42] The α-Li_3PS_4 structure primarily exhibits a bcc like S-sublattice and the most favorable lithium diffusion pathways, allowing for facile 3D lithium ion diffusivity in comparison to the β-Li_3PS_4 polymorph. Pathways for Li migration by experimental BVSE calculations based on neutron diffraction data are similar to those previously predicted by AIMD, with an E_a of 0.22 eV - a little higher than calculated from AIMD (0.18 eV)[72] – and in accord with that expected, since BVEL often slightly overestimates E_a. These factors are undoubtedly responsible for the ultra-high conductivity predicted by AIMD simulations. Not only is the overall E_a much lower for the α vs. β-phase by about 0.14 eV but it is evident that the α-phase is a true 3D conductor with highly delocalized Li-density in both the *ab, bc*, and *ac* planes.

Determination of the Li-substructure of the bulk β-phase (350°C - 450°C) allows a better understanding of transport in this material. The most facile migration pathway found here is the same as the nanoporous β-phase (*ac* plane). However, whereas the latter is reported to be a 2D ion conductor, bulk β-Li_3PS_4 also exhibits low energy 3D pathways owing to split Li site populations, with an overall E_a of 0.36 eV from BVSE calculations based on the refined neutron diffraction data. This value is much higher than the experimental E_a of 0.16 eV measured at high temperature,[69] but in full accord with other estimates. That, in turn, suggests that the "hypothetical" room temperature conductivity for bulk β-Li_3PS_4 of 8.9×10^{-7} S·cm^{-1} extrapolated from high temperature (assuming an activation energy of 0.16 eV) is orders of magnitude too low.[70] Thus, it is possible that the three-orders-of-magnitude greater conductivity of nanoporous β-Li_3PS_4 *vis a vis* hypothetical bulk β-Li_3PS_4 at room temperature may be overestimated. Finally, while nanoporous β-Li_3PS_4 is quite stable at

intermediate temperatures, not surprisingly the structure cannot be maintained after an amorphous hydrogen containing component that stabilizes the phase is completely removed upon heating above 400°C (presumably the nanopores begin to collapse). Si-substitution of Li_3PS_4 stabilizes the β'-$Li_{3.25}Si_{0.25}P_{0.75}S_4$ phase at room temperature and, interestingly, also prevents phase transformation to the α polymorph upon heating owing to its larger lattice volume.

This work provides in-depth elucidation of the structural details and ion transport in various Li_3PS_4 polymorphs and their related analogues, which have long been of interest due to their history as a basis for designing and modeling new ion-conductors. Moreover, the findings further the current understanding of ion transport in solid electrolytes, which may lead to the discovery of new materials based on the results presented in this study.

3.5 Methods

3.5.1 γ-Li_3PS_4 Synthesis

Stoichiometric molar ratios of the precursors, Li_2S (Sigma Aldrich, 99.98%) and P_2S_5 (Sigma Aldrich, 99%), were ground together in a mortar inside an Ar filled glovebox. The powder was pelletized and placed in a glassy carbon crucible which was sealed inside a vacuumed quartz tube. The material was heated at 520°C for 14 hours and then cooled back to room temperature at a rate of 5°C per minute.

3.5.2 Nanoporous β-Li_3PS_4 Synthesis

The precursor for the synthesis, the Li_3PS_4·3THF complex, was obtained from BASF. The powder was dried under vacuum at a temperature of 160°C for 16 hours to give pure β-Li_3PS_4 as determined by XRD analysis.

3.5.3 $Li_{3.25}Si_{0.25}P_{0.75}S_4$ Synthesis

Li_2S (Sigma Aldrich, 99.98%), P_2S_5 (Sigma Aldrich, 99%), Si (Sigma-Aldrich, 99%) and sulfur (Sigma-Aldrich, 99.5%) were mixed together in a mortar at the targeted ratio, and 5 wt.% excess sulfur was added to fully oxidize the Si. The mixture was pelletized and placed in a glassy-carbon crucible in a sealed quartz tube under vacuum. The sample was heated to 750°C, slowly cooled to 725°C over a period of 18 hours, and then cooled to room temperature under ambient conditions.

3.5.4 Neutron Powder Diffraction and Rietveld Refinement

Time-of-flight (TOF) neutron diffraction samples were loaded into a 6 mm vanadium can under He with a boronitride cover and molybdenum screws. Samples were collected on POWGEN (Beamline 11A) at the Spallation Neutron Source (SNS) at Oak Ridge National Laboratory. Data was collected using a beam of neutrons with a center wavelength of 1.5 Å. The resulting diffraction patterns were refined by the Rietveld method using TOPAS version 6 (Bruker – AXS). The S-sublattice was analyzed using the polyhedral template matching algorithm implemented in the software Ovito.[86] Structural images and maps were drawn using VESTA.[87] Experimental nuclear density extracted from Rietveld refinement of the neutron diffraction data was reconstructed using the Maximum Entropy Method (MEM) implemented with the software Dysnomia.[88] The refined crystal structure was used as input for Bond Valence Site Energy (BVSE) calculations, which were performed with the software SoftBV,[82] using the bond-valence parameters from the softBV database.[89]

Chapter 4

Correlation of Structure and Fast Ion Conductivity in the Solid Solution Series $Li_{1+2x}Zn_{1-x}PS_4$

This section is reproduced in part with permission from:
Kavish Kaup, Fabien Lalère, Ashfia Huq, Abhinandan Shyamsunder, Torben Adermann, Pascal Hartmann, and Linda F. Nazar, *Chemistry of Materials*, **2018**, 30, 3, 592–596 (DOI: 10.1021/acs.chemmater.7b05108).

* Dr. Fabien Lalère helped synthesize the ZnS nanoparticle precursors and refine the synchrotron X-ray diffraction data.

* Dr. Ashfia Huq collected the neutron diffraction data at Oak Ridge National Lab.

* Abhinandan Shyamsunder assisted with the analysis of the local structure.

4.1 Introduction

Richards et al.[90] used density functional theory and *ab initio* molecular dynamics to investigate the $Li_{1+2x}Zn_{1-x}PS_4$ (LZPS) system, which exhibits a body-centered cubic (bcc) sulfur sublattice. Theory suggests that this arrangement of sulfur atoms, which is also adopted by two other fast ion conductors ($Li_7P_3S_{11}$ and LGPS), is correlated to a low lithium migration barrier.[79] The stoichiometric parent phase $LiZnPS_4$ and its optical properties have been previously reported but no ionic conductivity data was provided.[91,92] Its structure consists of a framework of PS_4^{3-} and ZnS_4^{6-} tetrahedra that house Li^+ ions, where Li fully occupies the 2b site and Zn fully occupies the 2a site (**Figure 4.1A**). In the $Li_{1+2x}Zn_{1-x}PS_4$ non-stoichiometric phases (Figure 4.1B) the additional Li ions shares the 2a site with Zn as shown below, with the excess Li distributing equally between the 2a and an additional site, 2d. This 2d site is close to the "interstitial" site that was not explicitly identified in the theoretical work.[90]

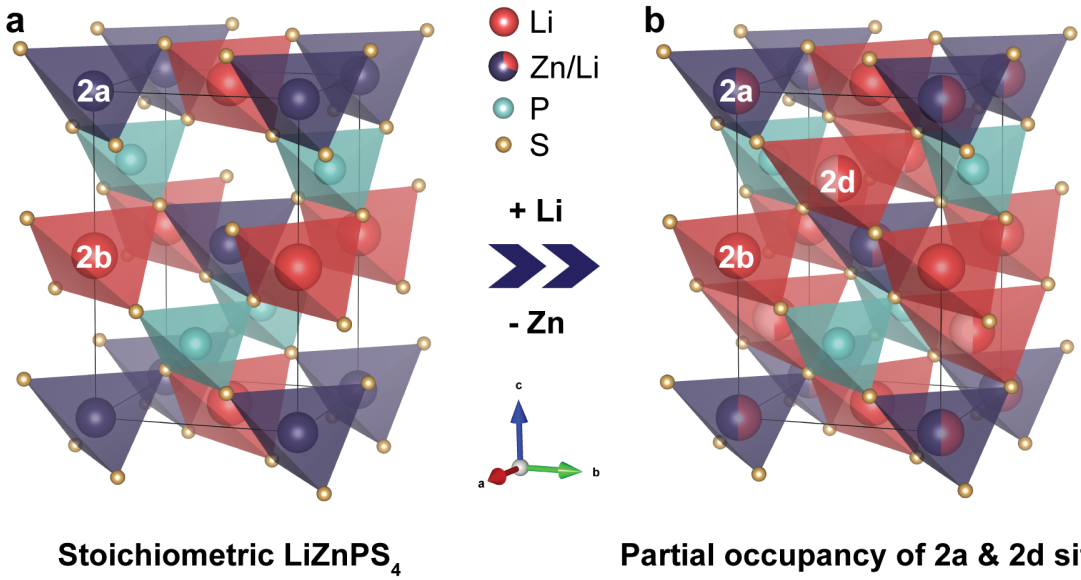

Figure 4.1: a) Crystal structure of stoichiometric $LiZnPS_4$; b) non-stoichiometric, showing addition of interstitial Li in the 2a site shared between Li and Zn and partial occupancy of Li on the 2d site.

The stoichiometric phase was predicted to have extremely poor conductivity based on first-principles calculations (1.81×10^{-12} S·cm^{-1}, E_a = 1.07 eV), while the introduction of interstitial lithium defects is predicted to yield ionic conductivities greater than 5×10^{-2} S·cm^{-1} (with E_a >0.17 eV) at room temperature up to a solid solution solubility limit of x = 0.5;[90] i.e., $Li_2Zn_{0.5}PS_4$. Here, the synthesis of the solid solution series, and the structure of the members within the solubility limit with the highest predicted conductivity, derived from combined X-ray and neutron powder diffraction analysis are reported.

4.2 Results and Discussion

4.2.1 Formation and Structure of LZPS Phases

The highest value of x (i.e. of lithium excess) in a well crystallized sample was x = 0.35, corresponding to $Li_{1.7}Zn_{0.65}PS_4$. Lithium occupation of the 2d site was unequivocally identified, which is charge compensated by substitution of Zn^{2+} ions in the 2a site with Li^+ ions and is crucial for improving ionic transport. Experimental ionic conductivities (σ_i) measured by electrochemical impedance spectroscopy (EIS) show that the σ_i of the most highly conductive phases are in the range of >10^{-4} S·cm^{-1} at 25°C: a very significant improvement over $LiZnPS_4$, albeit less than predicted. Phases with high values of x (>0.5) were experimentally unattainable as relatively pure crystalline phases, however. The observations found in this study demonstrate the enhancement in ionic conductivity for the x = 0.75 phase is likely due to a glass-ceramic matrix effect rather than from its inherent crystalline structure. $Li_{1+2x}Zn_{1-x}PS_4$ compositions were prepared at x = 0.25, 0.5, and 0.75 using solid-state synthesis consisting of ball-milling and annealing. Their synchrotron XRD patterns are shown in **Figure 4.2**. The compositions contain small impurities of $Li_4P_2S_6$ and ZnS which form upon slight decomposition of the LZPS solid solutions because of their metastable nature. As the lithium content increases (up to x = 0.75), the formation of significant γ-Li_3PS_4 impurities becomes evident, in accord with the pseudo-binary phase diagram calculated by Richards et al.[90]

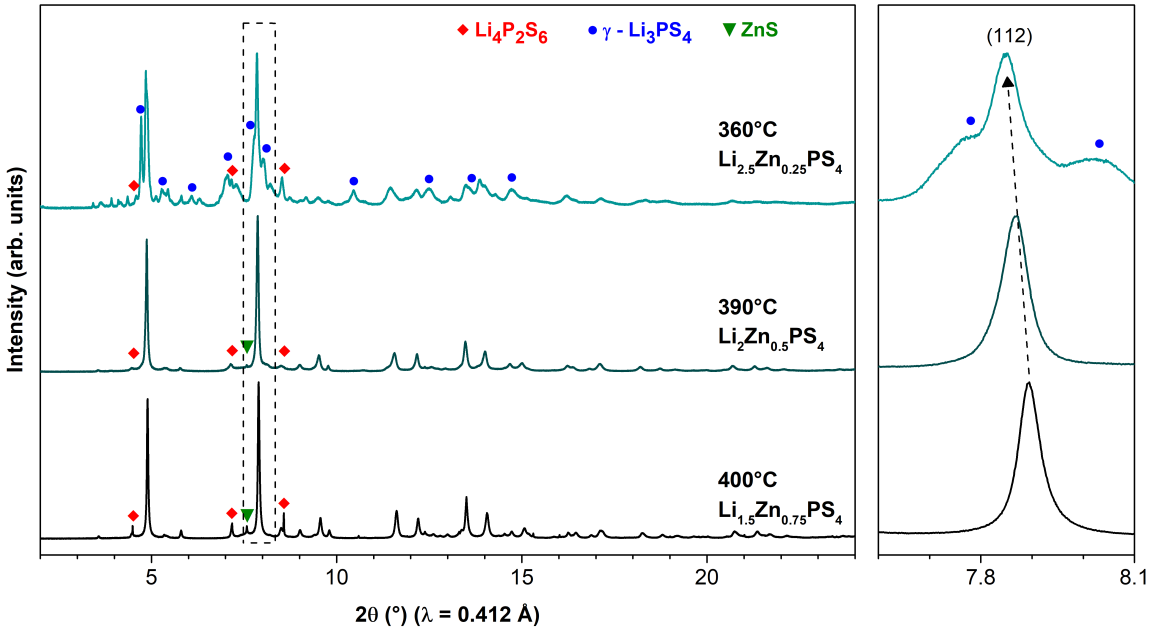

Figure 4.2: Synchrotron powder XRD patterns (25°C) of $Li_{1.5}Zn_{0.75}PS_4$ (x = 0.25), $Li_2Zn_{0.5}PS_4$ (x = 0.5), and $Li_2Zn_{0.5}PS_4$ (x = 0.75) with impurities of $Li_4P_2S_6$, ZnS, and Li_3PS_4 as marked. Region with the dashed box is expanded on the right, indicating the shift in the (112) reflection ($I\bar{4}$ space group) toward higher angle. The corresponding synthesis temperatures are listed above the compositions.

The a and c lattice parameters were extracted by performing a Pawley full powder pattern fit of the synchrotron XRD patterns in the $I\bar{4}$ space group. The trends are shown in **Figure 4.3** (with exact values given in **Table 4.1**), indicating that the cell volume increases with increased lithium content (293 Å^3 to 301 Å^3). The increase in cell volume stems from a significant increase in the a lattice parameter (with a small decrease in the c lattice parameter). Larger lattice volume often correlates to an improvement in ionic conductivity due to a reduced Li^+ ion migration barrier.[79,93] Since the targeted $Li_2Zn_{0.5}PS_4$ phase is expected to have the highest ionic conductivity within the solid solution solubility limit, its crystal structure was refined against combined synchrotron powder XRD data (λ = 0.412 Å) and TOF neutron diffraction data.

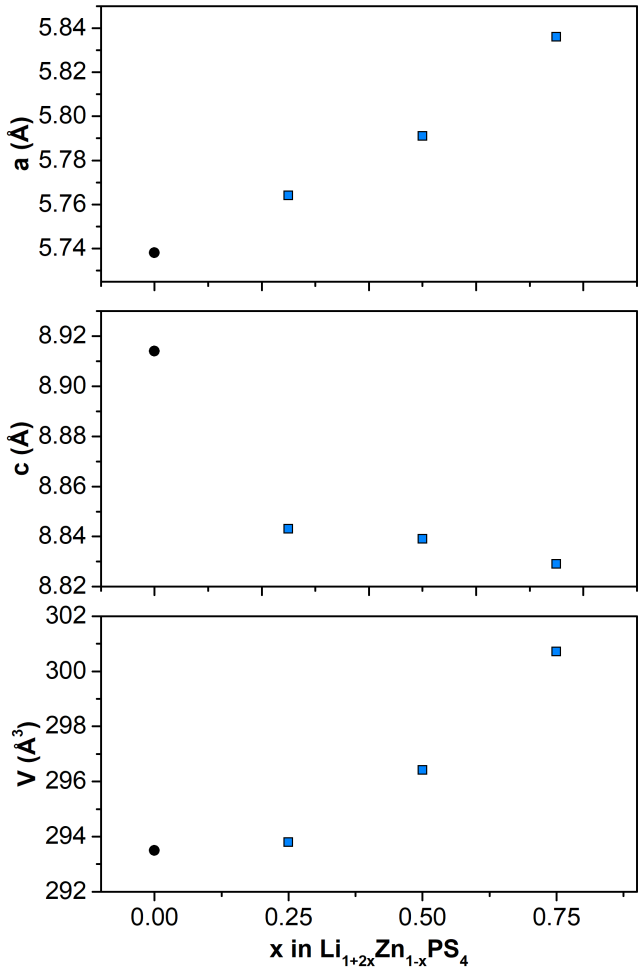

Figure 4.3: Lattice parameter and volume change in $Li_{1+2x}Zn_{1-x}PS_4$ for x = 0, 0.25, 0.5, and 0.75. Solid black circles are from single crystal data taken from the literature[91] and blue squares are experimental data from this work (values are listed in Table 4.1).

Table 4.1: Comparison of lattice parameters for $Li_{1+2x}Zn_{1-x}PS_4$ for the full range of x values.

Composition	**x**	**Space Group**	***a*** **(Å)**	***b*** **(Å)**	***c*** **(Å)**	**Volume (Å³)**
$LiZnPS_4$ *	0	$I\bar{4}$	5.738	5.738	8.914	293.49
$Li_{1.5}Zn_{0.75}PS_4$	0.25	$I\bar{4}$	5.764	5.764	8.843	293.79
$Li_2Zn_{0.5}PS_4$	0.5	$I\bar{4}$	5.795	5.795	8.834	296.66
$Li_{2.5}Zn_{0.25}PS_4$	0.75	$I\bar{4}$	5.836	5.836	8.829	300.71
γ-Li_3PS_4 *	1	*Pnma*	6.101	8.015	13.066	638.92

* values taken from literature[71,91]

The reflections were assigned to a body-centered tetragonal cell (space group $I\bar{4}$, no. 82) with lattice parameters refined to $a = 5.7945$ Å, and $c = 8.8337$ Å. The crystallographic details are summarized in **Table 4.2** (note that bond lengths, **Table B.1**, are typical for all environments) while the fit for the synchrotron and neutron data is shown in **Figure 4.4**.

Table 4.2: Atomic coordinates, Wyckoff symbols, and isotropic displacement parameters for the targeted $Li_2Zn_{0.5}PS_4$ phase in the space group $I\bar{4}$ (no. 82).

Atom	**Wyck. Pos.**	**x**	**y**	**z**	**Occ.**	**B_{iso} (Å^2)**
Li1	2d	0	0.5	0.75	0.345(9)	6
Li2	2b	0	0	0.5	1	8
Li3	2a	0	0	0	0.344(4)	1.49(7)
Zn3	2a	0	0	0	0.656(4)	1.49(7)
P1	2c	0	0.5	0.25	1	0.81(4)
S1	8g	0.7952(2)	0.2821(2)	0.1220(2)	1	1.71(4)

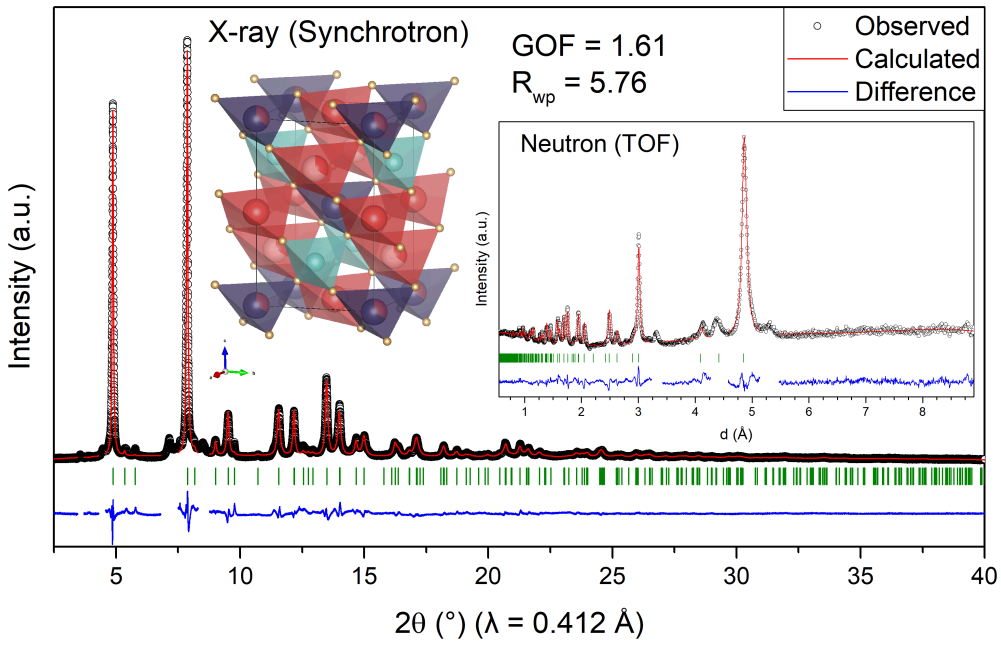

Figure 4.4: Combined Rietveld refinement of $Li_2Zn_{0.5}PS_4$ based on synchrotron XRD and neutron diffraction data. Visual representation of the refined crystal structure (refined to a composition of $Li_{1.7}Zn_{0.65}PS_4$) is shown as an inset. Excluded regions correspond to impurity phases, mainly $Li_4P_2S_6$ which comprises < 5 % of the total (see Figure 4.2).

The results of the refinement indicate that the actual lithium content of the crystalline material is x ≈ 0.35; lower than that targeted (i.e. x = 0.5). The crystalline $Li_{1.687}Zn_{0.656}PS_4$ (i.e., $Li_{1.7}Zn_{0.65}PS_4$) phase thus exists in an amorphous Li-rich thiophosphate matrix. The degree of crystallinity was estimated to be 69% using Si as an internal reference (**Figure B.1**). A proposed mixture of 77% $Li_{1.7}Zn_{0.65}PS_4$ + 23% amorphous-Li_3PS_4 accounts for the overall $Li_2Zn_{0.5}PS_4$ target. The 8% discrepancy may be attributed to the impurity phases (Figure 4.2). The refined structure of $Li_{1.7}Zn_{0.65}PS_4$ shows that the 2a sites are partially occupied by Li (34%) and Zn (66%) while the 2d site has partial occupancy of Li (34%) as visually represented in the inset in Figure 4.4. Owing to the well-known difficulty in simultaneously refining thermal parameters and occupancies of mobile ions, the thermal parameters for the 2d and 2b site were fixed to average values from the literature.[24,26,94,95] This resulted in convergence to site occupancies that yielded perfect charge balance of the compound and an equal distribution of excess Li on the 2d and 2a sites as expected. The results are in excellent accord with *ab initio* molecular dynamics studies that predict significant lithium ion density on an "interstitial site",[90] which is similar to the 2d Wyckoff site identified here.

While $Li_{2.5}Zn_{0.25}PS_4$ (x = 0.75) was projected by theory to have the highest conductivity (1.14×10^{-1} S·cm^{-1}),[90] its structure could not be refined owing to the low quality of the X-ray and neutron data for this poorly crystallized compound. This is in accord with it lying just outside of the predicted solubility limit.[90] The structure of $Li_{1.5}Zn_{0.75}PS_4$ was refined from the synchrotron X-ray data owing to its low lithium content (and a paucity of neutron time); and these results are shown in **Table 4.3**. The fit is shown in **Figure 4.5** and refined bond lengths (Table B.1) correspond to typical values for all environments. The lattice parameters refined to a = 5.7641 Å and c = 8.8438 Å. Since lithium can not be accurately refined from X-ray data, lithium occupation in the 2d and 2a site was fixed to be equal, as determined by the $Li_{1+2x}Zn_{1-x}PS_4$ formulation. The Zn occupancy was refined and the vacant occupancy was assumed to be lithium given that the 2a site occupancy is constrained to 1. The refined composition of $Li_{1.2}Zn_{0.9}PS_4$ (with a 70% degree of crystallinity determined

by standard addition) shows that the target composition was also not achieved in this case. This may be due to slow kinetics of the reaction that prevent achievement of the targeted lithium contents, despite the employment of nano-sized ZnS in the synthesis. However, synthesis at higher temperature or longer times is limited by thermodynamics: due to the metastability of the substoichiometric phases, the LZPS structure partially decomposes to $Li_4P_2S_6$. The formation of such impurity phases can be prevented by heating at lower temperatures; however, this comes at the cost of reduced degree of crystallinity.

Table 4.3: Atomic coordinates, Wyckoff symbols, and isotropic displacement parameters for the targeted $Li_{1.5}Zn_{0.75}PS_4$ phase in the space group $I\bar{4}$ (no. 82).

Atom	**Wyck. Pos.**	**x**	**y**	**z**	**SOF**	**B_{iso} (Å²)**
Li1	2d	0	0.5	0.75	0.097	6
Li2	2b	0	0	0.5	1	8
Li3	2a	0	0	0	0.097	1.30
Zn3	2a	0	0	0	0.903(4)	1.30 (6)
P1	2c	0	0.5	0.25	1	2.3(1)
S1	8g	0.7865(2)	0.2709(3)	0.1294(2)	1	0.89(4)

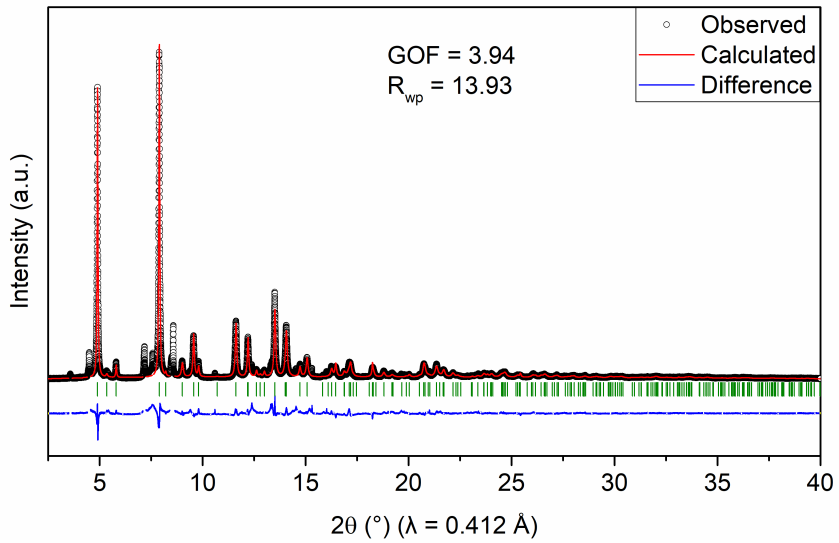

Figure 4.5: Rietveld refinement of $Li_{1.5}Zn_{0.75}PS_4$ based on synchrotron XRD data only. Excluded regions correspond to impurity phases, mainly $Li_4P_2S_6$ which comprises < 10 % of the total (see Figure 4.2).

The importance of excess phonon free energy in stabilizing defect-type ionic conductors with highly mobile Li^+ ion lattices has been previously invoked, for example, in $Li_7P_3S_{11}$, and especially in $Li_{1+2x}Zn_{1-x}PS_4$.[90] The limiting composition $Li_{1.7}Zn_{0.65}PS_4$ (x = 0.35) is approximately halfway between the predicted solubility limit for the solid solution series without phonon contributions (x = 0.15) and with phonon contributions (x = 0.5).[90] Clearly $Li_{1.2}Zn_{0.9}PS_4$ (x = 0.1) falls within in the regime where phonon contributions are not necessary to stabilize the material. All experimental attempts to increase the degree of lithium substitution to attain x = 0.5 were unsuccessful - irrespective of temperature, time and processing conditions - and resulted in significant levels of impurity phases. These results confirm that phonon contributions do play a vital role in stabilizing these defect structures but likely to a lower degree than presumed.

4.2.2 Ionic Conductivity of Crystalline LZPS

Partial occupancy of Li in the 2a and 2d site in the LZPS structure should facilitate the ion conduction by creating low energy percolating pathways through the structure. The Li^+ ion conductivity of the various LZPS compositions was studied using EIS on pressed pellets at variable temperatures. The impedance spectra in Nyquist form showed classic semicircles at high frequency, and a linear Warburg component in the low-frequency range (**Figure 4.6A**). Fitting the data (see inset for equivalent circuit and **Table B.2** for fit parameters) resulted in experimental conductivities at 25°C plotted in Figure 4.6B as a function of lithium content. The activation energy (E_a) was determined from a linear fit of the Arrhenius plots of $\ln(\sigma T)$ vs. $1/T$ but plotted as $\log_{10}(\sigma)$ vs. $1/T$ for convenience.

The conductivities range from 5.40×10^{-8} S·cm^{-1} at x = 0 to 8.4×10^{-4} S·cm^{-1} at x = 0.75. The conductivity of the refined phase $Li_{1.7}Zn_{0.65}PS_4$ was 1.30×10^{-4} S·cm^{-1}, which is lower than predicted for either $Li_2Zn_{0.5}PS_4$ (5.38×10^{-2} S·cm^{-1}) or $Li_{1.5}Zn_{0.75}PS_4$ (2.77×10^{-2} S·cm^{-1}) as shown in Figure 4.6. The amorphous content may be responsible, although temperature-dependent conductivity measurements exhibit Arrhenius behavior with a low activation energy (E_a) of 0.22 eV. This value is close to the range predicted by MD simula-

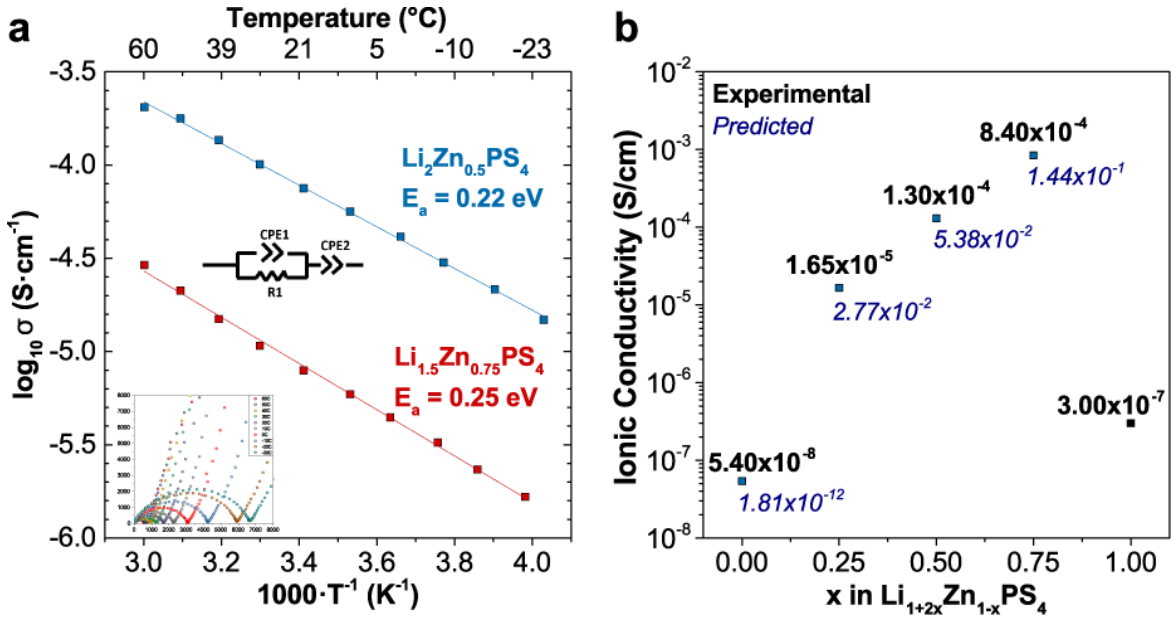

Figure 4.6: A) Activation energy plot of $Li_2Zn_{0.5}PS_4$ and $Li_{1.5}Zn_{0.75}PS_4$ along with an inset of the Nyquist plots at each temperature plus the equivalent circuit used to fit the impedance data and B) Li^+ ion conductivity at 25°C versus x in $Li_{1+2x}Zn_{1-x}PS_4$.

tions for the defect phases,[90] namely 0.165 eV ($Li_2Zn_{0.5}PS_4$) and 0.181 eV ($Li_{1.5}Zn_{0.75}PS_4$). While the possible amorphous phase (i.e., amorphous LPS; $\sigma_i = 2.8\times10^{-4}$ S·cm^{-1})[96] may contribute to the overall conductivity, its much lower reported E_a of 0.4 eV suggests that the σ_i of $Li_{1.7}Zn_{0.65}PS_4$ dominates. Similarly, the refined phase $Li_{1.2}Zn_{0.9}PS_4$ has a room temperature ionic conductivity of 1.65×10^{-5} S·cm^{-1}, lower than the predicted $Li_{1.25}Zn_{0.875}PS_4$ phase (3.44×10^{-3} S·cm^{-1}), but the E_a is 0.25 eV, quite close to theory (0.252 eV).[90]

4.2.3 Enhanced Ionic Conductivity from the Glass-Ceramic

The highest ionic conductivity of 8.4×10^{-4} S·cm^{-1} was achieved when the x = 0.75 glassy precursor was heated at lower temperatures (230°C) to form a very poorly crystallized material. An SEM image of its featureless morphology is shown in **Figure 4.7**. Heating above that temperature results in a lower ionic conductivity of 2.4×10^{-4} S·cm^{-1}, and clear phase separation of the LZPS solid solution and γ-Li_3PS_4. The high conductivity in the glassy phase formed at low temperature is exclusive to the x = 0.75 compound (**Table 4.4**).

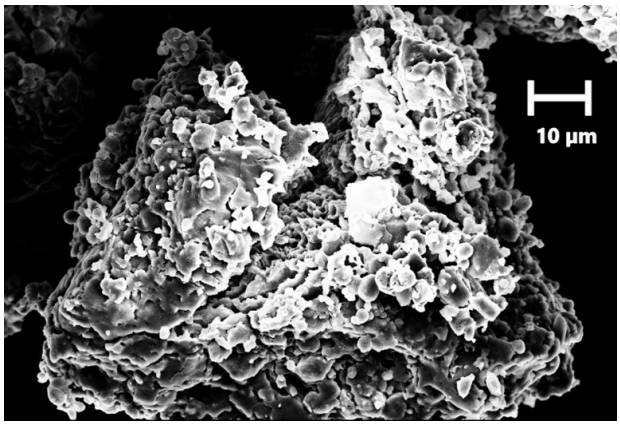

Figure 4.7: SEM image of the $Li_{2.5}Zn_{0.25}PS_4$ glass-ceramic compound after low-temperature annealing showing its glassy morphology.

Table 4.4: Ionic conductivity of compositions obtained at different synthesis temperatures.

	Ionic Conductivity (S·cm^{-1})	
Composition	**High temp. synthesis (360 - 400°C)**	**Low temp. synthesis (230 - 250°C)**
$Li_{1.5}Zn_{0.75}PS_4$	3.9×10^{-6}	1.6×10^{-6}
$Li_{2.5}Zn_{0.25}PS_4$	1.3×10^{-4}	9.4×10^{-5}
$Li_{2.5}Zn_{0.25}PS_4$	2.4×10^{-4}	8.4×10^{-4}

Postulating that the improvement in ionic conductivity arises from the glass-ceramic nature of the material, the local structure of $Li_{2.5}Zn_{0.25}PS_4$ was probed via Raman spectroscopy, and compared to the other two phases (**Figure 4.8**). While $Li_2Zn_{0.5}PS_4$ and $Li_{1.5}Zn_{0.75}PS_4$ show predominantly PS_4^{3-} moieties characteristic of the crystalline structure (along with $Li_4P_2S_6$ impurity), the more highly conductive $Li_{2.5}Zn_{0.25}PS_4$ synthesized at low-temperature has an additional peak in the Raman spectrum not present in the other two compositions. As shown in previous studies,[97] it corresponds to the characteristic symmetric P-S stretching in $P_2S_7^{4-}$ units (P-S-P at 406 cm^{-1}); inherent building blocks in the crystalline fast lithium ion conductor $Li_7P_3S_{11}$.[98] They exist in its amorphous precursor (70:30 Li_2S-P_2S_5 glass), which is known to have very high conductivities of $>10^{-4}$ S·cm^{-1} before annealing.[96] The glassy matrix likely play a significant role in the high ionic conductivity of "$Li_{2.5}Zn_{0.25}PS_4$", rather than inherently enhanced pathways in the structure.

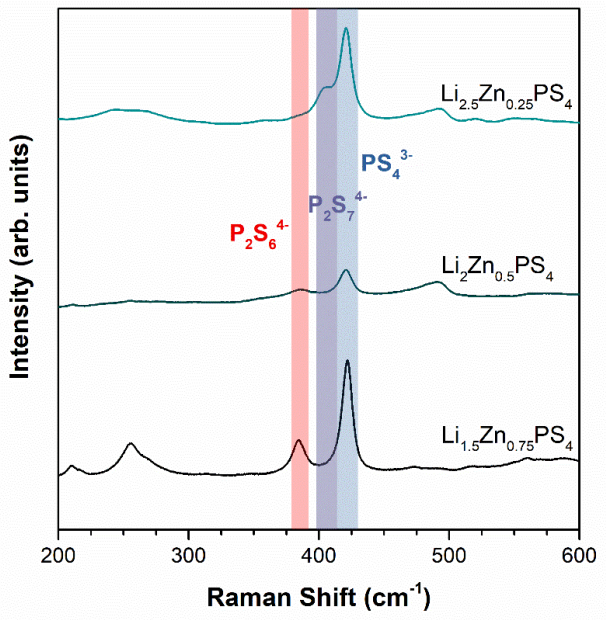

Figure 4.8: Raman spectra of glass and glass-ceramics for $Li_{1+2x}Zn_{1-x}PS_4$ compositions x = 0.25, 0.5 and 0.75 showing the characteristic bands for the PS_4, P_2S_7 and P_2S_6 moieties as labelled.

4.3 Conclusion

In summary, these results provide an understanding of ion transport in the $Li_{1+2x}Zn_{1-x}PS_4$ solid solution series by defining the complex relationship between lithium site occupation/position and ionic conductivity. *Ab initio* computational techniques provide inspiration and guidance in the search for new solid-state ion conductors. Here, the results of introducing interstitial lithium defects in in the solid solution regime $Li_{1+2x}Zn_{1-x}PS_4$ predicted by theory are compared with that of experiment. The stability of the defect phases owing to phonon contributions may be somewhat overestimated by theory, as all phases are found to be highly metastable. Such metastability results in difficulty in overcoming the kinetics necessary for mass transport in order to access the pure phases at the low temperatures required for their synthesis. Nonetheless, phases close to the targeted $Li_2Zn_{0.5}PS_4$ and $Li_{1.5}Zn_{0.75}PS_4$ were successfully synthesized. Their structures were elucidated via refinement of neutron and synchrotron XRD data.

The obtained phases, $Li_{1.7}Zn_{0.65}PS_4$ and $Li_{1.2}Zn_{0.9}PS_4$ respectively, demonstrated ionic conductivities of 1.30×10^{-4} S·cm^{-1} and 1.65×10^{-5} S·cm^{-1}. These values are more than four orders of magnitude higher compared to that of the parent $LiZnPS_4$, owing to occupation of the 2d interstitial site in the lattice as predicted by theory. This represents a good demonstration of how information from *ab initio* molecular dynamics can augment experiment, similar to $Li_{10}GeP_2S_{12}$, where early reports using powder diffraction alone could not locate a lithium site important to 3D mobility, but a combination of theory and single crystal diffraction enabled full structure resolution.[24,99–101] While the experimental lithium ion conductivities were lower than predicted, this can be ascribed to a combination of not fully accessing the targeted lithium defect concentrations (owing to the limitations of kinetics and thermodynamics), and the accompanying reality of the presence of amorphous and potentially poorly conductive materials. The fact that solid solutions close to the predicted superionic phases can be synthesized is encouraging, however, and suggests that alternate highly non-equilibrium synthetic routes may be required to access pure phases. This should provide further inspiration for future endeavors. Moreover, LZPS compositions at high lithium contents – $Li_{2.5}Zn_{0.25}PS_4$ - exhibit conductivities up to 8×10^{-4} S·cm^{-1}, showing that a glassy matrix can play a key role in governing fast lithium ion conduction.

4.4 Experimental Methods

4.4.1 Material synthesis and characterization

ZnS nanoparticles were prepared by literature methods[102] and used as a precursor along with Li_2S and P_2S_5. Starting materials of Li_2S (Sigma Aldrich, 99.98%), P_2S_5 (Sigma Aldrich, 99%) and ZnS were ground together in a mortar and pestle inside an Ar filled glovebox. Amorphous precursors of the $Li_{1+2x}Zn_{1-x}PS_4$ compositions were prepared by mechanochemical synthesis. The powder was placed in 45 mL Si_3N_4 jars with Si_3N_4 balls and milled for 10 hours using a high energy planetary ball mill (Fritsch PULVERISETTE 7 Premium). The samples (200 mg) were cold pressed at 2 metric tons into 10-13 mm

diameter pellets. These amorphous materials were crystallized via heat-treatment under an Ar atmosphere. Samples with the highest crystallinity were synthesized by placing the sample directly in the furnace at a temperature of 360 - 400°C for 0.5 h in a glassy carbon crucible, and cooled to room temperature.

4.4.2 Synchrotron X-ray and neutron diffraction of solid electrolytes

The synchrotron XRD samples were loaded into 1.5 mm diameter Kapton capillaries and sealed with epoxy inside an Ar filled glovebox. The samples were measured on 11-BM at the Advanced Photon Source at the Argonne National Laboratory. TOF neutron diffraction samples were loaded into a vanadium can sealed with a copper gasket and aluminum lid. Samples were collected on POWGEN at the Spallation Neutron Source (SNS) in Oak Ridge National Laboratory. The resulting diffraction patterns were refined using TOPAS version 6 (Bruker - AXS). The $LiZnPS_4$ structure in the space group $I\overline{4}$ by Mewis *et al.* was used as a starting point for refinement.[91]

4.4.3 Raman spectroscopy of solid electrolytes

Samples were pelletized and then placed on a microscope slide, covered by a glass coverslip, and sealed with epoxy. Raman spectra of the materials were obtained using a 514 nm laser (Raman HORIBA HR800).

4.4.4 Conductivity measurements of solid electrolytes

Ionic conductivity was measured using AC impedance spectroscopy. The powder was pelletized in a 10 mm diameter custom-made Swagelok cell. The pellet was placed in between two In foils in order to maintain a good interface at varying temperatures. The cell was placed in an ITS oven (Bio-Logic) connected to a MTZ-35 impedance analyzer (Bio-Logic), controlled by the software MT-LAB (Bio-Logic). The impedance was measured from 35 MHz to 1 Hz at temperatures ranging from -25°C to 60°C.

4.4.5 Degree of crystallinity measurements

The laboratory X-ray powder diffraction data was collected on a Panalytical Empyrean diffractometer outfitted with a PIXcel two-dimensional detector using Cu-Kα radiation. The ground samples were loaded and sealed in a 0.3 mm diameter quartz capillary. Patterns were recorded in Debye-Scherrer geometry using a parabolic X-ray mirror in the incident beam. For the calculations of degree of crystallinity, samples were ground together with approximately 10-11 weight percent of Si, which was used as an internal standard in the Rietveld refinements.

Chapter 5

A Lithium Oxythioborosilicate Solid Electrolyte Glass with Superionic Conductivity

This section is reproduced in part with permission from John Wiley & Sons, Inc. publishing:
Kavish Kaup, J. David Bazak, Shahrzad Hosseini Vajargah, Xiaohan Wu, Joern Kulisch, Gillian R. Goward, and Linda F. Nazar, *Advanced Energy Materials*, **2020**, 10, 8, 1902783 (DOI: 10.1002/aenm.201902783)

* Dr. David Bazak and Prof. Gillian Goward carried out the MAS-NMR experiments at McMaster University. The interpretation and analysis of the data was done by myself with assistance from Dr. Bazak.

* Dr. Shahrzad Vajargah carried out the STEM and EELS measurements.

* Dr. Xiaohan Wu and Dr. Joern Kulisch provided elemental analysis of the glass sample.

5.1 Introduction

Oxides and sulfides based materials are amongst the most extensively studied groups of solid electrolytes. Garnet-type oxides,[22,103] phosphates such as lithium aluminum titanium phosphates, and anti-perovskites[104] typically lead to better chemical and electrochemical stability. In contrast, thiophosphates[105–107] usually exhibit higher ionic conductivity - ranging up to 10^{-2} S·cm^{-1} - coupled with easier processability, but a relatively narrow electrochemical stability window.[29] While the PS_4^{3-} anion in thiophosphates are reduced in contact with Li metal, this reaction can fortuitously form a passivating layer by in-situ redox chemistry at the interface.[108] However, a study of crystalline materials including β-Li_3PS_4 and the garnet LLZO showed they did not prevent Li dendrite penetration due to the presence of micro-cracks, whereas only a defect-free surface of glassy Li_2S-P_2S_5 exhibited Li deposition without Li metal penetration into the solid electrolyte at current densities up to 5 mA·cm^{-2}.[34] There is thus strong motivation to develop amorphous monolithic glasses with minimal surface defects that can also combine the good chemical and electrochemical stability of oxides with the soft nature of sulfides.

Glasses have long been investigated as solid state electrolytes. LiPON is probably the best known glassy SE which has been widely studied and utilized in thin-film batteries.[15] While its very low electronic conductivity has been proposed to be critical in inhibiting dendrite penetration at high current densities,[109] its low ionic conductivity (σ_i) of $\sim 10^{-6}$ S·cm^{-1} limits its use to thin-film cells, not bulk solid state batteries.[110] Pivotal efforts have been made to transform garnet oxides into an amorphous glass via sputtering, but unfortunately the resultant ionic conductivity ($\sim 10^{-8}$ S·cm^{-1}) again limits this approach to thin-film batteries, at least to date.[111] Generally speaking, oxide-based glasses exhibit rather low conductivity but better stability, whereas principally, only sulfide-based amorphous materials have achieved conductivities greater than 10^{-4} S·cm^{-1}, allowing them to be used in bulk-type cells. For example, non-annealed glassy Li_2S-P_2S_5[96] and Li_2S-P_2S_5-LiI[112] exhibit conductivities of 2.8×10^{-4} and $5.6\times\ 10^{-4}$ S·cm^{-1}, respectively, while 10^{-3} S·cm^{-1} is gen-

erally considered a benchmark for practical thick-electrode cells.[113] While sulfide glasses exhibit favourable mechanical properties and enable easy low-temperature processability, they suffer from moisture stability.[114] Oxysulfide glasses have been explored as a middle-ground to provide an acceptable compromise, but to date, only very limited amounts of oxygen have been incorporated in the glasses – for example as lithium ortho-oxosalts (e.g. 4-5 mole % Li_4SiO_4, Li_3PO_4)[115,116] - without incurring a penalty in conductivity. Typically, amorphous glasses contain Li_2S in addition to a network glass former and modifier such as P_2S_5, SiS_2, or GeS_2,[114,117] and lithium halide salts (e.g. LiX - X = Cl, Br, I)[118] to increase the lithium concentration. B_2S_3 is also a glass former that was explored 20-30 years ago,[119–121] but has since received little attention. Most glasses are prepared by ball-milling (which is also utilised for Li_2S-P_2S_5 glass-ceramics) that can present limitations in terms of scale-up. In vitreous glasses which can be synthesized directly via a melt, the absence of any crystalline conduction pathways or particulate interfaces leads to isotropic ion mobility without any grain boundary resistance. The absence of grain boundaries should (in principle) disfavor dendrite formation, and dense films can be formed by a melt-quench approach.

Here, the synthesis of the first quaternary glass compositions that achieve lithium ion conductivities up to 2×10^{-3} $S\cdot cm^{-1}$ is reported, meeting the target for utilization in a bulk-type solid state cell. These lithium oxythioborate halide glasses (Li_2S – B_2S_3 – SiO_2 – LiI, or "LIBOSS") are obtained directly from the melt, without ball-milling. Moreover, as a result of SiO_2 content as high as 50 mole%, they exhibit low H_2S evolution upon exposure to moisture under ambient conditions. The incorporation of the iodide provides a favorable interface with Li metal as demonstrated by stable stripping/plating in a symmetric cell, with polarization about 10 fold lower than β-Li_3PS_4. Solid-state MAS NMR is utilized to correlate the structural entities in the glass with the significant changes in ionic conductivity as a function of SiO_2 content. The incorporation of silica re-structures the thioborate network to enable much greater dissolution of LiI within the glass matrix, which increases both Li-ion concentration and mobility. These properties directly translate to excellent cell performance

of an all-solid-state battery at room temperature that exhibits stable cycling for over 130 cycles at room temperature with $> 99.9\%$ capacity retention, and close to 100% Coulombic efficiency.

The quaternary compositions Li_2S – B_2S_3 – SiO_2 – LiI can be described by the general phase diagram shown in **Figure 5.1**. A wide range of compositions was examined to screen for glass forming ability coupled with good ion conductivity. The generalized formula (Li_2S, B_2S_3, and LiI sum to 1):

$$aLi_2S + yB_2S_3 + zLiI + xSiO_2 \rightarrow Li_{2a+z}B_{2y}Si_xO_{2x}S_{a+3y}; \;\; a+y+z=1; \qquad 0 \leq x \leq 1$$

provides a description of a single horizontal slice in the quaternary phase diagram, as shown in Figure 5.1 (right). A line on the quaternary phase diagram in Figure 5.1 was explored using $30Li_2S$-$25B_2S_3$-45LiI with variable SiO_2 content (x), namely $30Li_2S$-$25B_2S_3$-45LiI-$xSiO_2$ ($Li_{1.05}B_{0.5}Si_xO_{2x}S_{1.05}I_{0.45}$). These compositions were found to be on the cusp of the glass forming region. The compositions in mole % can also be normalized to compare Li, O and S content (where the precursors sum to 1):

$$aLi_2S + yB_2S_3 + zLiI + xSiO_2 \rightarrow Li_{2a+z}B_{2y}Si_xO_{2x}S_{a+3y}I_z; \quad a+y+z+x=1$$

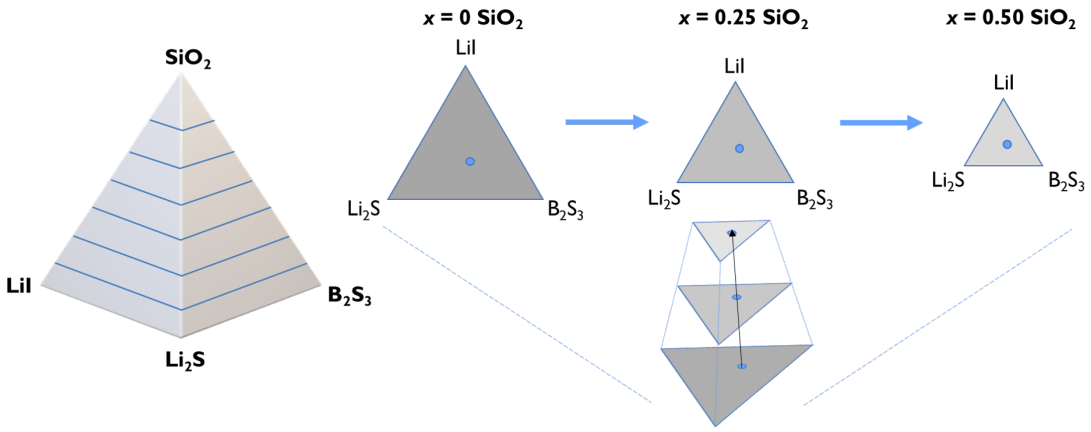

Figure 5.1: Schematic of the quaternary phase diagram (left) with horizontal slices indicating the conversion from the normalized to a general representation (right).

5.2 Results and Discussion

5.2.1 Glass Forming Region and Conductivity

Glass precursors described above (Li_2S, B_2S_3, LiI, and SiO_2) were mixed in the targetted stoichiometric ratio, and melted in a crucible at 800°C. As energy-intensive ball-milling is not required, melt processing achieves higher yields because all the material can be easily removed from the container. The product was extracted, ground and subjected to X-ray diffraction (XRD) analysis to map out the glass forming domain of the phase diagram. The patterns shown in **Figure 5.2** indicate that the x = 0 material, $30Li_2S$-$25B_2S_3$-45LiI, contains a significant contribution of crystalline LiI (∼28 wt% based on standard addition methods, see **Figure C.1** in **Appendix C** for the fits) despite this composition ostensibly being within the reported glass forming region (although no diffraction data were provided in the report[120–122]). Most importantly, the addition of even a small fraction of SiO_2 (x = 0.125) dissolves most of the LiI into the glass owing to its strong network-forming ability. The small remaining reflections in the XRD pattern suggest that this composition is near the cusp of the fully amorphous glass forming domain. Between SiO_2 fractions of x = 0.25 and up to x = 0.75, all of the LiI is dissolved into the matrix evidenced by the lack of (or extremely weak) reflections in the XRD pattern. Analysis of the glass at x = 0.25 by inductively coupled plasma methods confirmed a composition of $Li_{0.85}B_{0.39}Si_{0.17}O_{0.41}S_{0.76}I_{0.43}$), very close to that targeted ($Li_{0.84}B_{0.40}Si_{0.2}O_{0.4}S_{0.84}I_{0.36}$; see **Table 5.1** for details). The strong modification of the thioborate network by silica that enables the high fraction of dissolution of LiI may be explained by the formation of tetrahedral SiS_4 moities (as observed by ^{29}Si NMR, see below), which act as "glass-expanders" to create additional free volume that accommodates the LiI. This is discussed in detail later in the section on local structure. Beyond a critical concentration (x = 0.75), however, the solubility limit of LiI (and SiO_2) is reached and their exsolvation is observed as minority crystalline phases. Outside of the glass region from $0.25 \leq x \leq 0.75$, the material can be regarded as a composite or glass

ceramic. The incorporation of SiO_2 also results in materials that exhibit suitable moisture stability (see below), which is a common drawback of pure sulfide-based solid electrolytes, whether they are glasses or ceramics.

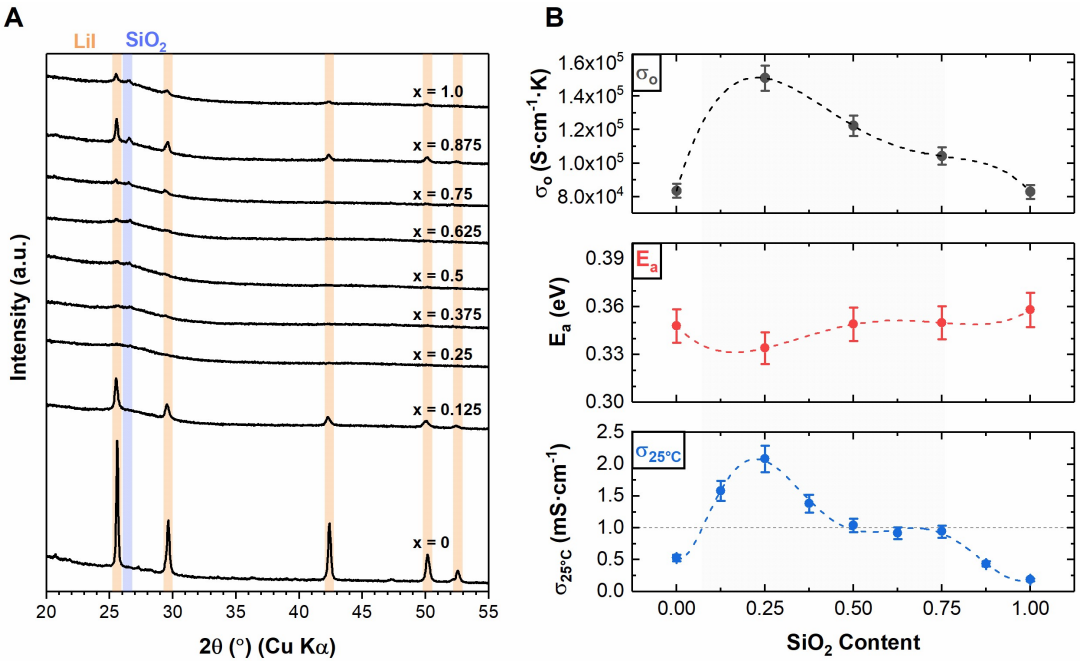

Figure 5.2: Compositions $Li_{1.05}B_{0.5}Si_xO_{2x}S_{1.05}I_{0.45}$ where $0 \leq x \leq 1$ A) XRD patterns indicating the glass forming region. Peaks corresponding to LiI and SiO_2 are shown as labeled. B) Room temperature conductivity, activation energy, and pre-exponential factor.

Table 5.1: Inductively coupled plasma elemental analysis on LIBOSS x = 0.25 composition.

Element	Mass (g/100 g)
Iodine	54
Sulfur	24.4
Boron	4.2
Lithium	5.9
Silicon	4.9

The trend in ionic conductivity determined from electrochemical impedance spectroscopy (EIS) is displayed in Figure 5.2B, and the compositions and their respective conductivities are summarized in **Table 5.2** (see **Figure 5.3** for corresponding Nyquist plots). No semicircles are observed in the Nyquist plots due to the low resistance of the electrolytes and

instrument limited frequency range of the measurements. Thus, a linear fit of the diffusive tail at low frequencies was performed to determine the total resistance (intersection with the x-axis) and subsequently used to calculate the ionic conductivity. Only a small fraction of SiO_2 is sufficient to increase the lithium ion conductivity from 5×10^{-4} S·cm^{-1} (x = 0) to 1.6×10^{-3} S·cm^{-1} (x = 0.125). An optimal and quadrupled (with respect to x = 0) value of 2.1×10^{-3} S·cm^{-1} is reached at a silica content of x = 0.25 ("LIBOSS-25") where no features are visible in the XRD pattern. Although nanodomains of LiI may still exist, these would be below the scattering length that diffraction is able to probe (*ca.* 20 nm).

Table 5.2: Summary of room temperature conductivity and activation energy for the compositions $Li_{1.05}B_{0.5}Si_xO_{2x}S_{1.05}I_{0.45}$ for $0\leq x\leq 1$.

Composition (Generalized)	SiO_2 (x-value)	Composition (Normalized)	Room Temp. Conductivity (S·cm^{-1})	Activation Energy (eV)
$30Li_2S$-$25B_2S_3$-45LiI-$12.5SiO_2$	0.125	$Li_{0.93}B_{0.44}Si_{0.11}O_{0.22}S_{0.93}I_{0.4}$	1.6×10^{-3}	
$30Li_2S$-$25B_2S_3$-45LiI-$25SiO_2$	0.25	$Li_{0.84}B_{0.40}Si_{0.2}O_{0.4}S_{0.84}I_{0.36}$	2.1×10^{-3}	0.33
$30Li_2S$-$25B_2S_3$-45LiI-$37.5SiO_2$	0.375	$Li_{0.76}B_{0.36}Si_{0.27}O_{0.55}S_{0.76}I_{0.33}$	1.4×10^{-3}	
$30Li_2S$-$25B_2S_3$-45LiI-$50SiO_2$	0.5	$Li_{0.70}B_{0.33}Si_{0.33}O_{0.67}S_{0.7}I_{0.3}$	1.0×10^{-3}	0.35
$30Li_2S$-$25B_2S_3$-45LiI-$62.5SiO_2$	0.625	$Li_{0.65}B_{0.31}Si_{0.38}O_{0.77}S_{0.65}I_{0.28}$	9.2×10^{-4}	
$30Li_2S$-$25B_2S_3$-45LiI-$75SiO_2$	0.75	$Li_{0.60}B_{0.29}Si_{0.43}O_{0.86}S_{0.6}I_{0.26}$	9.4×10^{-4}	0.35
$30Li_2S$-$25B_2S_3$-45LiI-$82.5SiO_2$	0.825	$Li_{0.56}B_{0.27}Si_{0.47}O_{0.93}S_{0.56}I_{0.24}$	4.3×10^{-4}	
$30Li_2S$-$25B_2S_3$-45LiI-$100SiO_2$	1.0	$Li_{0.53}B_{0.25}Si_{0.50}OS_{0.53}I_{0.23}$	1.8×10^{-4}	0.36

In order to verify that ionic conduction is dominant, DC polarization measurements were performed on this composition, determining a low electronic conductivity on the order of 10^{-9} S·cm^{-1} (see **Figure 5.4** for representative *I-V* curves). Scanning electron microscopy (SEM) images and their respective energy dispersive X-ray (EDX) analysis (**Figure 5.5**), and scanning transmission electron microscopy (STEM) analysis with the accompanying electron energy loss spectra (EELS) (**Figure 5.6**), indicate that LIBOSS-25 possesses uniform elemental homogeneity, at least on the submicron scale.

As the silica content increases above x = 0.25 the ionic conductivity decreases, but minority crystalline phases are significantly less than what is observed even for the x = 0.125 composition. A conductivity of 9×10^{-4} S·cm^{-1} is still maintained up to x = 0.75. Beyond x = 0.75, crystalline SiO_2 and LiI are observed in the XRD patterns, signalling the limit

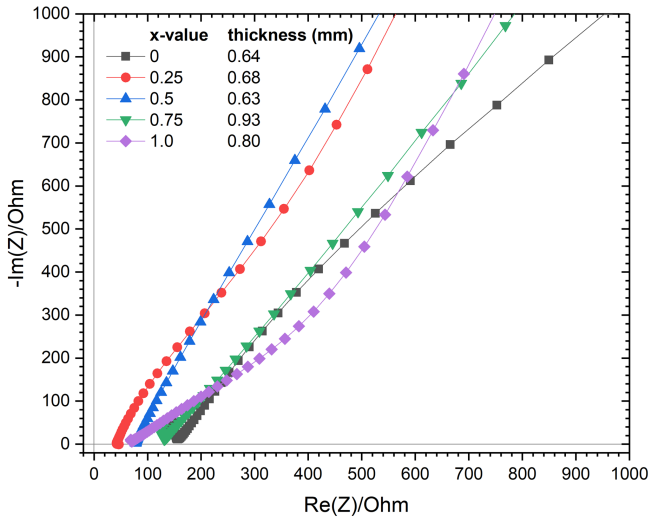

Figure 5.3: Nyquist plots of glass composition x = 0, 0.25, 0.5, 0.75, and 1.0 measured using EIS (100 mV, 1 MHz to 100 mHz) in a stainless-steel/SE/stainless-steel cell configuration.

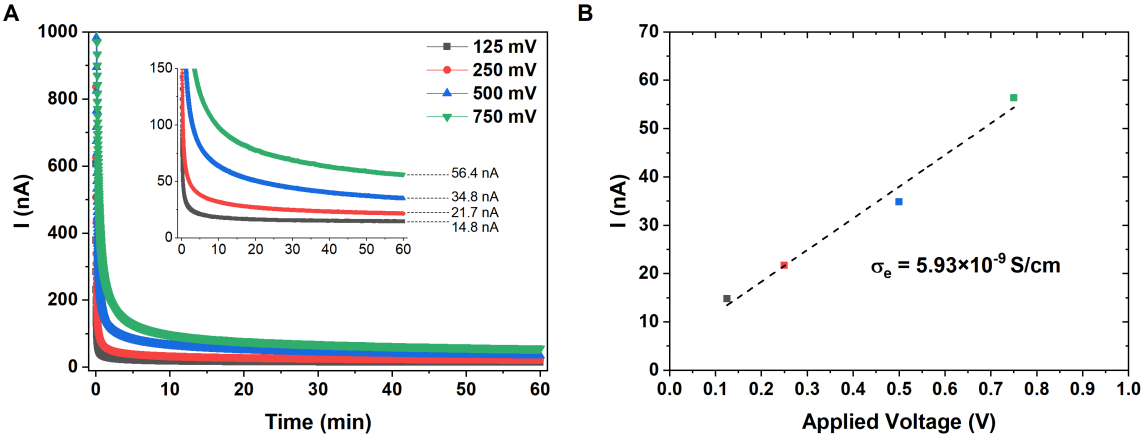

Figure 5.4: A) DC polarization curves for V = 125, 250, 500 and 750 mV and B) I-V curve for the determination of the electronic conductivity for the x = 0.25 composition at room temperature.

of SiO_2 solubility in the $30Li_2S$-$25B_2S_3$-45LiI-$xSiO_2$ compositional range. At x = 1 a drop in conductivity to 1.8×10^{-4} S·cm^{-1} occurs, in part owing to the lower Li^+ ion concentration/unit volume. Notably, the glass compositions from $0.25 \leq x \leq 0.75$ encompass very high oxygen: sulfur ratios - more than to 1:1 - yet still maintain conductivity of 10^{-3} S·cm^{-1}. Typically, oxygen substitution in sulfides decreases the ionic conductivity quite

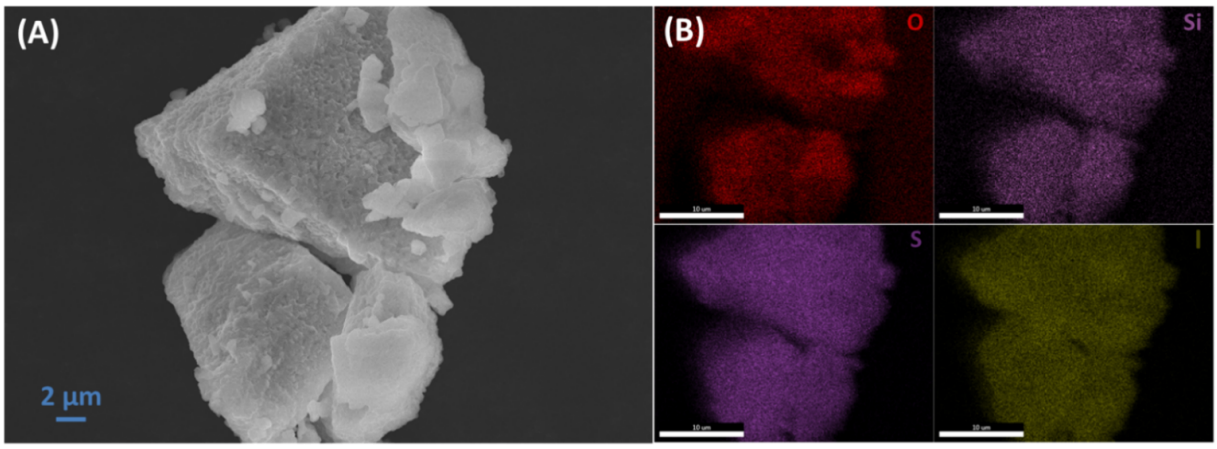

Figure 5.5: (A) SEM image of a glass particle, (B) corresponding EDX analysis, and (C) elemental mapping showing homogenous distribution of elements through the glassy particle.

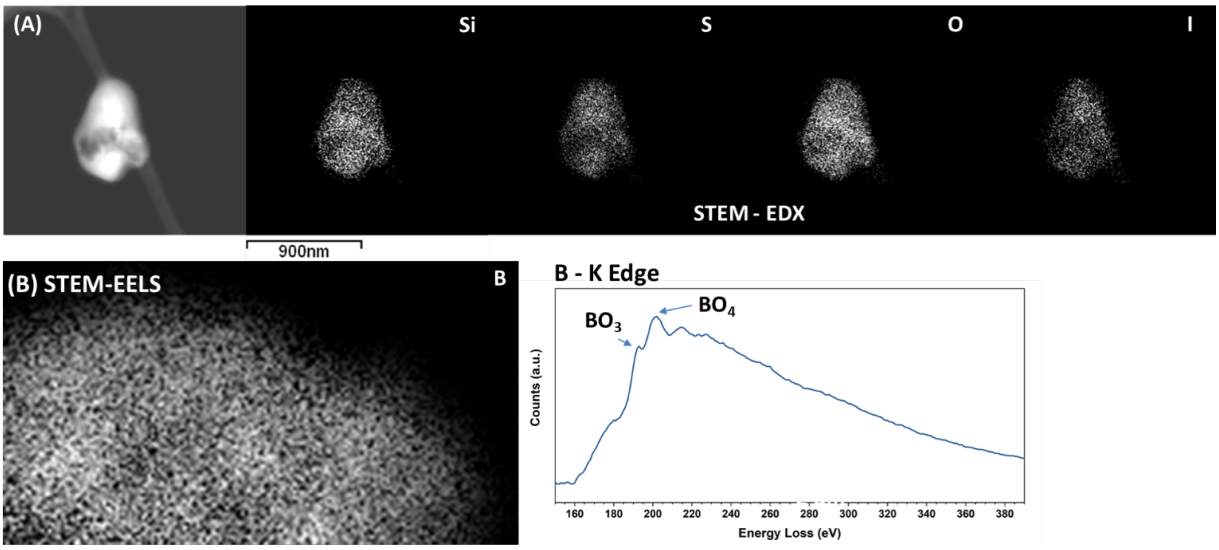

Figure 5.6: (A) STEM images and corresponding EDX, and (B) STEM-EELS indicates presence of boron through the particle with the motifs indicated.

significantly owing to stronger electrostatic attraction of the Li ions to the less polarizable O^{2-} anions. Most prior reports of oxygen substitution in sulfide glass, glass ceramic, and crystalline materials have reported low O:S ratios of ∼1:5 to maintain conductivity of this order of magnitude.[115,116] In principle, more oxygen can be incorporated into a sulfide glass in comparison to a crystalline material owing to the large difference in size between the

two chalcogenide anions (ionic radius of 1.4 Å for O^{2-} and 1.8 Å for S^{2-}), and the rigid structural requirements of a crystalline lattice. One of the highest oxygen contents in a crystalline sulfide that has been reported is for $Li_{9.42}Si_{1.02}P_{2.1}S_{9.96}O_{2.04}$, that exhibits a conductivity of 3.2×10^{-4} S·cm^{-1}.[123] In a glass, one is also limited by the solubility of the oxide, but the constraints are fewer.

The temperature dependence of the ionic conductivity for all the compositions was examined and found to obey the Arrhenius law of the form $\sigma = \frac{\sigma_o}{T} e^{-\frac{E_a}{kT}}$ in the investigated temperature range (see **Figure 5.7** for Arrhenius and Nyquist plots). Despite the wide frequency range used (10 MHz to 100 mHz), circuit fitting of the Nyquist plots were complicated due to inductance effects at high frequency and some additional semicircles, which is attributed to multiple secondary phases (as seen in the XRD patterns for high SiO_2 contents). There may also be an additional interface present between the solid electrolyte and In foil, as seen by the emergence of a low-frequency semicircle before the diffusive tail. Figure 5.2B shows there is no clear dependence of the activation energy on the oxygen content in the halosulfide glass. Even at the x = 0.5 composition where the S:O ratio is approximately 1:1, the activation energy (0.35 eV) is the same as x = 0 (see Table 5.2). There is only a very weak correlation between activation energy and conductivity unlike that observed for most ion conductors.[41] The prefactor σ_o of the Arrhenius equation can be described as:

$$\sigma_o = \frac{zn(Ze)^2}{k_B} e^{\frac{\Delta S_m}{k_B}} a_o^2 \nu_o$$

where σ_o is composed of the Boltzmann constant k_B, a geometrical factor z, the density of mobile charge carriers n, the charge of the ions Ze, the entropy of migration ΔS_m, the jump distance a_o, and the jump frequency ν_o. In this case, the activation energy is also not correlated with the decrease in the prefactor in the glass regime from $0.25 \leq x \leq 0.75$, as is the case for fast-ion conductors that follow the Meyer-Neldel rule,[41,124] although such a relationship may be obscured by the magnitude of the error bars on E_a and the presence of crystalline precipitates in some of the glass compositions. In summary, the increase in

conductivity from x = 0 to 0.25 is explained by the increase in density of Li-ion carriers as more LiI is solubilized into the glass matrix; in turn, the subsequent decrease in conductivity and prefactor (x>0.25) can be ascribed to a combination of decrease in the carrier density (n) and the jump frequency, ν_o. The composition at x = 0.25 represents an optimum.

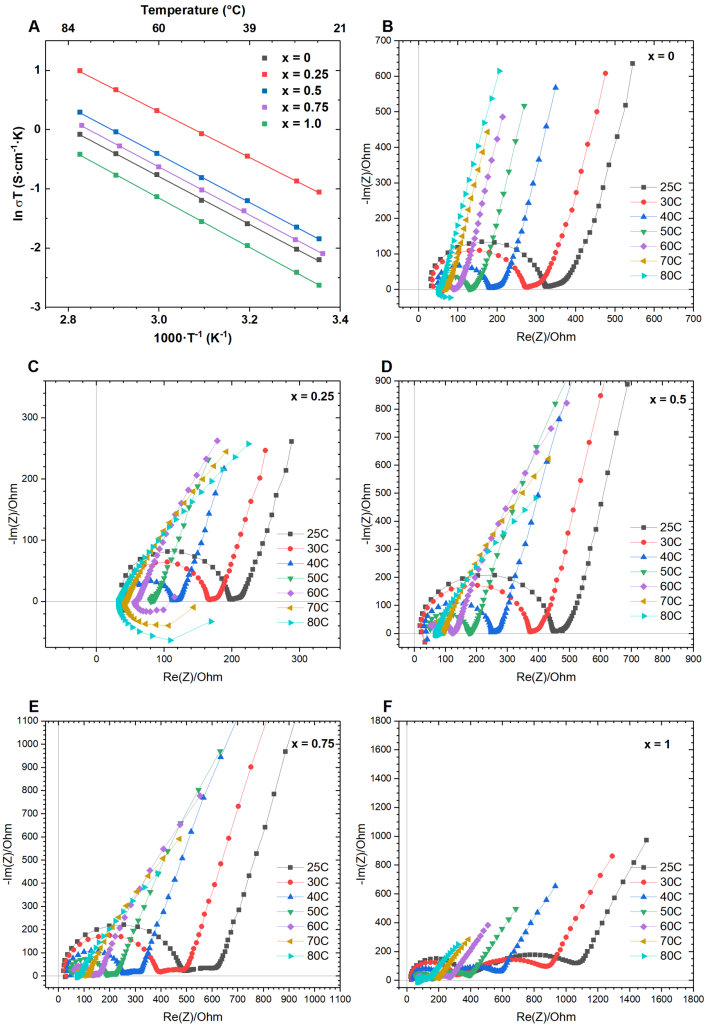

Figure 5.7: A) Arrhenius plots and B-F) corresponding Nyquist plots (10 MHz to 100 mHz) for compositions $Li_{1.05}B_{0.5}Si_xO_{2x}S_{1.05}I_{0.45}$ where $0 \leq x \leq 1$ in In/SE/In cell configuration.

5.2.2 Thermal Behavior

The thermal stability of the glass can be characterized by the softening (glass transition) temperature (T_g) and the stability against crystallization, which is measured by the temperature difference of the onset of crystallization (T_x) and T_g. Differential scanning calorimetry (DSC) studies of the compositions in **Figure 5.8** show that for x = 0, the T_g is observed at 267°C, with a subsequent T_x at 272°C. This crystallization peak corresponds to LiI crystallization, as confirmed by XRD measurements on samples annealed just above T_x. A large endothermic peak corresponding to melting (T_l) occurs at 374°C. The origin of this melting is unknown but may be the melting of mixed LiI with hydrated LiI. LiI and its hydrates have been shown to have congruent melting points.[125]

In the case of the x = 0.25 composition, a very broad exotherm (T_x = 330°C) is present after the glass transition temperature, which appear a lot sharper in other compositions. Subsequent annealing at 375°C, after the exotherm, results in exsolvation of LiI from the amorphous matrix as in the case for the x = 0 composition. The various T_l's seen in the DSC curves do not correspond to the melting of the glass itself but are a result of the melting of the LiI (with a slight trace of moisture picked up from the N_2 flow, that slightly lowers the melt temperature as it is a function of hydrate content), which was previously recrystallized from the glass.

Upon incorporation of SiO_2 into the network, there is only a small increase in T_g of about 30°C. The value of T_g, 300 °C, is only a little higher than that of the classic thiophosphate glass ion conductor, $0.30P_2S_5$-$0.70Li_2S$ (212 °C).[33] The fact that there is a linear correlation between the softening temperature and the elastic (Young's) modulus[126] is in accord with the observations here that both the thiophosphate and these oxythioborate glasses are easily pelletized and relatively ductile. Both T_x and T_l are increased by about 60 °C, and the thermal stability of each composition is summarized in **Table 5.3**. In effect, silica incorporation into the glass increases the thermal stability parameter, ΔT_x (T_x-T_g) from 5 (at x = 0) to 36 (at x = 0.5), implying that the modified glass has greater stability with

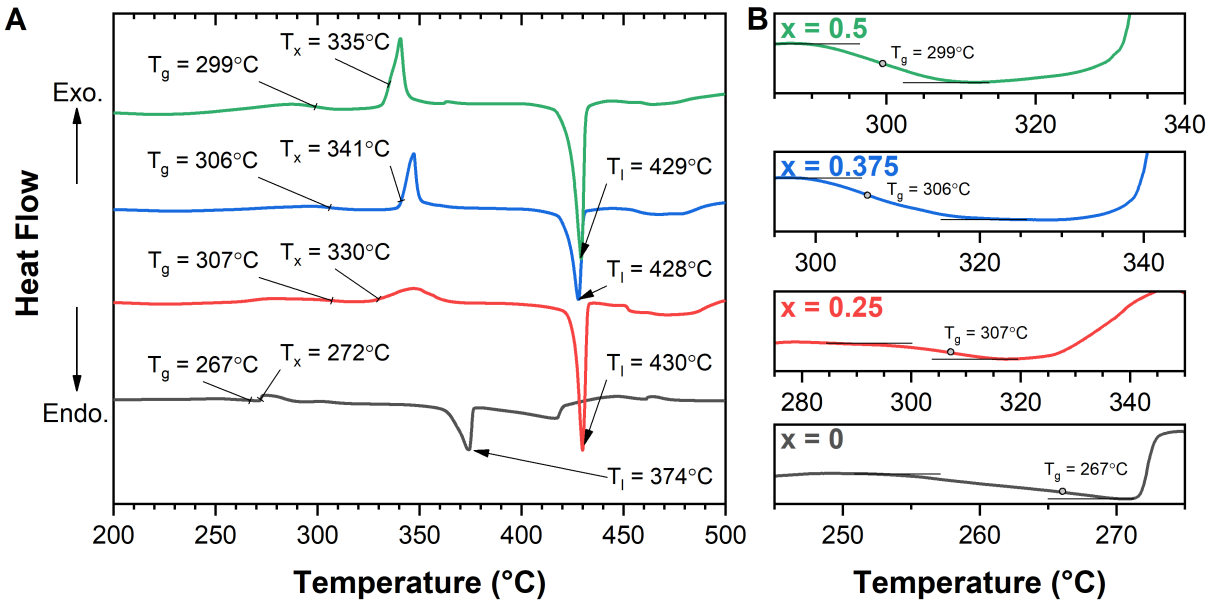

Figure 5.8: A) Differential scanning calorimetry curves of x = 0, 0.25, 0.375 and 0.5 compositions under a N_2 flow of 50 mL/min; T_g = glass transition temperature; T_x = onset of LiI crystallisation; T_l = melting of LiI; B) close-up of region where T_g occurs – this is measured as the highest slope in the drop of the DSC baseline before the exothermic crystallization peak.

respect to the crystallization of its vitreous structure.

Table 5.3: Summary of T_g, T_x, T_l, and calculated thermal stability parameters for $Li_{1.05}B_{0.5}Si_xO_{2x}S_{1.05}I_{0.45}$.

Composn. (x)	Glass Transition (T_g, °C)	Crystallization (T_x, °C)	Melting (T_l, °C)	Thermal Stability ($\Delta T_x = T_x$-T_g)
0	267	272	374	5
0.25	307	330	430	23
0.375	306	341	428	35
0.5	299	335	429	36

5.2.3 Air Stability

The incorporation of oxygen into the glass matrix also significantly improves stability to hydrolysis in moist air that produces H_2S. **Figure 5.9** shows the results of monitoring H_2S evolution from pelletized samples of two glass compositions (x = 0.25; 0.5) subjected to

ambient air exposure over the period of 3 hours (relative humidity; $R_H \sim$ 30-35%).

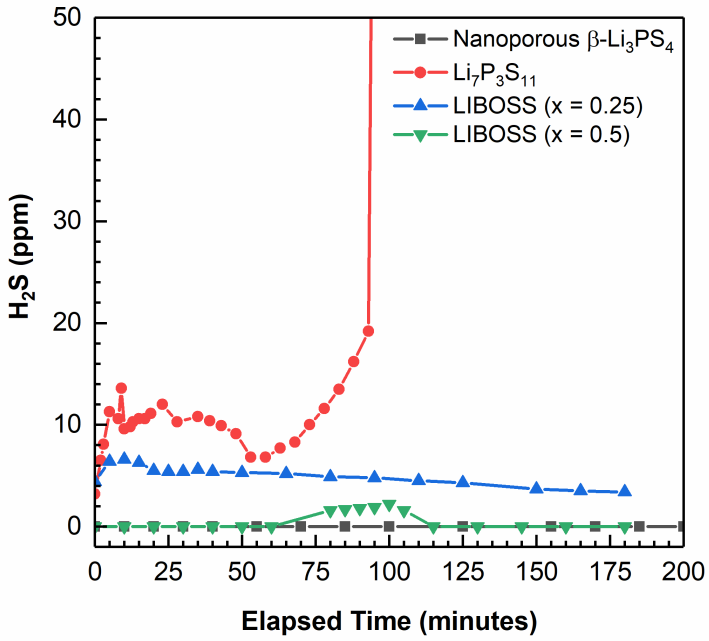

Figure 5.9: H_2S evolution from pelletized β-Li_3PS_4, $Li_7P_3S_{11}$, LIBOSS (x = 0.25), and LIBOSS (x = 0.5) upon exposure to ambient air.

The results are compared with those of two other well very known fast-ion conductors, $Li_7P_3S_{11}$ and β-Li_3PS_4. The latter, with an average conductivity of $\sigma_i = 2\times10^{-4}$ S·cm^{-1}, was prepared via a solution route because the β-polymorph is not stable at room temperature.[53] It showed no H_2S evolution, likely due to residual organic solvent in the material arising from its low processing temperatures that aid in stabilizing the material. As anticipated, $Li_7P_3S_{11}$ exhibits poor stability, showing rapid H_2S evolution that reached more than 200 ppm after 100 minutes. At this point, the experiment was curtailed because the levels surpassed the limits of the detector. In contrast, the two glass compositions were much more stable to moisture. H_2S evolution from the more oxygen-rich glass (x = 0.5) was negligible, and comparable to nanoporous β-Li_3PS_4. The glass with the lower oxygen content (LIBOSS-25) exhibited slightly higher H_2S evolution, but this was relatively stable - unlike $Li_7P_3S_{11}$ - and

even decreased over the monitoring duration possibly due to the formation of a passivating layer on the surface. Since lithium-ion batteries are processed under dry-room conditions with significantly lower moisture (typically $< 1\%$ relative humidity), these results obtained under more extreme conditions indicate that by tuning the SiO_2 content, the thioborosilicate glasses provide an acceptable middle ground for moisture sensitivity.

5.2.4 Local Structure

A combination of ^{11}B, ^{29}Si and ^{7}Li fast spinning MAS NMR, and Raman spectroscopies described below, conducted on three compositions (x = 0, 0.25, 0.5) reveal that addition of SiO_2 results in partial fragmentation of the Li-B-S network when it is added as a secondary glass former to the Li_2S-B_2S_3-LiI matrix.

The high-field, fast MAS ^{11}B NMR spectra reveal a multitude of peaks that can be assigned to specific moieties based on known assignments in the literature,[127,128] as depicted in **Figure 5.10A**. Boron in a tetrahedral sulfur environment typically appears at a range of chemical shifts from -3 to 7 ppm, and the presence of bridging S at the apices shifts the signal to lower frequency.[129] Accordingly for the x = 0 composition, the intense symmetric peak at -2.9 ppm is assigned to BS_4 with two to four BS ("bridging sulfur") at the apices, while the slightly higher frequency neighbouring peak at -0.5 ppm corresponds to either isolated BS_4 tetrahedra or BS_4 with one bridging sulfur. As more SiO_2 is added to the matrix (x = 0.25 and 0.5), the relative intensities of the two peaks swap. Thus, the BS_4 tetrahedra play less of a bridging role when SiO_2 is incorporated, favouring the formation of more isolated or network terminating (one BS) tetrahedra. The increase in the number of non-bridging sulfur (NBS) moieties generates smaller inorganic units, and increases the solubility of LiI in the matrix (hence increasing the Li ion carrier density in the glass). Boron in a trigonal environment appear at higher chemical shifts compared to boron in a tetrahedral environment. The chenmical shift can have a large spread, depending on the anion around the central boron and whether the anions are bridging. Pure thioborate trigonal units are typically found around 60 ppm, while pure borate units can appear at

5-15 ppm.[127] Peaks of mixed oxysulfide trigonal boron units are spread within this range. The ratio of tetrahedral B to trigonal B units is high in the absence of SiO_2 addition, while the fraction of mixed oxy-sulfide trigonal boron units (BOS_2/BO_2S) increases with SiO_2 content. There is a preference for the BO_3 moiety as boron has a stronger affinity for oxygen compared to sulfur. When the SiO_2 content is high (x = 0.5), isolated BO_3 units (at 15 ppm), and BO_3 groups with multiple bridging oxygen anions (at 11 ppm) become more prominent.

The ^{29}Si NMR (Figure 5.10B) spectra show that the ratio of the SiS_4 (7 ppm) signal to that of the $SiOS_3$ (-4.5 ppm)[115,130,131] slightly increases for x = 0.5 compared to x = 0.25. Therefore, by increasing the SiO_2 content in the overall composition, the fraction of SiS_4 structural units in the glass increases relative to the $SiOS_3$ units. While this may seem counterintuitive, a more negative ΔG of formation for B_2O_3 vs SiO_2 again suggests that because boron has a stronger affinity for oxygen compared to sulfur, the sulfur preferentially bonds with silicon. This is in accord with the increase in the trigonal boron units ($B(S/O)_3$) as a function of higher oxygen content observed in the ^{11}B spectra, which are predominantly oxygen based. The conversion of a glass with predominantly BS_4 units at x = 0 to a significant fraction of larger SiS_4 units at x = 0.5 (a 1:1 ratio, based on the normalized composition, Table 5.2) is anticipated to expand the free volume of the glass. This is proposed to be responsible for the dissolution of the significant concentrations of LiI. The results from the ^{29}Si NMR and ^{11}B spectra also correlate well with the results of Raman spectroscopy, where a variety of tetrahedral silicon and both trigonal and tetrahedral boron species are found to be present in the glass.

Incorporation of SiO_2 into the ternary Li_2S-B_2S_3-LiI composition shows a significant change in the Raman spectra with as little as x = 0.25 SiO_2 in LIBOSS-25 (**Figure 5.11**). The Raman peak widths are broadened dramatically with the emergence of overlapping peaks around 375 cm^{-1}. The broadening is indicative of the amorphous nature of the glass. The broad nature and overlap of these Si and B based peaks make the peak assignments difficult. Nonetheless, from the apparent peak positions, the possible speciation can be

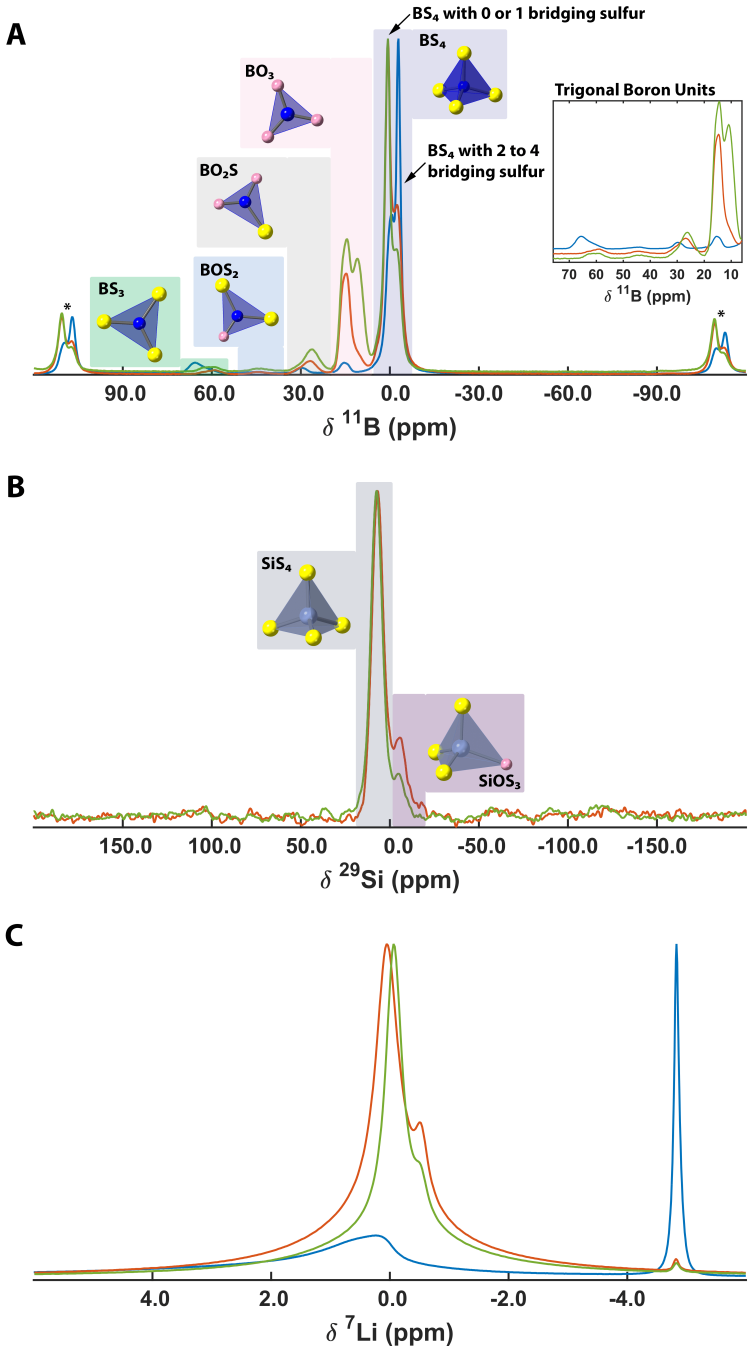

Figure 5.10: MAS NMR of the compositions $LiB_{0.5}Si_xO_{2x}SI_{0.5}$ for x = 0 (blue), 0.25 (orange) and 0.5 (green); A) ^{11}B with an inset showing the trigonal peaks from 5 to 75 ppm, the entire spectral width can be found in Figure C.2; B) ^{29}Si; C) ^{7}Li. The asterisk indicates spinning sidebands.

postulated and correlated with the solid-state NMR spectra. The intensity of several peaks corresponding to the boron network decreases with increasing SiO_2 content, indicating the transition to a silicon-based glass network structure. For example, the peaks at 296 and 315 cm^{-1} (unassigned) rapidly disappear with increasing x, as well as the peak at 448 cm^{-1} (assigned to BS_3 with three BS). At higher wavenumbers, the peaks at 687 cm^{-1} (unassigned), 743 cm^{-1} (BS_4 with four BS), 762 cm^{-1} (BO_4 with zero or one BO), and 790 cm^{-1} (BS_3 with one BS) display similar behaviour with a drop in intensity as SiO_2 is incorporated into the glass.

The broad peak around 375 cm^{-1} slowly increases in intensity as x increases and slightly shifts to larger wavenumber (380 cm^{-1} at $x = 0.5$). This band can be considered as consisting of two to three overlapping peaks at approximately 375, 400, and 405 cm^{-1}. These features may correspond to the symmetric vibration of the shared tetrahedral (bi-tetrahedral) motifs which are indicative of chain-like units in the glass.[132,133] An alternative description is that assignment of the peak at 375 cm^{-1} is to silicon tetrahedra with one or two bridging sulfurs (BS) while the band at 405 cm^{-1} is ascribed to zero BS (i.e. tetrahedral links, terminal chain ends and free tetrahedra in the glass). Thus, the slight intensity increase of these overlapping bands around 375 cm^{-1} and 405 cm^{-1} bands is proposed to be the result of the creation of tetrahedral silicon with either sulfur bridges.[127,134]

Additional peaks associated with the B and Si network appear in the 500-700 cm^{-1} range which are assigned to BS_3 units with up to two bridging sulfur (498 cm^{-1}), or BO_3 units with up to three BO. Two peaks that correspond to BS_3 with two BS may be seen at 437 cm^{-1} and 498 cm^{-1}, with the latter also containing some overlapping contribution from bridging BS_3 and BO_3 units, which may be indicative of mixed oxysulfide boron units. The small peak at 435 cm^{-1} also has an overlapping contribution related to the I^- content in the glass as this peak is present in the $x = 0$ composition and is constant with increasing SiO_2 content. Although this feature is not well understood, it has previously been explained on the basis that iodine does not modify the structure of the glass but the large negatively charged I^- anions may have a repulsive interaction with non-bridging sulfur.[135] Finally, the

low-frequency broad signals around 213 cm^{-1} for the x = 0 composition may correspond to Li cation frequency modes with non-bridging sulfur (NBS) in the glass (e.g. Li^+ $^-$S-B=).[127,135] With increasing x (SiO_2 content) several broad peaks likely overlap (125-215 cm^{-1}) that correspond to lithium interaction with silicon and boron NBS in addition to NBO.

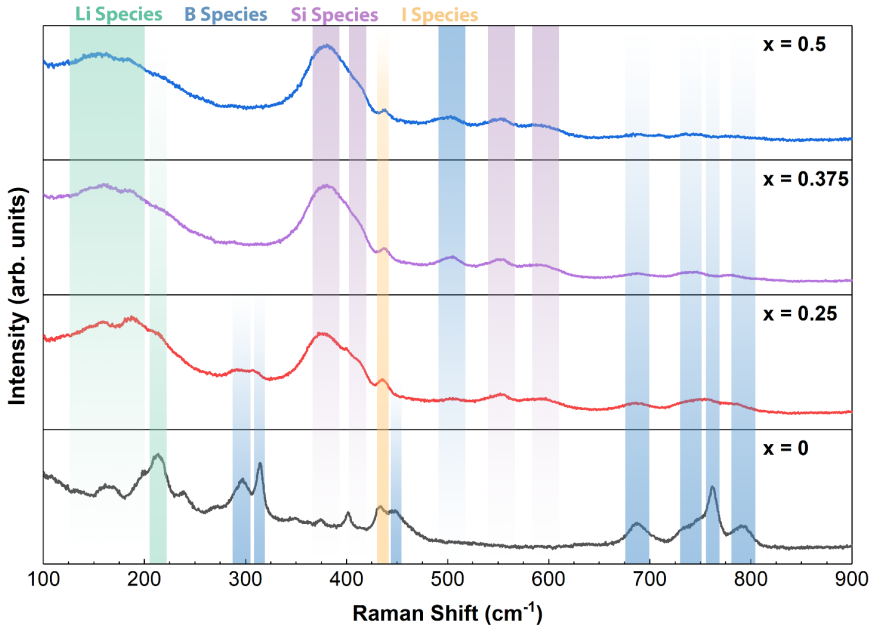

Figure 5.11: Raman spectra of the compositions $Li_{1.05}B_{0.5}Si_xO_{2x}S_{1.05}I_{0.45}$. The samples were measured up to 1500 cm^{-1} but there are no peaks observed above 900 cm^{-1}.

The ^{7}Li NMR (Figure 5.10C) spectra exhibit two major features in all cases. The peak at 4.5 ppm is assigned to LiI,[136] and for the composition without any SiO_2, its peak intensity is high. This correlates with the observation of about 28 wt% LiI in the XRD pattern for the x = 0 composition (Figure 5.2A). The ^{7}Li NMR peak near 0 ppm corresponds to Li in an environment next to either non-bridging sulfur (x = 0) or a mixture of sulfur/oxygen (x = 0.25, 0.5).[137] It shifts slightly to lower frequency with increasing oxygen content as expected for a more "ionic" interaction between the Li and the glass network. At x > 0, as the LiI becomes solubilised, a shoulder on this peak appears at -0.5 ppm that may reflect Li in a slightly more ionic environment (i.e., in the vicinity of I^- within the glass matrix).

The 0 ppm peak undergoes very substantial motional narrowing with the addition of SiO_2, indicating a dramatic jump in the local Li-ion mobility. Note that at x = 0.5, the small decrease in line width suggests more motional narrowing of the ^{7}Li MAS signal, despite the lower ionic conductivity of this composition. Of course, the Li-ion carrier density is lower for the more SiO_2-rich glass, and NMR is a local probe of Li-ion hopping, not of long-range conductivity. Local phase segregation may also occur within the x = 0.5 glass. For x = 0.25 and 0.5, even though LiI is not evident in the XRD patterns, a small peak is still present in the NMR spectra, which exhibits a larger ratio relative to the major peak at 0 ppm for x = 0.5. This may indicate the increasing presence of nano-aggregates of LiI, whose domains are below the scattering length that can be probed by XRD but are nonetheless present in the glass, as postulated by Vinatier *et al.*[137] Such nano-aggregates would hinder the ion conduction on a macroscopic scale, irrespective of the local lithium ion mobility.[137]

Overall, the effect on the local structure by adding SiO_2 to the matrix is to increase the fraction of non-bridging sulfur/oxygen (NBS/NBO) anions relative to their bridging sulfur/oxygen (BS/BO) counterparts, resulting in smaller inorganic-polymer units. These smaller inorganic units allow for a greater degree of freedom of the glass network, and more terminal chalcogenide anions, that in turn, likely generates a higher fraction of mobile Li^+ ions. Beyond x = 0.25, the observed decrease in Li-ion conductivity is correlated to the formation of structural units with non-bridging sulfur/oxygen. The ionic character of the structural entities likely dominates, resulting in greater electrostatic attraction of the Li ions to their sites near the non-bridging chalcogen, and reducing their mobility. This would give rise to a decrease in the jump frequency (see above). While resolving the structure of amorphous materials is a longstanding challenge, the combination of NMR and Raman spectroscopies is a very useful local probe. Techniques such as *ab initio* molecular dynamics coupled with neutron pair distribution function (PDF) analysis have also proven to be powerful tools for elucidation of the local structure in LiPON.[138] These methods, along with detailed NMR studies of Li diffusion will be employed in subsequent studies to gain a better understanding of ion conduction in these oxysulfide glasses.

5.2.5 Electrochemical Studies

Interfacial reactivity of solid electrolytes with lithium metal is typically evaluated using a combination of electrochemical impedance spectroscopy (EIS) in conjunction with galvanostatic cycling measurements of symmetric Li|solid electrolyte|Li cells, as reported for Nb-doped $Li_7La_3Zr_2O_{12}$ (LLZO) where the increase in impedance over time demonstrated that Nb reduction occurs.[139] Such studies of pressed pellets (*ca.* 0.12 mm thick) of LIBOSS-25 in symmetric Li|solid-electrolyte|Li cells were conducted here and compared to nanoporous β-Li_3PS_4 as a electrolyte (**Figure 5.12A**).[53] The cells were prepared and galvanostatically cycled at a current density of 0.1 mA/cm^2 to an areal capacity of 0.05 and 0.1 mAh/cm^2, respectively. Simultaneously, the resistance of the cell was measured every 5 cycles using EIS, Figure 5.12B (see **Figure 5.13** for the corresponding Nyquist plots). The Nyquist plots for Li_3PS_4 (Figure 5.13A) show a typical spectra for a non-blocking configuration, composed of semicircles with no linear diffusive tail at low frequencies. The spectra for the LIBOSS cell (Figure 5.13B) show only the end of the semicircle due to the low resistance of the electrolyte, and an additional feature at low frequencies that likely corresponds to an interphase layer formed in contact with lithium metal upon cell assembly.

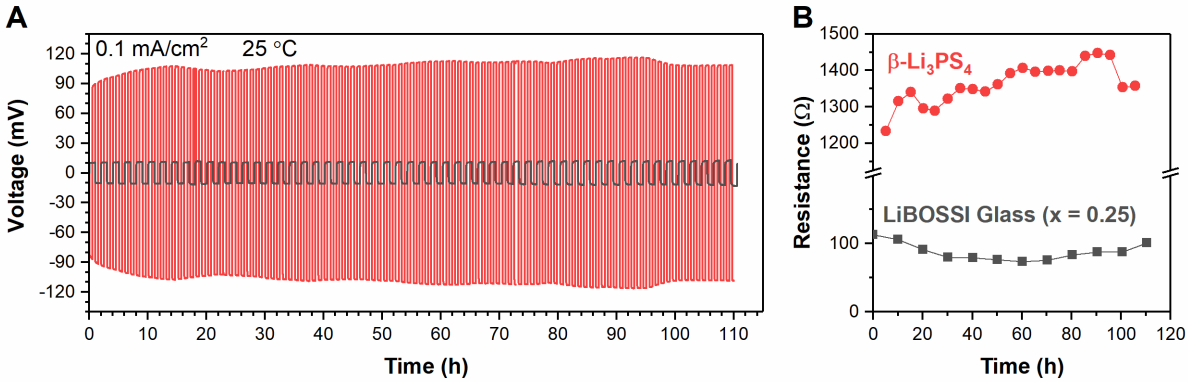

Figure 5.12: A) Galvanostatic cycling of Li symmetric cells run at 25°C using β-Li_3PS_4 (red lines) and LIBOSS-25 glass (black lines) at 0.1 mA·cm^{-2} to a capacity of 0.05 and 0.1 mAh·cm^{-2}, respectively. B) EIS measurements of the cell resistance change due to SEI formation, monitored every 5 cycles at an applied voltage of 100 mV.

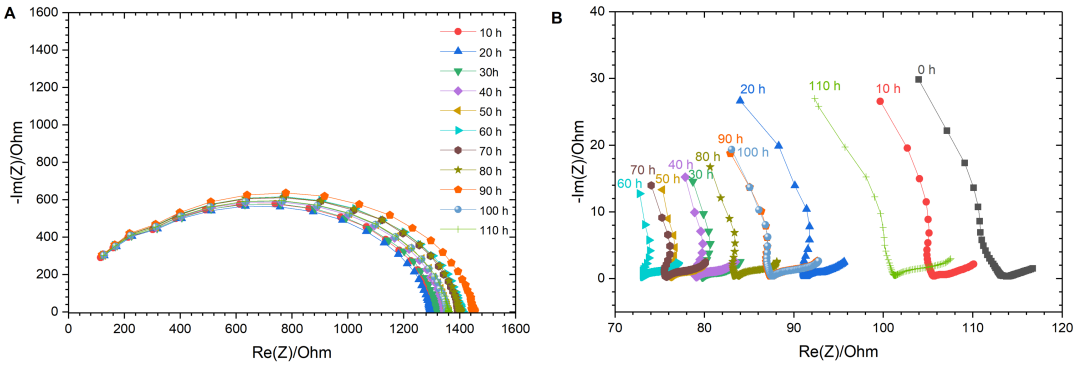

Figure 5.13: Nyquist plots corresponding to lithium symmetric cells upon cycling of A) β-Li_3PS_4 and B) LIBOSS-25. EIS was measured from 1 MHz to 100 mHz with an applied voltage of 100 mV.

The LIBOSS glass exhibits stable cycling for 110 hours with one-tenth the polarization voltage (10 mV) of β-Li_3PS_4 (100 mV), in large part owing to the much higher ionic conductivity of the glass. The resistance of the β-Li_3PS_4 cell appears to fluctuate but toward higher resistance over cycling, in good accord with findings reported elsewhere for Li symmetric cells.[53] This increasing resistance has been attributed to the formation of a passivating interphase composed of Li_2S and Li_3P.[140] Because of this, β-Li_3PS_4 is widely regarded as one of the most stable solid-electrolytes with Li metal, by comparison to other well-known materials.[108,141,142] The stripping/plating performance of the LIBOSS glass is markedly improved over the β-Li_3PS_4 cell that shows an increase in resistance over this period (Figure 5.12B). This effect may stem from the incorporation of LiI, which has been shown to have stabilizing effects *vis a vis* Li metal, whether incorporated into a glass such as Li_3PS_4-LiI,[113] or a crystalline material.[143,144] Naturally, one cannot also expect an iodide-containing material to be oxidatively stable to high potential; in this context, solid state cells employing coated high voltage cathode materials, or dual solid electrolytes - one stable at high potential and one stable at low potential - may be the most suitable option.[145]

A bulk-type all-solid-state cell was assembled using the x = 0.25 LIBOSS glass electrolyte. The electrolyte layer was sandwiched between the anode and a TiS_2 composite cathode (1:1 TiS_2 and LIBOSS; this cell configuration is simply used to demonstrate the applicability

of the electrolyte in a full cell, rather than to optimize a solid-state cell with high energy density). Li-In was used as a test negative platform owing to its robustness to dendrite formation over the long cycling duration, as non-fully densified glass pellets were utilized as the electrolyte instead of a monolithic melt-cast glass. The cells were charged and discharged at C/10 in the voltage range 0.9 to 2.4 V vs. Li-In (1.5 to 3 V vs. Li) at room temperature (∼25°C). **Figure 5.14A** shows that upon the first cycle charge at 2.7 V vs. Li, a tiny irreversible capacity (6 mAh/g) is evident, which is attributed to initial electrolyte oxidation at the cathode interface. The potential is similar to what has been observed in thiophosphate-based electrolytes, where S^{2-} undergoes oxidation.[29,146]

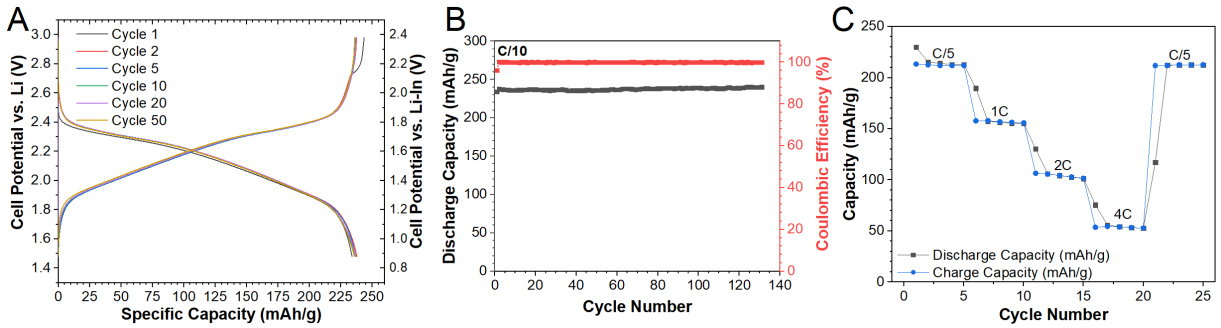

Figure 5.14: A) Charge–discharge curves of Li-In/LIBOSS/TiS_2 all-solid-state cell cycled at C/10 at 25°C, and B) cycling performance of the cell at C/10 at 25°C; C) rate capability study; D) cycling data at 60°C at a 1C rate.

This process is more clearly seen in the corresponding dQ/dV plots in **Figure 5.15**, where the feature at 2.15 V vs. Li-In exhibits a rapid drop in intensity after the first cycle and completely disappears by cycle 10, suggesting the formation of a stable cathode-electrolyte interface. After the first cycle, the cell shows excellent cycling performance at C/10, with virtually no capacity fade over three months of cycling. The cell maintains a capacity of ∼239 mAh/g (TiS_2 theoretical capacity: 240 mAh/g) for more than 130 cycles with high coulombic efficiencies of 99.9% on average (Figure 5.14B). Rate capabilities on an identical cell cycled within the same voltage range and at 25 °C are shown in Figure 5.14C. Initially, the cell cycled at C/5 achieves a capacity of 213 mAh/g, which represents 90%

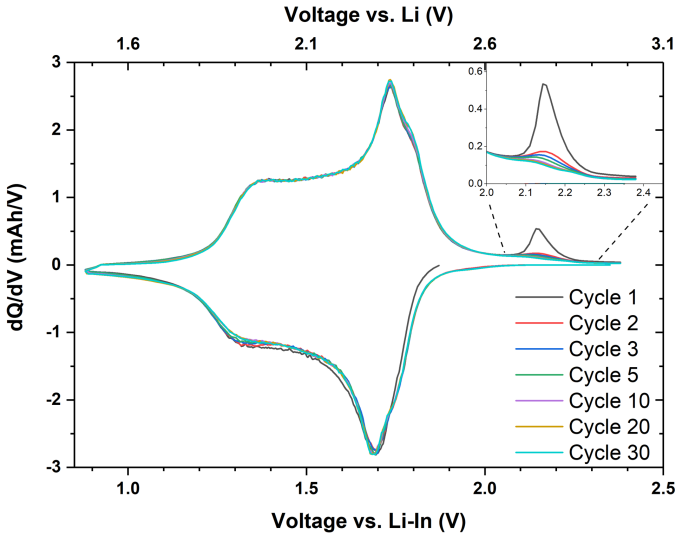

Figure 5.15: dQ/dV plots for several charge-discharge cycles of Li-In/LIBOSS-25/TiS_2 all-solid-state cell cycled at C/10 at 25°C.

capacity retention on doubling the current density. On subsequent increase of the current density to a 1C rate, 75% of the capacity is retained and the capacity is fully recovered upon returning to the initial C/5 rate. This performance augurs well for further development of such glasses and their future implementation in high energy density solid state batteries.

5.3 Conclusions

In summary, a new class of vitreous lithium oxythioborate halides is reported, which are prepared directly from a melt. This method improves scalability and (in principle), can allow for roll-casting into vitreous sheets in the future if dry room conditions could be employed. Contrary to the popular belief that oxygen doping reduces ionic conductivity in sulfide-based materials due to the less polarizable anion sublattice, it is shown here that fast ion conduction is possible even up to levels of 30-40 mole percent silica. These new glasses exhibit ionic conductivities up to 2×10^{-3} S·cm^{-1}, one of the highest for any known lithium-ion conducting glasses. This is further coupled with improved moisture stability with increasing SiO_2 content, and in comparison with other well known solid state ion

conductors. The origin of the rise in conductivity is elucidated by an understanding of the structural units present in the amorphous matrix. A delicate balance is achieved between the covalent network composed of BS/BO and the NBS/NBO units that are required for fast ionic conduction. An optimized fraction of mobile lithium cations is achieved at the x = 0.25 composition due to the partial fragmentation of the glass chains. As initial proof-of-concept, an all-solid-state battery with a TiS_2 cathode and LIBOSS (x = 0.25) electrolyte shows near theoretical capacity with extremely stable cycling for over 130 cycles. This promising material class with its enhanced material properties make it a strong candidate for use in all-solid-state lithium batteries. Furthermore, although a selected part of this quaternary phase diagram is reported here, this concept can extend to a broader scope that includes alternative halides and glass forming oxides, leading to a new avenue in the development of solid electrolytes for all-solid-state batteries.

5.4 Experimental Methods

5.4.1 Synthesis

Stoichiometric masses of Li_2S (Sigma Aldrich, 99.98%), ^{11}B (Sigma Aldrich, 99%), S, LiI, and SiO_2 were ground together. As the glasses are sensitive to the LiI content and the purity of the precursors. precursors were dried under vacuum before use. All handling of powders was carried out in an Ar filled glovebox. The precursor mixture was pelletized and supported in a glassy carbon crucible which was placed in a quartz tube. The quartz tubes were sealed under vacuum and placed vertically in a furnace. The tube was heated up to 500°C and held for 12 hours, then at 800°C for 20 hours, and the melt was finally quenched in ice water to obtain a glass. The final product was ground to a powder for processing as a solid electrolyte, as the specialized facilities for melt casting a monolithic glass under a moisture-free atmosphere were not available.

Nanoporous β-Li_3PS_4 was synthesized by the conventional procedure mixing Li_2S and P_2S_5 in THF as reported by Liang *et. al.*[53] $Li_7P_3S_{11}$ glass-ceramic was synthesized by first mixing

and grinding Li_2S (Sigma Aldrich, 99.98%) and P_2S_5 (Sigma Aldrich, 99%) in stoichiometric quantities. The precursor mixture was pelletized and supported in a glassy carbon crucible which was placed in a quartz tube. The quartz tubes were sealed under vacuum and placed vertically in a furnace. The tube was heated up to 750°C and held for 10 hours, and the melt was finally quenched in ice water to obtain a glass. The glass was then re-ground and further heat-treated inside a furnace placed inside an argon-filled glovebox. The powder was placed in an alumina crucible and heated at 335°C for 30 minutes to crystallize the material. Phase-pure $Li_7P_3S_{11}$ was verified using X-ray diffraction.

5.4.2 X-ray Diffraction

XRD was conducted at room temperature on a PANalytical Empyrean diffractometer using Cu-Kα radiation equipped with a PIXcel bidimensional detector with a Ni Kβ filter using θ-θ Bragg-Brentano geometry. Powders were maintained under argon atmosphere using a zero-background sample holder covered in Kapton film to avoid air exposure during collection of the XRD pattern.

5.4.3 Weight Percent Measurements using Standard Addition

The ground samples were loaded and sealed in a 0.3 mm diameter quartz capillary. Patterns were recorded in Debye-Scherrer geometry using a parabolic X-ray mirror in the incident beam. For the calculations of the amount of crystalline LiI not dissolved in the glass, samples were ground together with approximately 10 weight percent of Si, which was used as an internal standard in the Rietveld refinements.

5.4.4 AC Impedance Spectroscopy

Bulk resistance of the samples was determined from electrochemical impedance spectroscopy (EIS) with an amplitude of 100 mV in the frequency range 10 MHz to 100 mHz using a Bio-logic MTZ-35 impedance analyzer (or 1 MHz to 100 mHz using a Bio-logic VMP-3). The measurements were carried out in the temperature 25°C to 80°C. The powder was

pelletized in a 10 mm diameter modified Swagelok cell. The electrolyte pellet (thickness of 1 to 2 mm for activation energy measurements) was sandwiched between indium foils in order to obtain good contact at variable temperatures.

5.4.5 DC Polarization

The electronic conductivity was determined via DC polarization using a 10 mm diameter modified Swagelok cell, where powder was pressed between two stainless steel pistons. A voltage of 0.125, 0.25, 0.5, and 0.75 V was applied for 1 hour for each measurement.

5.4.6 Symmetric Cell Assembly and Cycling

Cells were assembled in a glovebox filled with an argon atmosphere. LIBOSS-25 and β-Li_3PS_4 solid electrolyte was pressed in a 10 mm diameter PEEK cylinder to form a pellet of thickness around 0.12 mm. Li metal foil (Sigma Aldrich) was pressed on either side and in contact with the solid electrolyte. The cell was then sandwiched between two stainless steel rods and held under pressure using a custom-made cell. The cell was tightened with a torque wrench set at a pressure of 4 N·m. Galvanostatic cycling of the LIBOSS-25 and β-Li_3PS_4 cells was performed at 0.1 mA/cm^2 to 0.1 mAh/cm^2 and 0.05 mAh/cm^2, respectively. Cells were cycled at room temperature using a Bio-Logic VMP-3.

5.4.7 Full Cell Assembly and Battery Cycling

The composite cathode was prepared by mixing solid electrolyte (LIBOSS-25, x = 0.25) and TiS_2 (Sigma Aldrich, 99.9%, particle size 75 µm) in a 1:1 weight ratio with a mortar and pestle. Cells were assembled in a glovebox filled with an argon atmosphere. The composite cathode was used as the positive electrode, LIBOSS-25 as the solid electrolyte, and Li-In alloy as the negative electrode. The positive electrode (8 mg; TiS_2 content corresponding to 5.13 mg·cm^{-2}), and solid electrolyte (60 mg) were pressed in a 10 mm diameter PEEK cylinder to form a bilayer pellet. The Li-In alloy was formed by pressing Li-foil with an In foil in a 0.5 molar ratio, and placed in contact with the solid electrolyte. The cell was then

sandwiched between two stainless steel rods and held under pressure using a custom-made cell. The cell was allowed to rest for 8 hours before cycling in order to allow for pressure relaxation of the cell, whose areal capacity was 1.2 $mAh \cdot cm^{-2}$. Galvanostatic cycling was performed from 1.5 to 3.0 V vs. Li/Li^+ (0.88 V to 2.38 V vs. In/LiIn) at a C-rate of C/10. Cells were cycled at room temperature using a Bio-Logic VMP-3.

5.4.8 Differential Scanning Calorimetry

Approximately 5-10 mg of sample was loaded into an aluminum pan and hermetically sealed in an argon filled glovebox with a Tzero sample press. The measurement was conducted using a TA Instruments Q2000 DSC under nitrogen flow. Samples were heated at a rate of 5°C/min from 25°C to 500°C.

5.4.9 Air Stability

Electrolyte powder (100 mg) was pressed into 10 mm diameter pellets. An air pump was run in reverse in order to flow ambient air into a three-neck round bottom flask as the container. The second neck contained a probe that was directly connected to an H_2S sensor (BW GasAlertMicro 5 Multi-Gas Detector). The probe was placed directly above the solid electrolyte pellet in order to ensure accurate H_2S monitoring. The third neck was used as an exhaust/outlet port. The air temperature was approximately 23-25°C with a relative humidity of 40-50%.

5.4.10 Raman spectroscopy of solid electrolytes

Samples were pelletized and then placed on a microscope slide, covered by a glass coverslip, and sealed with epoxy inside an Ar filled glovebox. Raman spectra of the materials were obtained using a 633 nm laser (Raman HORIBA HR800). Spectra were obtained using 3 to 5 accumulations with acquisition times ranging from 10-20 seconds under a 10x objective lens. A laser power of 50% was used to prevent sample damage or heating.

5.4.11 ^{7}Li,^{11}B, and ^{29}Si MAS-NMR of solid electrolytes

Samples were packed in 1.9 mm and 3.2 mm zirconia rotors inside an argon-filled glovebox. Magic Angle Spinning (NMR) NMR measurements were obtained at 20T and 298 K on a 850 MHz Bruker Avance III HD spectrometer operating at 330 MHz and 273 MHz for ^{7}Li and ^{11}B, respectively, at a spinning rate of 30 kHz using a 1.9 mm broadband-tunable probe. The ^{29}Si NMR NMR spectra were again acquired at 20T (169 MHz Larmor frequency), but instead using a 3.2 mm probe with a dedicated ^{29}Si channel to obviate the possibility of background signals and spinning at 16 kHz. The ^{7}Li, ^{11}B, and ^{29}Si spectra were referenced using external samples of 1M LiCl (aq), 0.1M boric acid (19.6 ppm versus $BF_3{\cdot}Et_2O$ at zero ppm), and tetrikis trimethylsilyl silane (TTMSS; -9.8 ppm versus TMS at zero ppm), respectively. ^{7}Li spectra were acquired with a 3.25 μs $\pi/2$ pulse at 110 W, with 8 scans collected using a 60 s recycle delay, which was established with a one-dimensional inversion recovery experiment. For the ^{11}B spectra, the very wide static linewidth and the probe background were addressed using a two- $\pi/2$ solid echo sequence, with the echo delay stretched to 100 µs to effectively T2-filter the probe background. The $\pi/2$ pulse was 1.8 µs at 220 W, and 2048 scans were acquired using a 6 s recycle delay, which was found to be sufficient for complete signal recovery. Using brief 64-scan saturation recovery experiments, the recycle delay for the ^{29}Si experiments was established as 48 s; spectra were then acquired using 4800 scans, for a total experimental time of 64 hours, with a $\pi/2$ pulse of 5.25 µs at 120 W.

Chapter 6

Fast Li-Ion Conductivity in Superadamantanoid Thioborate Halides

This section is reproduced in part with permission from John Wiley & Sons, Inc. publishing:
Kavish Kaup, Abdeljalil Assoud, Jue Liu, and Linda F. Nazar, *Angewandte Chemie*, **2020**, 60, 13, 6975-6980 (DOI: 10.1002/anie.202013339)

* Dr. Abdeljalil Assoud performed the single-crystal XRD measurements and corresponding single-crystal refinements.

* Dr. Jue Liu provided guidance for conducting the neutron powder diffraction measurements and performed the neutron PDF measurements at Oak Ridge National Lab.

6.1 Introduction

Lithium thiophosphates, are the most promising material class for ASSBs because of their high ionic conductivity (>10^{-3} S·cm^{-1}) and excellent ductility,[28,49,114,147] which allows for easy processing into batteries. Lithium thioborates, a material class with similar properties to lithium thiophosphates, have been neglected in comparison, despite having shown great promise.[148] This phase space has been revived recently with computational studies on lithium thioborate materials pointing to extremely fast ion conductivities and improved electrochemical stability over lithium thiophosphate materials.[149] Seminal work on thioborates during the 1980s-1990s focused on Li_2S-B_2S_3 and Li_2S-B_2S_3-LiI fast-ion conducting glasses;[120] which was expanded on recently by exploring the quaternary Li_2S-B_2S_3-LiI-SiO_2 system.[150] Concomitant with the glass, Li_2S-B_2S_3 crystalline analogues were discovered by Krebs et al.[151] One such thioborate is $Li_{6+2x}[B_{10}S_{18}]S_x$ (x $\approx$ 2),[152] which exhibits a thioborate network composed of supertetrahedral clusters (also referred to as superadamantanoid) $B_{10}S_{20}$ structural units. Similar supertetrahedral structures were observed in lithium and sodium phosphidosilicates,[153,154] lithium nitridophosphates,[155] sodium and silver thioborates such as $Ag_6B_{10}S_{18}$ and $Na_6B_{10}S_{18}$,[156,157] and many other sulphide-based materials.[158–162] Supertetrahedral networks are of interest because the structure forces cations and anions to distribute into the void spaces between the clusters. For frameworks with a large void space, the cations are weakly bonded to the surrounding anions, which facilitates cation mobility within the structure. For such materials, the highest reported room-temperature ionic conductivity is only 4×10^{-4} S·cm^{-1} for sodium phosphidosilicates,[154] and $\sim10^{-7}$ S·cm^{-1} for lithium phosphidosilicates.[163] An ionic conductivity greater than 10^{-4} S·cm^{-1} is typically considered "fast", but at least 10^{-3} S·cm^{-1} is necessary to achieve practical solid-state batteries.[16]

The material $Li_{6+2x}[B_{10}S_{18}]S_x$ (x $\approx$ 2), exhibits large three-dimensional channels between the clusters that contain highly disordered lithium and sulphide ions.[152] ^{7}Li NMR studies of the lithium dynamics revealed a low activation energy of 12 kJ/mol (equivalent to 0.12

eV),[152] implying the thioborate is a fast-ion conductor; however, ionic conductivity was not reported. Anion disorder in the form of substitutional disorder (e.g. argyrodite Li_6PS_5Cl family),[164] or rotational disorder (e.g. Li_3PS_4 family),[165,166] both strongly influence Li^+ ion conduction. Additionally, the polarizability of the sublattice affects Li^+ ion conduction by weakening the interactions between the mobile Li^+ ions and its surrounding anions.[27] Thus, increasing the polarizability of the anion (S^{2-}) in the large channels of $Li_{6+2x}[B_{10}S_{18}]S_x$ (where Li^+ is coordinated by disordered S^{2-}) should boost the lithium-ion mobility.

Here, three new lithium-ion conducting materials are reported, prepared by full substitution of S^{2-} with monovalent X^- (Cl^-, Br^-, and I^-) to form $Li_{7.5}B_{10}S_{18}X_{1.5}$. They exhibit high room-temperature (25°C) lithium-ion conductivities (0.5, 0.9, and 1.4×10^{-3} $S\cdot cm^{-1}$, respectively) that are indeed tuned by the polarizability of the anion in the channel. Their crystal structures were analyzed using a combination of single-crystal X-ray diffraction (XRD), neutron powder diffraction (NPD), and neutron pair distribution function (PDF) analysis to elucidate the critical effect of anion and cation disorder on lithium ion conductivity in these supertetrahedral structures. This work is the first report on a new class of superionic conductors - crystalline halogenated lithium thioborates - that form an unprecedented fast-ion conducting superadamantanoid material.

6.2 Results and Discussion

6.2.1 Sublattice Polarizability Effect on Ion Transport

Synthesis of the previously reported $Li_{6+2x}[B_{10}S_{18}]S_x$ ($x \approx 2$)[152] resulted in a significant fraction of $Li_5B_7S_{13}$ and Li_3BS_3 impurities. Utilizing halides in place of sulfide (i.e., chlorine, bromine, and iodine), new halide isomorphs were synthesized, $Li_{7.5}B_{10}S_{18}X_{1.5}$ (X = Cl, Br, and I), that exhibit ionic conductivities up to 1.4×10^{-3} $S\cdot cm^{-1}$, depending on the halide in the channel. Li^+ ion conductivities were measured using electrochemical impedance spectroscopy (EIS). The ion conductivity obeys the Arrhenius law of the form $\sigma = \frac{\sigma_o}{T} e^{-\frac{E_a}{kT}}$ in the investigated temperature range as shown in **Figure 6.1A**. Corresponding Nyquist

plots and a representative circuit fit are shown in **Figure 6.2**, **Figure 6.3**, and **Table 6.1**. Details on the fitting procedure can be found in **Appendix D** (section D.1).

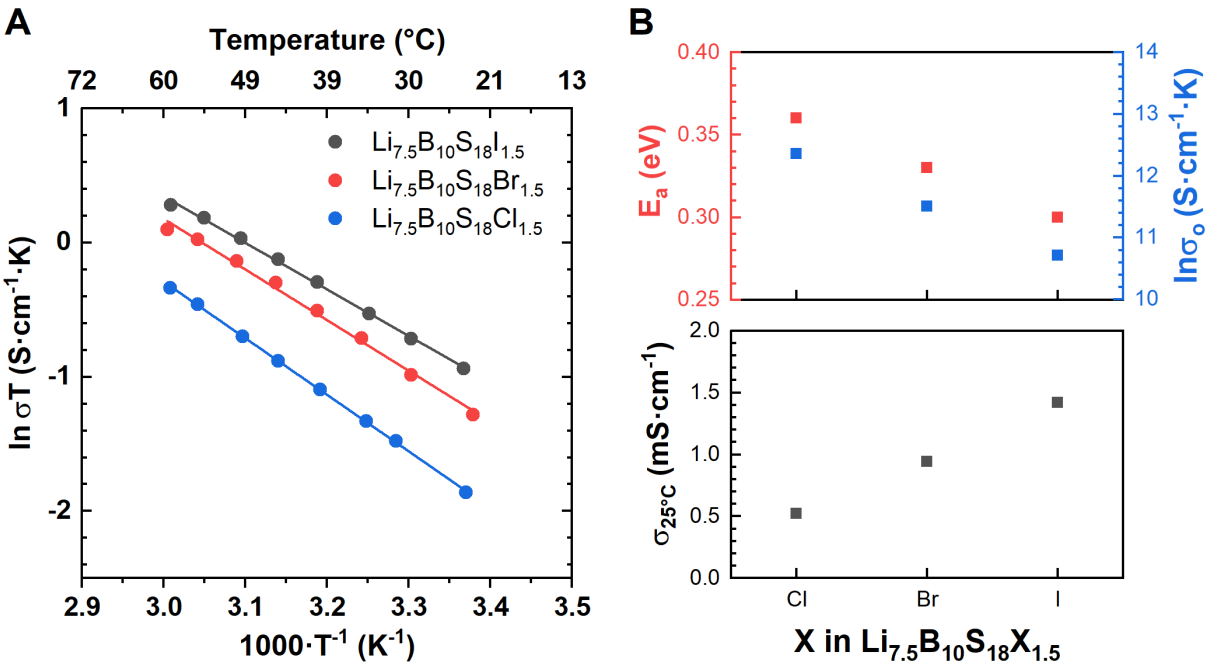

Figure 6.1: A) Arrhenius plots obtained from temperature dependent EIS measurements of targeted $Li_{7.5}B_{10}S_{18}X_{1.5}$ (X = Cl, Br, I) and the corresponding B) room temperature conductivity (25°C), activation energy, and pre-exponential factor.

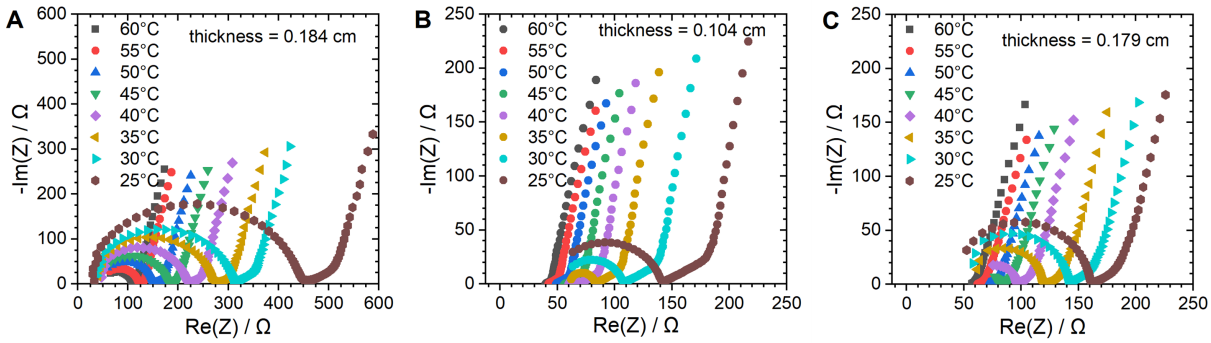

Figure 6.2: Nyquist plots of A) $Li_{7.5}B_{10}S_{18}Cl_{1.5}$, B) $Li_{7.5}B_{10}S_{18}Br_{1.5}$, and C) $Li_{7.5}B_{10}S_{18}I_{1.5}$ at each temperature used to extract the ionic conductivity values for activation energy measurements.

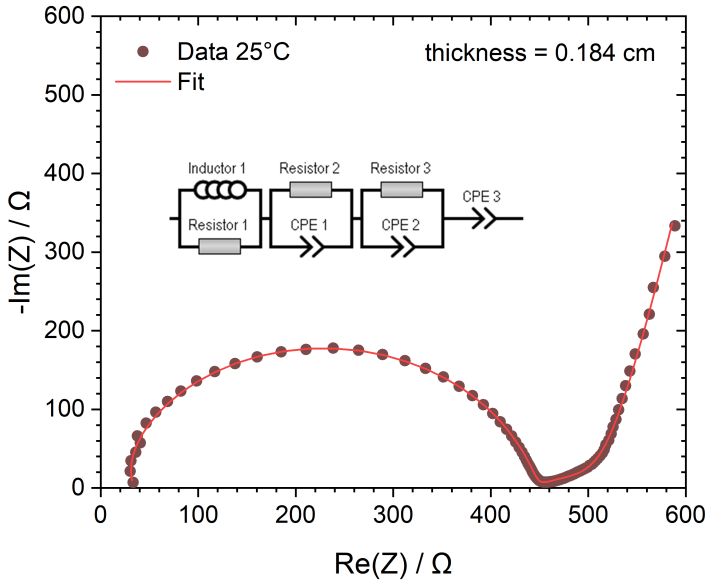

Figure 6.3: Representative EIS measurement of $Li_{7.5}B_{10}S_{18}Cl_{1.5}$ at 25°C and corresponding fit and fit parameters with the accompany circuit model. Details of the fitting procedure are provided in Appendix D.

Table 6.1: Parameters of the fit for the impedance data of $Li_{7.5}B_{10}S_{18}Cl_{1.5}$ at 25°C.

Description	Element	Value	C_{eff}
Stray	L1	5.38×10^{-7} H	
	R1	96.46 Ω	
Electrolyte	R2	443.73 Ω	
	CPE1 – Q1	2.67×10^{-9} F·s$^{\alpha-1}$	3.4×10^{-10} F
	α1	0.869	
Interface	R3	102.45 Ω	
	CPE2 – Q2	3.08×10^{-3} F·s$^{\alpha-1}$	3.2×10^{-4} F
	α2	0.336	
Electrode	CPE3 – Q3	4.78×10^{-3} F·s$^{\alpha-1}$	
	α3	0.885	

Activation energies and prefactors obtained from linear fits of the Arrhenius plots are shown in Figure 6.1B. Both decrease with an increase in anion polarizability. This correlation has been demonstrated in thiophosphate materials (e.g. argyrodite, Li_6PS_5X, X=Cl, Br, I), where a softer sublattice lowers the activation barrier for a jump but simultaneously

decreases the attempt frequency of the jump and the entropy of migration, which directly influences the prefactor.[27] The activation energy for $Li_{7.5}B_{10}S_{18}X_{1.5}$ is 0.36, 0.33, and 0.30 eV for X = Cl, Br, and I, respectively. The more polarizable anion (I^-) results in a weaker coulombic interaction with Li^+, which facilitates transport. The activation energy is more influential than prefactor and the decrease consequently leads to high Li^+ ion conductivities of 0.5, 0.9, and 1.4×10^{-3} S·cm^{-1} (X = Cl, Br, and I) at room temperature (Figure 6.1B). Thus, by changing the anion in the channels, the ionic conductivity of the superadamantanoid materials can be tuned. It is assumed that the halide ions do not significantly add to the conductivity - especially in the case of the very large iodide ion (diameter: 4.4 Å).

6.2.2 Framework from Single-Crystal X-Ray Diffraction

The framework of the $Li_{7.5}B_{10}S_{18}X_{1.5}$ (X = Cl, Br, I) materials was unequivocally solved using single-crystal XRD in the monoclinic space group $C2/c$. All three compounds have a framework composed of BS_4-based supertetrahedral clusters. Ten condensed ${BS_4}^{5-}$ anions form a three-dimensional superadamantanoid network, $[{B_{10}S_{18}}^{-6}]_n$, where each $B_{10}S_{20}$ macro-tetrahedron is connected by one of its corner sulphur anions to form the framework shown in **Figure 6.4**. Large interpenetrating voids exist between the rigid supertetrahedral units, where a highly disordered partial sublattice composed of lithium cations and halide anions reside. Complete crystallographic data from all the single-crystal XRD measurements are presented in **Table D.1-D.7**. The largest channel is approximately 12×8 Å for all three compounds (Figure 6.4A), where the lithium ions are coordinated by free halide ions in the tunnel. The smaller channels (∼4.5 × 4.5 Å for all three compounds) along the a and b axis (Figure 6.4B and C) intersect the larger tunnel along the c axis, forming 3D diffusion pathways. The halide ions only reside in the larger channel and are modelled as a disordered array over 7-8 atomic sites with varying occupancies for the refinements. This was determined in conjunction with refinement of neutron diffraction data, which is described in detail below. Lithium ions, on the other hand, are distributed through the large channel as well as the "smaller" channels. Note that the Li^+ and X^- ions in the void

spaces are difficult to precisely resolve due to significant lithium and halide disorder.

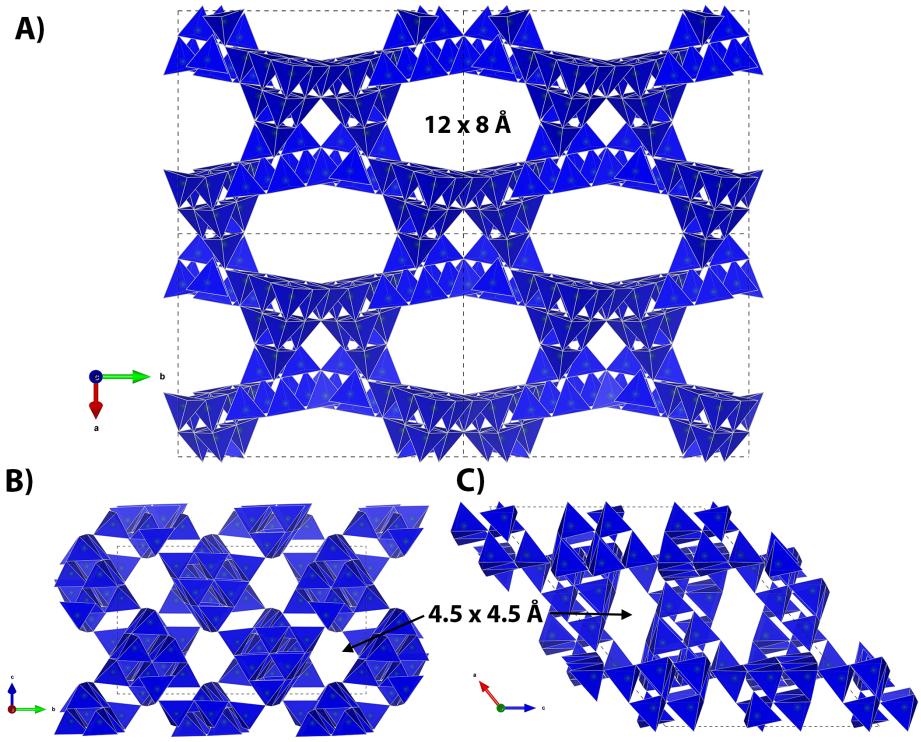

Figure 6.4: Polyhedral representation of the $[B_{10}S_{18}{}^{-6}]_n$ framework: projected along A) [001], B) [100], and C) [010]. The unit cell is represented by the dashed lines. Sulphur atoms in the tetrahedral clusters, and lithium and halide atoms in the channels (voids) are omitted for clarity here.

6.2.3 Variations Between Single-Crystals and Bulk Powder

The compositions can be described as $Li_6[B_{10}S_{18}]$-$(LiX)_n$, where $Li_6[B_{10}S_{18}]$ describes the framework and its accompanying Li^+ ions bound as Li-S polyhedra. The latter (LiX) describes the lithium-halide pairs in the tunnels whose distribution is discussed below. They represent a "glassy salt", where both the Li^+ cations and X^- anions form a "liquid-like" disordered sublattice in the large channel. The value of n varies from 1.6 to 1.8. Due to the weak scattering of lithium by X-rays, it was difficult to find all the Li^+ in the structure by single-crystal XRD. The refined lithium contents from single-crystal XRD are deficient in lithium for charge balance (**Table 6.2**). To ensure crystal quality was not a factor, three

different crystals were measured for the iodine composition, two at a temperature of 280 K and one at 150 K. All three crystals refined to an iodine content of 1.6. Given the variation in the S/I ratio measured by EDX (see below), it is assumed that the $I_{1.6}$ composition must form high-quality crystals, making them easy to isolate and measure. The refined halide contents from single-crystal XRD (1.8, 1.7, and 1.6 for X = Cl, Br, and I, respectively) for all three phases are larger than expected (1.5) because the halide disorder makes it difficult to determine the exact site occupancies. Thus, the single crystal composition is not necessarily representative of the bulk powder. A comparison of the targeted to the refined and estimated compositions discussed hereafter are summarized in **Table 6.3**.

Table 6.2: Targeted and refined compositions from single crystal analysis and crystallographic data for $Li_{7.5}B_{10}S_{18}X_{1.5}$ (X = Cl, Br, I) based on TOF neutron powder diffraction measured at 300 K.

Composition (targeted)	$Li_{7.5}B_{10}S_{18}Cl_{1.5}$	$Li_{7.5}B_{10}S_{18}Br_{1.5}$	$Li_{7.5}B_{10}S_{18}I_{1.5}$
Single crystal			
Refined composition	$Li_{4.4}B_{10}S_{18}Cl_{1.8}$	$Li_{5.6}B_{10}S_{18}Br_{1.7}$	$Li_{6.8}B_{10}S_{18}I_{1.6}$
Neutron powder diffraction			
Refined composition	$Li_{7.5}B_{10}S_{18}Cl_{2.5}$	$Li_7B_{10}S_{18}Br_{2.7}$	$Li_7B_{10}S_{18}I_{3.2}$
LiX impurity; percent	LiCl; 0 %	LiBr; 5.9-7.3%	LiI; 6.8-9.9%
Temperature (NPD)	300 K	300 K	300 K
Space Group	$C2/c$ (15)	$C2/c$ (15)	$C2/c$ (15)
a (Å)	21.1445(11)	21.1741(6)	21.2826(3)
b (Å)	21.1983(11)	21.4467(7)	21.4205(3)
c (Å)	16.2202(8)	16.1145(5)	16.1530(2)
β(°)	128.675(3)	128.678(2)	128.7163(10)
Volume (Å^3)	5676.0(6)	5712.8(3)	5745.68(17)

The bulk powder samples encompass compositional inhomogeneity and are comprised of a narrow distribution of stoichiometries in the superadamatanoid phases - i.e. $Li_6[B_{10}S_{18}]$-$(LiX)_n$ (X = Br, I) and thus a variation in "n". Examination of microcrystalline powders by Scanning Electron Microscopy (SEM) and Energy-dispersive X-ray spectroscopy (EDX) showed that crystalline regions in the samples contained variability in the sulphur/halide ratios and a slight deviation from the targeted stoichiometry of $Li_{7.5}B_{10}S_{18}X_{1.5}$ (X = Br, I). EDX was not performed on the chlorine substituted materials as elemental contrast between

Table 6.3: Comparison of the targeted, refined and estimated compositions by single-crystal XRD, EDX, NPD, estimated from side phase content, and neutron PDF.

Composition (targeted)	$Li_{7.5}B_{10}S_{18}Cl_{1.5}$	$Li_{7.5}B_{10}S_{18}Br_{1.5}$	$Li_{7.5}B_{10}S_{18}I_{1.5}$
Single crystal Refined composition	$Li_{4.4}B_{10}S_{18}Cl_{1.8}$	$Li_{5.6}B_{10}S_{18}Br_{1.7}$	$Li_{6.8}B_{10}S_{18}I_{1.6}$
EDX Estimated Composition	N/A	$Li_{6.9}B_{10}S_{18}Br_{0.9}$	$Li_{6.9}B_{10}S_{18}I_{0.9}$
Neutron powder diffraction Refined composition LiX impurity; percent	$Li_{7.5}B_{10}S_{18}Cl_{2.5}$ LiCl; 0 %	$Li_{7.8}B_{10}S_{18}Br_{2.7}$ LiBr; 5.9-7.3%	$Li_7B_{10}S_{18}I_{3.2}$ LiI; 6.8-9.9%
Composition estimated from side phase content of NPD	$Li_{7.5}B_{10}S_{18}Cl_{1.5}$	$Li_{6.8}B_{10}S_{18}Br_{0.81}$	$Li_{6.94}B_{10}S_{18}I_{0.94}$
Neutron PDF Refined composition	$Li_{7.5}B_{10}S_{18}Cl_{2.3}$	$Li_7B_{10}S_{18}Br_{2.5}$	$Li_7B_{10}S_{18}I_{2.5}$

S and Cl is not possible due to their close characteristic X-ray energies (2.31 keV for S-Kα and 2.63 keV for Cl-Kα). For the iodide, the S/I ratio ranges from 15-24 (iodine = 0.75 to 1.2) and averages to 20, which corresponds to an iodine-deficient composition of $Li_{6.9}B_{10}S_{18}I_{0.9}$. SEM images and EDX analysis are shown in **Figure 6.5**. Note that the large area EDX analysis has a S/I ratio of approximately 12 (**Figure 6.6**), which matches the weighed-in stoichiometry. The bromide has a similar variation in the S/Br ratio corresponding to a bromine deficient stoichiometry of $Li_{6.9}B_{10}S_{18}Br_{0.9}$, estimated based on EDX analysis (**Figure 6.7**). The halide deficiency in the individual crystals result in compositions less than targeted but agrees with the impurity levels of exsolved LiX (X = Br, I; < 10 wt.% LiBr or LiI) as determined by Rietveld refinement of the neutron powder diffraction (described below). Note that the compositions from EDX are estimates, the S/I ratio may be slightly lower than 20; and an average composition of $Li_7B_{10}S_{18}X$ is likely. The chloride analogue, $Li_{7.5}B_{10}S_{18}Cl_{1.5}$ has no impurity reflections of LiCl in the diffraction patterns, unlike its bromide and iodide counterparts, suggesting it is more stable.

Although stoichiometrically the iodide/bromide content is likely around 1.5, this is difficult to attain in the large-scale preparation of the material. Indeed, attempted synthesis of $n = 1$, $Li_7B_{10}S_{18}I$ showed that powder XRD patterns still contain LiI impurities

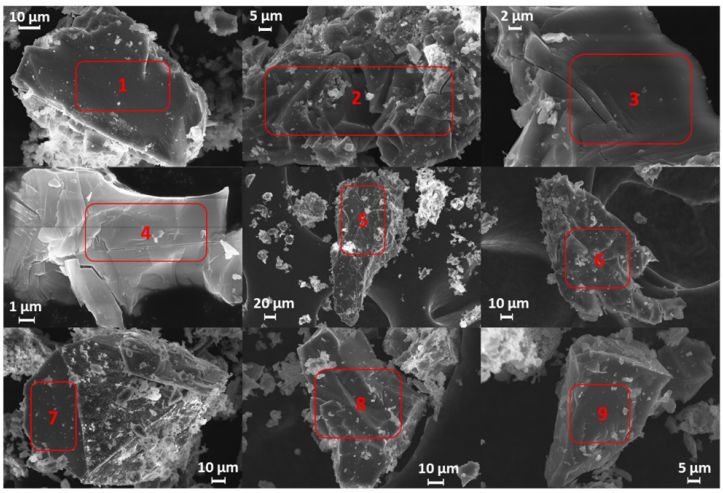

Point #	At. % S	At. % I	S/I
1	68.06	3.18	21.40
2	51.80	2.47	20.97
3	39.57	1.78	22.23
4	24.23	1.37	17.69
5	62.02	3.30	18.79
6	34.03	1.42	23.96
7	50.66	3.38	14.99
8	53.37	2.59	20.61
9	48.38	2.15	22.50
		Average S/I:	20.35

Target Composition: $Li_{7.5}B_{10}S_{18}I_{1.5}$
Expected S/I Ratio: 12
Estimated Composition from EDX: $Li_{6.9}B_{10}S_{18}I_{0.9}$

Figure 6.5: SEM images of selected crystalline areas in the $Li_{7.5}B_{10}S_{18}I_{1.5}$ sample and the corresponding S/I ratios for each point determined by EDX.

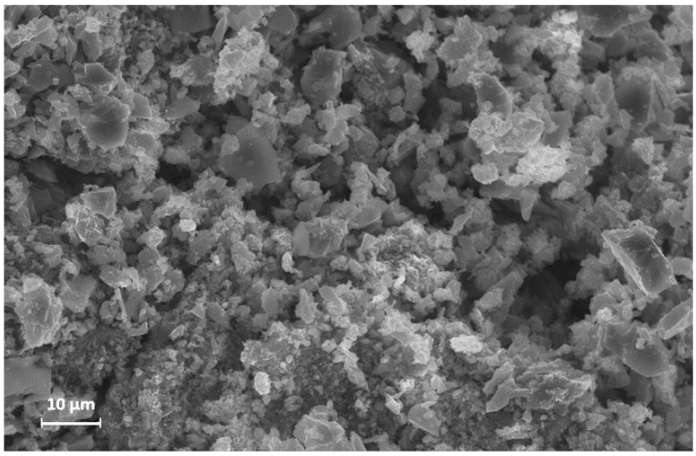

Element	At. %
Sulfur	43.23
Iodine	3.63
S/I Ratio	11.91

Figure 6.6: Large area SEM image and EDX of the $Li_{7.5}B_{10}S_{18}I_{1.5}$ sample. The corresponding S/I ratio of the entire area is ∼12 as expected from the targeted stoichiometry.

(**Figure D.1**), confirming its thermodynamic instability. The adamantanoid phase may be in a relatively deep local energy minimum and has not completely reconfigured to the global minimum, which implies the phase is metastable. The variability of the S/halide ratio from crystalline region to region poses an inherent problem of inhomogeneity in the powder, making it a challenge to precisely fit peak intensities in the Rietveld refinement of the NPD data (see below). Table 6.2 summarizes the data from both single crystal and neutron diffraction refinements for the three halide compositions, both targeted and refined.

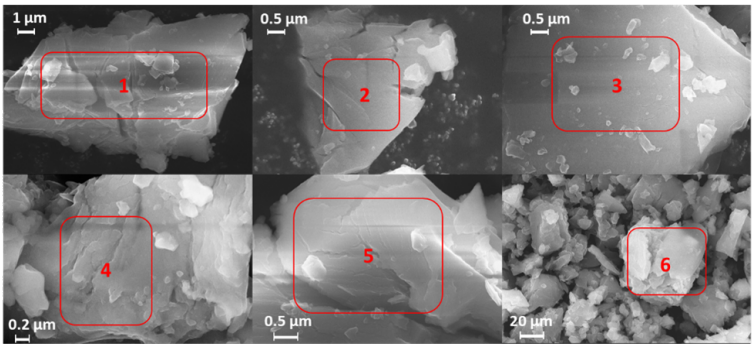

Point #	At. % S	At. % Br	S/Br
1	16.74	0.74	22.62
2	11.90	0.51	23.33
3	23.10	1.01	22.87
4	34.82	1.92	18.14
5	35.83	1.69	21.20
6	33.69	2.02	16.68
		Average S/Br:	20.81

Target Composition: $Li_{7.5}B_{10}S_{18}Br_{1.5}$
Expected S/Br Ratio: 12
Estimated Composition from EDX: $Li_{6.9}B_{10}S_{18}Br_{0.9}$

Figure 6.7: SEM images of selected crystalline areas in the $Li_{7.5}B_{10}S_{18}Br_{1.5}$ sample and the corresponding S/Br ratios for each point determined by EDX.

6.2.4 Lithium and Halide Sublattices Studied by Neutron Powder Diffraction

Because the halides have large neutron scattering lengths (b = 9.6, 6.8, and 5.3 fm for Cl, Br, and I, respectively) and lithium has a negative neutron scattering length (b = -1.9 fm), to better define the disordered lithium and halide sublattices neutron powder diffraction (NPD) was performed. The model determined from single-crystal XRD was used as a starting point for the NPD refinements. Neutron diffraction data was collected at a temperature of 300 K, as well as 10 K to minimize the impact of lithium and halide disorder. The full crystallographic data from the NPD refinements are provided in **Table D.8-D.13** and fits of the NPD data are provided in **Figure 6.8** (300 K measurement) and **Figure D.2** (10 K measurement). The unit cell volume at 300 K (Table 6.2) exhibits a minor expansion from 5676 Å^3 to 5745 Å^3 with increasing halogen radius (Cl^- = 1.81 Å, Br^- = 1.96 Å, and I^- = 2.20 Å). Despite the significant difference in anion dimension, the lattice volume increases by only 1% because the large voids easily accommodate the halide anions. The structure does not change at 10 K and maintains monoclinic symmetry (space group $C2/c$). However, lithium and halide ions are still extremely disordered, perhaps because rapid cooling may have frozen the lithium and halide disorder in place.

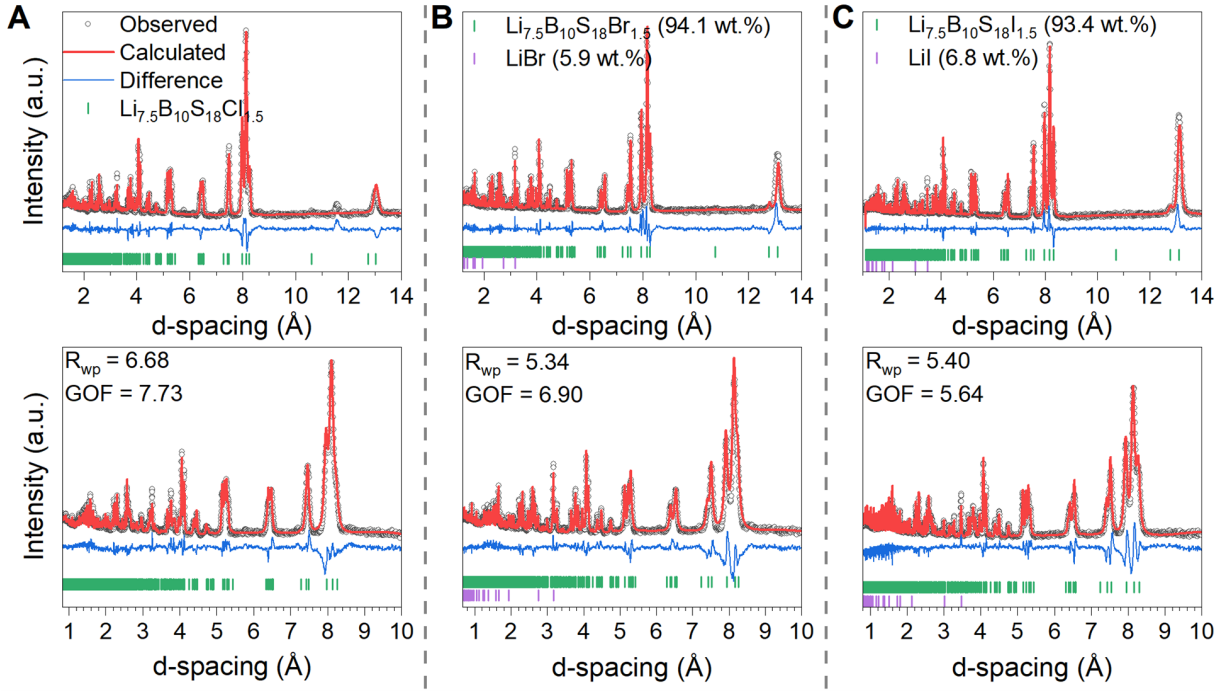

Figure 6.8: Time-of-flight neutron diffraction patterns at 300 K and the corresponding combined Rietveld refinement fits for 'bank 2' (CW 1.5 Å, bottom row) and 'bank 3' (CW 2.665 Å, top row) of $Li_{7.5}B_{10}S_{18}Cl_{1.5}$, B) $Li_{7.5}B_{10}S_{18}Br_{1.5}$, and C) $Li_{7.5}B_{10}S_{18}I_{1.5}$. R_{wp} and GOF are the weighted profile R-factor and goodness of fit, respectively.

In the NPD refinements, the total lithium occupancy was constrained to 7 for the bromide and iodide compounds, and 7.5 for the chloride compound. The Li contents were calculated by charge balancing the average halide content from EDX analysis, which closely matches the calculated Li contents accounting for LiX impurities (i.e. $Li_{6.94}B_{10}S_{18}I_{0.94}$, $Li_{6.81}B_{10}S_{18}Br_{0.81}$; see Appendix D.2 for calculation of Li and halide contents based on impurity amounts from refinement). Many highly disordered lithium sites made it difficult to precisely determine site occupancies, although site positions were well established using the single crystal data and Fourier difference mapping of the NPD data. The lithium was modelled with 11 to 13 sites containing major lithium density (some weak density was also found between the sites by Fourier mapping). The total lithium content was evenly distributed across all the sites and the partial occupancy of each lithium site was fixed for the refinement. This disordered model is in accord with the single-crystal data, and

provides a picture of a high degree of Li^+ ion delocalization in the channels (**Figure 6.9A**) - i.e., dynamic disorder - as expected for fast-ion conductors.[167,168] The model is a suitable representation of the disorder as it gives a reasonable fit to the powder data and agrees with previous ^{7}Li NMR studies on $Li_{6+2x}[B_{10}S_{18}]S_x$ (x ≈ 2), suggesting that the Li^+ ions are randomly distributed among a large number of sites within the channels of the structure.[169]

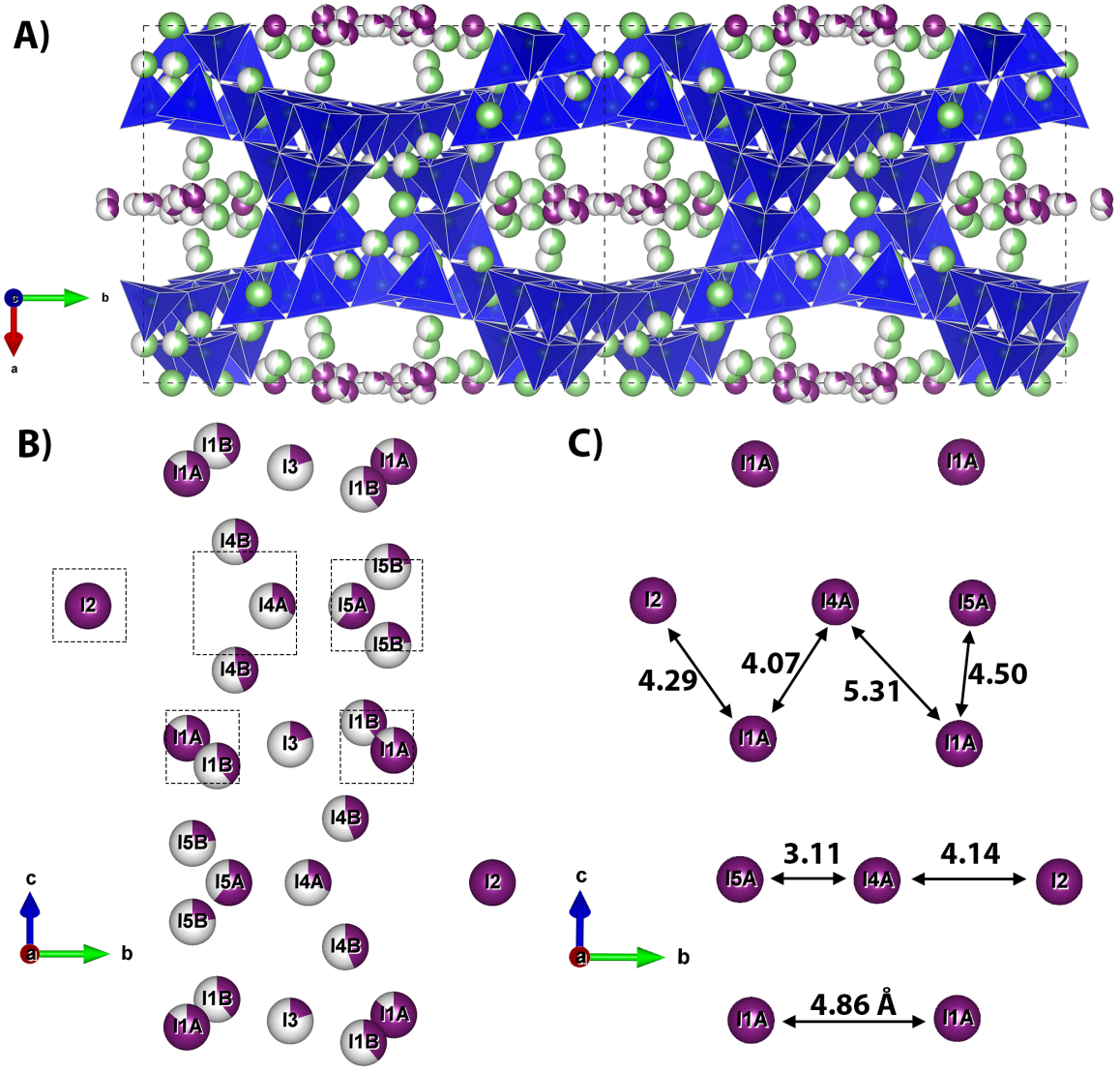

Figure 6.9: A) $Li_{7.5}B_{10}S_{18}Cl_{1.5}$ structure with lithium and iodine in the channels. B) Average structure (refined from NPD at 300 K) and C) local structure (refined from neutron PDF at 290 K) of iodine in the tunnels.

Regarding the halide anions, while their general location in the large channels is easily identified in NPD Fourier difference maps (**Figure D.3**), it was not possible to precisely refine their occupancies owing to the combined problem of extensive disorder and variable content "n" in the inhomogeneous powder samples. Refinements were affected by smearing of the density, which skewed the halide site occupancies. Constraining the total halide content to 1.5 led to mismatched peak intensities and a poor-quality fit. When the halide sites were allowed to freely refine, and the halide was distributed across many sites to model the nuclear density (Figure 6.9B), the refined halide contents from both low and room temperature NPD are higher than the targeted compositions. The stoichiometries were refined to $Li_{7.5}B_{10}S_{18}Cl_{2.5}$, $Li_7B_{10}S_{18}Br_{2.7}$, and $Li_7B_{10}S_{18}I_3$. The NPD patterns at high Q also contained broad ripples, indicative of possible local structure variations that stem from the lithium and halide sublattices. Hence it is difficult to discern the halide sublattice without resorting to PDF analysis as a probe of local structure.

6.2.5 Local Structure of the Halide Sublattice

Neutron total scattering analysis was performed to analyze the PDF of each material based on the average structure model generated from the difference Fourier maps and single-crystal data. In this model, the halide forms a plane in the large channel, distributed across many sites and surrounded by lithium ions as shown in Figure 6.9A. The average structure of the iodide sublattice is a disordered array of I^- ions (Figure 6.9B). The iodide ions distributed through the channel are positioned in "groups", as indicated by the dashed boxes. These groups correspond to areas of high nuclear density, and when analyzed on a local scale, show ordering of the iodide position. Similar local structure deviation in solid electrolytes has been reported for the argyrodite $Li_6PS_{5-x}Se_xBr$, where the substitution of S^{2-} by Se^{2-} results in local ordering of the anions, and hence affects the ionic transport.[170]

The presence of short-range order or local distortion was apparent because the average structural model used for the NPD refinements fits poorly for the PDF in the 1-10 Å range (**Figure 6.10A**). Removing the disordered halide sites and freely refining the remaining

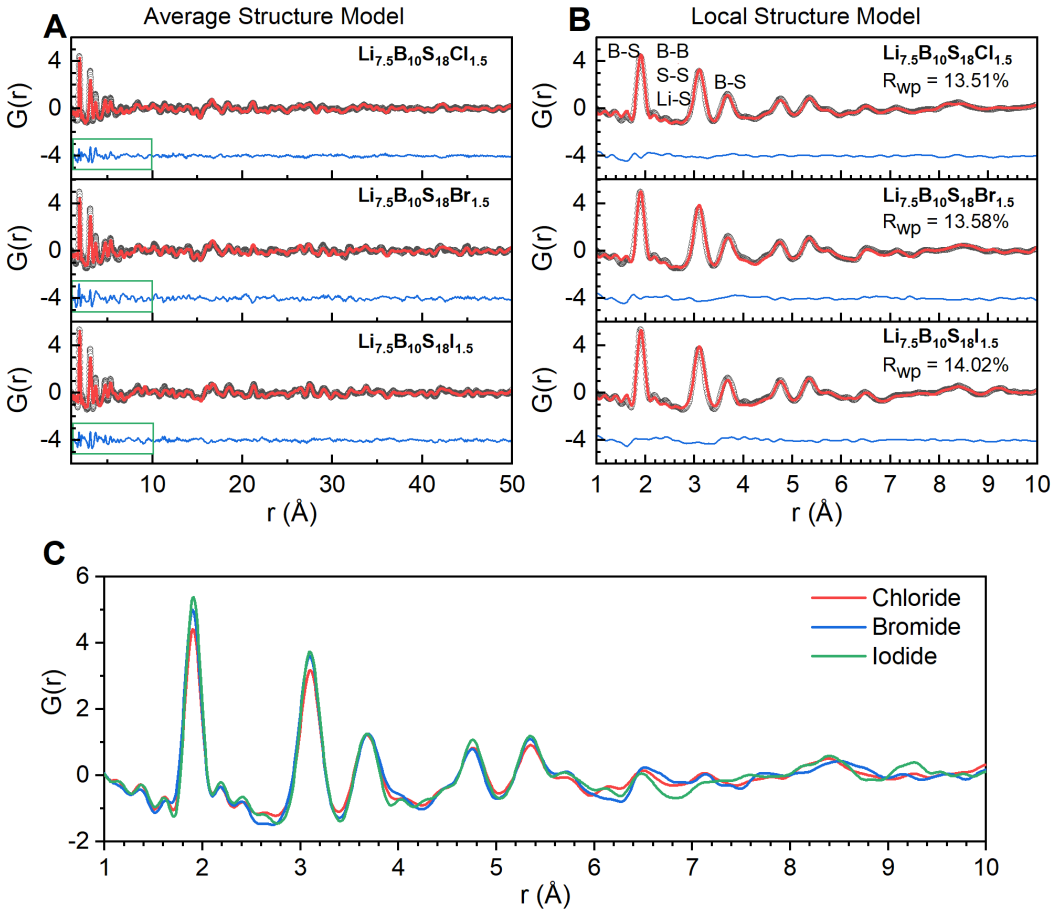

Figure 6.10: Refinement of the A) average structure model (1-50 Å) and B) local structure models (1-10 Å) of $Li_{7.5}B_{10}S_{18}X_{1.5}$ (X = Cl, Br, I) using neutron PDF analysis. Green boxes highlight the larger difference from 1-10 Å, which suggest a deviation from the average structure (i.e. difference in the local structure). C) Neutron PDFs (1-10 Å) overlaid to show the effect of different halide interactions on the PDF pattern.

sites shows halide ordering in the channels with a significantly improved fit at a range of less than 10 Å (Figure 6.10B). In general, the iodide sites sit far apart and are separated by a distribution of distances from 3.1 to 5.3 Å (Figure 6.9C). These values are larger than the bond lengths expected for polyiodides, and rule out halide-halide bonding in the channels.[171] Intense peaks corresponding to halide bonding would be expected around 2.2-3.5 Å and are not present in the PDF profiles.[172,173] Although the PDFs are dominated by the B-S, B-B and S-S interactions (peaks labelled at 1.9, 3.1 and 3.7 angstroms in

Figure 6.10), the weaker Li-halide interactions still influence the PDF. This difference is clear in the overlay of the three patterns shown in Figure 6.10C. A similar ordering of the halide sublattice occurs for the chloride and bromide compounds (**Figure D.4** and **Figure D.5**), and the corresponding crystallographic data for the local structure of each material is provided in **Table D.14-D.16**. Due to the compositional inhomogeneity of the powder samples, the PDF refinements also result in excess halide contents as in the NPD refinements. With neutron PDF, however, local ordering of the halide ions is evident, allowing for determination of the location of the halide in the channel.

6.3 Conclusions

Neutron PDF is an invaluable tool to study the local structure when faced with the challenge of treating extreme cation and anion disorder. In this study, structural models were developed that encompass a wide distribution of lithium and halide sites in the lattice to simulate the disorder in these supertetrahedral frameworks. PDF refinements using these models reveal local structure ordering of the halide anions in the large channel. Only Li^+ cations sit in the smaller but still spacious 4.5 × 4.5 Å channels, while both halide anions and Li^+ cations reside in the large channels. The weak bonding of the anion-cation pairs leads to an overall fast-ion conductivity. This unique combination of a highly crystalline framework with large voids containing a disordered or "glassy salt" produces a system conducive to fast-ion mobility. The lithium-ion conductivity is increased up to 1.4×10^{-3} S·cm^{-1} by altering the polarizability of the halide sublattice in the channels. Substituting Cl^- for the more polarizable Br^- and I^- anions leads to a softer sublattice, and consequently a systematic decrease in the activation energy, which in turn leads to an increase in ionic conductivity. Lithium thioborate-based solid electrolytes present fascinating new model systems to study the effect of disordered sublattices on ion-conduction. Furthermore, given the substantial volume of the channels in the structure, an extensive phase space of alkali thioborate materials can be discovered through facile substitution of either cations (lithium) or anions (halide) in the channels.

6.4 Experimental Procedures

6.4.1 Preparation of $Li_{7.5}B_{10}S_{18}X_{1.5}$ (X = Cl, Br, I)

Stoichiometric amounts of Li_2S (Sigma Aldrich, 99.98%), ^{11}B (Cambridge Isotope Labs, 99%), S (recrystallized from hot toluene), and LiCl/LiBr/LiI (Sigma Aldrich, >99.9%) were ground together. All handling of powders was carried out in an Ar filled glovebox. The precursor mixture was pelletized and supported in a glassy carbon crucible, which was placed in a quartz tube. The quartz tubes were sealed under vacuum and placed vertically in a furnace. The tube was heated up to 750°C in 49 hours and held for 3 hours, then cooled to 550°C in 7 hours and held for 24 hours, cooled to 500°C in 10 hours and held for 60 hours, and finally cooled to room temperature in 9 hours. The resulting powder was ground and then used for subsequent analysis. For single crystal growth the cooling was slower. The tube was heated up to 750°C in 49 hours and held for 3 hours, then cooled to 550°C in 7 hours and held for 3 hours, cooled to 500°C in 120 hours and held for 100 hours, and finally cooled to room temperature in 9 hours. The final product was gently separated to find single crystals suitable for single-crystal X-ray diffraction.

6.4.2 Single-crystal XRD

Several colorless single crystals with dimensions of approximate 0.02 x 0.1 x 0.1 mm^3 were scanned to determine their quality. The data were collected on a BRUKER KAPPA diffractometer equipped with a SMART APEX II CCD, utilizing graphite-monochromated Mo-Kα radiation. The crystals were protected by Paratone-N oil and a liquid nitrogen flow using an OXFORD Cryostream controller 700 at 200-280K to ensure no reactivity of the materials occurred. The data were collected by scanning ω and ϕ of 0.3° or 0.5° in a few groups of frames at different ω and ϕ and an exposure time of 30 or 60 seconds per frame. The data were corrected for Lorentz and polarization effects. The absorption corrections were carried out by the multi-scan method using SADABS since the crystals

don't have clear faces. The Cell_now software was used to check for potential twinning. The structures were solved using direct method to locate the positions of B, S, and X (X= Cl, Br or I) atoms. After locating the B-S framework and the heavy halide sites, first, their atomic positions were anisotropically refined using the least squares method incorporated in the SHELXTL package, and then the Li positions were located in the remaining electron density in the Fourier map, which revealed Li-S bonds very similar in length to those found in binary and ternary Li sulfides. Subsequently, the Li site occupancies were freely and anisotropically refined. The refinements were converged to good residual values R1 and wR2. No constraints were used during the structure refinements. Indexing the unit cell reflections (with I/sigma below 5) to check for a possible supercell was carried out, but no supercells with either completely or partially ordered atomic positions were found for any single crystal composition.

6.4.3 Neutron Powder Diffraction

^{11}B was specifically used as a precursor in the synthesis because of the large absorption cross section of natural B and ^{10}B. Time-of-flight (TOF) neutron powder diffraction samples were loaded into a 6 mm vanadium can under He with a copper gasket and aluminum lid. Samples were collected on POWGEN (Beamline 1B) at the Spallation Neutron Source (SNS) in Oak Ridge National Laboratory. Data was also collected at two different center wavelengths; 1.5 Å, which can provide high resolution data up to d_{max}∼12 Å (and Q_{max}∼12 Å^{-1}), and 2.665 Å, which can provide data up to d_{max}∼21 Å (and Q_{max}∼6 Å^{-1}). The second dataset is necessary because the (110) reflection occurs at approximately d=13 Å, outside the range of the 1.5 Å bank. Each sample was measured at temperature of 10 and 300 K. The resulting diffraction patterns were refined by the Rietveld method using TOPAS version 6 (Bruker - AXS). Standard NIST Si 640d was used as external calibrants for the instrument. Time-of-flight (TOF) data were converted to d-spacing data using the modified second order polynomial TOF = ZERO + DIFC*d + DIFA*d2 +DIFB/d, where ZERO is a constant, DIFC is the diffractometer constant, DIFA and DIFB are empirical terms to

correct the sample displacement and absorption caused peak shift.[174] During the refinement, ZERO and DIFC were determined from the refinement using a standard NIST Si 640d, while DIFA and DIFB were allowed to vary to account for the sample displacements/absorption. A back to back exponential function convoluted with symmetrical pseudo Voigt function were used to describe the peak profile.

6.4.4 Neutron Total Scattering

Neutron total scattering data was collected on NOMAD (Beamline 11A) at the Spallation Neutron Source (SNS) in Oak Ridge National Laboratory. The same samples measured on POWGEN were later loaded on NOMAD. Four 48 min scans were collected for each powder sample and then summed together to improve the statistics. The obtained diffraction data were normalized against a vanadium rod, the background was subtracted. An ad-hoc polynomial function was used to correct the inelastic (Placzek) scattering. The total scattering structure function S(Q) data were transformed to the reduced pair distribution function data G(r). The Q range used for the Fourier transfer is 0.2 $Å^{-1}$ to 28 $Å^{-1}$ for the samples. For PDF data, small box refinements were carried out using TOPAS 6. The instrumental parameters dQ and Q_{broad} were set to be 0.04607 and 0.02607 based on the refinement of the NIST Si 640e standard.

6.4.5 Ionic Conductivity and Activation Energy Measurements

Bulk resistance of the samples was determined from electrochemical impedance spectroscopy (EIS) with an amplitude of 100 mV in the frequency range 1 MHz to 100 mHz using a Bio-logic VMP3 potentiostat/galvanostat. Approximately 150 mg of sample was placed between two titanium rods in a custom-made Swagelok cell and pressed into a 10 mm diameter pellet with a hydraulic press at 3 tons in an Ar filled glovebox.

For activation energy measurements, approximately 100-200 mg of powder was placed between two titanium rods in a custom-made cell and pressed into a 10 mm diameter pellet with a hydraulic press at 3 tons. In foil was attached on either side of the electrolyte pellet

to ensure good contact. EIS was measured from 35 MHz to 100 mHz with an amplitude of 100 mV using a Bio-logic MTZ-35 impedance analyzer. The measurements were carried out in the temperature range 25°C to 60°C.

6.4.6 Scanning Electron Microscopy (SEM) and Energy Dispersive X-ray Spectroscopy (EDX)

Imaging and estimation of S/Halide ratios was performed using a LEO 1530 Zeiss field emission scanning electron microscope equipped with an energy dispersive X-ray spectrometer. Samples were mounted on an SEM holder with carbon tape inside an argon glovebox. The samples were placed in a vial and sealed using parafilm. The sample vials were taken out of the glovebox, opened under ambient air for less than 10 seconds, and immediately transferred into the SEM sample chamber to minimize moisture exposure and oxygen contamination.

Chapter 7

$Li_6B_7S_{13}I$: a fast-ion conducting thioboracite with a perovskite topology and argyrodite-like lithium substructure

This section is reproduced in part with permission from:
Kavish Kaup, Kevin Bishop, Abdeljalil Assoud, Jue Liu, and Linda F. Nazar, *Journal of the American Chemical Society*, **2021**. DOI: 10.1021/jacs.1c00941.

* Dr. Kevin Bishop was involved in discussions regarding the implementation of the AIMD calculations.

* Dr. Abdeljalil Assoud performed the single crystal XRD measurements and corresponding refinements.

* Dr. Jue Liu provided guidance for conducting the neutron diffraction measurements at Oak Ridge National Lab.

7.1 Introduction

Development of solid-electrolytes has been centered around oxide and sulfide-based electrolytes,[147] with a strong focus on thiophosphates because of their high ionic conductivity and good ductility that makes them amenable to cell fabrication.[175] Amongst the many thiophosphates, argyrodites are notable for their relative stability and ease of preparation, where conductivities up to 10^{-2} S·cm^{-1} have been achieved with excellent performance in ASSBs.[28,176] Many fast-ion conductors are predicted to be metastable at intermediate temperature but can be stabilized by entropic contributions upon heating to higher temperatures. Some sodium and lithium anti-perovskites are formed this way,[177,178] as well as the thiophosphate $Li_7P_3S_{11}$.[179] As in the case of Na_3PS_4, metastable polymorphs can be accessed by varying the synthesis conditions, which also influences the ionic conductivity.[180] These techniques have led to the discovery of alternative lithium-ion conducting material classes such as phosphidosilicates[181] and rare-earth halides.[182] Here, a new and unusual superionic thioborate is reported, $Li_6B_7S_{13}I$, that has an unprecedented perovskite topology combined with an argyrodite-like lithium substructure. It was synthesized, not by a classic heat-and-beat solid-state approach, but by a strategy termed here as "simmering", which exploits the reactivity of a metastable solid with a molten salt at intermediate temperatures. The presence of the liquid-solid interface, together with highly facile ion mobility in both reactant - and product (as confirmed here by theory) - likely favors the kinetics of the solid transformation.

Despite having similar material properties to thiophosphates, Li-ion conducting thioborates have been surprisingly underexplored, resulting in a paucity of candidates for theoretical and experimental investigation. Thioborate glasses have shown high ionic conductivities,[120,150] and have similar favorable mechanical properties to thiophosphate given the highly polarizable nature of the S^{2-} anion. However, to date, only a few crystalline thioborates exist, most of which exhibit supertetrahedral frameworks such as $Li_{6+2x}[B_{10}S_{18}]S_x$ (x=2),[152] $Li_5B_7S_{13}$,[183] and $Li_9B_{19}S_{33}$.[183] These networks create large void spaces that form

three-dimensional channels for cations to diffuse through the structure. However, revisitation of the Li_2S-B_2S_3 binary phase space in the last three years has uncovered some very promising findings. Theoretical work on the lithium thioborate, Li_3BS_3, predicted a very low activation energy barrier for ion migration of 0.25 eV, although no experimental ionic conductivity was reported.[184] A recent and exciting report on *ab-initio* molecular dynamics (AIMD) simulations of $Li_5B_7S_{13}$ predicted extremely high ionic conductivities of 6.2×10^{-2} S·cm^{-1},[149,185,186] much higher than any known superionic lithium conductor. These findings inspired exploration of the ternary system Li_2S-B_2S_3-LiI in this study, leading to the discovery of the novel cubic $Li_6B_7S_{13}I$ described here. This fast-ion conductor represents an entirely new family of solid electrolyte materials. *Ab initio* molecular dynamics simulations in this study reveal facile three dimensional pathways for superionic (5×10^{-3} S·cm^{-1}) lithium-ion conduction in this thioboracite; the first to be reported.

7.2 Results and Discussion

7.2.1 Synthesis and Framework

$Li_6B_7S_{13}I$ was synthesized by deliberately annealing a composition close to the recently reported superionic supertetrahedral lithium thioborate, $Li_{7.5}B_{10}S_{18}I_{1.5}$.[187] This highly non-stoichiometric material exhibits thermodynamic instability resulting in ex-solvation of LiI impurities upon cooling. The mechanism for the synthesis of cubic $Li_6B_7S_{13}I$ exploits the reactivity of this kinetically preferred metastable supertetrahedral phase that initially crystallizes from a mixture with a stoichiometric composition equivalent to $Li_6B_7S_{13}I$ (i.e., [supertetrahedral $Li_{7.14+x}B_{10}S_{18}S_{0.57}I_x$ + (1.43-x)LiI impurities]), based on the powder XRD pattern (**Figure 7.1**, black line). Fine-grinding of the solid mixture is necessary to reduce the particle size and homogenize the components, which are subsequently annealed at 500°C. The LiI component melts at 470°C, creating a liquid-solid interface that accelerates the diffusion and triggers transformation to the thermodynamically stable cubic $Li_6B_7S_{13}I$ phase. A significant activation energy is required to overcome the unfavorable kinetics of

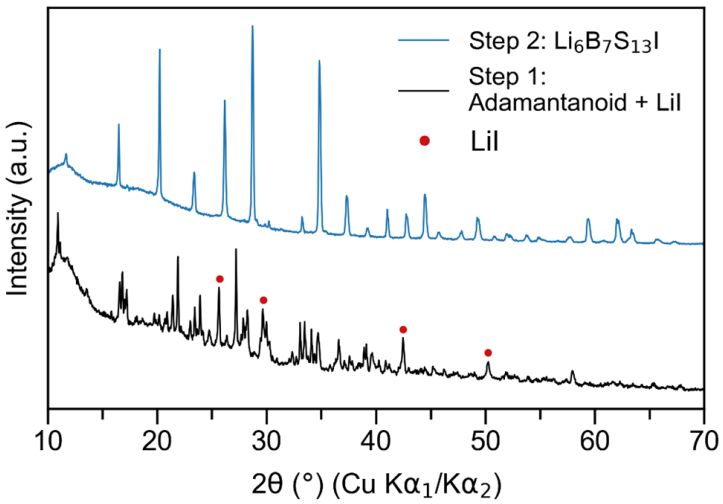

Figure 7.1: Powder XRD pattern of targeted $Li_6B_7S_{13}I$ after step 1 of heat-treatment (black line) resulting in adamantanoid phase $Li_{7.14+x}B_{10}S_{18}S_{0.57}I_x$ + LiI and after step 2 re-annealing resulting in pure cubic $Li_6B_7S_{13}I$ (blue line).

the solid transformation, as indicated by the fact that no reaction occurs if the mixture is simply annealed without grinding. A low-temperature direct synthesis route was also attempted. Grinding the precursors and annealing just above the LiI melting point for two weeks resulted in the supertetrahedral phase along with LiI, further highlighting the kinetic limitations of the reaction. Adopting the "simmering" approach overcomes these limitations and the resulting material is a pure single phase (based on powder XRD, Figure 7.1). The measured S/I ratio determined by EDX agrees with the targeted stoichiometry (**Figure 7.2**; SEM images and EDX analysis). The structure of $Li_6B_7S_{13}I$ (space group F-43c) was unequivocally solved by single-crystal XRD and is shown in **Figure 7.3A**. The crystallographic details are described in **Table 7.1-7.2** (see **Table E.1** for additional details on the single-crystal refinement).

Based on the empirical formula, it might be expected that the structure of $Li_6B_7S_{13}I$ is related to the halogen-free $Li_5B_7S_{13}$ phase that was proposed to have high lithium mobility based on activation energies of 0.3 eV measured by NMR.[183,188] To compare the structures, $Li_5B_7S_{13}$ was targeted for synthesis, which resulted in a multi-phase mixture that also encompassed $Li_{6+2x}B_{10}S_{18}S_x$ and $Li_9B_{19}S_{33}$ (thus precluding ionic conductivity

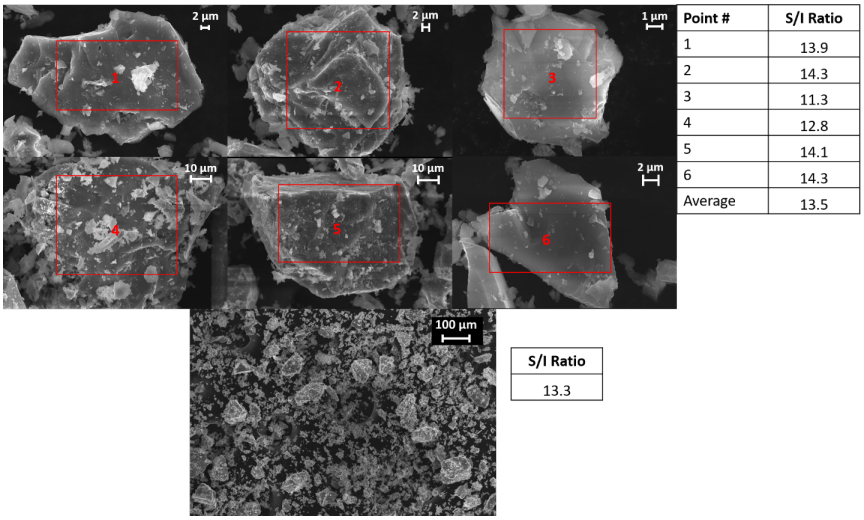

Point #	S/I Ratio
1	13.9
2	14.3
3	11.3
4	12.8
5	14.1
6	14.3
Average	13.5

S/I Ratio
13.3

Figure 7.2: SEM images of selected crystalline areas and a large area of the cubic $Li_6B_7S_{13}I$ sample and the corresponding S/I ratios determined by EDX.

Table 7.1: Atomic coordinates, occupation factor, and equivalent isotropic displacement parameters of the cubic $Li_6B_7S_{13}I$ obtained from single-crystal XRD measured at 280 K.

Space Group: F-43c, a = 15.245(2) Å, V = 3543.1(14), Z = 8						
Atom	**Wyck. Pos.**	**x**	**y**	**z**	**Occ.**	**U_{eq} (Å^2)**
I1	8a	0.5	0.5	0.5	1	0.0287(2)
S1	96h	0.64478(7)	0.73643(6)	0.56936(6)	1	0.0107(3)
S2	8b	0.75	0.75	0.75	1	0.0082(3)
B1	24c	0.75	0.75	0.5	1	0.0041(13)
B2	32e	0.6730(3)	0.6730(3)	0.6730(3)	1	0.0041(13)
Li1	32e	0.6088(8)	0.8912(8)	0.6088(8)	1	0.054(3)
Li2	24d	0.5	0.75	0.5	0.68(11)	0.12(3)

Table 7.2: Anisotropic displacement parameters of $Li_6B_7S_{13}I$ obtained from single-crystal X-ray diffraction measured at 280 K.

Atom	**U_{11}**	**U_{22}**	**U_{33}**	**U_{23}**	**U_{13}**	**U_{12}**
I1	0.0287(3)	0.0287(3)	0.0287(3)	0	0	0
S1	0.0084(4)	0.0142(5)	0.0096(4)	0.0026(3)	0.0005(3)	0.0016(4)
S2	0.0082(5)	0.0082(5)	0.0082(5)	0	0	0
B1	0.0052(16)	0.0052(16)	0.002(3)	0	0	0
B2	0.0052(16)	0.0052(16)	0.002(3)	0	0	0
Li1	0.054(5)	0.054(5)	0.054(5)	0.010(5)	-0.010(5)	0.010(5)
Li2	0.042(16)	0.26(8)	0.042(16)	0	0	0

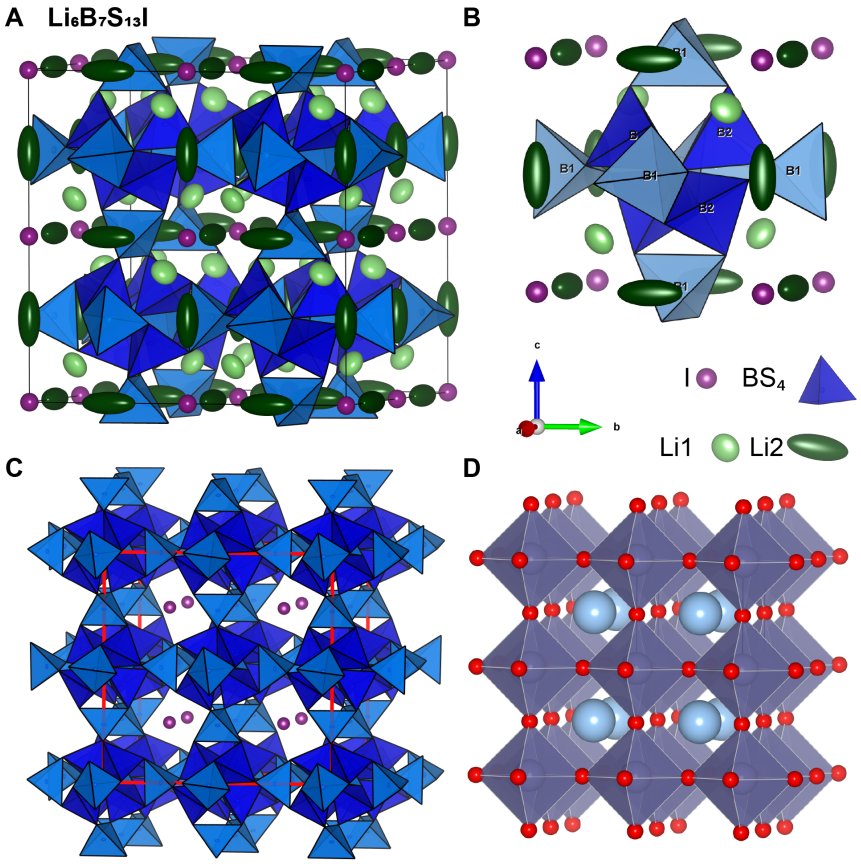

Figure 7.3: A) Structure of cubic $Li_6B_7S_{13}I$ from single-crystal XRD with Li^+ and I^- ions shown as probability displacement ellipsoids (S^{2-} ions omitted), s.g. F-43c, a = 15.245 Å; B) one octant of the cube showing the large boron-sulfur anion cluster; the clusters are centered at each of the eight octants in the cubic lattice, and an additional corner sharing BS_4 anion at all six sides connect neighboring cluster (light blue tetrahedra), C) $Li_6B_7S_{13}I$ unit cell with the origin shifted, and D) a general perovskite AMX_3 framework.

measurement). A single crystals of $Li_5B_7S_{13}$ was isolated from the mixture and Rietveld refinement showed that it crystallizes in the tetragonal space group $I4_1/a$ (Table E.1 and **Table E.2-E.3**), in slight contradiction to the original assignment in the space group $C2/c$.[183] The condensed B_4S_{10} and $B_{10}S_{20}$ supertetrahedra in the $Li_5B_7S_{13}$ framework (**Figure 7.4**) are representative of previously reported superadamantanoid phases.[152,183,187] However, surprisingly, it was found here that the incorporation of lithium and iodine into the $Li_5B_7S_{13}$ lattice to form $Li_6B_7S_{13}I$ triggers the transformation to a boracite crystal structure ($M_3B_7O_{13}X$, where M is an alkali-earth or transition metal divalent cation and X is typically

a halide) shown in Figure 7.3A. $Li_6B_7S_{13}I$ has a three-dimensional framework composed of corner sharing BS_4 tetrahedra that form unique B_4S_{13} anion clusters (dark blue tetrahedra in Figure 7.3B). The building blocks can also be described as a central sulfur coordinated by four boron atoms to form an SB_4 tetrahedra bonded to six BS_4 tetrahedra, i.e., a $[B_4S(BS_4)_6]^{20-}$ structural unit. This structural framework is unprecedented in boron-sulfur chemistry although "zeolitic-like" sulfide hydrates $Na_5Ga_7S_{13}{\cdot}6H_2O$ and $Na_5In_7S_{13}{\cdot}6H_2O$ also possess the same extended metal-sulfur clusters.[189,190]

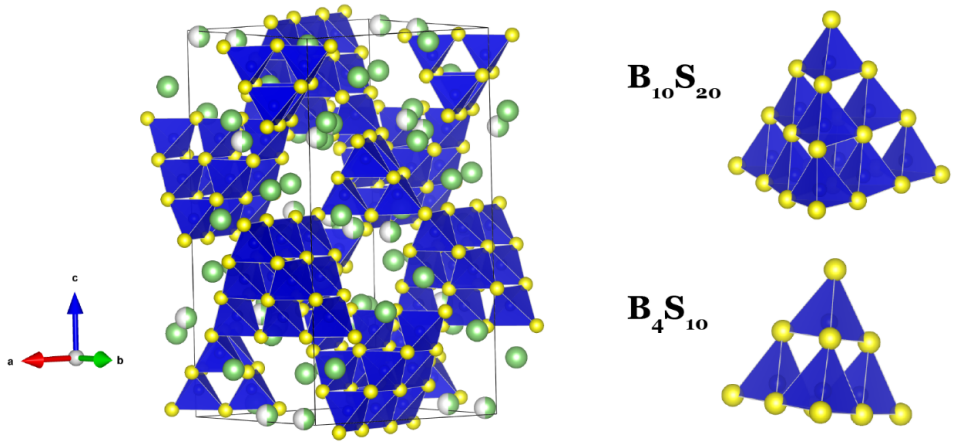

Figure 7.4: Structure of tetragonal $Li_5B_7S_{13}$ solved from single-crystal XRD, containing B_4S_{10} and $B_{10}S_{20}$ supertetrahedra.

While boracites only form cubic polymorphs at high temperature, the thioboracite is cubic at room temperature which - importantly - leads to isotropic ion conduction properties (see below). The tetrahedral boron-sulfur framework of $Li_6B_7S_{13}I$ also results in a large unit cell volume (3543 $Å^3$), which typically leads to enlarged diffusion pathways favorable for high lithium-ion mobility,[79,191] and may allow for some structural modification by isovalent or aliovalent substitution.[43] Remarkably, $Li_6B_7S_{13}I$ is the first known thioboracite and by extension, the first sulfide-based lithium-ion conductor based on such phases. While not adopting the same structure as a perovskite (AMX_3 - e.g. $CsPbBr_3$), it can be considered to exhibit a "perovskite topology"; where in the case of $Li_6B_7S_{13}I$, the $[PbBr_6]^{4-}$ octahedra

are replaced by the $[B_4S(BS_4)_6]^{20-}$ clusters, and the Cs^+ cations are replaced by I^- anions and Li^+ cations (Figure 7.3C and D). All other known lithium-ion conducting solid electrolytes with a perovskite (or anti-perovskite) framework are oxide-based materials such as $Li_{3x}La_{2/3-x}\square_{1/3-2x}TiO_3$ (LLTO)[192,193] and Li_3OCl.[58,104] For example, the long-sought-after Li_3SI antiperovskite that is anticipated to be a fast-ion conductor remains elusive.[178]

7.2.2 AIMD Simulations of Li-ion Transport

The Li substructure in $Li_6B_7S_{13}I$ facilitates excellent lithium-ion conduction, as determined by AIMD simulations using VASP[48] and starting from the refined single-crystal structure shown in Figure 7.3A. The two lithium sites in $Li_6B_7S_{13}I$ have distinct coordination environments (Table 7.1). The fully occupied Li1 site is tetrahedrally coordinated (LiS_3I), while the partially occupied Li2 site (occ. 0.68) sites in an elongated octahedra with iodine apices (LiS_4I_2), having long Li-I bonds of 3.81 Å. AIMD calculations were carried out at elevated temperatures of 600 to 900 K to accelerate the diffusion, which shortens the overall simulation time. The Li-ion probability density isosurface from AIMD at 750 K shown in **Figure 7.5A** demonstrates the 3D diffusion pathways in the structure and significant Li-ion mobility along the Li1-Li2-Li1 pathways. Given the cubic symmetry, this leads to ideal three-dimensional isotropic conduction. Note that the Li2 site has a very anisotropic probability density, consistent with the anisotropic atomic displacement parameters (ADP) refined by single-crystal XRD and shown earlier in Figure 7.3.

7.2.3 Lithium substructure comparison to argyrodite

The Li^+ ions in $Li_6B_7S_{13}I$ move in a localized trajectory that forms a cage around the iodine site, where long-range ionic diffusion between cages is enabled by the connection via the partially occupied and highly anisotropic Li2 site (Figure 7.5B). This comparison is better viewed in an alternative representation generated by shifting the origin of the cell, shown in Figure 7.3C. This illustrates that the iodide ions sit at the center of all eight octants of the cube, surrounded by a cage of Li-ions (Figure 7.5B and **Figure 7.6A**).

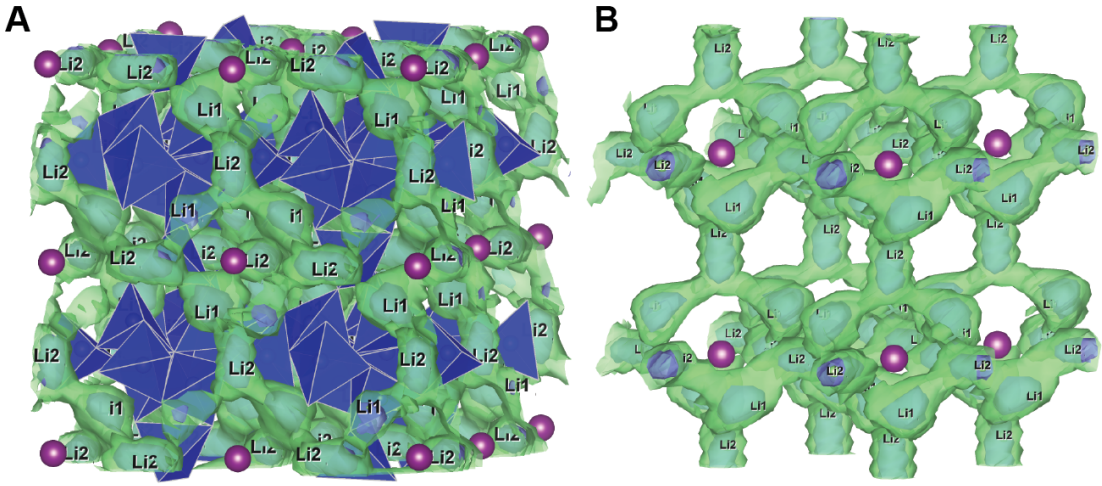

Figure 7.5: Li^+ probability density distribution of $Li_6B_7S_{13}I$ obtained from AIMD simulations at 750 K in A) cubic F-43c representation and B) the corresponding Li cages around iodine atoms.

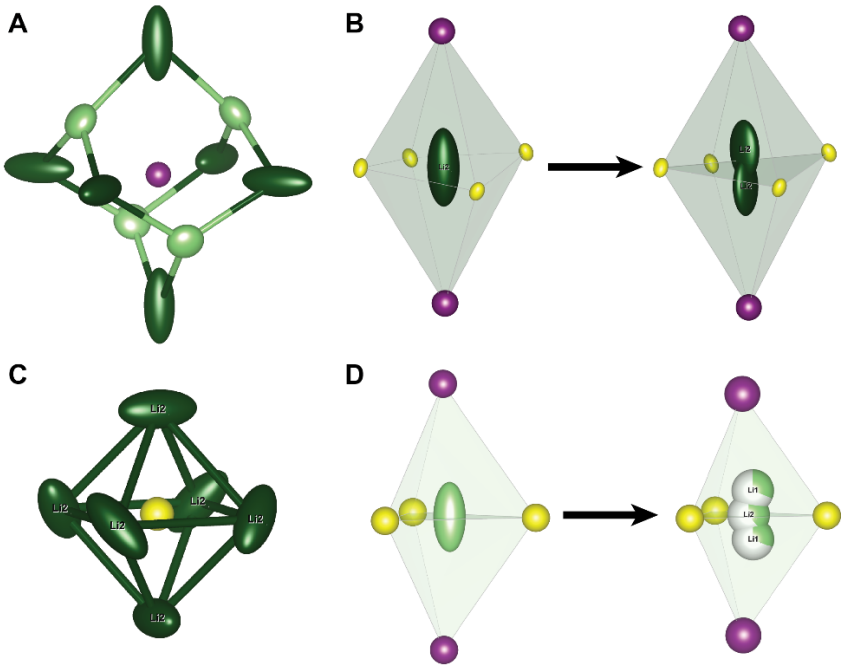

Figure 7.6: A) Li^+ forms a cage around the I^- in $Li_6B_7S_{13}I$, B) LiS_4I_2 octahedron in $Li_6B_7S_{13}I$ (F-43c) with a large anisotropic displacement of the Li2 site (24d) and its split site representation (48f) as two square pyramids LiS_4I. C) Li^+ cages in argyrodite Li_6PS_5I, D) LiS_3I_2 double tetrahedra in Li_6PS_5I (F-43m) with a large anisotropic displacement of the 24g site and its common split site representation as face-sharing LiS_3I tetrahedra.

The large anisotropic ADP of Li2 (visually represented by the dark green thermal ellipsoids) can also be represented as a split site with the lithium ions separated by about 1 Å (Figure 7.6B). The lithium substructure of $Li_6B_7S_{13}I$ bears strong similarities to the argyrodites, Li_6PS_5X (X = Cl, Br, or I; space group F-43m), where Li-ions form cages around disordered halide/sulfur sites (Figure 7.6C). In the argyrodite structure, the Li-ions that resides at the center of a double tetrahedron also exhibit an anisotropic displacement, which can be alternatively represented as split Li sites (Figure 7.6D). Ion conductivity in the argyrodite structure is primarily dictated by the Li^+ intra and intercage jump distances.[27,194] The Li1 and Li2 sites in $Li_6B_7S_{13}I$ also form cages around the I^- ions as shown in Figure 7.6A and 7.5B (Li1-Li2 distance of 3.18 Å or 2.89 Å considering site splitting), and the Li2 site connects adjoining cages. The cubic symmetry enables isotropic three-dimensional transport, as demonstrated by the AIMD simulations described earlier (Figure 7.5).

7.2.4 Li-ion Diffusivity and Conductivity

The Li^+ diffusivities for cubic-$Li_6B_7S_{13}I$ were calculated from the mean square displacement of the Li ions from the AIMD calculations. **Figure 7.7A** shows the Arrhenius plot of ionic conductivity derived from the diffusion coefficients at a temperature from 600 to 900 K. Using this region, the diffusion coefficient extrapolates to a value of 6.3×10^{-8} $cm^2 \cdot s^{-1}$ at 300 K. This represents very high diffusivity, comparable to the superionic conductor $Li_{10}GeP_2S_{12}$, whose average diffusivity is approximately 2×10^{-8} $cm^2 \cdot s^{-1}$ from AIMD calculations[101] and NMR spectroscopic measurements.[195] The room temperature lithium-ion conductivity is derived from the Nernst-Einstein equation:

$$\sigma_{Li} = \frac{N\,(Ze)^2}{k_B T} D_{Li}$$

where k_B refers to the Boltzmann constant; T denotes the temperature; N is the number density of the mobile lithium ions in the unit cell, Z is the charge of the lithium ions, e is the electron charge, and D_{Li} is the diffusion coefficient of the lithium ions. Using this

expression, the calculated ionic conductivity of $Li_6B_7S_{13}I$ is 5.2×10^{-3} S·cm^{-1} at 300 K. The ionic conductivities at each temperature were calculated in the same manner, and a linear fit of the data gives a bulk activation energy of 0.23 eV.

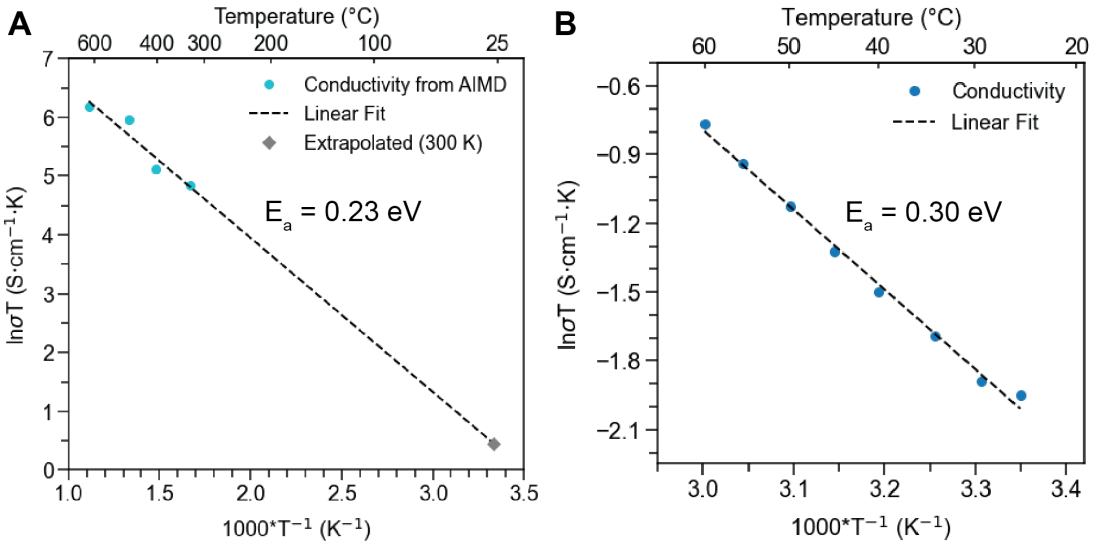

Figure 7.7: Arrhenius plots of $Li_6B_7S_{13}I$ obtained from temperature dependent A) AIMD simulations and B) EIS measurements.

To compare theory to experiment, the ionic conductivity of a powder pellet of cubic-$Li_6B_7S_{13}I$ was measured by electrochemical impedance spectroscopy over a temperature range of 298 to 333 K. Nyquist plots measured at each temperature are shown in **Figure 7.8A**. The electronic conductivity is very low (σ_{el} = 1.25×10^{-9} S·cm^{-1}) and has a negligible influence on the total conductivity (DC polarization curve can be found in **Figure E.1**). The total resistance, as determined by a linear fit of the Warburg impedance, was used to calculate the ionic conductivity at each temperature. The experimental ionic conductivity of cubic-$Li_6B_7S_{13}I$ at room temperature is 5×10^{-4} S·cm^{-1} with an overall activation energy of 0.30 eV, determined by a linear fit of the Arrhenius plot (Figure 7.7B). There is no discontinuity over this temperature range and linear Arrhenius behavior is observed, indicating phase stability. Differential scanning calorimetry (DSC) results also confirm that no phase transition occurs over a temperature range of 233 to 373 K (**Figure 7.9**). The conductivity is lower than the calculated value of 5.2×10^{-3} S·cm^{-1} at 300 K (while

the activation energy is slightly higher than 0.23 eV), which is likely because the AIMD simulations capture the bulk properties and EIS measures both bulk and grain boundary processes.[179] Although grain boundaries in sulfide materials are typically assumed to have a negligible influence on the total ion conductivity, they have been shown to significantly impact the conductivity by more than an order of magnitude in some sulfides.[107,179,196]

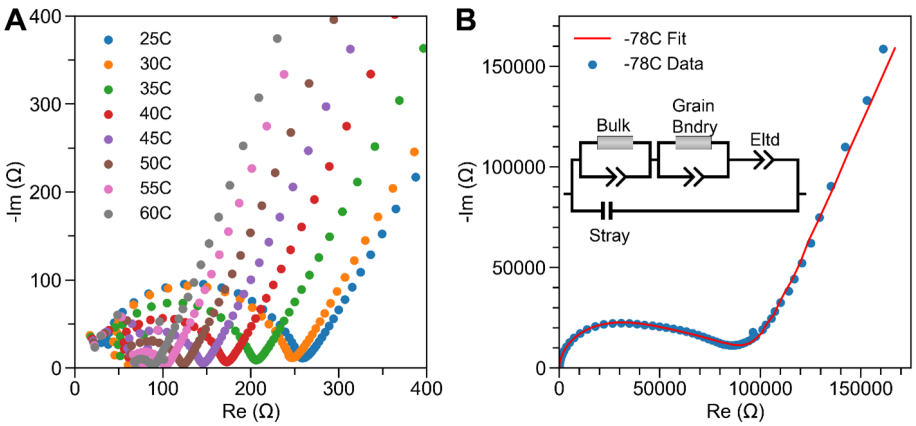

Figure 7.8: A) Nyquist plots of $Li_6B_7S_{13}I$ at each temperature used to extract the ionic conductivity values for activation energy measurements and B) a low-temperature Nyquist plot at -78°C and the corresponding equivalent circuit and fit.

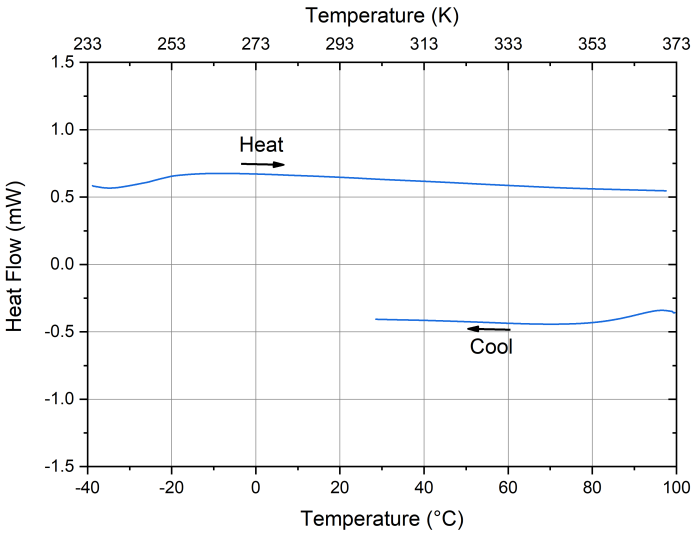

Figure 7.9: Differential scanning calorimetry curve of cubic-$Li_6B_7S_{13}I$ under a N_2 flow of 50 mL/min.

Therefore, low-temperature EIS measurements at 195 K (-78°C) were performed to deconvolute the grain and grain boundary processes (Figure 7.8B and **Table 7.3**). The capacitances obtained from the equivalent circuit fit of the low-temperature Nyquist plot were in the expected range; 3.4×10^{-11} F for the bulk process (22 kΩ) and 1.5×10^{-9} F for the grain boundary process (79 kΩ). The relatively low α value (0.42) implies there may be overlapping semi-circles, and high resistance of the grain boundaries - almost four-fold that of the bulk - suggests the presence of amorphous B_2S_3 or Li-B-S impurities at the grain boundaries because there are no crystalline impurities in the powder XRD (see Figure 7.1). These impurities are indeed apparent from the SEM images that show a predominance of speckled particles on the crystalline surfaces (Figure 7.2). Despite the likely deleterious effect of grain boundary resistance, the activation energy of 0.30 eV is identical to supertetrahedral $Li_{7.5}B_{10}S_{18}I_{1.5}$ and lower than the reported values for the argyrodites Li_6PS_5I and Li_6PS_5Cl (0.39 eV and 0.45 eV).[27,164,197] This value is also on par with Li_6PS_5Br (0.30 eV)[27] and Cl-rich $Li_{5.5}PS_{4.5}Cl_{1.5}$ (0.29 eV),[164] indicating that $Li_6B_7S_{13}I$ has a favorable energy landscape for Li^+ ion migration. Considering the negative influence of grain boundaries, the measured conductivity (and activation energy) is likely lower (higher) than the inherent bulk value. Nonetheless, the values are in reasonable agreement, and it may be possible to enhance the experimentally measured conductivity by optimization of the synthesis to reduce the grain boundary resistance.

Table 7.3: Parameters of the fit for the impedance data of cubic-$Li_6B_7S_{13}I$ at -78°C.

Description	**Element**	**Value**	**C_{eff}**
Bulk	R1 CPE1 – Q1 α1	21722 Ω 2.415×10^{-10} F·s$^{α-1}$ 0.8616	3.43×10^{-11} F
Grain Boundary	R2 CPE2 – Q2 α2	79159 Ω 3.826×10^{-7} F·s$^{α-1}$ 0.4215	1.53×10^{-9} F
Electrode Polarization	CPE3 – Q3 α3	8.373×10^{-6} F·s$^{α-1}$ 0.7422	
Stray	C1	3.434×10^{-10} F	

Note that $Li_6B_7S_{13}I$ exhibits an ionic conductivity that is three orders of magnitude higher than the argyrodite Li_6PS_5I (5×10^{-7} S·cm^{-1}).[194,197] Similar to Li_6PS_5I, it may be possible to improve the ionic conductivity of $Li_6B_7S_{13}I$ by either aliovalent substitution,[28] or by ball milling to induce a defect rich nanostructure.[198] Substitution of I^- for Cl^-, Br^-, or even S^{2-} to induce halide disorder may also improve the ionic conductivity.

7.2.5 Tetragonal Polymorph

Akin to the perovskites, the cubic $Li_6B_7S_{13}I$ structure is prone to subtle structural distortions. By varying the synthesis conditions (see experimental section for details), a tetragonal polymorph of $Li_6B_7S_{13}I$ is obtained, where changes in the B-S framework and Li siting distorts the cell to reduce the symmetry. The formation of different phases depending on the preparation method has also been observed in other solid electrolyte materials such as the sodium thiophosphates.[180] The distortion of the cubic symmetry is apparent from the peak splitting in the powder XRD patterns shown in **Figure 7.10A**.

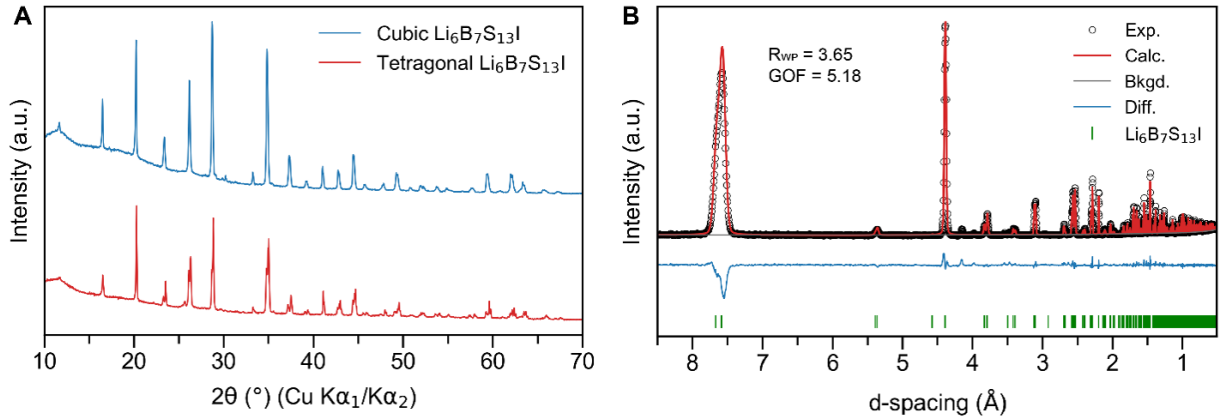

Figure 7.10: A) Powder XRD pattern of cubic and tetragonal $Li_6B_7S_{13}I$. No LiI impurities are present in both samples. B) TOF NPD patterns of tetragonal $Li_6B_7S_{13}I$ at 298 K and the corresponding Rietveld refinement fit.

The new structure was determined using neutron powder diffraction and the data was refined using a model derived from the transformation of the cubic space group F-43c to its tetragonal subgroup I-4c2 (Figure 7.10B). A visual representation of the transformation to

the tetragonal structure is shown in **Figure 7.11** and crystallographic data from refinement of the NPD data is provided in **Table 7.4**.

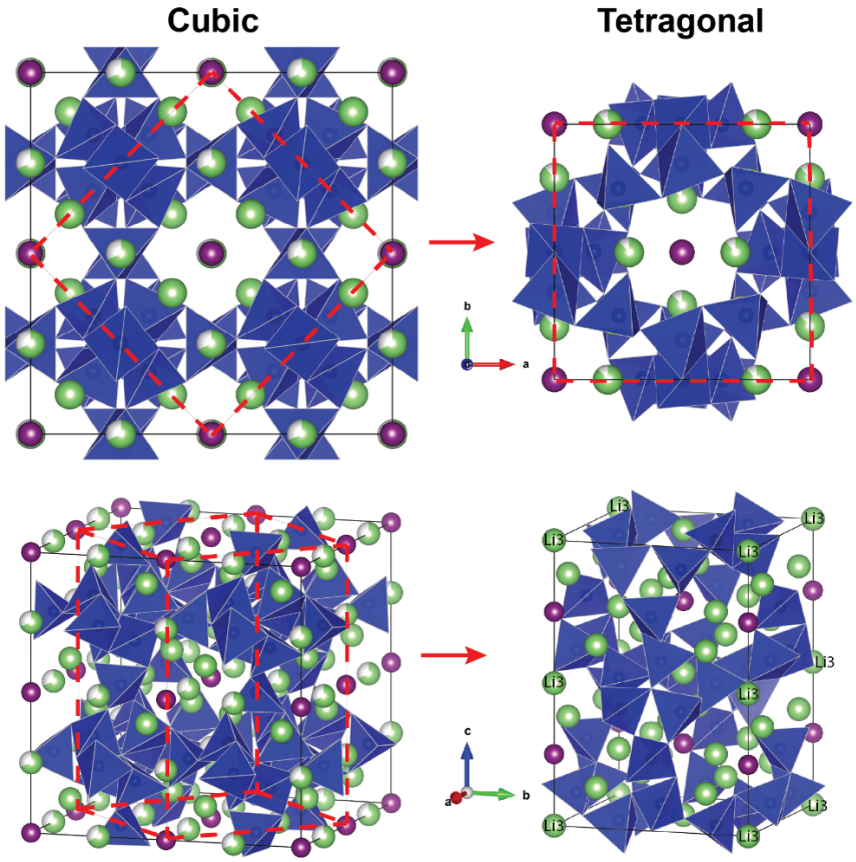

Figure 7.11: Cubic $Li_6B_7S_{13}I$ with lattice parameter a can be represented as a tetragonal cell by the transformation a' = a/$\sqrt{2}$ and c' = a. The origin of the tetragonal unit cell is shifted in the c-direction by ¼.

Orthorhombic distortions were considered as well but did not yield an improved fit over the tetragonal modification. The two boron sites and two lithium sites in the cubic space group should each become three crystallographically distinct sites in the tetragonal structure due to the site splitting. However, Li ordering in the tetragonal structure gives rise to unoccupation of the Li3 (4b) site, a factor that elongates the *c*-axis due to the electrostatic repulsion of neighbouring I^- ions. The resultant Li ordering also impedes conduction in the tetragonal polymorph, reducing the room temperature ionic conductivity to 1.5×10^{-4} S·cm^{-1}, compared to 5×10^{-4} S·cm^{-1} for the cubic modification.

Table 7.4: Atomic coordinates, occupation factor, and isotropic displacement parameters of the tetragonal $Li_6B_7S_{13}I$ obtained from neutron powder diffraction measured at 298 K.

Space Group: *I*-4*c*2, *a* = 10.72640(6) Å, *c* = 15.3355(2) Å, V = 1764.43(3), Z = 4						
Atom	**Wyck. Pos.**	**x**	**y**	**z**	**Occ.**	**U_{eq} (Å^2)**
I1	4a	0	0	0.25	1	0.0180(8)
S1	16i	0.9043(4)	0.3864(4)	0.3201(3)	1	0.0039(4)
S2	16i	0.9214(4)	0.2107(4)	0.4821(2)	1	0.0056(6)
S3	16i	0.1649(4)	0.3060(4)	0.3962(2)	1	0.0039(4)
S4	4d	0	0.5	0.5	1	0.0056(6)
B1	4c	0	0.5	0.25	1	0.0056(5)
B2	8h	0.2492(3)	0.7492(3)	0	1	0.0047(3)
B3	16i	-0.0025(3)	0.34562(11)	0.42168(9)	1	0.0061(2)
Li1	16i	0.7086(6)	0.5079(14)	0.3756(6)	1	0.037(2)
Li2	8e	0.7315(7)	0.7315(7)	0.25	1	0.029(3)
Li3	4b	0	0	0.5	0	-

To confirm that the tetragonal $Li_6B_7S_{13}I$ structure is metastable vis a vis the cubic polymorph, phonon calculations were performed on both materials to determine whether they lie at a local minimum (dynamically stable) or a saddle point (dynamically unstable) on the potential energy surface. Imaginary frequencies are present in the phonon dispersions of the tetragonal structure but not in the cubic structure (see phonon band structures and DOS in **Figure 7.12**), indicating that the cubic structure is dynamically stable and at an energy minimum. The tetragonal structure is likely at a saddle point on the potential energy surface but is presumably stabilized by entropic contributions at finite (non-zero) temperature. This does not mean the tetragonal is more stable than the cubic polymorph at elevated temperatures. The mechanism for the formation of the tetragonal phase is unclear at present and will be explored in the future. The thermodynamic stability for the cubic phase was also evaluated using a convex hull analysis. The convex hull connects phases that are lower in energy than any other phase or linear combination of phases at the respective composition. Thus, it provides a direct measure of the stability as phases that lie on the convex hull are considered thermodynamically stable compounds (energy above hull, E_{hull}, of 0), whereas ones above are metastable or unstable, and a large E_{hull} implies greater

instability of the compound.[199] The E_{hull} of cubic-$Li_6B_7S_{13}I$ is 0 meV/atom, indicating that it is a stable compound. The calculated 0 K Li-B-S-I phase diagram and the pseudo-ternary Li_2S–B_2S_3–LiI phase diagram are shown in **Figure E.2**.

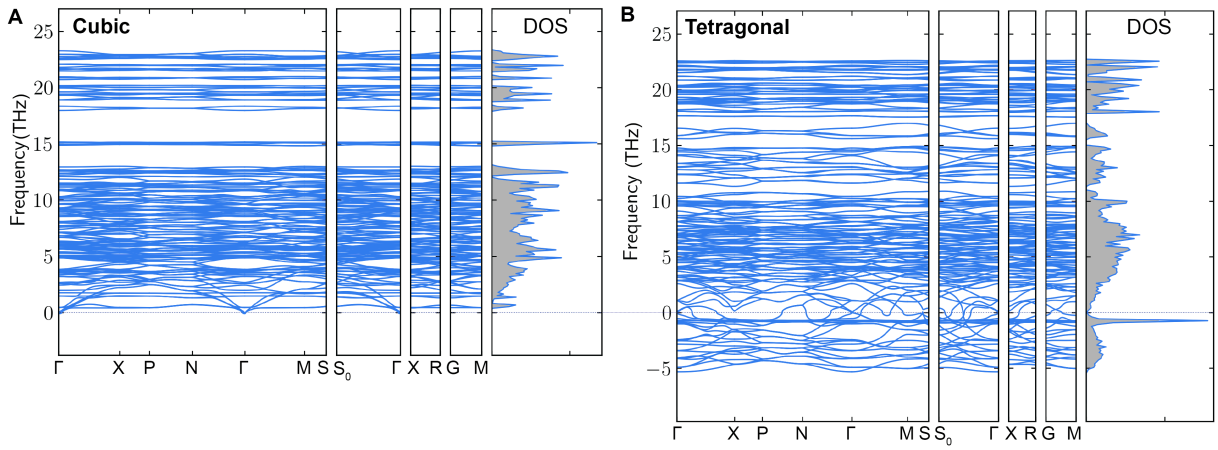

Figure 7.12: Calculated phonon band structure and phonon DOS of A) Cubic and B) Tetragonal $Li_6B_7S_{13}I$.

7.2.6 Electrochemical Stability

The electrochemical stability window of most lithium thiophosphate-based materials tends to be narrow (∼0.3 V).[29] These materials are reduced in contact with lithium metal and undergo oxidation when paired with high-voltage (> 4 V) cathodes. Thiophosphates such as Li_3PS_4, $Li_7P_3S_{11}$, $Li_{10}GeP_2S_{12}$ (LGPS) and Li_6PS_5Cl exhibits oxidative stability up to 2.5 V.[29] Calculations on $Li_6B_7S_{13}I$ show a comparable electrochemical stability window of 1.6-2.1 V vs. Li/Li^+ for $Li_6B_7S_{13}I$ (see **Figure 7.13** for the plot of Li uptake per formula unit), which is verified experimentally by cyclic voltammetry (**Figure 7.14**). A comparable voltage window for the $Li_5B_7S_{13}$ system was recently predicted, although it has been suggested that a passivating layer composed of superionic mixtures of Li-B-S phases can kinetically stabilize the interface up to 4.0 V and down to 1.0 V.[149] Although argyrodites decompose at the lithium metal interface, they form kinetically passivating interface layers composed of electronic and ionically insulating Li_2S, Li_3P, and LiCl in the case of Li_6PS_5Cl.[200] Similar properties for $Li_6B_7S_{13}I$ are expected, where Li_2S and LiI will

form as an interphase layer. The incorporation of nano-sized coating layers could further stabilize both these interfaces.

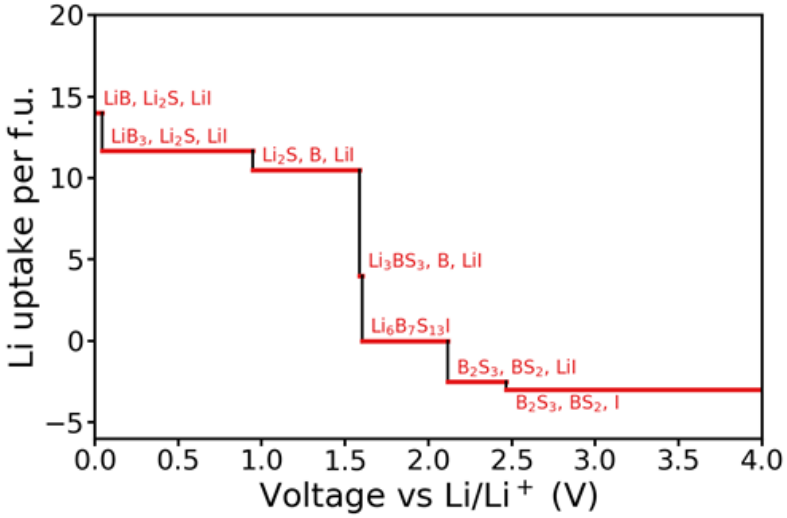

Figure 7.13: Plot of Li uptake per formula unit (f.u.) of $Li_6B_7S_{13}I$ against voltage vs Li/Li^+. Text indicates the predicted phase equilibria at corresponding regions of the profile.

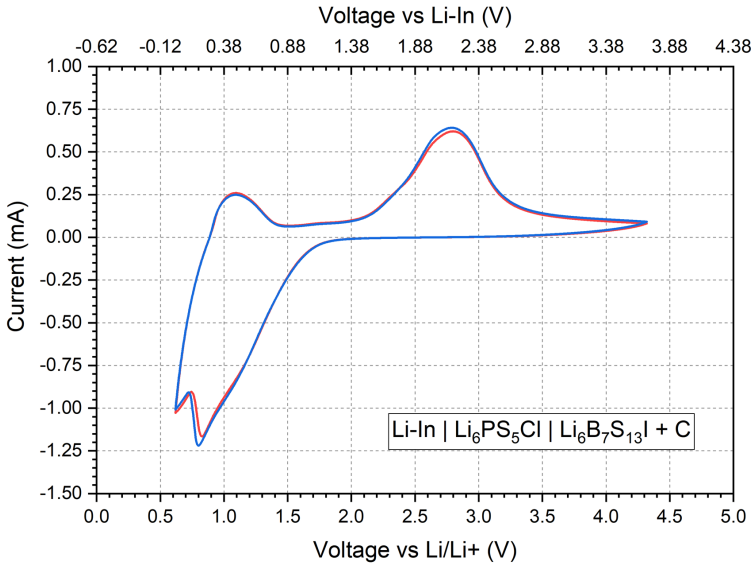

Figure 7.14: Cyclic voltammetry of cubic-$Li_6B_7S_{13}I$ mixed with carbon (Super P) at 25°C, scanned over a potential range of 0 to 3.7 V vs. Li-In (0.62 – 4.32 V vs. Li/Li^+) at scan rate of 1 mV/s.

7.3 Conclusion

This study reveals a new class of ion conductive materials based on $Li_6B_7S_{13}I$, a promising thioborate-based solid electrolyte with a high theoretical ionic conductivity of 5.2×10^{-3} S·cm^{-1}, owing to its partially occupied Li sites in the cubic lattice structure (solved from single-crystal XRD and neutron diffraction). It exhibits an ordered anion arrangement akin to a perovskite framework, with an argyroditelike lithium substructure in which the Li^+ ions form three-dimensional diffusion pathways connected by lithium sites in a cage-like fashion. AIMD simulations verify the highly delocalized Li substructure conducive to fast-ion mobility and determine a low energy barrier of 0.23 eV, close to the experimental value of 0.30 eV. This new class of materials provides an exciting platform for manipulating the conductivity by aliovalent substitution or by inducing anion disorder via changes in composition. Such methods have been remarkably successful in ultimately increasing the conductivity of argryodites such as Li_6PS_5I and Li_6SbS_5I by a factor of 10^4; for example, superionic $Li_{6.6}P_{0.4}Ge_{0.6}S_5I$ (1.8×10^{-2} S·cm^{-1})[28] and $Li_{6.6}Si_{0.6}Sb_{0.4}S_5I$ (2.4×10^{-2} S·cm^{-1}).[201]

This work also highlights the importance of controlling (i.e., minimizing) the grain boundary resistance. The grain boundary resistance of sulfides is typically assumed to have a negligible effect on the ion conductivity because of their ductility and can be lowered by sintering for a clean interface; however, this is not the case when amorphous impurities are present. Here, the presence of even minor amounts of a glassy phase at the interface between grains can strongly influence the total ion conductivity, and likely underlies the lower experimental total conductivity of 5×10^{-4} S·cm^{-1} as indicated by EIS measurements of $Li_6B_7S_{13}I$ that show high grain boundary impedance. The necessity to carry out low-temperature EIS measurements on superionic conductors to deconvolute the bulk and grain boundary components is emphasized, since the high conductivity typically prevents their resolution at room temperature owing to frequency analyzer limits.

This is especially true when searching for new materials where the phase space is not well mapped out. Differences in ion conductivity of an order of magnitude between

theory and experiment are often the case for metastable glass ceramics such as $Li_7P_3S_{11}$, where the presence of less conductive glassy phases in the grain boundaries formed as a result of incongruent melting are a negative influence: for example, AIMD simulations predict the inherent theoretical conductivity of $Li_7P_3S_{11}$ is 5.7×10^{-2} S·cm^{-1} whereas the measured values are on the order of 1.3×10^{-3} S·cm^{-1}.[179] In contrast, for congruent melting ceramic materials that form single-phase crystalline compositions such as $Li_{10}GeP_2S_{12}$ or $Na_{11}Sn_2PS_{12}$, theory and experimental conductivity values are similar. For the latter, AIMD simulations predict 2.4×10^{-3} S·cm^{-1} in good agreement with the experimental value of 1.4×10^{-3} S·cm^{-1} and for the former, theory predicts 9×10^{-3} S·cm^{-1} whereas the experimental value is slightly higher at 1.2×10^{-2} S·cm^{-1}.[105,202]

The synthesis of $Li_6B_7S_{13}I$ relies on two factors: achieving intimate mixing of the metastable supertetrahedral precursor with LiI and taking advantage of the solid-liquid interface formed by the molten halide salt. While the precise reaction mechanism is not yet understood, dissolution of the adamantanoid into the molten salt and subsequent crystallization of the cubic phase from the melt can be ruled out because the fraction of LiI is too low. This reaction may occur via a quasi solid-state conversion process at 500°C – at the LiI liquid interface - that is greatly aided by high diffusivity of lithium (and iodine) ions in the solid-state. The latter would facilitate rearrangement of the adamantanoid framework to form the boracite. Furthermore, by subtle variations in the second step of the synthesis, a Li-ordered tetragonal polymorph of $Li_6B_7S_{13}I$ can be formed, which phonon calculations determined to be dynamically unstable on the potential energy surface. Thus, synthetic control is required to form cubic $Li_6B_7S_{13}I$.

Future studies of this new thioboracite material class will aim at the discovery of related isostructural, and ionically conductive materials that will provide a novel platform to study and build on the fundamental understanding of ion-conduction.

7.4 Experimental Procedures

7.4.1 Preparation of $Li_6B_7S_{13}I$

Stoichiometric amounts of Li_2S (Sigma Aldrich, 99.98%), ^{11}B (Cambridge Isotope Labs, 99%), S (recrystallized from hot toluene), and LiI (Sigma Aldrich, >99.9%) with a total mass of 500 mg were ground together. All handling of powders was carried out in an Ar-filled glovebox. The precursor mixture was pelletized and supported in a glassy carbon crucible, which was placed in a quartz tube. The quartz tubes were sealed under vacuum and placed vertically in a furnace. The sample was heated following the same procedure to synthesize $Li_{7.5}B_{10}S_{18}I_{1.5}$.[187] After heat treatment, the powder was ground and pelletized again. The tube was heated up to 500°C at a heating rate of 1°C/minute and held for 36 hours, followed by cooling to room temperature at a rate of 0.5°C/minute. The resulting powder was ground and then used for subsequent analysis. The final product was gently separated to pick out crystals suitable for single-crystal X-ray diffraction.

The tetragonal variant was prepared similarly by upscaling the total powder quantity to 2 grams. The larger mass may lead to slower heat transfer across the material in the crucible, altering the cooling rate so that the tetragonal polymorph is stabilized, although the exact reason for these conditions favoring the tetragonal phase is not yet well understood.

7.4.2 Preparation of $Li_5B_7S_{13}$

Following the same procedure above, stoichiometric amounts of Li_2S, ^{11}B, and S were ground together. The tube was heated up to 550°C at 1°C/minute and held for 3 hours, cooled to 500°C at 0.4°C/minute and held for 100 hours, and then finally cooled to room temperature at 0.25°C/minute. The resulting material was a multi-phase mixture of $Li_5B_7S_{13}$, $Li_{6+2x}B_{10}S_{18}S_x$, Li_2S, and Li_3BS_3. The powder was gently separated to pick out single crystals of $Li_5B_7S_{13}$.

7.4.3 Powder X-ray Diffraction

Laboratory X-ray powder diffraction data was collected on a Panalytical Empyrean diffractometer outfitted with a PIXcel two-dimensional detector using Cu-Kα radiation. The ground samples were spread on a zero-background Si holder. The surface of the Si was covered with a thin layer of vacuum grease over which the powder was spread, and then sealed with a Kapton film and vacuum grease to prevent any atmospheric exposure during measurement. The measurement was recorded in Bragg-Brentano geometry.

7.4.4 Single-crystal X-ray Diffraction and Structure Resolution

Colorless single crystals with dimensions of $0.01\times0.04\times0.08$ mm^3 were covered by Paratone-N oil, selected under an optical microscope, and scanned to determine their quality. The data was collected on a diffractometer (BRUKER KAPPA equipped with a SMART APEX II CCD) using graphite-monochromated Mo-Kα radiation. A flow of liquid nitrogen using an OXFORD Cryostream controller 700 at 280K was used to prevent reactivity of the crystals with air and moisture. The data was collected by scanning ω and ϕ of 0.36°in a few groups of frames at different ϕ angles with an exposure time of 50 and 30 seconds per frame for $Li_6B_7S_{13}I$ and $Li_5B_7S_{13}$ respectively. The data was corrected for Lorentz and polarization effects. The absorption corrections were carried out by the multi-scan method using SADABS since the crystals do not have clear faces. The Cell_now software was used to check for potential twinning. The structures were solved using direct method to locate the positions of B, S, and I atoms. After locating the B-S framework and the heavy iodide sites, first, their atomic positions were anisotropically refined using the least squares method (SHELXTL package), and then the Li positions were located from the electron density in the Fourier map (Li-S bonds were very similar in length to those found in binary and ternary Li sulfides). Li site occupancies were then anisotropically refined. The refinements converged to good residual values R1 and wR2. No constraints were used during the refinements.

For $Li_6B_7S_{13}I$, a lower symmetry refinement was carried out in the tetragonal space

group I-4c2 (No. 120), which showed lead to an unstable refinement and negative atomic displacement parameters on the boron atoms, confirming that the high-symmetry cubic space group is correct for the single-crystal measurement.

7.4.5 Neutron Powder Diffraction (NPD) and Refinement

^{11}B was used as a precursor in the synthesis because of the large absorption cross-section of natural B containing ^{10}B. Powder samples were loaded into a 6 mm vanadium can under He atmosphere with a copper gasket and aluminum lid. Samples were collected on POWGEN (Beamline 1B) at the Spallation Neutron Source (SNS) in Oak Ridge National Laboratory with a center wavelength of 1.5 Å, which can provide high resolution data up to $d_{max} \sim$ Å (and $Q_{max} \sim$12 Å^{-1}). The sample was measured at a temperature of 300 K. The resulting diffraction patterns were refined by the Rietveld method using TOPAS version 6 (Bruker – AXS). NIST Si 640d was used as an external standard for instrument calibration. Time-of-flight (TOF) data was converted to d-spacing data using the modified second-order polynomial TOF = ZERO + DIFC*d + DIFA*d2 +DIFB/d, where ZERO is a constant, DIFC is the diffractometer constant, DIFA and DIFB are empirical terms to correct the sample displacement and absorption caused peak shift.[174] ZERO and DIFC were determined from the refinement of the standard, while DIFA and DIFB were allowed to vary to account for the sample displacements/absorption. To describe the peak profile, a back-to-back exponential function convoluted with a symmetrical pseudo-Voigt function were used.

7.4.6 Ionic Conductivity and Activation Energy Measurements

For activation energy measurements, 100-200 mg of powder was pressed between two titanium rods in a custom-made 10 mm diameter cell with a hydraulic press at 3 tons in an Ar-filled glovebox. Electrochemical impedance spectroscopy (EIS) was measured from 7 MHz to 100 mHz with an amplitude of 100 mV using a Bio-logic MTZ-35 impedance analyzer. The measurements were carried out in the temperature range of 25°C to 60°C.

7.4.7 Cyclic Voltammetry

Handling and pressing of all powders were performed in an argon-filled glovebox. Approximately 60 mg of argyrodite (Li_6PS_5Cl) was pressed between two titanium rods in a 10 mm diameter cell with a hydraulic press at 2 tons. Cubic-$Li_6B_7S_{13}I$ was ground with dried carbon (Super P) in a 9:1 mass ratio and 12 mg of the composite was pressed on top at 2 tons. A 10 mm diameter In foil was layered with an 8 mm diameter Li foil to form the Li-In negative electrode on the other side of the argyrodite layer. The cyclic voltammogram was measured with a scan rate of 1 mV/s between 0 to 3.7 V vs Li-In (0.62 – 4.32 V vs. Li/Li^+) at room temperature (25°C).

7.4.8 Density Functional Theory (DFT) Calculations

DFT calculations were carried out using the Vienna *ab initio* simulation package (VASP)[48] using the projected augmented wave (PAW) approach.[203] The Perdew-Burke-Ernzerhof (PBE) generalized gradient approximation (GGA) was used for the exchange-correlation functional.[204] The Python Materials Genomics (pymatgen)[80] library and the pymatgen-diffusion add-on package[199] were used for some of the pre and post-processing of input files. Due to the small amount of lithium disorder in the crystal structure, enumeration of symmetrically distinct atomic configurations of the primitive cell was carried out using pymatgen's wrapper to Hart and Forcade's enumlib.[205] The two unique structures that were derived were fully relaxed by employing DFT calculations to calculate their energies and identify the lowest energy ordering. Geometry optimization was performed on the primitive cell (54 atoms) with a plane wave energy cutoff set to 520 eV and a k-point density of approximately 1000/atom. The total energy was converged to 10^{-6} eV.

7.4.9 Phase and Electrochemical Stability Calculation

Phase stability of cubic-$Li_6B_7S_{13}I$ was calculated by building a 0 K Li-B-S-I phase diagram. The thermodynamic stability was predicted by constructing the convex hull of the DFT

total energy for each phase. If a phase is not on the hull it can be quantified by its energy above the hull (E_{hull}) - the driving force for decomposition to the ground states.

A grand potential phase diagram was made to estimate the phase equilibria at the solid electrolyte/electrode interface.[93,206] The SE/anode and SE/cathode interfaces are approximated as open systems (assuming Li^+ is the only mobile species) at $\mu_{Li} = \mu^0_{Li}$ and $\mu_{Li} = \mu^0_{Li} - e\Delta V$, respectively, where μ^0_{Li} is the chemical potential of Li metal, e is the elementary charge, and ΔV is the voltage of the charged cathode versus Li/Li^+. The thermodynamic potential at 0 K is the lithium grand potential; $\phi = E - \mu_{Li}N_{Li}$, where E is the enthalpy per formula unit (approximately equal to the computed DFT energy), and N_{Li} is the number of Li atoms per formula unit for a specific phase. The phase equilibria can be predicted as the composition changes with lithium chemical potential by using a similar phase diagram with ϕ instead of E. To speed up the computation, the Materials Project (MP)[207] open database was used for the computed energies of all known phases in the Li-B-S-I phase space. The phase diagram can then be constructed using the phase_diagram module in pymatgen. The calculation parameters detailed earlier were chosen accordingly to match those used in the MP for compatibility.

7.4.10 *Ab-initio* molecular dynamics (AIMD) simulations

AIMD simulations were performed in the canonical (NVT) ensemble with a Nosé-Hoover thermostat.[208,209] Cell parameters were fixed at the values obtained from the DFT structural optimization step at 0 K. The initial temperature was set to 100 K after static calculations and the samples were first heated up to the targeted temperature (600, 675, 750, 900 K) by velocity scaling for 2 ps, and then equilibrated at the desired temperature for 5 ps. The MD simulations at each temperature were carried out for 100 ps with a timestep of 1 fs. Non-spin polarized calculations with a plane-wave energy cutoff of 520 eV and a Γ-centered 1×1×1 k-point grid was used.

From an AIMD simulation the diffusivity can be extracted using the relation:

$$D = \frac{1}{2dt} \left\langle [\Delta \mathbf{r}(t)]^2 \right\rangle$$

Where d is the dimensionality factor (3 for three-dimensional crystal structures). $\left\langle [\Delta r(t)]^2 \right\rangle$ is the average mean square displacement (MSD) over a time duration t and is given as:

$$\left\langle [\Delta \mathbf{r}(t)]^2 \right\rangle = \frac{1}{N} \sum_{i=1}^{N} \left\langle [\mathbf{r_i}(t + t_0)]^2 - [\mathbf{r_i}(t_0)]^2 \right\rangle$$

Which represents the average displacement of Li atoms over a time t. N is the number of lithium ions, $\boldsymbol{r_i}$(t) is the displacement of an individual Li atom at time t, and t_o is the initial time.

The diffusivity is obtained by performing a linear fit of the MSD vs $2dt$ plot and follows the Arrhenius relation:

$$D = D_o e^{-E_a/k_B T}$$

where E_a is the activation energy, D_o is the diffusivity at infinite temperature, k_B is the Boltzmann constant, and T is the temperature. AIMD simulations are carried out at several temperatures, and the activation energy is extracted from a linear fit of an Arrhenius plot of $\ln(D_o)$ vs. $1/T$.

The trajectories from the simulations are analyzed and the probability density function is used to determine the low energy (high probability) sites in the crystal structure and the migration pathways. The probability density function can be defined in a uniform spatial grid and is determined by averaging the number of lithium ions at each grid point for a given time scale.

7.4.11 Phonon Calculations

Phonon dispersion calculations were performed using the VASP implementation of density functional perturbation theory (DFPT) and the PHONOPY software package.[210] For the

structure relaxation, the same parameters listed above were used. The DFPT was performed with a convergence criterion for the total energy set to 10^{-8} eV. Phonon calculations were performed on the primitive cell, with lattice vectors larger than 10 Å. The high-symmetry band paths in the Brillouin zone of the crystal structures were determined using the SeeK-path tool implemented in python.[211]

Chapter 8

Summary and Outlook

This thesis presents many different solid electrolytes for all-solid-state batteries with a focus on sulfide-based materials. This includes both crystalline and amorphous solid electrolyte materials. Experimental and computational investigations into the structure of these materials is used to identify the factors that dictate fast ion transport. Depending on the structural framework, different approaches can be used to tune or improve the conductivity.

The archetypal thiophosphate material, Li_3PS_4, was studied using *in-situ* variable temperature neutron powder diffraction in chapter 3. Li_3PS_4 has been widely studied and used as starting point to develop many other ion conductors, however, an in-depth understanding of the lithium substructure in the three polymorphs had been lacking. Using MEMs and BVSE techniques with NPD to analyze the structure, it was discovered that the high-temperature α-polymorph has superior three-dimensional Li^+ diffusion pathways compared to its β and γ polymorphs, which leads to a favourable energy landscape for Li^+ migration. This is correlated to the bcc anion framework of the α-phase that favours the formation of edge and face-sharing Li tetrahedra. Additionally, the highly conductive nanoporous stabilized β-Li_3PS_4 and Si-doped $Li_{3.25}Si_{0.25}P_{0.75}S_4$ phases were studied. It was found that a significant amount of hydrogen containing amorphous component was present in the nanoporous material. Heating resulted in the removal of the hydrogen containing

component and the β-phase is no longer maintained, transforming back to the poorly conducting γ-polymorph when cooled. Thus, the presence of this amorphous component is what stabilizes the nanoporous β phase at room-temperature. The Si-substituted variant on the other hand results in stabilization of the β structure by inducing entropic disorder of the lithium, and the phase transition to an analogous α-polymorph upon heating is suppressed.

Building on the concepts pertaining to the Li_3PS_4 material, a new thiophosphate, $Li_{1+2x}Zn_{1-x}PS_4$, was synthesized and is presented in chapter 4. This compound stems from a solid solution between a mixture of $LiZnPS_4$ and Li_3PS_4. It had previously been predicted by computational methods to have high ionic conductivity based on its bcc anion framework. The crystal structure was studied using synchrotron XRD and NPD, which allowed for clear determination of interstitial lithium defects. The introduction of Li interstitials was found to induce Li/Zn site disordering, and significantly increase the ionic conductivity. However, the increased conductivity comes at the cost of an increased degree of metastability, ultimately making the very lithium rich phases difficult to stabilize at room temperature. Despite this challenge, a glass-ceramic variant of the lithium rich $Li_{2.5}Zn_{0.25}PS_4$ phase can be formed with ion conductivity approaching 10^{-3} S·cm^{-1}.

The subsequent chapters turn the focus away from thiophosphates, to a relatively underexplored class of sulfides, thioborates. In chapter 5, a different approach focusing of glassy solid electrolytes was undertaken. Glasses in general are advantageous because they can be processed into grain boundary and defect free monolithic sheets, which is ideal to prevent dendrite formation through the electrolyte layer. A new amorphous thioborosilicate lithium-ion conductor (termed 'LIBOSS') was synthesized by adding a SiO_2 glass former to the Li_2S-B_2S_3-LiI thioborate mixture. This oxysulfide glass has unique advantages - it is truly an oxysulfide ion conductor with high ionic conductivities ($>1\times10^{-3}$ S·cm^{-1}) and a very high oxygen:sulfur content of 1:1, which improves the air stability compared to pure sulfide materials such as Li_3PS_4. The optimal composition has an ionic conductivity of 2.1×10^{-3} S·cm^{-1} and is one of the fastest amorphous lithium-ion conductors to date. The structure of the glass was also studied using high-resolution MAS-NMR to understand

what factors drive the high-level of ion transport. It was found that an optimum amount of fragmented units must be achieved, which appears to be critical for increasing the number of mobile lithium carriers in the glass. An all-solid-state battery using the LIBOSS glass electrolyte with a TiS_2 cathode shows excellent cycling performance with near theoretical capacity for over 130 cycles. The LIBOSS glass is a promising material to explore for both developing the understanding of transport in glasses and for practical application. This concept can extend to a broader scope that includes alternative halides and glass forming oxides, creating a new avenue in the development of solid electrolytes for all-solid-state batteries.

The topic of thioborates is continued in chapter 6 and 7, but the focus is shifted to crystalline materials. In chapter 6, a new lithium-ion conductor, $Li_{7.5}B_{10}S_{18}X_{1.5}$ (X = Cl, Br, I), with a unique superadamantanoid structure is presented. The materials were studied using single-crystal XRD and NPD. $Li_{7.5}B_{10}S_{18}X_{1.5}$ forms an ordered supertetrahedral framework with a highly disordered "glassy salt" sublattice within the void spaces. Neutron PDF was used to study the local structure of this disordered sublattice, where clear local structure ordering of the halide is present within the channels. The weak bonding of the anion-cation pairs and the highly disordered sublattice leads to overall fast-ion conduction, which can be effectively increased by modifying the polarizability of the anion sublattice. The lithium-ion conductivity is increased up to 1.4×10^{-3} S·cm^{-1} by substituting Cl^- or Br^- for the more polarizable I^- anion. A softer sublattice consequently leads to a decrease in the activation energy, which in turn leads to an increase in ionic conductivity.

Continuing the exploration of these superadamantanoid phases, a new thermodynamically stable thioboracite material was discovered. In chapter 7, a promising thioborate-based solid electrolyte is discovered by using a quasi solid-state conversion process, which facilitates the rearrangement of the adamantanoid framework. $Li_6B_7S_{13}I$ is the first material with a thio-boracite structure, which crystallizes in a cubic space group, resulting in a perovskite topology and argyrodite-like lithium substructure that leads to a high theoretical lithium ion conductivity of 5.2×10^{-3} S·cm^{-1}. The fast Li^+ transport is explored using both

computational (DFT and AIMD) and experimental techniques (diffraction and EIS). By altering the synthesis slightly, a less stable (confirmed by phonon calculations) and less conductive Li-ordered tetragonal polymorph of $Li_6B_7S_{13}I$ can be formed. The importance of controlling (i.e., minimizing) the grain boundary resistance is also highlighted, which typically for sulfides are assumed to be negligible, but is shown here to be detrimental when amorphous impurities reside at the interface. This new class of materials provides an exciting platform for 1) manipulating the conductivity by aliovalent substitution or by inducing anion disorder via changes in composition and 2) studying and building on the fundamental understanding of ion-conduction.

The results of this thesis present some promising avenues for the development of solid electrolytes and are important to understand some of the factors that govern ion transport. These new classes of materials as well as a fundamental understanding of their structures and the ion transport within them will hopefully lead to the development of many new and improved fast-ion conductors. A solid electrolyte for commercial application should ideally be cost-effective and easily processed at scale. The electrolytes presented here use relatively cheap and abundant elements (e.g. sulfides and oxides of B, Si, P, etc.), although it remains to be seen if sulfide based materials can be processed cheaply at scale. Thus, research into alternate synthesis techniques and up-scaling is required. Amorphous electrolytes such as the ones presented in this thesis may be a strong candidate for large scale production because of the large glass manufacturing industry and the technical knowledge behind synthesizing thin and defect free sheets of glasses.

It is an insurmountable challenge to create a solid electrolyte that can address every single aspect of the battery - the positive electrode, the separating electrolyte, and the anode. The solution to this problem may be to use several different electrolytes: one that is kinetically stable with Li metal, a highly conductive material as the separator, and a high voltage stable material that can be used in the positive electrode. Future work will have to focus on the discovery of high-voltage electrolytes to pair with the cathode and kinetically stable electrolytes to pair with the anode. Sulfides in contact with high-voltage

cathodes tend to react and become ionic and electronic insulators, which passivate the interface. Thus, alternate chemistries such as oxide and halide solid electrolytes need to be explored that may be able to mitigate these issues. From the existing set of materials in the literature, higher voltage stable materials tend to have a less polarizable sublattice and may not be as ionically conductive as their sulfide counterparts. One way to mitigate this issue is to process these high-voltage stable electrolytes into thin nanometer coating layers on the surface of the cathode particles to act as a protective layer. Then, a sulfide electrolytes with lower stability but higher ion conductivity can be used in the positive electrode.

Finally, engineering the integration of these solid electrolytes into multi-layer stack cells with higher capacity is another crucial target for commercialization. Industry is already pursuing solid-state batteries and tackling these problems with very ambitious goals and timelines, where some automotive manufactures have announced commercial solid-state cells by 2022. Regardless of what stage of development they are in, solid-state batteries overall can benefit from improved solid electrolyte materials that are more intrinsically electrochemically and chemically stable and more ionically conductive. There is huge potential for solid-state batteries to help meet global energy demands and enable renewable energy sources, but a combination of creating the right materials and engineering to scale the manufacturing in a cost-effective manner is required to successfully commercialize this technology.

References

[1] M. S. Whittingham, "Electrical energy storage and intercalation chemistry," *Science*, vol. 192, no. 4244, pp. 1126–1127, 1976.

[2] K. Mizushima, P. C. Jones, P. J. Wiseman, and J. B. Goodenough, "Li_xCoO_2 ($0 < x < 1$): A new cathode material for batteries of high energy density," *Materials Research Bulletin*, vol. 15, no. 6, pp. 783–789, 1980.

[3] A. Yoshino, "The birth of the lithium-ion battery," *Angewandte Chemie*, vol. 51, no. 24, pp. 5798–5800, 2012.

[4] M. Li, J. Lu, Z. Chen, and K. Amine, "30 Years of Lithium-Ion Batteries," *Advanced Materials*, vol. 30, no. 33, p. 1800561, 2018.

[5] W. Li, E. M. Erickson, and A. Manthiram, "High-nickel layered oxide cathodes for lithium-based automotive batteries," *Nature Energy*, vol. 5, no. 1, pp. 26–34, 2020.

[6] K. M. Abraham, "Prospects and Limits of Energy Storage in Batteries," *Journal of Physical Chemistry Letters*, vol. 6, no. 5, pp. 830–844, 2015.

[7] F. Wu, J. Maier, and Y. Yu, "Guidelines and trends for next-generation rechargeable lithium and lithium-ion batteries," *Chemical Society Reviews*, vol. 49, no. 5, pp. 1569–1614, 2020.

[8] D. Andre, S.-J. Kim, P. Lamp, S. F. Lux, F. Maglia, O. Paschos, and B. Stiaszny, "Future generations of cathode materials: an automotive industry perspective," *Journal of Materials Chemistry A*, vol. 3, no. 13, pp. 6709–6732, 2015.

[9] A. Varzi, R. Raccichini, S. Passerini, and B. Scrosati, "Challenges and prospects of the role of solid electrolytes in the revitalization of lithium metal batteries," *Journal of Materials Chemistry A*, vol. 4, no. 44, pp. 17251–17259, 2016.

[10] Y.-K. Sun, "Promising All-Solid-State Batteries for Future Electric Vehicles," *ACS Energy Letters*, vol. 5, no. 10, pp. 3221–3223, 2020.

[11] Y. Yung-Fang Yu and J. T. Kummer, "Ion exchange properties of and rates of ionic diffusion in β-alumina," *Journal of Inorganic and Nuclear Chemistry*, vol. 29, no. 9, pp. 2453–2475, 1967.

[12] B. Knutz and S. Skaarup, "Cycling of $Li/Li_3N/TiS_2$ solid state cells," *Solid State Ionics*, vol. 9-10, pp. 371–374, 1983.

[13] K. Kanehori, K. Matsumoto, K. Miyauchi, and T. Kudo, "Thin film solid electrolyte and its application to secondary lithium cell," *Solid State Ionics*, vol. 9-10, pp. 1445–1448, 1983.

[14] D. E. Fenton, "Complexes of alkali metal ions with poly (ethylene oxide)," *Polymer*, vol. 14, p. 589, 1973.

[15] J. B. Bates, N. J. Dudney, G. R. Gruzalski, R. A. Zuhr, A. Choudhury, C. F. Luck, and J. D. Robertson, "Electrical-Properties of Amorphous Lithium Electrolyte Thin-Films," *Solid State Ionics*, vol. 53, pp. 647–654, 1992.

[16] R. Chen, Q. Li, X. Yu, L. Chen, and H. Li, "Approaching Practically Accessible Solid-State Batteries: Stability Issues Related to Solid Electrolytes and Interfaces," *Chemical Reviews*, vol. 120, no. 14, pp. 6820–6877, 2020.

[17] L. Xu, S. Tang, Y. Cheng, K. Wang, J. Liang, C. Liu, Y.-C. Cao, F. Wei, and L. Mai, "Interfaces in Solid-State Lithium Batteries," *Joule*, vol. 2, no. 10, pp. 1991–2015, 2018.

[18] A. Banerjee, X. Wang, C. Fang, E. A. Wu, and Y. S. Meng, "Interfaces and Interphases in All-Solid-State Batteries with Inorganic Solid Electrolytes," *Chemical Reviews*, vol. 120, no. 14, pp. 6878–6933, 2020.

[19] D. Y. Oh, Y. J. Nam, K. H. Park, S. H. Jung, S.-J. Cho, Y. K. Kim, Y.-G. Lee, S.-Y. Lee, and Y. S. Jung, "Excellent Compatibility of Solvate Ionic Liquids with Sulfide Solid Electrolytes: Toward Favorable Ionic Contacts in Bulk-Type All-Solid-State Lithium-Ion Batteries," *Advanced Energy Materials*, vol. 5, no. 22, p. 1500865, 2015.

[20] H. Aono, E. Sugimoto, Y. Sadaoka, N. Imanaka, and G. Adachi, "Ionic Conductivity of the Lithium Titanium Phosphate ($Li_{1+x}M_xTi_{2-x}(PO_4)_3$, M= Al, Sc, Y, and La) Systems," *Journal of The Electrochemical Society*, vol. 136, no. 2, pp. 590–591, 1989.

[21] M. Itoh, Y. Inaguma, W. Jung, L. Chen, and T. Nakamura, "High lithium ion conductivity in the perovskite-type compounds $Ln_{12}Li_{12}TiO_3$ (Ln=La,Pr,Nd,Sm)," *Solid State Ionics*, vol. 70-71, pp. 203–207, 1994.

[22] R. Murugan, V. Thangadurai, and W. Weppner, "Fast lithium ion conduction in garnet-type $Li_7La_3Zr_2O_{12}$," *Angewandte Chemie International Edition*, vol. 46, no. 41, pp. 7778–7781, 2007.

[23] S. Abouali, C.-H. Yim, A. Merati, Y. Abu-Lebdeh, and V. Thangadurai, "Garnet-Based Solid-State Li Batteries: From Materials Design to Battery Architecture," *ACS Energy Letters*, vol. 6, no. 5, pp. 1920–1941, 2021.

[24] N. Kamaya, K. Homma, Y. Yamakawa, M. Hirayama, R. Kanno, M. Yonemura, T. Kamiyama, Y. Kato, S. Hama, K. Kawamoto, and A. Mitsui, "A lithium superionic conductor," *Nature Materials*, vol. 10, no. 9, pp. 682–686, 2011.

[25] A. Hayashi, K. Minami, S. Ujiie, and M. Tatsumisago, "Preparation and ionic conductivity of $Li_7P_3S_{11-z}$ glass-ceramic electrolytes," *Journal of Non-Crystalline Solids*, vol. 356, no. 44-49, pp. 2670–2673, 2010.

[26] Y. Kato, S. Hori, T. Saito, K. Suzuki, M. Hirayama, A. Mitsui, M. Yonemura, H. Iba, and R. Kanno, "High-power all-solid-state batteries using sulfide superionic conductors," *Nature Energy*, vol. 1, no. 4, p. 16030, 2016.

[27] M. A. Kraft, S. P. Culver, M. Calderon, F. Bocher, T. Krauskopf, A. Senyshyn, C. Dietrich, A. Zevalkink, J. Janek, and W. G. Zeier, "Influence of Lattice Polarizability on the Ionic Conductivity in the Lithium Superionic Argyrodites Li_6PS_5X (X = Cl, Br, I)," *Journal of the American Chemical Society*, vol. 139, no. 31, pp. 10909–10918, 2017.

[28] M. A. Kraft, S. Ohno, T. Zinkevich, R. Koerver, S. P. Culver, T. Fuchs, A. Senyshyn, S. Indris, B. J. Morgan, and W. G. Zeier, "Inducing High Ionic Conductivity in the Lithium Superionic Argyrodites $Li_{6+x}P_{1-x}Ge_xS_5I$ for All-Solid-State Batteries," *Journal of the American Chemical Society*, vol. 140, no. 47, pp. 16330–16339, 2018.

[29] W. D. Richards, L. J. Miara, Y. Wang, J. C. Kim, and G. Ceder, "Interface Stability in Solid-State Batteries," *Chemistry of Materials*, vol. 28, no. 1, pp. 266–273, 2015.

[30] S. Ohno, A. Banik, G. F. Dewald, M. A. Kraft, T. Krauskopf, N. Minafra, P. Till, M. Weiss, and W. G. Zeier, "Materials design of ionic conductors for solid state batteries," *Progress in Energy*, vol. 2, no. 2, p. 022001, 2020.

[31] M. Tatsumisago, N. Machida, and T. Minami, "Mixed Anion Effect in Conductivity of Rapidly Quenched Li_4SiO_4-Li_3BO_3 Glasses," *Journal of the Ceramic Association, Japan*, vol. 95, no. 1098, pp. 197–201, 1987.

[32] X. H. Yu, J. B. Bates, G. E. Jellison, and F. X. Hart, "A stable thin-film lithium electrolyte: Lithium phosphorus oxynitride," *Journal of the Electrochemical Society*, vol. 144, no. 2, pp. 524–532, 1997.

[33] Z. Zhang and J. Kennedy, "Synthesis and characterization of the B_2S_3-Li_2S, the P_2S_5-Li_2S and the B_2S_3-P_2S_5-Li_2S glass systems," *Solid State Ionics*, vol. 38, no. 3-4, pp. 217–224, 1990.

[34] L. Porz, T. Swamy, B. W. Sheldon, D. Rettenwander, T. Frömling, H. L. Thaman, S. Berendts, R. Uecker, W. C. Carter, and Y.-M. Chiang, "Mechanism of Lithium Metal Penetration through Inorganic Solid Electrolytes," *Advanced Energy Materials*, vol. 7, no. 20, p. 1701003, 2017.

[35] A. Hayashi, K. Noi, A. Sakuda, and M. Tatsumisago, "Superionic glass-ceramic electrolytes for room-temperature rechargeable sodium batteries," *Nature Communications*, vol. 3, p. 856, 2012.

[36] T. Krauskopf, S. P. Culver, and W. G. Zeier, "Local Tetragonal Structure of the Cubic Superionic Conductor Na_3PS_4," *Inorganic Chemistry*, vol. 57, no. 8, pp. 4739–4744, 2018.

[37] M. Ghidiu, J. Ruhl, S. P. Culver, and W. G. Zeier, "Solution-based synthesis of lithium thiophosphate superionic conductors for solid-state batteries: a chemistry perspective," *Journal of Materials Chemistry A*, vol. 7, no. 30, pp. 17735–17753, 2019.

[38] T. Krauskopf, S. Muy, S. P. Culver, S. Ohno, O. Delaire, Y. Shao-Horn, and W. G. Zeier, "Comparing the Descriptors for Investigating the Influence of Lattice Dynamics on Ionic Transport Using the Superionic Conductor $Na_3PS_{4-x}Se_x$," *Journal of the American Chemical Society*, vol. 140, no. 43, pp. 14464–14473, 2018.

[39] S. Muy, J. C. Bachman, L. Giordano, H.-H. Chang, D. L. Abernathy, D. Bansal, O. Delaire, S. Hori, R. Kanno, F. Maglia, S. Lupart, P. Lamp, and Y. Shao-Horn, "Tuning mobility and stability of lithium ion conductors based on lattice dynamics," *Energy & Environmental Science*, vol. 11, no. 4, pp. 850–859, 2018.

[40] A. Yelon, B. Movaghar, and H. M. Branz, "Origin and consequences of the compensation (Meyer-Neldel) law," *Physical Review B*, vol. 46, no. 19, pp. 12244–12250, 1992.

[41] S. Muy, J. C. Bachman, H.-H. Chang, L. Giordano, F. Maglia, S. Lupart, P. Lamp, W. G. Zeier, and Y. Shao-Horn, "Lithium Conductivity and Meyer-Neldel Rule in Li_3PO_4–Li_3VO_4–Li_4GeO_4 Lithium Superionic Conductors," *Chemistry of Materials*, vol. 30, no. 16, pp. 5573–5582, 2018.

[42] X. He, Y. Zhu, and Y. Mo, "Origin of fast ion diffusion in super-ionic conductors," *Nature Communications*, vol. 8, p. 15893, 2017.

[43] S. P. Culver, A. G. Squires, N. Minafra, C. W. F. Armstrong, T. Krauskopf, F. Bocher, C. Li, B. J. Morgan, and W. G. Zeier, "Evidence for a Solid-Electrolyte Inductive Effect in the Superionic Conductor $Li_{10}Ge_{1-x}Sn_xP_2S_{12}$," *Journal of the American Chemical Society*, vol. 142, no. 50, pp. 21210–21219, 2020.

[44] A. R. West, *Solid State Chemistry and its Applications*. Wiley, 2 ed., 2014.

[45] P. Barnes, T. Csoka, and S. Jacques. http://pd.chem.ucl.ac.uk/pdnn/powintro/braggs.htm, 2006. Accessed: 2020-12-14.

[46] Oak Ridge National Lab. https://neutrons.ornl.gov/sns, 2012. Accessed: 2020-12-14.

[47] E. Barsoukov and J. R. Macdonald, *Impedance Spectroscopy: Theory, Experiment, and Applications*. Wiley, 3 ed., 2018.

[48] G. Kresse and J. Furthmuller, "Efficient iterative schemes for ab initio total-energy calculations using a plane-wave basis set," *Physical Review B*, vol. 54, no. 16, pp. 11169–11186, 1996.

[49] O. U. Kudu, T. Famprikis, B. Fleutot, M.-D. Braida, T. Le Mercier, M. S. Islam, and C. Masquelier, "A review of structural properties and synthesis methods of solid electrolyte materials in the Li_2S - P_2S_5 binary system," *Journal of Power Sources*, vol. 407, pp. 31–43, 2018.

[50] N. J. J. de Klerk, E. van der Maas, and M. Wagemaker, "Analysis of Diffusion in Solid-State Electrolytes through MD Simulations, Improvement of the Li-Ion Conductivity in β-Li_3PS_4 as an Example," *ACS Applied Energy Materials*, vol. 1, no. 7, pp. 3230–3242, 2018.

[51] M. Gobet, S. Greenbaum, G. Sahu, and C. Liang, "Structural Evolution and Li Dynamics in Nanophase Li_3PS_4 by Solid-State and Pulsed-Field Gradient NMR," *Chemistry of Materials*, vol. 26, no. 11, pp. 3558–3564, 2014.

[52] Y. Yang, Q. Wu, Y. Cui, Y. Chen, S. Shi, R. Z. Wang, and H. Yan, "Elastic Properties, Defect Thermodynamics, Electrochemical Window, Phase Stability, and Li^+ Mobility of Li_3PS_4: Insights from First-Principles Calculations," *ACS Applied Materials & Interfaces*, vol. 8, no. 38, pp. 25229–25242, 2016.

[53] Z. Liu, W. Fu, E. A. Payzant, X. Yu, Z. Wu, N. J. Dudney, J. Kiggans, K. Hong, A. J. Rondinone, and C. Liang, "Anomalous high ionic conductivity of nanoporous β-Li_3PS_4," *Journal of the American Chemical Society*, vol. 135, no. 3, pp. 975–978, 2013.

[54] H.-D. Lim, X. Yue, X. Xing, V. Petrova, M. Gonzalez, H. Liu, and P. Liu, "Designing solution chemistries for the low-temperature synthesis of sulfide-based solid electrolytes," *Journal of Materials Chemistry A*, vol. 6, no. 17, pp. 7370–7374, 2018.

[55] N. H. H. Phuc, K. Morikawa, M. Totani, H. Muto, and A. Matsuda, "Chemical synthesis of Li_3PS_4 precursor suspension by liquid-phase shaking," *Solid State Ionics*, vol. 285, pp. 2–5, 2016.

[56] S. Teragawa, K. Aso, K. Tadanaga, A. Hayashi, and M. Tatsumisago, "Liquid-phase synthesis of a Li_3PS_4 solid electrolyte using N-methylformamide for all-solid-state lithium batteries," *Journal of Materials Chemistry A*, vol. 2, no. 14, pp. 5095–5099, 2014.

[57] H. Wang, Z. D. Hood, Y. Xia, and C. Liang, "Fabrication of ultrathin solid electrolyte membranes of β-Li_3PS_4 nanoflakes by evaporation-induced self-assembly for all-solid-state batteries," *Journal of Materials Chemistry A*, vol. 4, no. 21, pp. 8091–8096, 2016.

[58] J. A. Dawson, P. Canepa, T. Famprikis, C. Masquelier, and M. S. Islam, "Atomic-Scale Influence of Grain Boundaries on Li-Ion Conduction in Solid Electrolytes for All-Solid-State Batteries," *Journal of the American Chemical Society*, vol. 140, no. 1, pp. 362–368, 2018.

[59] J. A. Dawson, P. Canepa, M. J. Clarke, T. Famprikis, D. Ghosh, and M. S. Islam, "Toward Understanding the Different Influences of Grain Boundaries on Ion Transport in Sulfide and Oxide Solid Electrolytes," *Chemistry of Materials*, vol. 31, no. 14, pp. 5296–5304, 2019.

[60] S. Ganapathy, C. Yu, E. R. H. van Eck, and M. Wagemaker, "Peeking across Grain Boundaries in a Solid-State Ionic Conductor," *ACS Energy Letters*, vol. 4, no. 5, pp. 1092–1097, 2019.

[61] L. Zhou, A. Assoud, A. Shyamsunder, A. Huq, Q. Zhang, P. Hartmann, J. Kulisch, and L. F. Nazar, "An Entropically Stabilized Fast-Ion Conductor: $Li_{3.25}[Si_{0.25}P_{0.75}]S_4$," *Chemistry of Materials*, vol. 31, no. 19, pp. 7801–7811, 2019.

[62] K. Hayamizu, Y. Aihara, T. Watanabe, T. Yamada, S. Ito, and N. Machida, "NMR studies on lithium ion migration in sulfide-based conductors, amorphous and crystalline Li_3PS_4," *Solid State Ionics*, vol. 285, pp. 51–58, 2016.

[63] Y. Chen, L. Cai, Z. Liu, C. R. dela Cruz, C. Liang, and K. An, "Correlation of anisotropy and directional conduction in β-Li_3PS_4 fast Li^+ conductor," *Applied Physics Letters*, vol. 107, no. 1, p. 013904, 2015.

[64] M.-S. Lim and S.-H. Jhi, "First-principles study of lithium-ion diffusion in β-Li_3PS_4 for solid-state electrolytes," *Current Applied Physics*, vol. 18, no. 5, pp. 541–545, 2018.

[65] G. K. Phani Dathar, J. Balachandran, P. R. C. Kent, A. J. Rondinone, and P. Ganesh, "Li-ion site disorder driven superionic conductivity in solid electrolytes: a first-principles investigation of β-Li_3PS_4," *Journal of Materials Chemistry A*, vol. 5, no. 3, pp. 1153–1159, 2017.

[66] H. Stöffler, T. Zinkevich, M. Yavuz, A. Senyshyn, J. Kulisch, P. Hartmann, T. Adermann, S. Randau, F. H. Richter, J. Janek, S. Indris, and H. Ehrenberg, "Li^+-Ion Dynamics in β-Li_3PS_4 Observed by NMR: Local Hopping and Long-Range Transport," *The Journal of Physical Chemistry C*, vol. 122, no. 28, pp. 15954–15965, 2018.

[67] X. Wang, R. Xiao, H. Li, and L. Chen, "Oxygen-driven transition from two-dimensional to three-dimensional transport behaviour in β-Li_3PS_4 electrolyte," *Physical Chemistry Chemical Physics*, vol. 18, no. 31, pp. 21269–21277, 2016.

[68] J. Yang and J. S. Tse, "First-principles molecular simulations of Li diffusion in solid electrolytes Li_3PS_4," *Computational Materials Science*, vol. 107, pp. 134–138, 2015.

[69] K. Homma, M. Yonemura, T. Kobayashi, M. Nagao, M. Hirayama, and R. Kanno, "Crystal structure and phase transitions of the lithium ionic conductor Li_3PS_4," *Solid State Ionics*, vol. 182, no. 1, pp. 53–58, 2011.

[70] K. Homma, M. Yonemura, M. Nagao, M. Hirayama, and R. Kanno, "Crystal Structure of High-Temperature Phase of Lithium Ionic Conductor, Li_3PS_4," *Journal of the Physical Society of Japan*, vol. 79, no. Suppl. A, pp. 90–93, 2010.

[71] R. Mercier, J. P. Malugani, B. Fahys, G. Robert, and J. Douglade, "Structure du tetrathiophosphate de lithium," *Acta Crystallographica Section B: Structural Crystallography and Crystal Chemistry*, vol. 38, no. 7, pp. 1887–1890, 1982.

[72] J. S. Kim, W. D. Jung, S. Choi, J. W. Son, B. K. Kim, J. H. Lee, and H. Kim, "Thermally Induced S-Sublattice Transition of Li_3PS_4 for Fast Lithium-Ion Conduction," *The Journal of Physical Chemistry Letters*, vol. 9, no. 18, pp. 5592–5597, 2018.

[73] J. Liang, X. Li, Y. Zhao, L. V. Goncharova, G. Wang, K. R. Adair, C. Wang, R. Li, Y. Zhu, Y. Qian, L. Zhang, R. Yang, S. Lu, and X. Sun, "In Situ Li_3PS_4 Solid-State Electrolyte Protection Layers for Superior Long-Life and High-Rate Lithium-Metal Anodes," *Advanced Materials*, vol. 30, no. 45, p. 1804684, 2018.

[74] Y. Lu, S. Gu, X. Hong, K. Rui, X. Huang, J. Jin, C. Chen, J. Yang, and Z. Wen, "Premodified Li_3PS_4 based interphase for lithium anode towards high-performance Li-S battery," *Energy Storage Materials*, vol. 11, pp. 16–23, 2018.

[75] Q. Pang, X. Liang, A. Shyamsunder, and L. F. Nazar, "An In Vivo Formed Solid Electrolyte Surface Layer Enables Stable Plating of Li Metal," *Joule*, vol. 1, no. 4, pp. 871–886, 2017.

[76] A. L. Spek, "checkCIF validation ALERTS: what they mean and how to respond," *Acta Crystallographica E*, vol. 76, no. Pt 1, pp. 1–11, 2020.

[77] L. Popovi, B. Manoun, D. de Waal, M. K. Nieuwoudt, and J. D. Comins, "Raman spectroscopic study of phase transitions in Li_3PO_4," *Journal of Raman Spectroscopy*, vol. 34, no. 1, pp. 77–83, 2003.

[78] E. Reculeau, A. Elfakir, and M. Quarton, "Caractérisation et prévision structurale d'une nouvelle variété de Li_3PO_4," *Journal of Solid State Chemistry*, vol. 79, no. 2, pp. 205–211, 1989.

[79] Y. Wang, W. D. Richards, S. P. Ong, L. J. Miara, J. C. Kim, Y. Mo, and G. Ceder, "Design principles for solid-state lithium superionic conductors," *Nature Materials*, vol. 14, no. 10, pp. 1026–1031, 2015.

[80] S. P. Ong, W. D. Richards, A. Jain, G. Hautier, M. Kocher, S. Cholia, D. Gunter, V. L. Chevrier, K. A. Persson, and G. Ceder, "Python Materials Genomics (pymatgen): A robust, open-source python library for materials analysis," *Computational Materials Science*, vol. 68, pp. 314–319, 2013.

[81] P. M. Larsen, S. Schmidt, and J. Schiøtz, "Robust structural identification via polyhedral template matching," *Modelling and Simulation in Materials Science and Engineering*, vol. 24, no. 5, p. 055007, 2016.

[82] H. Chen, L. L. Wong, and S. Adams, "SoftBV – a software tool for screening the materials genome of inorganic fast ion conductors," *Acta Crystallographica Section B Structural Science, Crystal Engineering and Materials*, vol. 75, no. 1, pp. 18–33, 2019.

[83] D. Prutsch, B. Gadermaier, H. Brandstätter, V. Pregartner, B. Stanje, D. Wohlmuth, V. Epp, D. Rettenwander, I. Hanzu, and H. M. R. Wilkening, "Nuclear Spin Relaxation in Nanocrystalline β-Li_3PS_4 Reveals Low-Dimensional Li Diffusion in an Isotropic Matrix," *Chemistry of Materials*, vol. 30, no. 21, pp. 7575–7586, 2018.

[84] S. P. Culver, R. Koerver, T. Krauskopf, and W. G. Zeier, "Designing Ionic Conductors: The Interplay between Structural Phenomena and Interfaces in Thiophosphate-Based Solid-State Batteries," *Chemistry of Materials*, vol. 30, no. 13, pp. 4179–4192, 2018.

[85] Z. Zhang, P. N. Roy, H. Li, M. Avdeev, and L. F. Nazar, "Coupled Cation-Anion Dynamics Enhances Cation Mobility in Room-Temperature Superionic Solid-State Electrolytes," *Journal of the American Chemical Society*, vol. 141, no. 49, pp. 19360–19372, 2019.

[86] A. Stukowski, "Visualization and analysis of atomistic simulation data with OVITO–the Open Visualization Tool," *Modelling and Simulation in Materials Science and Engineering*, vol. 18, no. 1, p. 015012, 2010.

[87] K. Momma and F. Izumi, "VESTA 3 for three-dimensional visualization of crystal, volumetric and morphology data," *Journal of Applied Crystallography*, vol. 44, no. 6, pp. 1272–1276, 2011.

[88] K. Momma, T. Ikeda, A. A. Belik, and F. Izumi, "Dysnomia, a computer program for maximum-entropy method (MEM) analysis and its performance in the MEM-based pattern fitting," *Powder Diffraction*, vol. 28, no. 3, pp. 184–193, 2013.

[89] H. Chen and S. Adams, "Bond softness sensitive bond-valence parameters for crystal structure plausibility tests," *IUCrJ*, vol. 4, no. Pt 5, pp. 614–625, 2017.

[90] W. D. Richards, Y. Wang, L. J. Miara, J. C. Kim, and G. Ceder, "Design of $Li_{1+2x}Zn_{1-x}PS_4$, a new lithium ion conductor," *Energy & Environmental Science*, vol. 9, no. 10, pp. 3272–3278, 2016.

[91] S. Jörgens, D. Johrendt, and A. Mewis, "Motive dichtester Kugelpackungen: Die Verbindungen $Zn_3(PS_4)_2$ und $LiZnPS_4$," *Zeitschrift für anorganische und allgemeine Chemie*, vol. 628, no. 8, 2002.

[92] M. Zhou, L. Kang, J. Yao, Z. Lin, Y. Wu, and C. Chen, "Midinfrared Nonlinear Optical Thiophosphates from $LiZnPS_4$ to $AgZnPS_4$: A Combined Experimental and Theoretical Study," *Inorganic Chemistry*, vol. 55, no. 8, pp. 3724–3726, 2016.

[93] S. P. Ong, Y. Mo, W. D. Richards, L. Miara, H. S. Lee, and G. Ceder, "Phase stability, electrochemical stability and ionic conductivity of the $Li_{10}MP_2X_{12}$ (M = Ge, Si, Sn, Al or P, and X = O, S or Se) family of superionic conductors," *Energy & Environmental Science*, vol. 6, no. 1, pp. 148–156, 2013.

[94] D. A. Weber, A. Senyshyn, K. S. Weldert, S. Wenzel, W. Zhang, R. Kaiser, S. Berendts, J. Janek, and W. G. Zeier, "Structural Insights and 3D Diffusion Pathways within the Lithium Superionic Conductor $Li_{10}GeP_2S_{12}$," *Chemistry of Materials*, vol. 28, no. 16, pp. 5905–5915, 2016.

[95] C. Yu, S. Ganapathy, E. R. H. van Eck, L. van Eijck, S. Basak, Y. Liu, L. Zhang, H. Zandbergen, and M. Wagemaker, "Revealing the relation between the structure, Li-ion conductivity and solid-state battery performance of the argyrodite Li_6PS_5Br solid electrolyte," *Journal of Materials Chemistry A*, vol. 5, no. 40, pp. 21178–21188, 2017.

[96] C. Dietrich, D. A. Weber, S. J. Sedlmaier, S. Indris, S. P. Culver, D. Walter, J. Janek, and W. G. Zeier, "Lithium ion conductivity in Li_2S–P_2S_5 glasses – building units and local structure evolution during the crystallization of superionic conductors Li_3PS_4, $Li_7P_3S_{11}$ and $Li_4P_2S_7$," *Journal of Materials Chemistry A*, vol. 5, no. 34, pp. 18111–18119, 2017.

[97] M. Tachez, J. Malugani, R. Mercier, and G. Robert, "Ionic conductivity of and phase transition in lithium thiophosphate Li_3PS_4," *Solid State Ionics*, vol. 14, no. 3, pp. 181–185, 1984.

[98] H. Yamane, M. Shibata, Y. Shimane, T. Junke, Y. Seino, S. Adams, K. Minami, A. Hayashi, and M. Tatsumisago, "Crystal structure of a superionic conductor, $Li_7P_3S_{11}$," *Solid State Ionics*, vol. 178, no. 15-18, pp. 1163–1167, 2007.

[99] S. Adams and R. Prasada Rao, "Structural requirements for fast lithium ion migration in $Li_{10}GeP_2S_{12}$," *Journal of Materials Chemistry*, vol. 22, no. 16, pp. 7687–7691, 2012.

[100] A. Kuhn, J. Kohler, and B. V. Lotsch, "Single-crystal X-ray structure analysis of the superionic conductor $Li_{10}GeP_2S_{12}$," *Physical Chemistry Chemical Physics*, vol. 15, no. 28, pp. 11620–11622, 2013.

[101] Y. Mo, S. P. Ong, and G. Ceder, "First Principles Study of the $Li_{10}GeP_2S_{12}$ Lithium Super Ionic Conductor Material," *Chemistry of Materials*, vol. 24, no. 1, pp. 15–17, 2011.

[102] W. Phoohinkong and T. Sukonket, "A Simple Method for Large-Scale Synthesis of Nano-Sized Zinc Sulfide," *Advanced Materials Research*, vol. 979, pp. 188–191, 2014.

[103] S. Yu and D. J. Siegel, "Grain Boundary Contributions to Li-Ion Transport in the Solid Electrolyte $Li_7La_3Zr_2O_{12}$ (LLZO)," *Chemistry of Materials*, vol. 29, no. 22, pp. 9639–9647, 2017.

[104] Y. Zhao and L. L. Daemen, "Superionic conductivity in lithium-rich anti-perovskites," *Journal of the American Chemical Society*, vol. 134, no. 36, pp. 15042–15047, 2012.

[105] M. R. Busche, D. A. Weber, Y. Schneider, C. Dietrich, S. Wenzel, T. Leichtweiss, D. Schröder, W. Zhang, H. Weigand, D. Walter, S. J. Sedlmaier, D. Houtarde, L. F. Nazar, and J. Janek, "In Situ Monitoring of Fast Li-Ion Conductor $Li_7P_3S_{11}$ Crystallization Inside a Hot-Press Setup," *Chemistry of Materials*, vol. 28, no. 17, pp. 6152–6165, 2016.

[106] R. Kanno, T. Hata, Y. Kawamoto, and M. Irie, "Synthesis of a new lithium ionic conductor, thio-LISICON–lithium germanium sulfide system," *Solid State Ionics*, vol. 130, no. 1-2, pp. 97–104, 2000.

[107] Y. Seino, T. Ota, K. Takada, A. Hayashi, and M. Tatsumisago, "A sulphide lithium super ion conductor is superior to liquid ion conductors for use in rechargeable batteries," *Energy & Environmental Science*, vol. 7, no. 2, pp. 627–631, 2014.

[108] S. Wenzel, D. A. Weber, T. Leichtweiss, M. R. Busche, J. Sann, and J. Janek, "Interphase formation and degradation of charge transfer kinetics between a lithium metal anode and highly crystalline $Li_7P_3S_{11}$ solid electrolyte," *Solid State Ionics*, vol. 286, pp. 24–33, 2016.

[109] F. Han, A. S. Westover, J. Yue, X. Fan, F. Wang, M. Chi, D. N. Leonard, N. J. Dudney, H. Wang, and C. Wang, "High electronic conductivity as the origin of lithium dendrite formation within solid electrolytes," *Nature Energy*, 2019.

[110] J. Li, C. Ma, M. Chi, C. Liang, and N. J. Dudney, "Solid Electrolyte: the Key for High-Voltage Lithium Batteries," *Advanced Energy Materials*, vol. 5, no. 4, p. 1401408, 2015.

[111] I. Garbayo, M. Struzik, W. J. Bowman, R. Pfenninger, E. Stilp, and J. L. M. Rupp, "Glass-Type Polyamorphism in Li-Garnet Thin Film Solid State Battery Conductors," *Advanced Energy Materials*, vol. 8, no. 12, p. 1702265, 2018.

[112] S. Ujiie, A. Hayashi, and M. Tatsumisago, "Structure, ionic conductivity and electrochemical stability of Li_2S–P_2S_5–LiI glass and glass–ceramic electrolytes," *Solid State Ionics*, vol. 211, pp. 42–45, 2012.

[113] Y. Aihara, S. Ito, R. Omoda, T. Yamada, S. Fujiki, T. Watanabe, Y. Park, and S. Doo, "The Electrochemical Characteristics and Applicability of an Amorphous Sulfide-Based solid ion conductor for the next-generation solid-state lithium secondary Batteries," *Frontiers in Energy Research*, vol. 4, no. 18, 2016.

[114] J. Lau, R. H. DeBlock, D. M. Butts, D. S. Ashby, C. S. Choi, and B. S. Dunn, "Sulfide Solid Electrolytes for Lithium Battery Applications," *Advanced Energy Materials*, vol. 8, no. 27, p. 1800933, 2018.

[115] T. Minami, A. Hayashi, and M. Tatsumisago, "Preparation and characterization of lithium ion-conducting oxysulfide glasses," *Solid State Ionics*, vol. 136-137, no. 1-2, pp. 1015–1023, 2000.

[116] Y. Seino, K. Takada, B. Kim, L. Zhang, N. Ohta, H. Wada, M. Osada, and T. Sasaki, "Synthesis and electrochemical properties of Li_2S–B_2S_3–Li_4SiO_4," *Solid State Ionics*, vol. 177, no. 26-32, pp. 2601–2603, 2006.

[117] A. Hayashi, A. Sakuda, and M. Tatsumisago, "Development of Sulfide Solid Electrolytes and Interface Formation Processes for Bulk-Type All-Solid-State Li and Na Batteries," *Frontiers in Energy Research*, vol. 4, no. 25, 2016.

[118] S. Ujiie, T. Inagaki, A. Hayashi, and M. Tatsumisago, "Conductivity of $70Li_2S$-$30P_2S_5$ glasses and glass–ceramics added with lithium halides," *Solid State Ionics*, vol. 263, pp. 57–61, 2014.

[119] M. Menetrier, "Electrochemical Properties of B_2S_3-Li_2S-LiI Vitreous Electrolytes," *Journal of The Electrochemical Society*, vol. 131, no. 9, p. 1971, 1984.

[120] M. Ménétrier, C. Estournès, A. Levasseur, and K. J. Rao, "Ionic conduction in B_2S_3-Li_2S-Li_2S-LiI glasses," *Solid State Ionics*, vol. 53-56, pp. 1208–1213, 1992.

[121] H. Wada, M. Menetrier, A. Levasseur, and P. Hagenmuller, "Preparation and ionic conductivity of new B_2S_3–Li_2S–LiI glasses," *Materials Research Bulletin*, vol. 18, no. 2, pp. 189–193, 1983.

[122] W. Burckhardt, M. Makyta, A. Levasseur, and P. Hagenmuller, "Fast Li^+ ion transport in iodine-thioborate glasses," *Materials Research Bulletin*, vol. 19, no. 8, pp. 1083–1089, 1984.

[123] S. Hori, K. Suzuki, M. Hirayama, Y. Kato, and R. Kanno, "Lithium Superionic Conductor $Li_{9.42}Si_{1.02}P_{2.1}S_{9.96}O_{2.04}$ with $Li_{10}GeP_2S_{12}$-Type Structure in the Li_2S–P_2S_5–SiO_2 Pseudoternary System: Synthesis, Electrochemical Properties, and Structure–Composition Relationships," *Frontiers in Energy Research*, vol. 4, no. 38, 2016.

[124] K. Ngai, "Meyer–Neldel rule and anti Meyer–Neldel rule of ionic conductivity: Conclusions from the coupling model," *Solid State Ionics*, vol. 105, no. 1-4, pp. 231–235, 1998.

[125] J. Sohr, H. Schmidt, and W. Voigt, "Higher hydrates of lithium chloride, lithium bromide and lithium iodide," *Acta Crystallographica C*, vol. 74, no. Pt 2, pp. 194–202, 2018.

[126] B. D. Sanditov, S. S. Sangadiev, and D. S. Sanditov, "Relation between elastic modulus and glass softening temperature in the delocalized atom model," *Journal of Experimental and Theoretical Physics*, vol. 115, no. 3, pp. 445–454, 2012.

[127] B. Curtis, C. Francis, S. Kmiec, and S. W. Martin, "Investigation of the short range order structures in sodium thioborosilicate mixed glass former glasses," *Journal of Non-Crystalline Solids*, vol. 521, p. 119456, 2019.

[128] S. W. Martin, R. Christensen, G. Olson, J. Kieffer, and W. Wang, "New Interpretation of Na^+-Ion Conduction in and the Structures and Properties of Sodium Borosilicate Mixed Glass Former Glasses," *The Journal of Physical Chemistry C*, vol. 123, no. 10, pp. 5853–5870, 2019.

[129] S. J. Hwang, C. Fernandez, J. P. Amoureux, J. W. Han, J. Cho, S. W. Martin, and M. Pruski, "Structural Study of $xNa_2S + (1\text{-}x)B_2S_3$ Glasses and Polycrystals by Multiple-Quantum MAS NMR of ^{11}B and ^{23}Na," *Journal of the American Chemical Society*, vol. 120, no. 29, pp. 7337–7346, 1998.

[130] A. Hayashi, R. Araki, K. Tadanaga, M. Tatsumisago, and T. Minami, "High resolution solid state NMR studies of ionically conductive Li_2S–SiS_2–Li_2O–P_2O_5 oxysulphide glasses," *Physics and Chemistry of Glasses*, vol. 40, no. 3, pp. 140–145, 1999.

[131] A. Hayashi, H. Yamashita, M. Tatsumisago, and T. Minami, "Characterization of Li_2S–SiS_2–Li_xMO_y (M = Si, P, Ge) amorphous solid electrolytes prepared by melt-quenching and mechanical milling," *Solid State Ionics*, vol. 148, no. 3-4, pp. 381–389, 2002.

[132] J. Schrooten, B. Meyer, and S. W. Martin, "Structural characterization of silver thioborosilicate glasses," *Journal of Non-Crystalline Solids*, vol. 318, no. 1-2, pp. 27–36, 2003.

[133] D. E. Watson and S. W. Martin, "Short range order characterization of the Na_2S + SiS_2 glass system using Raman, infrared and ^{29}Si magic angle spinning nuclear magnetic resonance spectroscopies," *Journal of Non-Crystalline Solids*, vol. 471, pp. 39–50, 2017.

[134] B. Meyer, F. Borsa, and S. W. Martin, "Structure and properties of lithium thio-borogermanate glasses," *Journal of Non-Crystalline Solids*, vol. 337, no. 2, pp. 166–173, 2004.

[135] M. Menetrier, A. Hojjaji, A. Levasseur, M. Couzi, and K. J. Rao, "Structural Hypotheses and Raman-Spectroscopy Investigations of Glasses Belonging to the B_2S_3–Li_2S–LiI System," *Physics and Chemistry of Glasses*, vol. 33, no. 6, pp. 222–227, 1992.

[136] S. Hayashi and K. Hayamizu, "Accurate Determination of NMR Chemical Shifts in Alkali Halides and Their Correlation with Structural Factors," *Bulletin of the Chemical Society of Japan*, vol. 63, no. 3, pp. 913–919, 1990.

[137] P. Vinatier, "Aggregation of the doping salt in B_2S_3–Li_2S–LiI glasses, effect on the dynamical properties," *Solid State Ionics*, vol. 116, no. 1-2, pp. 35–45, 1999.

[138] V. Lacivita, A. S. Westover, A. Kercher, N. D. Phillip, G. Yang, G. Veith, G. Ceder, and N. J. Dudney, "Resolving the Amorphous Structure of Lithium Phosphorus Oxynitride (Lipon)," *Journal of the American Chemical Society*, vol. 140, no. 35, pp. 11029–11038, 2018.

[139] Y. Zhu, J. G. Connell, S. Tepavcevic, P. Zapol, R. Garcia-Mendez, N. J. Taylor, J. Sakamoto, B. J. Ingram, L. A. Curtiss, J. W. Freeland, D. D. Fong, and N. M. Markovic, "Dopant-Dependent Stability of Garnet Solid Electrolyte Interfaces with Lithium Metal," *Advanced Energy Materials*, vol. 9, no. 12, p. 1803440, 2019.

[140] K. N. Wood, K. X. Steirer, S. E. Hafner, C. Ban, S. Santhanagopalan, S. H. Lee, and G. Teeter, "Operando X-ray photoelectron spectroscopy of solid electrolyte interphase formation and evolution in Li_2S-P_2S_5 solid-state electrolytes," *Nature Communications*, vol. 9, no. 1, p. 2490, 2018.

[141] S. Wenzel, T. Leichtweiss, D. Krüger, J. Sann, and J. Janek, "Interphase formation on lithium solid electrolytes — An in situ approach to study interfacial reactions by photoelectron spectroscopy," *Solid State Ionics*, vol. 278, pp. 98–105, 2015.

[142] S. Wenzel, S. Randau, T. Leichtweiß, D. A. Weber, J. Sann, W. G. Zeier, and J. Janek, "Direct Observation of the Interfacial Instability of the Fast Ionic Conductor $Li_{10}GeP_2S_{12}$ at the Lithium Metal Anode," *Chemistry of Materials*, vol. 28, no. 7, pp. 2400–2407, 2016.

[143] F. D. Han, J. Yue, X. Y. Zhu, and C. S. Wang, "Suppressing Li Dendrite Formation in Li_2S-P_2S_5 Solid Electrolyte by LiI Incorporation," *Advanced Energy Materials*, vol. 8, no. 18, p. 1703644, 2018.

[144] E. Rangasamy, Z. Liu, M. Gobet, K. Pilar, G. Sahu, W. Zhou, H. Wu, S. Greenbaum, and C. Liang, "An iodide-based $Li_7P_2S_8I$ superionic conductor," *Journal of the American Chemical Society*, vol. 137, no. 4, pp. 1384–1387, 2015.

[145] B. R. Shin, Y. J. Nam, D. Y. Oh, D. H. Kim, J. W. Kim, and Y. S. Jung, "Comparative Study of TiS_2/Li-In All-Solid-State Lithium Batteries Using Glass-Ceramic Li_3PS_4 and $Li_{10}GeP_2S_{12}$ Solid Electrolytes," *Electrochimica Acta*, vol. 146, pp. 395–402, 2014.

[146] R. Koerver, F. Walther, I. Aygün, J. Sann, C. Dietrich, W. G. Zeier, and J. Janek, "Redox-active cathode interphases in solid-state batteries," *Journal of Materials Chemistry A*, vol. 5, no. 43, pp. 22750–22760, 2017.

[147] T. Famprikis, P. Canepa, J. A. Dawson, M. S. Islam, and C. Masquelier, "Fundamentals of inorganic solid-state electrolytes for batteries," *Nature Materials*, vol. 18, no. 12, pp. 1278–1291, 2019.

[148] M. Menetrier, V. Levasseur, C. Delmas, J. Audebert, and P. Hagenmuller, "New secondary batteries for room temperature applications using a vitreous electrolyte," *Solid State Ionics*, vol. 14, no. 3, pp. 257–261, 1984.

[149] A. D. Sendek, E. R. Antoniuk, E. D. Cubuk, B. Ransom, B. E. Francisco, J. Buettner-Garrett, Y. Cui, and E. J. Reed, "Combining Superionic Conduction and Favorable Decomposition Products in the Crystalline Lithium-Boron-Sulfur System: A New Mechanism for Stabilizing Solid Li-Ion Electrolytes," *ACS Applied Materials & Interfaces*, vol. 12, no. 34, pp. 37957–37966, 2020.

[150] K. Kaup, J. D. Bazak, S. H. Vajargah, X. Wu, J. Kulisch, G. R. Goward, and L. F. Nazar, "A Lithium Oxythioborosilicate Solid Electrolyte Glass with Superionic Conductivity," *Advanced Energy Materials*, vol. 10, no. 8, p. 1902783, 2020.

[151] O. Conrad, C. Jansen, and B. Krebs, "Boron-Sulfur and Boron-Selenium Compounds—From Unique Molecular Structural Principles to Novel Polymeric Materials," *Angewandte Chemie International Edition*, vol. 37, no. 23, pp. 3208–3218, 1998.

[152] P. Zum Hebel, B. Krebs, M. Grune, and W. Muller-Warmuth, "Preparation, crystal structure and ^{7}Li NMR of $Li_{6+2x}[B_{10}S_{18}]S_x$(x≈2)," *Solid State Ionics*, vol. 43, pp. 133–142, 1990.

[153] A. Haffner, T. Brauniger, and D. Johrendt, "Supertetrahedral Networks and Lithium-Ion Mobility in Li_2SiP_2 and $LiSi_2P_3$," *Angewandte Chemie International Edition*, vol. 55, no. 43, pp. 13585–13588, 2016.

[154] A. Haffner, A. K. Hatz, I. Moudrakovski, B. V. Lotsch, and D. Johrendt, "Fast Sodium-Ion Conductivity in Supertetrahedral Phosphidosilicates," *Angewandte Chemie International Edition*, vol. 57, no. 21, pp. 6155–6160, 2018.

[155] E. M. Bertschler, C. Dietrich, T. Leichtweiss, J. Janek, and W. Schnick, "Li^+ Ion Conductors with Adamantane-Type Nitridophosphate Anions β-$Li_{10}P_4N_{10}$ and $Li_{13}P_4N_{10}X_3$ with X = Cl, Br," *Chemistry: A European Journal*, vol. 24, no. 1, pp. 196–205, 2018.

[156] A. Hammerschmidt, P. Z. Hebel, F. Hiltmann, and B. Krebs, "Darstellung und Kristallstrukturen von $Li_{4-2x}Sr_{2+x}B_{10}S_{19}$ (x ≈ 0.27) und $Na_{610}S_{18}$. Zwei neue Thioborate mit hochpolymeren Makrotetraeder-Netzwerken," *Zeitschrift für anorganische und allgemeine Chemie*, vol. 622, no. 1, pp. 76–84, 1996.

[157] B. Krebs and H. Diercks, "$Ag_6B_{10}S_{18}$: Ein neues Thioborat mit tetraedrischer Koordination des Bors," *Zeitschrift für anorganische und allgemeine Chemie*, vol. 518, no. 11, pp. 101–114, 1984.

[158] G. Ferey, "Supertetrahedra in sulfides: matter against mathematical series?," *Angewandte Chemie International Edition*, vol. 42, no. 23, pp. 2576–2579, 2003.

[159] H. Li, J. Kim, M. O'Keeffe, and O. M. Yaghi, "$[Cd_{16}In_{64}S_{134}]^{44-}$: 31-Å tetrahedron with a large cavity," *Angewandte Chemie International Edition*, vol. 42, no. 16, pp. 1819–1821, 2003.

[160] T. Wu, F. Zuo, L. Wang, X. Bu, S. T. Zheng, R. Ma, and P. Feng, "A large indium sulfide supertetrahedral cluster built from integration of ZnS-like tetrahedral shell with NaCl-like octahedral core," *Journal of the American Chemical Society*, vol. 133, no. 40, pp. 15886–15889, 2011.

[161] X. Xu, W. Wang, D. Liu, D. Hu, T. Wu, X. Bu, and P. Feng, "Pushing up the Size Limit of Metal Chalcogenide Supertetrahedral Nanocluster," *Journal of the American Chemical Society*, vol. 140, no. 3, pp. 888–891, 2018.

[162] X. M. Zhang, D. Sarma, Y. Q. Wu, L. Wang, Z. X. Ning, F. Q. Zhang, and M. G. Kanatzidis, "Open-Framework Oxysulfide Based on the Supertetrahedral $[In_4Sn_{16}O_{10}S^{34}](^{12-})$ Cluster and Efficient Sequestration of Heavy Metals," *Journal of the American Chemical Society*, vol. 138, no. 17, pp. 5543–5546, 2016.

[163] L. Toffoletti, H. Kirchhain, J. Landesfeind, W. Klein, L. van Wullen, H. A. Gasteiger, and T. F. Fassler, "Lithium Ion Mobility in Lithium Phosphidosilicates: Crystal Structure, ^{7}Li, ^{29}Si, and ^{31}P MAS NMR Spectroscopy, and Impedance Spectroscopy of Li_8SiP_4 and Li_2SiP_2," *Chemistry: A European Journal*, vol. 22, no. 49, pp. 17635–17645, 2016.

[164] P. Adeli, J. D. Bazak, K. H. Park, I. Kochetkov, A. Huq, G. R. Goward, and L. F. Nazar, "Boosting Solid-State Diffusivity and Conductivity in Lithium Superionic Argyrodites by Halide Substitution," *Angewandte Chemie International Edition*, vol. 58, no. 26, pp. 8681–8686, 2019.

[165] J. G. Smith and D. J. Siegel, "Low-temperature paddlewheel effect in glassy solid electrolytes," *Nature Communications*, vol. 11, no. 1, p. 1483, 2020.

[166] Z. Zhang, H. Li, K. Kaup, L. Zhou, P.-N. Roy, and L. F. Nazar, "Targeting Superionic Conductivity by Turning on Anion Rotation at Room Temperature in Fast Ion Conductors," *Matter*, vol. 2, no. 6, pp. 1667–1684, 2020.

[167] C. Giacovazzo, C. Giacovazzo, H. L. Monaco, G. Artioli, D. Viterbo, M. Milanesio, G. Gilli, P. Gilli, G. Zanotti, G. Ferraris, and M. Catti, *Fundamentals of Crystallography*. Oxford University Press, 2011.

[168] M. Ladd and R. Palmer, *Structure Determination by X-ray Crystallography*. Springer, 2013.

[169] M. Grune, W. Mullerwarmuth, P. Zumhebel, and B. Krebs, "Unusual lithium dynamics and NMR relaxation in a novel crystalline thioborate-sulfide," *Solid State Ionics*, vol. 66, no. 1-2, pp. 165–173, 1993.

[170] T. Bernges, S. P. Culver, N. Minafra, R. Koerver, and W. G. Zeier, "Competing Structural Influences in the Li Superionic Conducting Argyrodites $Li_6PS_{5-x}Se_xBr$ ($0 \leq x \leq 1$) upon Se Substitution," *Inorganic Chemistry*, vol. 57, no. 21, pp. 13920–13928, 2018.

[171] K. Sonnenberg, P. Prohm, N. Schwarze, C. Muller, H. Beckers, and S. Riedel, "Investigation of Large Polychloride Anions: $[Cl_{11}]^-$, $[Cl_{12}]^{2-}$, and $[Cl_{13}]^-$," *Angewandte Chemie International Edition*, vol. 57, no. 29, pp. 9136–9140, 2018.

[172] K. Sonnenberg, L. Mann, F. A. Redeker, B. Schmidt, and S. Riedel, "Polyhalogen and Polyinterhalogen Anions from Fluorine to Iodine," *Angewandte Chemie International Edition*, vol. 59, no. 14, pp. 5464–5493, 2020.

[173] P. H. Svensson and L. Kloo, "Synthesis, structure, and bonding in polyiodide and metal iodide-iodine systems," *Chemical Reviews*, vol. 103, no. 5, pp. 1649–84, 2003.

[174] A. Larson and R. V. Dreele, "General Structure Analysis System (GSAS)," *Los Alamos National Laboratory Report LAUR 86-748*, 2004.

[175] J. Wu, S. Liu, F. Han, X. Yao, and C. Wang, "Lithium/Sulfide All-Solid-State Batteries using Sulfide Electrolytes," *Advanced Materials*, p. 2000751, 2020.

[176] X. Bai, Y. Duan, W. Zhuang, R. Yang, and J. Wang, "Research Progress of Li-argyrodite Solid-state Electrolytes," *Journal of Materials Chemistry A*, 2020.

[177] A. Emly, E. Kioupakis, and A. Van der Ven, "Phase Stability and Transport Mechanisms in Antiperovskite Li_3OCl and Li_3OBr Superionic Conductors," *Chemistry of Materials*, vol. 25, no. 23, pp. 4663–4670, 2013.

[178] L. Yin, M. Murphy, K. Kim, L. Hu, J. Cabana, D. J. Siegel, and S. H. Lapidus, "Synthesis of Antiperovskite Solid Electrolytes: Comparing Li_3SI, Na_3SI, and Ag_3SI," *Inorganic Chemistry*, vol. 59, no. 16, pp. 11244–11247, 2020.

[179] I. H. Chu, H. Nguyen, S. Hy, Y. C. Lin, Z. Wang, Z. Xu, Z. Deng, Y. S. Meng, and S. P. Ong, "Insights into the Performance Limits of the $Li_7P_3S_{11}$ Superionic Conductor: A Combined First-Principles and Experimental Study," *ACS Applied Materials & Interfaces*, vol. 8, no. 12, pp. 7843–53, 2016.

[180] T. Famprikis, O. U. Kudu, J. A. Dawson, P. Canepa, F. Fauth, E. Suard, M. Zbiri, D. Dambournet, O. J. Borkiewicz, H. Bouyanfif, S. P. Emge, S. Cretu, J. N. Chotard, C. P. Grey, W. G. Zeier, M. S. Islam, and C. Masquelier, "Under Pressure: Mechanochemical Effects on Structure and Ion Conduction in the Sodium-Ion Solid Electrolyte Na_3PS_4," *Journal of the American Chemical Society*, vol. 142, no. 43, pp. 18422–18436, 2020.

[181] S. Strangmuller, H. Eickhoff, D. Muller, W. Klein, G. Raudaschl-Sieber, H. Kirchhain, C. Sedlmeier, V. Baran, A. Senyshyn, V. L. Deringer, L. van Wullen, H. A. Gasteiger, and T. F. Fassler, "Fast Ionic Conductivity in the Most Lithium-Rich Phosphidosilicate $Li_{14}SiP_6$," *Journal of the American Chemical Society*, vol. 141, no. 36, pp. 14200–14209, 2019.

[182] J. Liang, X. Li, S. Wang, K. R. Adair, W. Li, Y. Zhao, C. Wang, Y. Hu, L. Zhang, S. Zhao, S. Lu, H. Huang, R. Li, Y. Mo, and X. Sun, "Site-Occupation-Tuned Superionic Li_xScCl_{3+x} Halide Solid Electrolytes for All-Solid-State Batteries," *Journal of the American Chemical Society*, vol. 142, no. 15, pp. 7012–7022, 2020.

[183] F. Hiltmann, P. Zum Hebel, A. Hammerschmidt, and B. Krebs, "$Li_5B_7S_{13}$ und $Li_9B_{19}S_{33}$: Zwei Lithiumthioborate mit neuen hochpolymeren Anionengerüsten," *Zeitschrift für anorganische und allgemeine Chemie*, vol. 619, no. 2, pp. 293–302, 1993.

[184] F. Bianchini, H. Fjellvåg, and P. Vajeeston, "A first-principle investigation of the Li diffusion mechanism in the super-ionic conductor lithium orthothioborate Li_3BS_3 structure," *Materials Letters*, vol. 219, pp. 186–189, 2018.

[185] A. D. Sendek, E. D. Cubuk, E. R. Antoniuk, G. Cheon, Y. Cui, and E. J. Reed, "Machine Learning-Assisted Discovery of Solid Li-Ion Conducting Materials," *Chemistry of Materials*, vol. 31, no. 2, pp. 342–352, 2018.

[186] A. D. Sendek, Q. Yang, E. D. Cubuk, K.-A. N. Duerloo, Y. Cui, and E. J. Reed, "Holistic computational structure screening of more than 12 000 candidates for solid lithium-ion conductor materials," *Energy & Environmental Science*, vol. 10, no. 1, pp. 306–320, 2017.

[187] K. Kaup, A. Assoud, J. Liu, and L. Nazar, "Fast Li-Ion Conductivity in Superadamantanoid Lithium Thioborate Halides," *Angewandte Chemie International Edition*, 2020.

[188] M. Grüne, "Complex lithium dynamics in the novel thioborate $Li_5B_7S_{13}$ revealed by NMR relaxation and lineshape studies," *Solid State Ionics*, vol. 78, no. 3-4, pp. 305–313, 1995.

[189] J. Rumble and P. Vaqueiro, "$Na_5(Ga_4S)(GaS_4)_3{\cdot}6H_2O$: A three-dimensional thiogallate containing a novel octahedral building block," *Solid State Sciences*, vol. 13, no. 5, pp. 1137–1142, 2011.

[190] N. Zheng, X. Bu, and P. Feng, "$Na_5(In_4S)(InS_4)3{\cdot}6H_2O$, a zeolite-like structure with unusual SIn_4 tetrahedra," *Journal of the American Ceramic Society*, vol. 127, no. 15, pp. 5286–7, 2005.

[191] J. C. Bachman, S. Muy, A. Grimaud, H. H. Chang, N. Pour, S. F. Lux, O. Paschos, F. Maglia, S. Lupart, P. Lamp, L. Giordano, and Y. Shao-Horn, "Inorganic Solid-State Electrolytes for Lithium Batteries: Mechanisms and Properties Governing Ion Conduction," *Chemical Reviews*, vol. 116, no. 1, pp. 140–62, 2016.

[192] S. Stramare, V. Thangadurai, and W. Weppner, "Lithium Lanthanum Titanates: A Review," *Chemistry of Materials*, vol. 15, no. 21, pp. 3974–3990, 2003.

[193] M. Yashima, M. Itoh, Y. Inaguma, and Y. Morii, "Crystal structure and diffusion path in the fast lithium-ion conductor $La_{0.62}Li_{0.16}TiO_3$," *Journal of the American Chemical Society*, vol. 127, no. 10, pp. 3491–5, 2005.

[194] P. R. Rayavarapu, N. Sharma, V. K. Peterson, and S. Adams, "Variation in structure and Li^+-ion migration in argyrodite-type Li_6PS_5X (X = Cl, Br, I) solid electrolytes," *Journal of Solid State Electrochemistry*, vol. 16, no. 5, pp. 1807–1813, 2011.

[195] A. Kuhn, V. Duppel, and B. V. Lotsch, "Tetragonal $Li_{10}GeP_2S_{12}$ and Li_7GePS_8 - exploring the Li ion dynamics in LGPS Li electrolytes," *Energy & Environmental Science*, vol. 6, no. 12, 2013.

[196] C. Yu, S. Ganapathy, N. J. J. de Klerk, E. R. H. van Eck, and M. Wagemaker, "Na-ion dynamics in tetragonal and cubic Na_3PS_4, a Na-ion conductor for solid state Na-ion batteries," *Journal of Materials Chemistry A*, vol. 4, no. 39, pp. 15095–15105, 2016.

[197] H.-J. Deiseroth, J. Maier, K. Weichert, V. Nickel, S.-T. Kong, and C. Reiner, "Li_7PS_6 and Li_6PS_5X (X: Cl, Br, I): Possible Three-dimensional Diffusion Pathways for Lithium Ions and Temperature Dependence of the Ionic Conductivity by Impedance Measurements," *Zeitschrift für anorganische und allgemeine Chemie*, vol. 637, no. 10, pp. 1287–1294, 2011.

[198] M. Brinek, C. Hiebl, K. Hogrefe, I. Hanghofer, and H. M. R. Wilkening, "Structural Disorder in Li_6PS_5I Speeds ^{7}Li Nuclear Spin Recovery and Slows Down ^{31}P Relaxation-Implications for Translational and Rotational Jumps as Seen by Nuclear Magnetic Resonance," *The Journal of Physical Chemistry C*, vol. 124, no. 42, pp. 22934–22940, 2020.

[199] Z. Deng, Z. Zhu, I.-H. Chu, and S. P. Ong, "Data-Driven First-Principles Methods for the Study and Design of Alkali Superionic Conductors," *Chemistry of Materials*, vol. 29, no. 1, pp. 281–288, 2016.

[200] S. Wenzel, S. J. Sedlmaier, C. Dietrich, W. G. Zeier, and J. Janek, "Interfacial reactivity and interphase growth of argyrodite solid electrolytes at lithium metal electrodes," *Solid State Ionics*, vol. 318, pp. 102–112, 2018.

[201] L. Zhou, A. Assoud, Q. Zhang, X. Wu, and L. F. Nazar, "New Family of Argyrodite Thioantimonate Lithium Superionic Conductors," *Journal of the American Chemical Society*, vol. 141, no. 48, pp. 19002–19013, 2019.

[202] Z. Zhang, E. Ramos, F. Lalère, A. Assoud, K. Kaup, P. Hartman, and L. F. Nazar, "$Na_{11}Sn_2PS_{12}$: a new solid state sodium superionic conductor," *Energy & Environmental Science*, vol. 11, no. 1, pp. 87–93, 2018.

[203] P. E. Blochl, "Projector augmented-wave method," *Physical Review B*, vol. 50, no. 24, pp. 17953–17979, 1994.

[204] J. P. Perdew, M. Ernzerhof, and K. Burke, "Rationale for mixing exact exchange with density functional approximations," *The Journal of Chemical Physics*, vol. 105, no. 22, pp. 9982–9985, 1996.

[205] G. L. W. Hart and R. W. Forcade, "Algorithm for generating derivative structures," *Physical Review B*, vol. 77, no. 22, 2008.

[206] S. P. Ong, L. Wang, B. Kang, and G. Ceder, "Li-Fe-P-O_2 Phase Diagram from First Principles Calculations," *Chemistry of Materials*, vol. 20, no. 5, pp. 1798–1807, 2008.

[207] A. Jain, S. P. Ong, G. Hautier, W. Chen, W. D. Richards, S. Dacek, S. Cholia, D. Gunter, D. Skinner, G. Ceder, and K. A. Persson, "Commentary: The Materials Project: A materials genome approach to accelerating materials innovation," *APL Materials*, vol. 1, no. 1, 2013.

[208] W. G. Hoover, "Canonical dynamics: Equilibrium phase-space distributions," *Physical Review A*, vol. 31, no. 3, pp. 1695–1697, 1985.

[209] S. Nosé, "A unified formulation of the constant temperature molecular dynamics methods," *The Journal of Chemical Physics*, vol. 81, no. 1, pp. 511–519, 1984.

[210] A. Togo and I. Tanaka, "First principles phonon calculations in materials science," *Scripta Materialia*, vol. 108, pp. 1–5, 2015.

[211] Y. Hinuma, G. Pizzi, Y. Kumagai, F. Oba, and I. Tanaka, "Band structure diagram paths based on crystallography," *Computational Materials Science*, vol. 128, pp. 140–184, 2017.

[212] P. Bron, S. Johansson, K. Zick, J. Schmedt auf der Gunne, S. Dehnen, and B. Roling, "$Li_{10}SnP_2S_{12}$: an affordable lithium superionic conductor," *Journal of the American Chemical Society*, vol. 135, no. 42, pp. 15694–15697, 2013.

[213] M. Chen and S. Adams, "High performance all-solid-state lithium/sulfur batteries using lithium argyrodite electrolyte," *Journal of Solid State Electrochemistry*, vol. 19, no. 3, pp. 697–702, 2014.

[214] R. Chen, W. Qu, X. Guo, L. Li, and F. Wu, "The pursuit of solid-state electrolytes for lithium batteries: from comprehensive insight to emerging horizons," *Materials Horizons*, vol. 3, no. 6, pp. 487–516, 2016.

[215] J. Janek and W. G. Zeier, "A solid future for battery development," *Nature Energy*, vol. 1, no. 9, 2016.

[216] Y. S. Jung, D. Y. Oh, Y. J. Nam, and K. H. Park, "Issues and Challenges for Bulk-Type All-Solid-State Rechargeable Lithium Batteries using Sulfide Solid Electrolytes," *Israel Journal of Chemistry*, vol. 55, no. 5, pp. 472–485, 2015.

[217] P. Knauth, "Inorganic solid Li ion conductors: An overview," *Solid State Ionics*, vol. 180, no. 14-16, pp. 911–916, 2009.

[218] A. Kuhn, O. Gerbig, C. Zhu, F. Falkenberg, J. Maier, and B. V. Lotsch, "A new ultrafast superionic Li-conductor: ion dynamics in $Li_{11}Si_2PS_{12}$ and comparison with other tetragonal LGPS-type electrolytes," *Physical Chemistry Chemical Physics*, vol. 16, no. 28, pp. 14669–14674, 2014.

[219] D. Liu, W. Zhu, Z. Feng, A. Guerfi, A. Vijh, and K. Zaghib, "Recent progress in sulfide-based solid electrolytes for Li-ion batteries," *Materials Science and Engineering: B*, vol. 213, pp. 169–176, 2016.

[220] Y. Sun, K. Suzuki, S. Hori, M. Hirayama, and R. Kanno, "Superionic Conductors: $Li_{10+\delta}[Sn_ySi_{1-y}]_{1+\delta}P_{2-\delta}S_{12}$ with a $Li_{10}GeP_2S_{12}$-type Structure in the Li_3PS_4-Li_4SnS_4-Li_4SiS_4 Quasi-ternary System," *Chemistry of Materials*, vol. 29, no. 14, pp. 5858–5864, 2017.

[221] S. Xin, Y. You, S. Wang, H.-C. Gao, Y.-X. Yin, and Y.-G. Guo, "Solid-State Lithium Metal Batteries Promoted by Nanotechnology: Progress and Prospects," *ACS Energy Letters*, vol. 2, no. 6, pp. 1385–1394, 2017.

[222] C. Yu, S. Ganapathy, N. J. de Klerk, I. Roslon, E. R. van Eck, A. P. Kentgens, and M. Wagemaker, "Unravelling Li-Ion Transport from Picoseconds to Seconds: Bulk versus Interfaces in an Argyrodite Li_6PS_5Cl-Li_2S All-Solid-State Li-Ion Battery," *Journal of the American Chemical Society*, vol. 138, no. 35, pp. 11192–201, 2016.

[223] C. Yu, S. Ganapathy, E. Eck, H. Wang, S. Basak, Z. Li, and M. Wagemaker, "Accessing the bottleneck in all-solid state batteries, lithium-ion transport over the solid-electrolyte-electrode interface," *Nature Communications*, vol. 8, no. 1, p. 1086, 2017.

[224] Z. Zhang, Y. Shao, B. Lotsch, Y.-S. Hu, H. Li, J. Janek, L. F. Nazar, C.-W. Nan, J. Maier, M. Armand, and L. Chen, "New horizons for inorganic solid state ion conductors," *Energy & Environmental Science*, vol. 11, no. 8, pp. 1945–1976, 2018.

[225] C.-Z. Zhao, B.-C. Zhao, C. Yan, X.-Q. Zhang, J.-Q. Huang, Y. Mo, X. Xu, H. Li, and Q. Zhang, "Liquid phase therapy to solid electrolyte–electrode interface in solid-state Li metal batteries: A review," *Energy Storage Materials*, 2019.

[226] J. T. S. Irvine, D. C. Sinclair, and A. R. West, "Electroceramics: Characterization by Impedance Spectroscopy," *Advanced Materials*, vol. 2, no. 3, pp. 132–138, 1990.

APPENDICES

Appendix A

Supplementary Information for: Impact of the Li substructure on the diffusion pathways in α and β-Li_3PS_4: an *in-situ* high temperature neutron diffraction study

A.1 List of Supplementary Figures and Tables

A.1.1 γ-Li_3PS_4

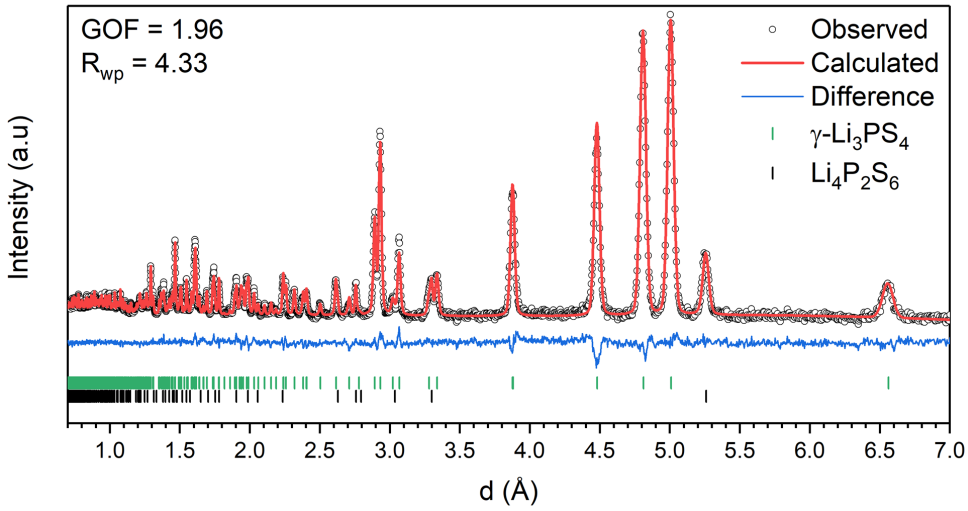

Figure A.1: Rietveld refinement of γ-Li_3PS_4 using TOF neutron powder diffraction data measured at 25°C (contains 9 wt.% $Li_4P_2S_6$ impurity).

Table A.1: Crystallographic data for γ-Li_3PS_4 obtained from Rietveld refinement of neutron powder diffraction at 25°C. Unit Cell: Orthorhombic $Pmn2_1$ (31). a = 7.7557(3) Å, b = 6.5627(3) Å, c = 6.1362(3) Å, V = 312.32(2) Å^3, Z = 2.

Label	**Wyck. Pos.**	**x**	**y**	**z**	**Occ.**	**B_{iso} (Å^2)**
Li1	4b	0.2441(7)	0.3122(10)	-0.0029(13)	1	1.50(9)
Li2	2a	0	0.1493(15)	0.475(2)	1	2.4(2)
P	2a	0	0.8174(5)	0.9955(4)	1	0.71(5)
S1	4b	0.2177(4)	0.6717(6)	0.8864(6)	1	0.76(7)
S2	2a	0	0.1115(8)	0.8935(9)	1	0.55(10)
S3	2a	0	0.8094(9)	0.3274(6)	1	0.64(11)

A.1.2 β-Li_3PS_4

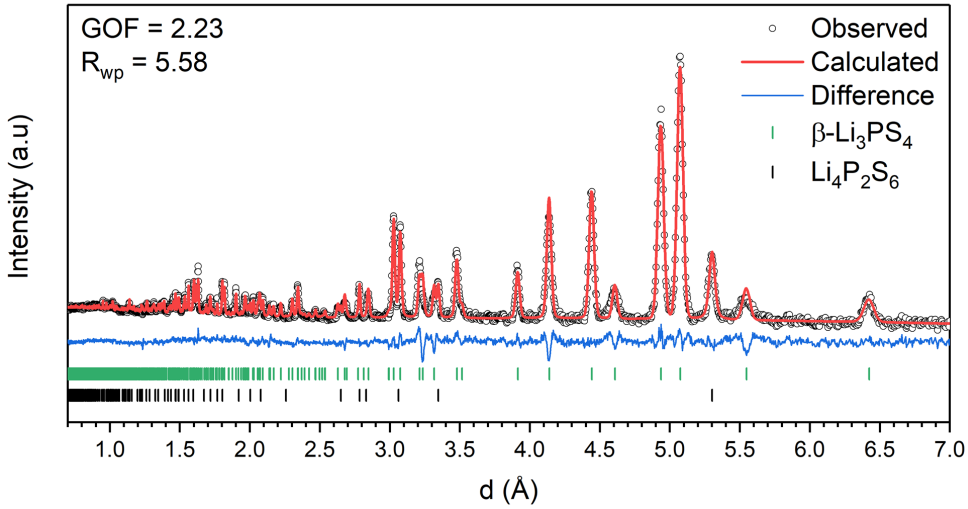

Figure A.2: Rietveld refinement of β-Li_3PS_4 using TOF neutron powder diffraction data measured at 350°C (contains 9 wt.% $Li_4P_2S_6$ impurity).

Table A.2: Crystallographic data of β-Li_3PS_4 obtained from Rietveld refinement of neutron powder diffraction at 350°C. Unit Cell: Orthorhombic *Pnma* (62). a = 12.8483(8) Å, b = 8.2772(5) Å, c = 6.1512(3) Å, V = 654.17(7) Å^3, Z = 4.

Label	Wyck. Pos.	x	y	z	Occ.	B_{iso} (Å^2)
Li1A	8d	0.8489(15)	0.032(2)	0.104(3)	0.666(14)	5.4(4)
Li1B	8d	0.841(3)	0.996(4)	0.371(6)	0.334(14)	5.4(4)
Li2	8d	0.009(3)	0.045(4)	0.582(5)	0.356(8)	5.4(4)
Li3	4c	0.916(5)	1/4	0.804(11)	0.288(16)	5.4(4)
P	4c	0.0876(4)	1/4	0.1772(10)	1	2.95(14)
S1	8d	0.1548(5)	0.0479(7)	0.2978(13)	1	2.50(11)
S2	4c	0.9360(7)	1/4	0.2543(17)	1	2.50(11)
S3	4c	0.1050(7)	1/4	0.8461(15)	1	2.50(11)

A.1.3 α-Li_3PS_4

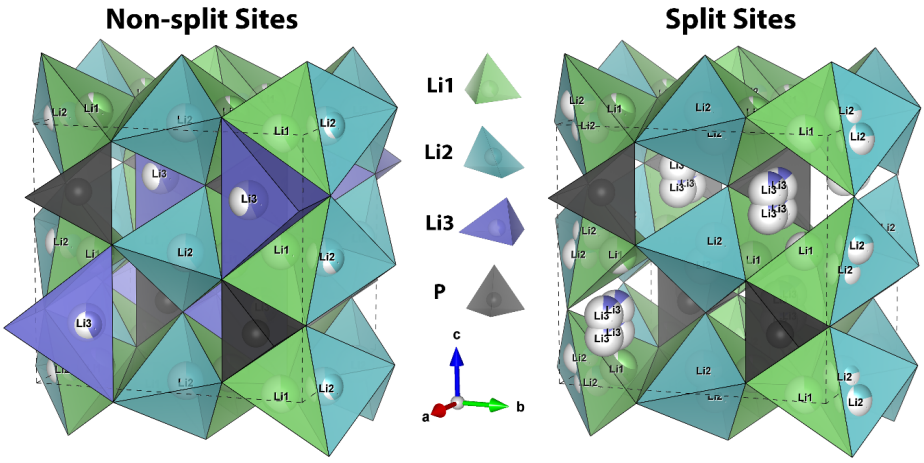

Figure A.3: Refined crystal structure of α-Li_3PS_4 using a model with no site splitting (left) compared to a model with all three lithium sites split (right). Sulfur atoms are omitted for clarity.

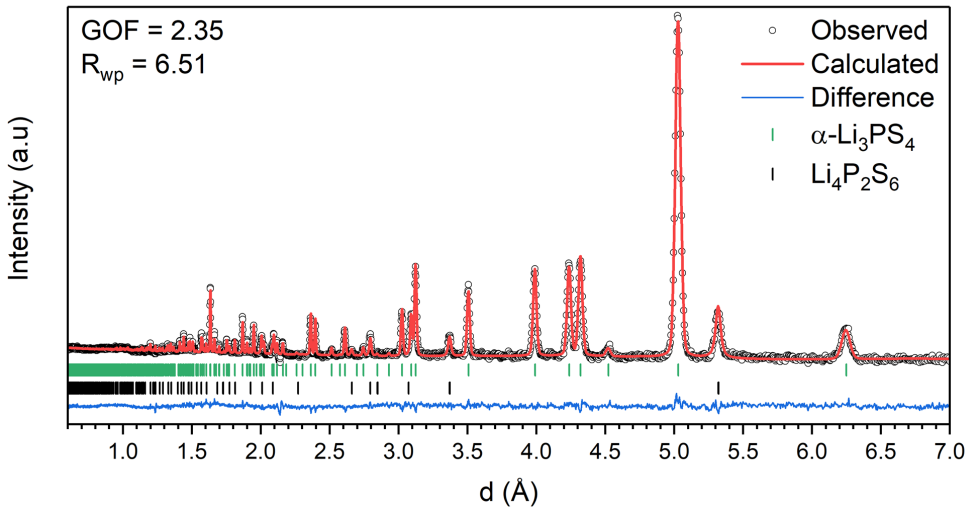

Figure A.4: Rietveld refinement of α-Li_3PS_4 (split-site model) using TOF neutron powder diffraction data measured at 500°C (contains 9 wt.% $Li_4P_2S_6$ impurity).

Table A.3: Crystallographic data of α-Li_3PS_4 (split-site model) obtained from Rietveld refinement of neutron powder diffraction at 500°C. Unit Cell: Orthorhombic *Cmcm* (63). a = 8.6437(5) Å, b = 9.0464(5) Å, c = 8.4781(5) Å, V = 662.94(7) Å^3, Z = 4.

Label	**Wyck. Pos.**	**x**	**y**	**z**	**Occ.**	**B_{iso} (Å^2)**
Li1	16h	0.724(2)	0.354(2)	0.528(2)	0.400(17)	7.9(8)
Li2	16h	0.716(4)	-0.021(6)	0.047(5)	0.219(11)	7.9(8)
Li3	16h	0.059(4)	0.196(5)	0.207(7)	0.130(15)	7.9(8)
P	4c	0	0.8315(5)	1/4	1	4.04(16)
S1	8g	0.3030(8)	0.4569(7)	1/4	1	5.91(17)
S2	8f	0	0.2944(7)	0.5547(8)	1	5.91(17)

Table A.4: Interatomic distances in α-Li_3PS_4 obtained from Rietveld refinement (using split-sites model) of neutron powder diffraction at 500°C.

Center Atom	**Second Atom**	**Interatomic Distance (Å)**
Li1	S2	2.45(2)
	S2	2.46(2)
	S1	2.54(2)
	S1	2.56(2)
Li2	S1	1.89(4)
	S2	2.65(5)
	S1	2.69(4)
	S2	2.77(5)
Li3	S2	2.45(6)
	S1	2.49(5)
	S1	3.11(4)
	S2	3.12(6)
P	S2	2.010(7) x 2
	S1	2.046(8) x 2

A.1.4 $Li_{3.25}Si_{0.25}P_{0.75}S_4$

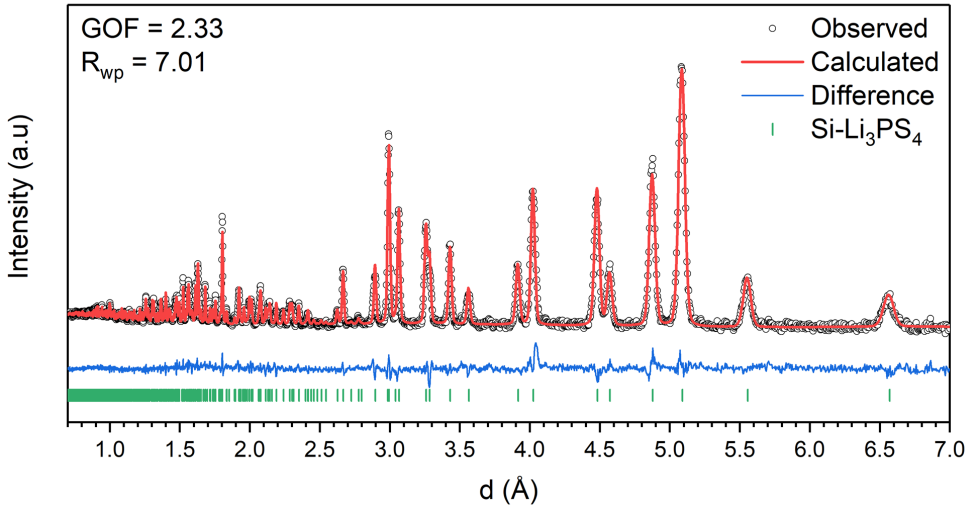

Figure A.5: Rietveld refinement of $Li_{3.25}Si_{0.25}P_{0.75}S_4$ using TOF neutron powder diffraction data measured at 25°C.

Table A.5: Crystallographic data of $Li_{3.25}Si_{0.25}P_{0.75}S_4$ obtained from Rietveld refinement of neutron powder diffraction at 25°C. Unit Cell: Orthorhombic *Pnma* (62). a = 13.1420(6) Å, b = 8.0510(3) Å, c = 6.1327(2) Å, V = 648.88(5) Å^3.

Label	Wyck. Pos.	x	y	z	Occ.	B_{iso} (Å^2)
Li1A	8d	0.3330(7)	0.0309(10)	0.3871(15)	0.886(13)	2.96(19)
Li1B	8d	0.360(4)	0.008(8)	0.223(11)	0.114(13)	2.96(19)
Li2	8d	0.0088(12)	0.0400(18)	0.558(2)	0.451(12)	2.1(4)
Li3A	4c	-0.087(5)	$\frac{1}{4}$	-0.159(15)	0.16(2)	2.0(8)
Li3B	4c	-0.080(4)	$\frac{1}{4}$	-0.301(10)	0.20(2)	2.0(8)
P	4c	0.0867(3)	$\frac{1}{4}$	0.1561(5)	0.75	1.58(7)
Si	4c	0.0867(3)	$\frac{1}{4}$	0.1561(5)	0.25	1.58(7)
S1	8d	0.1539(3)	0.0365(5)	0.2753(7)	1	2.02(10)
S2	4c	-0.0620(4)	$\frac{1}{4}$	0.2669(12)	1	1.59(12)
S3	4c	0.1029(4)	$\frac{1}{4}$	-0.1726(9)	1	1.39(11)

Appendix B

Supplementary Information for: Correlation of Structure and Fast Ion Conductivity in the Solid Solution Series $Li_{1+2x}Zn_{1-x}PS_4$

B.1 List of Supplementary Tables

Table B.1: Bond length data of the targeted $Li_{1.5}Zn_{0.75}PS_4$ (actual composition $Li_{1.194}Zn_{0.903}PS_4$ – i.e. $Li_{1.2}Zn_{0.9}PS_4$) and the targeted $Li_2Zn_{0.5}PS_4$ composition (actual composition $Li_{1.687}Zn_{0.656}PS_4$ – i.e. $Li_{1.7}Zn_{0.65}PS_4$) compared to the stoichiometric compound.

Composition	**Li - S (2b)**	**Li - S (2d)**	**Li/Zn - S (2a)**	**P-S**
$LiZnPS_4$	2.408	-	2.337	2.044
$Li_{1.194}Zn_{0.903}PS_4$	2.4044(15)*	2.5104(16)*	2.2939(17)	2.0967(16)
$Li_{1.687}Zn_{0.656}PS_4$	2.3837(14)	2.6222(14)	2.2897(15)	2.0689(14)

*refinement from synchrotron X-ray data; hence nominal value only

Table B.2: Fitted parameters for the impedance data of the targeted $Li_{1.5}Zn_{0.75}PS_4$ phase at 60°C.

Element	**Value**
CPE_1	1.054E-4 $F \cdot s^{a-1}$
a_1	0.7501
CPE_2	6.352E-10 $F \cdot s^{a-1}$
a_2	0.9301
R_2	3492 Ω

B.2 List of Supplementary Figures

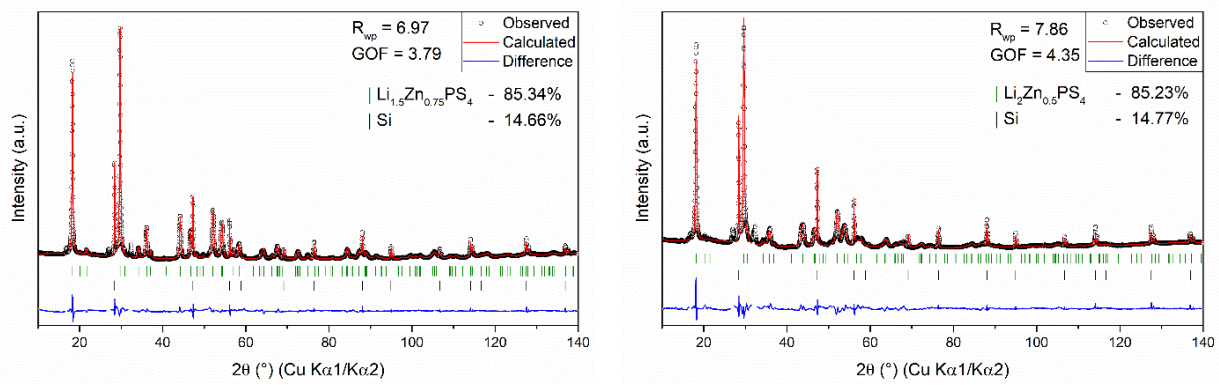

Figure B.1: Rietveld refinement of lab X-ray diffraction patterns of the targeted a) $Li_{1.5}Zn_{0.75}PS_4$ (70% crystallized) and b) $Li_2Zn_{0.5}PS_4$ (69% crystallized) phases mixed with 10 - 11% Si which was used as an internal standard to calculate degree of crystallinity.

Appendix C

Supplementary Information for: A Lithium Oxythioborosilicate Solid Electrolyte Glass with Superionic Conductivity

C.1 List of Supplementary Figures

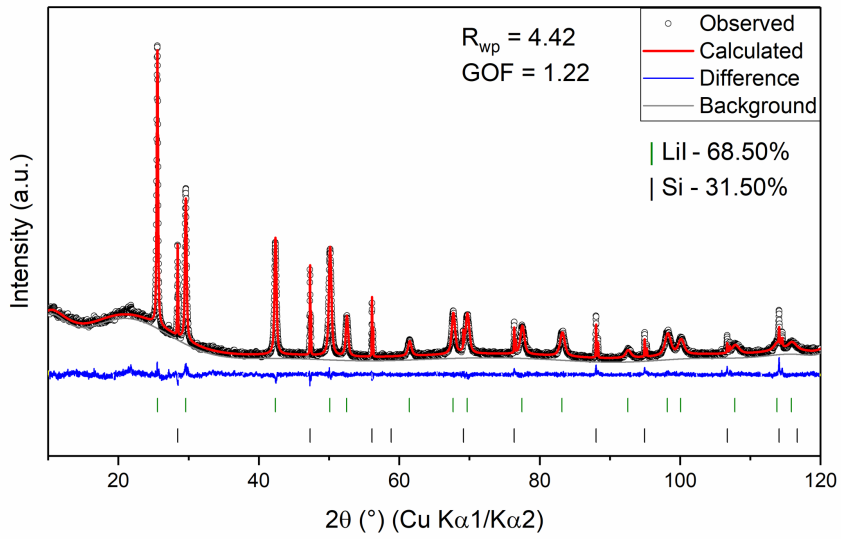

Figure C.1: Rietveld refinement of x = 0 composition mixed with approximately 10 weight percent Si, which was used as an internal standard to calculate the amount of crystalline LiI not dissolved in the glass.

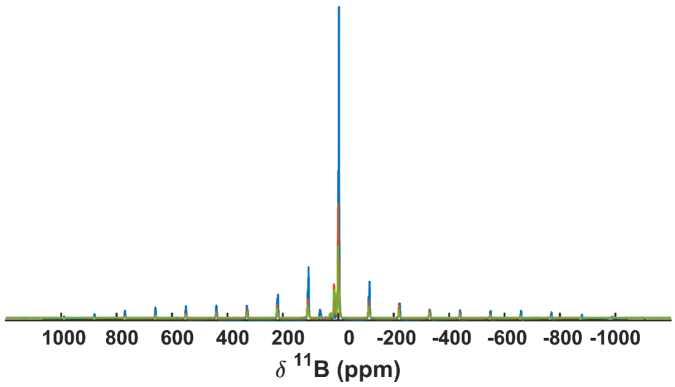

Figure C.2: ^{11}B NMR for the x = 0 (blue), 0.25 (orange) and 0.5 (green) compositions covering the entire spectral width showing the full size of the quadrupolar lineshape at high field and fast MAS, and without intensity scaling to reflect the boron dilution with increasing x.

Appendix D

Supporting Information for: Fast Li-Ion Conductivity in Superadamantanoid Thioborate Halides

D.1 Details of fitting Nyquist plots

Given that the measurement performed here is at very high frequencies (> 1 MHz), we see a pre-resistance that can be attributed to parasitic elements (e.g. stray inductance and resistance of wires/cell) This is simply modeled as parallel inductor and resistor (Inductor1 + Resistor 1), which gives rise to the initial shift and curvature at the beginning of the semi-circle.

In general, a semi-circle can be attributed to bulk or grain boundary conductivity. Since the CPE element is placed in parallel to a resistor (Resistor2 + CPE1), we can calculate the effective capacitance C_{eff} using the formula $C_{eff} = (RQ)^{1/\alpha}/R$. For the large semi-circle seen in Figure 6.3, a capacitance of 3.4×10^{-10} F is calculated, which implies the process stems from both grain and grain boundary contributions,[226] and thus the two contributions cannot be deconvoluted. The measured resistance represents the total.

Before the linear spike there is also a depressed semi-circle that we attribute to the solid electrolyte-indium interface. The effective capacitance for this component (Resistor 3 + CPE2) is 3.2×10^{-4} F, which is much higher than what is typically observed for any bulk or grain boundary contributions and close to what is expected for sample-electrode interfaces.[226] Finally, at low frequencies, we see a typical linear spike for cells measured in a blocking configuration (Warburg impedance) that is attributed to the accumulation of Li^+ ions at the interface. This is modelled by a CPE element (CPE 3).

In effect, the resistance of the large semi-circle (Resistor2) is equal to the value of the intersection of the semi-circle with the real part of the impedance (i.e. the higher value intercept with the x-axis). This resistance corresponds to the total resistance of the electrolyte and is used to calculate the total ionic conductivity of the electrolyte at each temperature.

D.2 Example of calculating Li and halide content based on impurity amount from refinement

Iodine material:

Approximately 8 wt%* of LiI impurity from refinement (for 1 g of $Li_{7.5}B_{10}S_{18}I_{1.5}$, ∼80 mg of LiI is in the mixture).

*Note: 8 wt% of LiI impurity in the final product corresponds to 37 mol% of the original LiI precursor.

$$x = 7.5 - a;\ y = 1.5 - a$$

$$Li_{7.5}B_{10}S_{18}I_{1.5} \rightarrow Li_xB_{10}S_{18}I_y + a \cdot LiI$$

- M_{LBSI}= 932.19 g/mol, m = 1g $n_1 = 1.07274\times10^{-3}$ mol
- M_{LiI} = 133.846 g/mol, m = 80 mg $n_2 = 5.977\times10^{-4}$ mol

$$a = \frac{n_2}{n_1} = 0.55566 \approx 0.56$$

$$x = 7.5 - 0.56 = 6.94$$

$$y = 1.5 - 0.56 = 0.94$$

Assuming no gaseous side products were formed during synthesis and assuming no amorphous phases are present in the mixture, the exact composition of the adamantane phase should be approximately $Li_{6.94}B_{10}S_{18}I_{0.94}$. Thus, Li content is then fixed to 7 in the Rietveld refinement.

Bromine material:

Approximately 7 wt%* of LiBr impurity from refinement (for 1 g of $Li_{7.5}B_{10}S_{18}Br_{1.5}$, ∼70 mg of LiBr is in the mixture)

*Note: 7 wt% of LiBr impurity in the final product corresponds to 46 mol% of the original LiBr precursor.

$$x = 7.5 - a;\ y = 1.5 - a$$

$$Li_{7.5}B_{10}S_{18}Br_{1.5} \rightarrow Li_xB_{10}S_{18}Br_y + a \cdot LiBr$$

- M_{LBSBr} = 857.19 g/mol, m = 1g $n_1 = 1.1666\times10^{-3}$ mol
- M_{LiBr} = 86.845 g/mol, m = 70 mg $n_2 = 8.0603\times10^{-4}$ mol

$$a = \frac{n_2}{n_1} = 0.690926 \approx 0.69$$

$$x = 7.5 - 0.69 = 6.81$$

$$y = 1.5 - 0.69 = 0.81$$

D.3 List of Supplementary Figures and Tables

D.3.1 Single-Crystal X-ray Diffraction

Table D.1: Crystallographic data for $Li_{7.5}B_{10}S_{18}X_{1.5}$ (X = Cl, Br, I) obtained from single crystal XRD.

Crystal Data			
Formula	$Li_{4.40}B_{10}S_{18}Cl_{1.80}$	$Li_{5.62}B_{10}S_{18}Br_{1.69}$	$Li_{6.75}B_{10}S_{18}I_{1.62}$
Formula Weight	779.54	859.17	937.06
Crystal System	Monoclinic	Monoclinic	Monoclinic
Space Group	$C2/c$ (No. 15)	$C2/c$ (No. 15)	$C2/c$ (No. 15)
a (Å)	21.162(2)	21.2106(13)	21.3186(12)
b (Å)	21.225(2)	21.2461(15)	21.2724(12)
c (Å)	16.1338(18)	16.2578(11)	16.2093(9)
β (°)	128.9178(19)	128.8222(14)	128.7696(14)
V (Å^3)	5638.3(10)	5708.0(7)	5731.3(6)
Z	8	8	8
Calc. Density (g/cm^3)	1.837	2.000	2.174
Abs.coef. μ (Mo Kα) (mm^{-1})	1.543	3.720	3.099
F(000)	3055	3312	3554
Crystal Size (mm)	0.04 × 0.13 × 0.13	0.02 × 0.09 × 0.10	0.02 × 0.07 × 0.1
Data Collection			
Temperature (K)	200	296	280
Radiation (Å)	Mo Kα, 0.71073	Mo Kα, 0.71073	Mo Kα, 0.71073
Theta range for data collection	1.6 - 28.0°	1.6 - 28.0°	1.6 - 28.0°
Index ranges	-27 ≤ h ≤ 24 27 ≤ k ≤ 28 -20 ≤ l ≤ 21	-28 ≤ h ≤ 28 -28 ≤ k ≤ 25 -21 ≤ l ≤ 21	-28 ≤ h ≤ 28 -28 ≤ k ≤ 28 -21 ≤ l ≤ 21
Reflections collected	30170	26218	31038
Independent reflections	6807 (R_{int} = 0.023)	6702 (R_{int} = 0.046)	6926 (R_{int} = 0.054)
Completeness to θ = 25.242°	100%	97%	100%
Absorption correction	Multi-scan	Multi-scan	Multi-scan
Max. and min. transmission	0.7460, 0.7025	0.7460, 0.6593	0.7460, 0.6605
Refinement			
Refinement method	Full-matrix least-squares on F^2	Full-matrix least-squares on F^2	Full-matrix least-squares on F^2
Data/restraints/parameters	6807/0/336	6702/0/377	6926/0/428
Goodness of fit on F^2	1.53	1.12	1.10
Final R indices [I>2sigma(I)]	R1 = 0.0636 wR2 = 0.1693	R1 = 0.0674 wR2 = 0.1656	R1 = 0.0510 wR2 = 0.1024
R indices (all data)	R1 = 0.0753 wR2 = 0.1693	R1 = 0.0971 wR2 = 0.1656	R1 = 0.0862 wR2 = 0.1024
Largest diff. peak and hole	-0.97 and 5.41 e·Å^{-3}	-1.72 and 2.30 e·Å^{-3}	-2.36 and 2.53 e·Å^{-3}

Table D.2: Atomic coordinates, occupation factor, and equivalent isotropic displacement parameters of $Li_{7.5}B_{10}S_{18}Cl_{1.5}$ obtained from single-crystal XRD measured at 200 K.

Atom	Wyck. Pos.	x	y	z	Occ.	U_{iso} (Å^2)
B1	8f	0.0440(4)	0.1592(3)	0.4661(6)	1	0.0128(13)
B2	8f	0.0891(4)	0.1314(3)	0.0169(5)	1	0.0115(12)
B3	8f	0.0910(4)	0.0687(3)	0.1937(5)	1	0.0104(12)
B4	8f	0.1230(4)	0.2137(3)	0.2019(5)	1	0.0112(12)
B5	8f	0.2260(4)	0.1028(3)	0.0106(5)	1	0.0125(13)
B6	8f	0.2294(4)	0.0416(3)	0.1825(5)	1	0.0110(12)
B7	8f	0.2621(4)	0.1853(3)	0.1904(5)	1	0.0115(12)
B8	8f	0.2658(4)	0.1225(3)	0.3682(5)	1	0.0107(12)
B9	8f	0.2673(4)	0.4838(3)	0.1425(5)	1	0.0118(12)
B10	8f	0.2938(4)	0.2633(3)	0.3688(5)	1	0.0127(13)
S1	8f	0.01133(9)	0.23054(7)	0.12779(12)	1	0.0130(3)
S2	8f	0.02093(9)	0.08456(7)	0.38396(12)	1	0.0122(3)
S3	8f	0.02223(9)	0.15068(7)	0.56457(12)	1	0.0133(3)
S4	8f	0.11349(9)	0.05420(7)	0.09646(11)	1	0.0104(3)
S5	8f	0.14748(9)	0.20413(7)	0.10545(11)	1	0.0105(3)
S6	8f	0.15082(9)	0.13929(7)	0.28833(11)	1	0.0103(3)
S7	8f	0.15868(9)	0.16299(7)	0.54412(12)	1	0.0121(3)
S8	8f	0.18066(9)	0.28315(7)	0.29265(12)	1	0.0136(3)
S9	8f	0.23855(9)	0.40373(7)	0.07278(12)	1	0.0125(3)
S10	8f	0.24071(9)	0.46785(7)	0.23463(12)	1	0.0127(3)
S11	8f	0.25636(9)	0.02703(7)	0.09308(12)	1	0.0119(3)
S12	8f	0.28791(10)	0.17457(7)	0.09852(13)	1	0.0159(3)
S13	8f	0.29452(9)	0.11056(7)	0.27714(11)	1	0.0101(3)
S14	8f	0.29407(9)	0.05157(7)	0.45509(12)	1	0.0135(3)
S15	8f	0.32286(9)	0.25500(7)	0.27837(12)	1	0.0135(3)
S16	8f	0.32579(9)	0.19109(7)	0.46079(12)	1	0.0121(3)
S17	8f	0.38324(9)	0.49629(7)	0.22272(12)	1	0.0129(3)
S18	8f	0.38883(9)	0.37926(7)	0.07896(12)	1	0.0135(3)
Li1	4e	0	0.1645(10)	0.25	0.81(8)	0.019(7)
Li2	4e	0.5	0.4368(14)	0.25	1.02(10)	0.050(9)
Li3	8f	0.1736(12)	-0.0569(9)	-0.0379(15)	0.76(6)	0.033(7)
Li4	8f	0.4711(14)	0.2399(14)	0.373(3)	0.65(7)	0.058(12)
Li5	8f	-0.0288(17)	0.3409(15)	0.074(3)	0.70(8)	0.085(17)
Li6	8f	0.342(2)	0.3843(17)	0.284(2)	0.58(7)	0.060(14)
Li7	4d	0.25	0.25	0.5	0.63(10)	0.056(16)
Li8	8f	0.348(3)	0.269(2)	0.084(4)	0.49(8)	0.08(2)
Cl1	4e	0.5	0.2329(3)	0.25	0.836(16)	0.080(3)
Cl2	8f	0.0297(3)	0.3591(2)	-0.0253(6)	0.853(14)	0.123(3)
Cl3	4e	0	0.5543(4)	0.25	1.06(2)	0.240(9)

Table D.3: Anisotropic displacement parameters of $Li_{7.5}B_{10}S_{18}Cl_{1.5}$ obtained from single-crystal XRD measured at 200 K.

Atom	$\mathbf{U_{11}}$	$\mathbf{U_{22}}$	$\mathbf{U_{33}}$	$\mathbf{U_{23}}$	$\mathbf{U_{13}}$	$\mathbf{U_{12}}$
B1	0.010(3)	0.013(3)	0.013(3)	-0.001(2)	0.006(3)	-0.001(2)
B2	0.010(3)	0.014(3)	0.011(3)	-0.001(2)	0.006(3)	-0.001(2)
B3	0.010(3)	0.012(3)	0.012(3)	0.000(2)	0.008(3)	-0.001(2)
B4	0.010(3)	0.012(3)	0.011(3)	0.000(2)	0.006(3)	-0.001(2)
B5	0.017(3)	0.012(3)	0.013(3)	-0.002(2)	0.011(3)	-0.002(3)
B6	0.012(3)	0.012(3)	0.010(3)	0.000(2)	0.008(3)	0.000(2)
B7	0.011(3)	0.013(3)	0.012(3)	-0.002(2)	0.008(3)	-0.001(2)
B8	0.010(3)	0.013(3)	0.011(3)	-0.001(2)	0.007(3)	-0.001(2)
B9	0.015(3)	0.011(3)	0.012(3)	-0.001(2)	0.010(3)	-0.001(2)
B10	0.010(3)	0.014(3)	0.012(3)	-0.004(2)	0.005(3)	-0.001(2)
S1	0.0085(6)	0.0145(7)	0.0145(7)	-0.0025(5)	0.0065(6)	-0.0006(5)
S2	0.0093(6)	0.0129(7)	0.0141(7)	-0.0014(5)	0.0072(6)	0.0004(5)
S3	0.0094(6)	0.0184(7)	0.0100(6)	-0.0005(5)	0.0050(6)	-0.0008(5)
S4	0.0111(6)	0.0111(6)	0.0105(6)	-0.0007(5)	0.0074(6)	-0.0007(5)
S5	0.0102(6)	0.0112(6)	0.0102(6)	-0.0006(5)	0.0065(6)	-0.0004(5)
S6	0.0093(6)	0.0123(7)	0.0105(6)	-0.0012(5)	0.0067(6)	-0.0007(5)
S7	0.0086(6)	0.0116(7)	0.0131(7)	-0.0034(5)	0.0054(6)	-0.0006(5)
S8	0.0103(7)	0.0132(7)	0.0147(7)	-0.0048(5)	0.0066(6)	-0.0010(5)
S9	0.0174(7)	0.0116(7)	0.0148(7)	-0.0025(5)	0.0131(6)	-0.0034(5)
S10	0.0165(7)	0.0119(7)	0.0143(7)	-0.0016(5)	0.0118(6)	-0.0022(5)
S11	0.0150(7)	0.0126(7)	0.0123(7)	-0.0010(5)	0.0106(6)	-0.0003(5)
S12	0.0220(8)	0.0155(7)	0.0199(8)	-0.0065(6)	0.0178(7)	-0.0075(6)
S13	0.0103(6)	0.0105(6)	0.0103(6)	-0.0007(5)	0.0069(6)	-0.0006(5)
S14	0.0164(7)	0.0126(7)	0.0101(7)	0.0000(5)	0.0076(6)	-0.0017(6)
S15	0.0143(7)	0.0127(7)	0.0152(7)	-0.0045(5)	0.0101(6)	-0.0044(5)
S16	0.0114(6)	0.0122(7)	0.0107(6)	-0.0025(5)	0.0059(6)	-0.0012(5)
S17	0.0126(7)	0.0131(7)	0.0143(7)	-0.0027(5)	0.0090(6)	0.0005(5)
S18	0.0143(7)	0.0174(7)	0.0109(7)	-0.0020(5)	0.0090(6)	-0.0015(6)
Li2	0.031(13)	0.070(19)	0.041(14)	0	0.019(11)	0
Li3	0.040(12)	0.038(12)	0.034(11)	-0.012(8)	0.030(10)	-0.016(8)
Li4	0.018(12)	0.057(19)	0.09(2)	-0.021(16)	0.026(14)	0.004(11)
Li5	0.031(15)	0.051(19)	0.09(3)	0.020(16)	-0.002(15)	-0.007(12)
Li6	0.06(2)	0.07(2)	0.036(17)	0.036(15)	0.022(16)	0.053(18)
Li8	0.07(3)	0.06(3)	0.08(3)	0.02(2)	0.04(3)	-0.03(2)
Cl1	0.063(4)	0.058(3)	0.152(7)	0	0.083(4)	0
Cl2	0.044(2)	0.083(4)	0.187(7)	0.035(4)	0.047(3)	-0.013(2)
Cl3	0.037(3)	0.085(5)	0.391(18)	0	0.035(6)	0

Table D.4: Atomic coordinates, occupation factor, and equivalent isotropic displacement parameters of $Li_{7.5}B_{10}S_{18}Br_{1.5}$ obtained from single-crystal XRD measured at 296 K.

Atom	Wyck. Pos.	x	y	z	Occ.	U_{iso} (Å^2)
B1	8f	0.0453(4)	0.1584(3)	0.4653(5)	1	0.0045(6)
B2	8f	0.0888(5)	0.1312(4)	0.0190(7)	1	0.0142(16)
B3	8f	0.0911(4)	0.0680(4)	0.1938(6)	1	0.0125(15)
B4	8f	0.1220(4)	0.2131(3)	0.2023(5)	1	0.0045(6)
B5	8f	0.2271(4)	0.1037(3)	0.0117(5)	1	0.0045(6)
B6	8f	0.2294(5)	0.0419(4)	0.1828(6)	1	0.0123(15)
B7	8f	0.2609(4)	0.1858(4)	0.1902(6)	1	0.0110(15)
B8	8f	0.2655(5)	0.1224(4)	0.3675(6)	1	0.0115(15)
B9	8f	0.2665(4)	0.4813(3)	0.1422(5)	1	0.0045(6)
B10	8f	0.2926(4)	0.2643(4)	0.3701(6)	1	0.0103(14)
S1	8f	0.01035(10)	0.22942(8)	0.12886(15)	1	0.0153(4)
S2	8f	0.02094(10)	0.08330(8)	0.38371(14)	1	0.0141(4)
S3	8f	0.02287(10)	0.15014(9)	0.56371(14)	1	0.0162(4)
S4	8f	0.11386(10)	0.05413(8)	0.09750(14)	1	0.0119(3)
S5	8f	0.14665(10)	0.20412(8)	0.10641(14)	1	0.0120(3)
S6	8f	0.15049(10)	0.13855(8)	0.28852(14)	1	0.0114(3)
S7	8f	0.15974(10)	0.16254(8)	0.54326(15)	1	0.0156(4)
S8	8f	0.17881(10)	0.28292(8)	0.29233(15)	1	0.0156(4)
S9	8f	0.23812(12)	0.40199(9)	0.07221(16)	1	0.0191(4)
S10	8f	0.23987(11)	0.46713(8)	0.23563(15)	1	0.0172(4)
S11	8f	0.25658(11)	0.02687(8)	0.09368(14)	1	0.0148(4)
S12	8f	0.28748(12)	0.17629(9)	0.10005(16)	1	0.0197(4)
S13	8f	0.29431(10)	0.11086(8)	0.27729(14)	1	0.0116(3)
S14	8f	0.29499(11)	0.05136(8)	0.45489(14)	1	0.0162(4)
S15	8f	0.32115(11)	0.25586(8)	0.27818(15)	1	0.0157(4)
S16	8f	0.32470(10)	0.19097(8)	0.45999(14)	1	0.0140(4)
S17	8f	0.38398(11)	0.49497(8)	0.22432(15)	1	0.0158(4)
S18	8f	0.39011(11)	0.37970(9)	0.07825(14)	1	0.0159(4)
Li1	4e	0	0.1628(11)	0.25	0.74(8)	0.016(8)
Li2	8f	0.4677(18)	0.1610(13)	0.580(3)	0.53(7)	0.040(12)
Li3	4e	0.5	0.4379(19)	0.25	0.50(8)	0.020(13)
Li4	8f	0.4680(18)	0.2368(15)	0.381(3)	0.48(6)	0.033(12)
Li5	4d	0.25	0.25	0.5	0.88(12)	0.13(3)
Li6	8f	0.351(3)	0.272(2)	0.088(4)	0.59(9)	0.09(2)
Li7	8f	0.168(5)	0.357(4)	0.167(5)	0.54(11)	0.25(9)
Li8	8f	0.114(3)	0.000(2)	-0.077(4)	0.59(9)	0.076(19)
Li9	8f	0.1745(16)	-0.0563(12)	-0.037(2)	0.72(7)	0.046(10)
Li10	8f	0.159(3)	0.113(3)	0.716(5)	0.79(13)	0.16(3)
Li11	8f	0.119(4)	0.070(4)	0.633(6)	0.32(9)	0.06(3)
Br1	4e	0.5	0.23172(12)	0.25	0.801(5)	0.0563(8)
Br2	8f	0.03096(19)	0.36638(19)	-0.0051(3)	0.474(6)	0.0966(19)
Br3	4e	0	0.3867(2)	0.25	0.448(8)	0.109(3)
Br4	4e	0.5	0.05272(19)	0.25	0.623(11)	0.228(6)
Br5	8f	0.5038(11)	0.0064(8)	0.5351(18)	0.111(5)	0.105(11)
Br6	8f	0.5164(6)	0.0754(6)	0.5436(10)	0.109(3)	0.0563(16)
Br7	8f	0.5202(11)	0.0850(11)	0.6420(19)	0.059(3)	0.0563(16)

Table D.5: Anisotropic displacement parameters of $Li_{7.5}B_{10}S_{18}Br_{1.5}$ obtained from single-crystal XRD measured at 296 K.

Atom	$\mathbf{U_{11}}$	$\mathbf{U_{22}}$	$\mathbf{U_{33}}$	$\mathbf{U_{23}}$	$\mathbf{U_{13}}$	$\mathbf{U_{12}}$
B1	0.0059(15)	0.0054(15)	0.0045(16)	-0.0008(12)	0.0044(13)	-0.0009(12)
B2	0.011(3)	0.014(4)	0.014(4)	-0.002(3)	0.006(3)	-0.002(3)
B3	0.008(3)	0.016(4)	0.014(4)	0.000(3)	0.007(3)	0.001(3)
B4	0.0059(15)	0.0054(15)	0.0045(16)	-0.0008(12)	0.0044(13)	-0.0009(12)
B5	0.0059(15)	0.0054(15)	0.0045(16)	-0.0008(12)	0.0044(13)	-0.0009(12)
B6	0.012(3)	0.015(4)	0.011(4)	0.000(3)	0.008(3)	0.001(3)
B7	0.008(3)	0.014(4)	0.013(4)	0.000(3)	0.008(3)	0.001(3)
B8	0.010(3)	0.013(4)	0.009(4)	0.001(3)	0.005(3)	-0.001(3)
B9	0.0059(15)	0.0054(15)	0.0045(16)	-0.0008(12)	0.0044(13)	-0.0009(12)
B10	0.006(3)	0.012(3)	0.010(4)	-0.003(3)	0.004(3)	-0.002(3)
S1	0.0107(8)	0.0168(8)	0.0165(9)	-0.0016(7)	0.0076(7)	0.0003(6)
S2	0.0107(7)	0.0163(8)	0.0154(9)	-0.0010(7)	0.0082(7)	0.0010(6)
S3	0.0106(8)	0.0226(9)	0.0129(9)	-0.0019(7)	0.0061(7)	-0.0021(7)
S4	0.0124(8)	0.0135(8)	0.0107(8)	-0.0002(6)	0.0077(7)	-0.0003(6)
S5	0.0119(7)	0.0129(8)	0.0118(8)	0.0003(6)	0.0077(7)	-0.0003(6)
S6	0.0109(7)	0.0128(8)	0.0116(8)	-0.0018(6)	0.0075(7)	-0.0015(6)
S7	0.0105(8)	0.0163(8)	0.0167(9)	-0.0018(7)	0.0068(7)	0.0001(6)
S8	0.0134(8)	0.0147(8)	0.0161(9)	-0.0046(7)	0.0079(7)	-0.0016(6)
S9	0.0230(9)	0.0198(9)	0.0188(10)	-0.0007(7)	0.0152(8)	-0.0015(7)
S10	0.0204(9)	0.0141(8)	0.0199(10)	-0.0037(7)	0.0141(8)	-0.0032(7)
S11	0.0163(8)	0.0175(8)	0.0147(9)	-0.0012(7)	0.0116(7)	0.0003(7)
S12	0.0254(9)	0.0208(9)	0.0254(10)	-0.0031(8)	0.0220(9)	-0.0046(7)
S13	0.0114(7)	0.0128(8)	0.0120(8)	0.0000(6)	0.0079(7)	-0.0001(6)
S14	0.0204(9)	0.0150(8)	0.0129(9)	0.0014(7)	0.0103(7)	-0.0005(7)
S15	0.0161(8)	0.0150(8)	0.0177(9)	-0.0038(7)	0.0114(8)	-0.0052(7)
S16	0.0129(8)	0.0147(8)	0.0122(9)	-0.0028(6)	0.0068(7)	-0.0013(6)
S17	0.0183(8)	0.0149(8)	0.0161(9)	-0.0024(7)	0.0117(7)	0.0009(7)
S18	0.0166(8)	0.0202(9)	0.0130(9)	-0.0014(7)	0.0102(7)	-0.0014(7)
Li2	0.026(16)	0.021(16)	0.06(2)	-0.017(14)	0.020(16)	0.002(11)
Li3	0.015(19)	0.04(2)	0.02(2)	0	0.016(17)	0
Li4	0.018(16)	0.027(18)	0.05(2)	-0.004(15)	0.020(16)	0.003(12)
Li5	0.24(7)	0.11(4)	0.08(3)	0.07(3)	0.12(4)	0.14(4)
Li6	0.07(3)	0.07(3)	0.10(4)	0.03(3)	0.04(3)	-0.02(2)
Li7	0.17(8)	0.22(9)	0.10(5)	0.10(6)	-0.04(5)	-0.17(7)
Li8	0.06(3)	0.07(3)	0.09(4)	0.01(2)	0.05(3)	-0.01(2)
Li9	0.050(17)	0.046(16)	0.056(18)	0.005(12)	0.039(15)	-0.011(12)
Li10	0.12(4)	0.14(5)	0.12(5)	0.03(4)	0.04(4)	0.08(4)
Li11	0.02(3)	0.08(6)	0.07(6)	0.02(4)	0.03(3)	0.02(3)
Br1	0.0325(10)	0.0697(14)	0.0686(15)	0	0.0326(10)	0
Br2	0.0453(18)	0.104(3)	0.102(3)	0.019(2)	0.0280(18)	-0.0285(18)
Br3	0.134(5)	0.038(2)	0.031(3)	0	-0.008(3)	0
Br4	0.048(3)	0.042(2)	0.369(12)	0	0.022(4)	0
Br5	0.048(7)	0.031(8)	0.17(3)	-0.021(10)	0.037(13)	0.003(6)
Br6	0.033(3)	0.0697(10)	0.0686(14)	0	0.0326(15)	0
Br7	0.033(3)	0.0697(10)	0.0686(14)	0	0.0326(15)	0

Table D.6: Atomic coordinates, occupation factor, and equivalent isotropic displacement parameters of $Li_{7.5}B_{10}S_{18}I_{1.5}$ obtained from single-crystal XRD measured at 280 K.

Atom	Wyck. Pos.	x	y	z	Occ.	U_{iso} (Å^2)
B1	8f	0.0473(3)	0.1607(3)	0.4681(4)	1	0.0122(10)
B2	8f	0.0836(3)	0.1328(3)	0.0130(4)	1	0.0134(11)
B3	8f	0.0866(3)	0.0700(3)	0.1896(4)	1	0.0130(11)
B4	8f	0.1186(3)	0.2153(3)	0.1986(4)	1	0.0135(11)
B5	8f	0.2190(3)	0.1027(2)	0.0049(4)	1	0.0089(10)
B6	8f	0.2229(3)	0.0419(3)	0.1767(4)	1	0.0130(11)
B7	8f	0.2559(3)	0.1852(3)	0.1854(4)	1	0.0152(11)
B8	8f	0.2604(3)	0.1229(3)	0.3632(4)	1	0.0149(11)
B9	8f	0.2730(3)	0.4829(2)	0.1480(4)	1	0.0097(10)
B10	8f	0.2897(3)	0.2628(3)	0.3665(4)	1	0.0136(11)
S1	8f	0.00796(7)	0.23261(6)	0.12446(10)	1	0.0163(3)
S2	8f	0.02430(7)	0.08617(6)	0.38664(10)	1	0.0155(3)
S3	8f	0.02652(7)	0.15279(6)	0.56746(9)	1	0.0174(3)
S4	8f	0.10788(7)	0.05538(6)	0.09169(9)	1	0.0129(2)
S5	8f	0.14277(7)	0.20534(6)	0.10186(9)	1	0.0132(2)
S6	8f	0.14631(7)	0.14030(6)	0.28427(9)	1	0.0126(2)
S7	8f	0.16117(7)	0.16451(6)	0.54477(9)	1	0.0152(3)
S8	8f	0.17715(7)	0.28382(6)	0.28997(10)	1	0.0166(3)
S9	8f	0.24509(7)	0.40363(6)	0.07749(10)	1	0.0162(3)
S10	8f	0.24727(8)	0.46806(6)	0.24080(10)	1	0.0177(3)
S11	8f	0.25040(7)	0.02752(6)	0.08865(9)	1	0.0152(2)
S12	8f	0.28069(8)	0.17479(6)	0.09305(10)	1	0.0177(3)
S13	8f	0.28781(7)	0.11066(6)	0.27139(9)	1	0.0130(2)
S14	8f	0.28873(7)	0.05146(6)	0.44970(9)	1	0.0163(3)
S15	8f	0.31812(7)	0.25422(6)	0.27517(10)	1	0.0166(3)
S16	8f	0.32116(7)	0.19033(6)	0.45636(9)	1	0.0159(3)
S17	8f	0.38813(7)	0.49736(6)	0.22730(10)	1	0.0164(3)
S18	8f	0.39486(7)	0.37861(6)	0.08337(9)	1	0.0166(3)
Li1	8f	0.1737(8)	-0.0583(7)	-0.0377(11)	0.88(4)	0.046(5)
Li2	8f	0.4651(11)	0.2291(9)	0.392(2)	0.63(5)	0.070(12)
Li3	4d	0.25	0.25	0.5	0.96(8)	0.14(2)
Li4	8f	0.336(2)	0.3803(15)	0.281(2)	0.63(6)	0.105(17)
Li5	8f	-0.0356(19)	0.3429(15)	0.083(3)	0.41(5)	0.071(16)
Li6	4e	0	0.1670(8)	0.25	0.92(6)	0.036(6)
Li7	4e	0	0.9388(9)	0.25	0.89(6)	0.038(7)
Li8	8f	0.152(3)	0.379(3)	0.189(4)	0.54(7)	0.29(7)
Li9	8f	0.104(2)	0.614(3)	0.381(4)	0.47(6)	0.16(4)
Li10	8f	0.390(4)	0.431(3)	0.379(7)	0.27(6)	0.09(4)
Li11	8f	0.3468(17)	0.2683(13)	0.081(2)	0.43(4)	0.055(13)
Li12	8f	0.109(5)	0.002(4)	-0.077(6)	0.12(4)	0.03(3)
Li13	8f	0.444(3)	0.208(3)	0.446(5)	0.16(4)	0.03(2)
I1A	8f	0.4735(3)	0.1133(5)	0.0085(3)	0.352(11)	0.1054(18)
I1B	8f	0.4811(3)	0.09940(19)	0.0069(5)	0.273(11)	0.086(2)
I2	4e	0	0.72079(4)	0.25	0.843(3)	0.0574(4)
I3	4b	0	0.5	0	0.119(4)	0.124(6)
I4A	4e	0	0.50156(18)	0.25	0.259(3)	0.0667(15)
I4B	8f	0.0053(5)	0.5478(4)	0.3138(9)	0.094(3)	0.116(5)
I5A	4e	0	0.4082(4)	0.25	0.252(8)	0.218(8)

Table D.7: Anisotropic displacement parameters of $Li_{7.5}B_{10}S_{18}I_{1.5}$ obtained from single-crystal XRD measured at 280 K.

Atom	U_{11}	U_{22}	U_{33}	U_{23}	U_{13}	U_{12}
B1	0.008(2)	0.014(3)	0.012(2)	-0.002(2)	0.005(2)	-0.001(2)
B2	0.013(2)	0.015(3)	0.013(3)	0.000(2)	0.008(2)	0.002(2)
B3	0.011(2)	0.013(3)	0.015(3)	0.000(2)	0.008(2)	-0.001(2)
B4	0.011(2)	0.016(3)	0.014(3)	-0.001(2)	0.008(2)	0.000(2)
B5	0.010(2)	0.010(2)	0.010(2)	0.000(2)	0.007(2)	0.000(2)
B6	0.012(2)	0.014(3)	0.014(3)	0.002(2)	0.008(2)	0.003(2)
B7	0.012(2)	0.018(3)	0.013(3)	-0.001(2)	0.007(2)	-0.001(2)
B8	0.011(2)	0.018(3)	0.012(3)	-0.001(2)	0.005(2)	-0.002(2)
B9	0.011(2)	0.013(3)	0.008(2)	-0.001(2)	0.007(2)	-0.001(2)
B10	0.009(2)	0.014(3)	0.015(3)	0.000(2)	0.005(2)	0.000(2)
S1	0.0098(5)	0.0169(6)	0.0190(6)	-0.0016(5)	0.0075(5)	0.0006(5)
S2	0.0094(5)	0.0163(6)	0.0183(6)	-0.0026(5)	0.0074(5)	-0.0003(5)
S3	0.0111(5)	0.0247(7)	0.0131(6)	-0.0019(5)	0.0060(5)	-0.0021(5)
S4	0.0115(5)	0.0141(6)	0.0125(5)	-0.0004(5)	0.0072(5)	-0.0001(5)
S5	0.0110(5)	0.0143(6)	0.0129(6)	0.0002(5)	0.0068(5)	-0.0004(5)
S6	0.0109(5)	0.0139(6)	0.0126(6)	-0.0014(5)	0.0071(5)	-0.0010(4)
S7	0.0094(5)	0.0145(6)	0.0174(6)	-0.0042(5)	0.0063(5)	-0.0015(5)
S8	0.0116(5)	0.0158(6)	0.0183(6)	-0.0044(5)	0.0074(5)	-0.0016(5)
S9	0.0184(6)	0.0164(6)	0.0179(6)	-0.0032(5)	0.0134(5)	-0.0035(5)
S10	0.0227(6)	0.0155(6)	0.0198(6)	-0.0036(5)	0.0158(5)	-0.0044(5)
S11	0.0169(6)	0.0166(6)	0.0153(6)	-0.0003(5)	0.0117(5)	0.0002(5)
S12	0.0205(6)	0.0188(6)	0.0210(6)	-0.0041(5)	0.0165(5)	-0.0056(5)
S13	0.0113(5)	0.0150(6)	0.0129(6)	-0.0009(5)	0.0077(5)	-0.0006(5)
S14	0.0170(6)	0.0155(6)	0.0141(6)	0.0027(5)	0.0087(5)	0.0009(5)
S15	0.0163(6)	0.0165(6)	0.0183(6)	-0.0042(5)	0.0115(5)	-0.0051(5)
S16	0.0137(5)	0.0157(6)	0.0134(6)	-0.0024(5)	0.0061(5)	-0.0011(5)
S17	0.0141(5)	0.0167(6)	0.0183(6)	-0.0039(5)	0.0102(5)	-0.0011(5)
S18	0.0147(6)	0.0224(7)	0.0132(6)	-0.0014(5)	0.0090(5)	-0.0004(5)
I1A	0.055(2)	0.196(5)	0.0521(18)	0.000(2)	0.0268(14)	-0.052(2)
I1B	0.0257(15)	0.034(3)	0.146(5)	0.0114(17)	0.0285(18)	-0.0004(12)
I2	0.0239(4)	0.0569(6)	0.0724(7)	0	0.0209(4)	0
I3	0.101(8)	0.057(6)	0.208(14)	-0.010(7)	0.094(9)	0.000(5)
I4A	0.0441(18)	0.081(3)	0.0429(19)	0	0.0117(14)	0
I4B	0.059(5)	0.071(6)	0.169(10)	-0.044(5)	0.048(6)	-0.009(4)
I5A	0.244(11)	0.214(9)	0.034(3)	0	0.008(4)	0
Li1	0.049(9)	0.048(9)	0.052(9)	-0.017(7)	0.037(8)	-0.024(7)
Li2	0.026(10)	0.023(11)	0.09(2)	-0.011(11)	0.006(11)	0.016(8)
Li3	0.22(4)	0.15(3)	0.17(3)	0.05(2)	0.18(3)	0.11(3)
Li4	0.13(3)	0.09(2)	0.07(2)	0.049(18)	0.05(2)	0.09(2)
Li5	0.05(2)	0.035(19)	0.06(2)	0.007(16)	-0.002(16)	-0.010(14)
Li6	0.060(12)	0.034(10)	0.041(11)	0	0.045(10)	0
Li7	0.024(9)	0.048(12)	0.037(11)	0	0.016(8)	0
Li8	0.15(5)	0.23(7)	0.15(5)	0.15(5)	-0.07(3)	-0.15(5)
Li9	0.03(2)	0.22(6)	0.14(5)	0.13(4)	0.01(2)	0.00(3)
Li10	0.08(5)	0.09(5)	0.14(7)	0.05(5)	0.08(5)	0.03(4)
Li11	0.053(19)	0.033(17)	0.054(19)	0.015(13)	0.021(15)	-0.028(13)

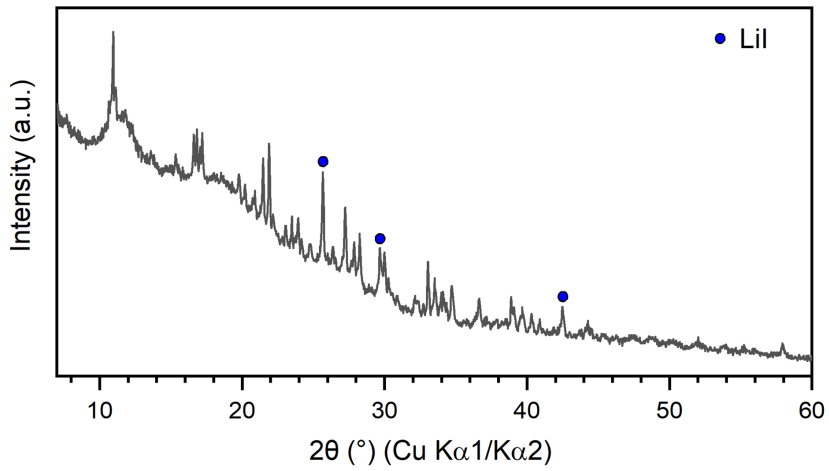

Figure D.1: Powder X-ray diffraction pattern of $Li_7B_{10}S_{18}I$ with LiI impurities (marked by blue circles). Large background comes from the vacuum grease and Kapton film used to protect the sample from air and moisture exposure during measurement.

D.3.2 TOF Neutron Powder Diffraction Data

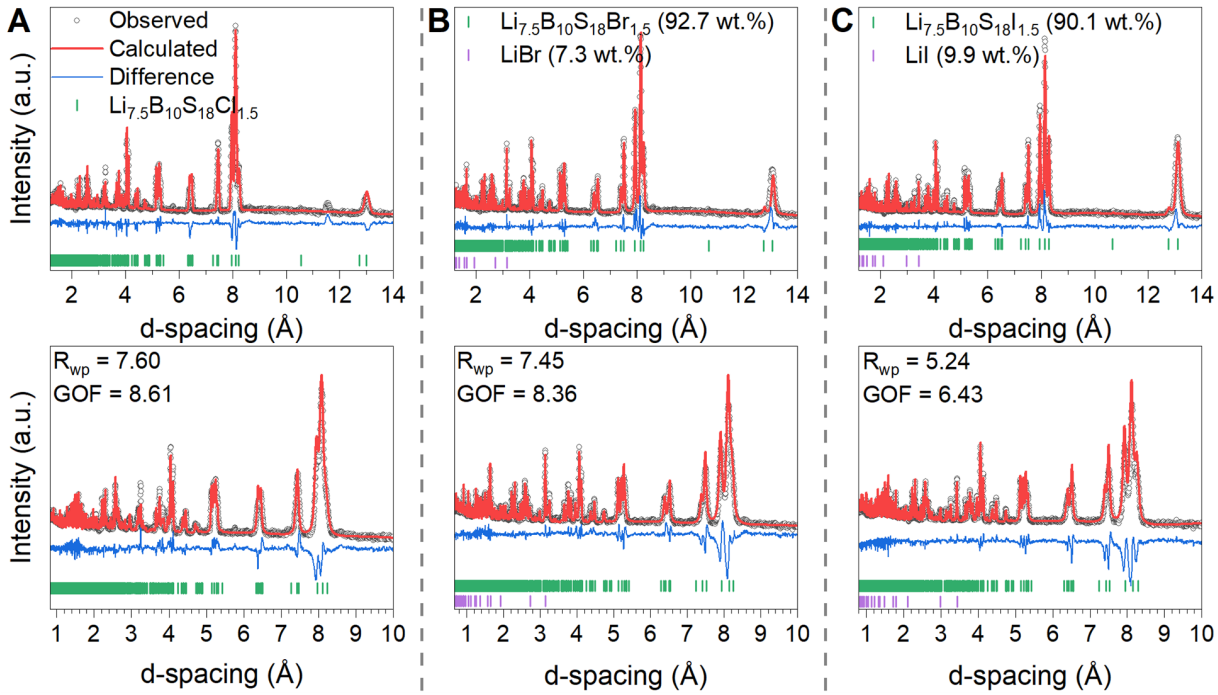

Figure D.2: Time-of-flight neutron diffraction patterns at 10 K and the corresponding combined Rietveld refinement fits for 'bank 2' (CW 1.5 Å, bottom row) and 'bank 3' (CW 2.665 Å, top row) of $Li_{7.5}B_{10}S_{18}Cl_{1.5}$, B) $Li_{7.5}B_{10}S_{18}Br_{1.5}$, and C) $Li_{7.5}B_{10}S_{18}I_{1.5}$. R_{wp} and GOF are the weighted profile R-factor and goodness of fit, respectively.

Table D.8: Crystallographic data, atomic coordinates, occupation factor, and equivalent isotropic displacement parameters of $Li_{7.5}B_{10}S_{18}Cl_{1.5}$ obtained from TOF neutron powder diffraction at 10 K.

$C2/c$ (no. 15): a = 21.1001(6) Å, b = 21.1291(6) Å, c = 16.2053(5) Å, β = 128.694(2) °						
Refined Compsn.: $Li_{7.5}B_{10}S_{18}Cl_{2.6}$, R_{wp} = 7.60, R_{exp} = 0.88, GOF = 8.61						
Atom	**Wyck. Pos.**	**x**	**y**	**z**	**Occ.**	**B_{iso} (Å^2)**
B(1-10)	8f	Fixed from single-crystal refinement			1	0.58(5)
S(1-18)	8f	Fixed from single-crystal refinement			1	0.13(9)
Li1	4e	0	0.1645	0.25	1	1.2(4)
Li2	4e	0.5	0.4368	0.25	1	1.2(4)
Li3	8f	0.1736	-0.0569	-0.0379	0.75	1.2(4)
Li4	8f	0.4711	0.2399	0.373	0.75	1.2(4)
Li5	8f	-0.0288	0.3409	0.074	0.75	1.2(4)
Li6	8f	0.342	0.3843	0.284	0.75	1.2(4)
Li7	4d	0.25	0.25	0.5	1	1.2(4)
Li8	8f	0.348	0.269	0.084	0.75	1.2(4)
Li9	8f	0.146	0.3731	0.172	0.75	1.2(4)
Li10	8f	0.4143	0.1414	0.131	0.75	1.2(4)
Li11	8f	0.1143	-0.0003	-0.0729	0.75	1.2(4)
Cl2	4e	0.5	0.2348(7)	0.25	0.89(2)	1.63(17)
Cl1A	8f	0.0234(13)	0.3625(10)	-0.0329(16)	0.476(15)	1.63(17)
Cl4A	4e	0	0.5498(10)	0.25	0.68(2)	1.63(17)
Cl1B	8f	0.0240(10)	0.4259(8)	0.0579(13)	0.583(17)	1.63(17)
Cl5	4e	0	0.3719(11)	0.25	0.592(19)	1.63(17)
Cl3	4b	0	0.5	0	0.17(2)	1.63(17)
Cl4B	8f	0.0308(17)	0.5938(13)	0.373(2)	0.353(14)	1.63(17)

Table D.9: Crystallographic data, atomic coordinates, occupation factor, and equivalent isotropic displacement parameters of $Li_{7.5}B_{10}S_{18}Cl_{1.5}$ obtained from TOF neutron powder diffraction at 300 K.

$C2/c$ (no. 15): a = 21.1445(11) Å, b = 21.1983(11) Å, c = 16.2202(8) Å, β= 128.675(3) °						
Refined Compsn.: $Li_{7.5}B_{10}S_{18}Cl_{2.5}$, R_{wp} = 6.68, R_{exp} = 0.86, GOF = 7.73						
Atom	**Wyck. Pos.**	**x**	**y**	**z**	**Occ.**	**B_{iso} (Å²)**
B(1-10)	8f	Fixed from single-crystal refinement			1	1.11(7)
S(1-18)	8f	Fixed from single-crystal refinement			1	0.64(11)
Li1	4e	0	0.1645	0.25	1	1.7(5)
Li2	4e	0.5	0.4368	0.25	1	1.7(5)
Li3	8f	0.1736	-0.0569	-0.0379	0.75	1.7(5)
Li4	8f	0.4711	0.2399	0.373	0.75	1.7(5)
Li5	8f	-0.0288	0.3409	0.074	0.75	1.7(5)
Li6	8f	0.342	0.3843	0.284	0.75	1.7(5)
Li7	4d	0.25	0.25	0.5	1	1.7(5)
Li8	8f	0.348	0.269	0.084	0.75	1.7(5)
Li9	8f	0.146	0.3731	0.172	0.75	1.7(5)
Li10	8f	0.4143	0.1414	0.131	0.75	1.7(5)
Li11	8f	0.1143	-0.0003	-0.0729	0.75	1.7(5)
Cl2	4e	0.5	0.2333(9)	0.25	0.87(2)	2.0(2)
Cl1A	8f	0.0247(17)	0.3659(12)	-0.030(2)	0.436(15)	2.0(2)
Cl4A	4e	0	0.5515(13)	0.25	0.64(2)	2.0(2)
Cl1B	8f	0.0181(13)	0.4239(10)	0.0541(17)	0.517(18)	2.0(2)
Cl5	4e	0	0.3807(12)	0.25	0.597(19)	2.0(2)
Cl3	4b	0	0.5	0	0.26(3)	2.0(2)
Cl4B	8f	0.020(2)	0.6083(15)	0.363(3)	0.331(14)	2.0(2)

Table D.10: Crystallographic data, atomic coordinates, occupation factor, and equivalent isotropic displacement parameters of $Li_{7.5}B_{10}S_{18}Br_{1.5}$ obtained from TOF neutron powder diffraction at 10 K.

$C2/c$ (no. 15): a = 21.1462(5) Å, b = 21.3827(4) Å, c = 16.0988(3) Å, β = 128.7373(14) °						
Refined Compsn.: $Li_7B_{10}S_{18}Br_{2.8}$, Impurity: 7.3 wt.% LiBr						
R_{wp} = 7.45, R_{exp} = 0.89, GOF = 8.36						
Atom	**Wyck. Pos.**	**x**	**y**	**z**	**Occ.**	**B_{iso} (Å²)**
B(1-10)	8f	Fixed from single-crystal refinement			1	0.79(4)
S(1-18)	8f	Fixed from single-crystal refinement			1	0.58(8)
Li1	4e	0	0.1626	0.25	1	1.4(4)
Li2	8f	0.4674	0.1607	0.58	0.6875	1.4(4)
Li3	4e	0.5	0.4376	0.25	1	1.4(4)
Li4	8f	0.4685	0.2368	0.38	0.6875	1.4(4)
Li5	4d	0.25	0.25	0.5	1	1.4(4)
Li6	8f	0.351	0.271	0.086	0.6875	1.4(4)
Li7	8f	0.182	0.346	0.161	0.6875	1.4(4)
Li8	8f	0.114	0	-0.076	0.6875	1.4(4)
Li9	8f	0.1746	-0.0562	-0.037	0.6875	1.4(4)
Li10	8f	0.159	0.113	0.714	0.6875	1.4(4)
Li11	8f	0.12	0.071	0.634	0.6875	1.4(4)
Br2	4e	0.5	0.2327(9)	0.25	0.88(3)	1.8(2)
Br1A	8f	0.0277(12)	0.3769(8)	-0.0152(15)	0.67(2)	1.8(2)
Br5A	4e	0	0.380(2)	0.25	0.35(3)	1.8(2)
Br4	4e	0.5	0.0507(15)	0.25	0.54(3)	1.8(2)
Br3	8f	0.4850(16)	-0.0558(13)	0.561(2)	0.45(2)	1.8(2)
Br1B	8f	0.506(2)	0.0747(15)	0.530(3)	0.37(2)	1.8(2)
Br5B	8f	0.5264(17)	0.0800(14)	0.685(2)	0.43(2)	1.8(2)

Table D.11: Crystallographic data, atomic coordinates, occupation factor, and equivalent isotropic displacement parameters of $Li_{7.5}B_{10}S_{18}Br_{1.5}$ obtained from TOF neutron powder diffraction at 300 K.

$C2/c$ (no. 15):a = 21.1741(6) Å, b = 21.4467(7) Å, c = 16.1145(5) Å, β = 128.678(2) °						
Refined Compsn.: $Li_7B_{10}S_{18}Br_{2.7}$, Impurity: 5.9 wt.% LiBr						
R_{wp} = 5.34, R_{exp} = 0.77, GOF = 6.9						
Atom	**Wyck. Pos.**	**x**	**y**	**z**	**Occ.**	**B_{iso} (Å²)**
B(1-10)	8f	Fixed from single-crystal refinement			1	0.95(4)
S(1-18)	8f	Fixed from single-crystal refinement			1	0.62(8)
Li1	4e	0	0.1626	0.25	1	2.2(5)
Li2	8f	0.4674	0.1607	0.58	0.6875	2.2(5)
Li3	4e	0.5	0.4376	0.25	1	2.2(5)
Li4	8f	0.4685	0.2368	0.38	0.6875	2.2(5)
Li5	4d	0.25	0.25	0.5	1	2.2(5)
Li6	8f	0.351	0.271	0.086	0.6875	2.2(5)
Li7	8f	0.182	0.346	0.161	0.6875	2.2(5)
Li8	8f	0.114	0	-0.076	0.6875	2.2(5)
Li9	8f	0.1746	-0.0562	-0.037	0.6875	2.2(5)
Li10	8f	0.159	0.113	0.714	0.6875	2.2(5)
Li11	8f	0.12	0.071	0.634	0.6875	2.2(5)
Br2	4e	0.5	0.2301(10)	0.25	0.85(3)	1.7(5)
Br1A	8f	0.0336(14)	0.3791(9)	-0.0101(17)	0.61(2)	1.7(5)
Br5A	4e	0	0.392(2)	0.25	0.35(3)	1.7(5)
Br4	4e	0.5	0.0463(15)	0.25	0.55(3)	1.7(5)
Br3	8f	0.4945(15)	-0.0582(12)	0.560(2)	0.48(2)	1.7(5)
Br1B	8f	0.520(3)	0.070(2)	0.548(4)	0.28(2)	1.7(5)
Br5B	8f	0.5245(18)	0.0787(15)	0.680(3)	0.41(2)	1.7(5)

Table D.12: Crystallographic data, atomic coordinates, occupation factor, and equivalent isotropic displacement parameters of $Li_{7.5}B_{10}S_{18}I_{1.5}$ obtained from TOF neutron powder diffraction at 10 K.

$C2/c$ (no. 15): a = 21.2432(3) Å, b = 21.3490(3) Å, c = 16.1396(2) Å, β = 128.7241(11) °						
Refined Compsn.: $Li_7B_{10}S_{18}I_{3.2}$, Impurity: 9.9 wt.% LiI						
R_{wp} = 5.24, R_{exp} = 0.82, GOF = 6.43						
Atom	**Wyck. Pos.**	**x**	**y**	**z**	**Occ.**	**B_{iso} (Å²)**
B(1-10)	8f	Fixed from single-crystal refinement			1	0.63(3)
S(1-18)	8f	Fixed from single-crystal refinement			1	0.50(6)
Li1	8f	0.1737	-0.0583	-0.0377	0.55	0.9(3)
Li2	8f	0.4651	0.2291	0.392	0.55	0.9(3)
Li3	4d	0.25	0.25	0.5	1	0.9(3)
Li4	8f	0.336	0.3803	0.281	0.55	0.9(3)
Li5	8f	-0.0356	0.3429	0.083	0.55	0.9(3)
Li6	4e	0	0.167	0.25	1	0.9(3)
Li7	4e	0	0.9388	0.25	1	0.9(3)
Li8	8f	0.152	0.379	0.189	0.55	0.9(3)
Li9	8f	0.104	0.614	0.381	0.55	0.9(3)
Li10	8f	0.39	0.431	0.379	0.55	0.9(3)
Li11	8f	0.3468	0.2683	0.081	0.55	0.9(3)
Li12	8f	0.109	0.002	-0.077	0.55	0.9(3)
Li13	8f	0.444	0.208	0.446	0.55	0.9(3)
I1A	8f	0.4771(9)	0.1114(7)	0.0166(12)	0.83(2)	2.3(2)
I1B	8f	0.4931(16)	0.0729(12)	-0.0379(19)	0.54(2)	2.3(2)
I2	4e	0	0.7173(9)	0.25	1.00(3)	2.3(2)
I3	4b	0	0.5	0	0.09(3)	2.3(2)
I4A	4e	0	0.524(2)	0.25	0.41(3)	2.3(2)
I4B	8f	0.0224(18)	0.5578(13)	0.377(2)	0.46(2)	2.3(2)
I5A	4e	0	0.4383(15)	0.25	0.61(3)	2.3(2)
I5B	8f	0.028(3)	0.398(2)	0.175(4)	0.28(2)	2.3(2)

Table D.13: Crystallographic data, atomic coordinates, occupation factor, and equivalent isotropic displacement parameters of $Li_{7.5}B_{10}S_{18}I_{1.5}$ obtained from TOF neutron powder diffraction at 300 K.

$C2/c$ (no. 15): a = 21.2826(3) Å, b = 21.4205(3) Å, c = 16.1530(2) Å, β = 128.7163(10) °						
Refined Compsn.: $Li_7B_{10}S_{18}I_3$, Impurity: 6.8 wt.% LiI						
R_{wp} = 5.40, R_{exp} = 0.96, GOF = 5.64						
Atom	**Wyck. Pos.**	**x**	**y**	**z**	**Occ.**	**B_{iso} (Å²)**
B(1-10)	8f	Fixed from single-crystal refinement			1	1.03(3)
S(1-18)	8f	Fixed from single-crystal refinement			1	0.92(6)
Li1	8f	0.1737	-0.0583	-0.0377	0.55	3.3(4)
Li2	8f	0.4651	0.2291	0.392	0.55	3.3(4)
Li3	4d	0.25	0.25	0.5	1	3.3(4)
Li4	8f	0.336	0.3803	0.281	0.55	3.3(4)
Li5	8f	-0.0356	0.3429	0.083	0.55	3.3(4)
Li6	4e	0	0.167	0.25	1	3.3(4)
Li7	4e	0	0.9388	0.25	1	3.3(4)
Li8	8f	0.152	0.379	0.189	0.55	3.3(4)
Li9	8f	0.104	0.614	0.381	0.55	3.3(4)
Li10	8f	0.39	0.431	0.379	0.55	3.3(4)
Li11	8f	0.3468	0.2683	0.081	0.55	3.3(4)
Li12	8f	0.109	0.002	-0.077	0.55	3.3(4)
Li13	8f	0.444	0.208	0.446	0.55	3.3(4)
I1A	8f	0.4772(10)	0.1101(9)	0.0110(14)	0.86(2)	4.3(4)
I1B	8f	0.486(2)	0.078(2)	-0.039(3)	0.39(3)	4.3(4)
I2	4e	0	0.7152(10)	0.25	1.00(3)	4.3(4)
I3	4b	0	0.5	0	0.20(3)	4.3(4)
I4A	4e	0	0.519(3)	0.25	0.31(3)	4.3(4)
I4B	8f	0.024(2)	0.5587(17)	0.366(3)	0.44(2)	4.3(4)
I5A	4e	0	0.4347(17)	0.25	0.61(3)	4.3(4)
I5B	8f	0.028(4)	0.396(3)	0.179(5)	0.23(2)	4.3(4)

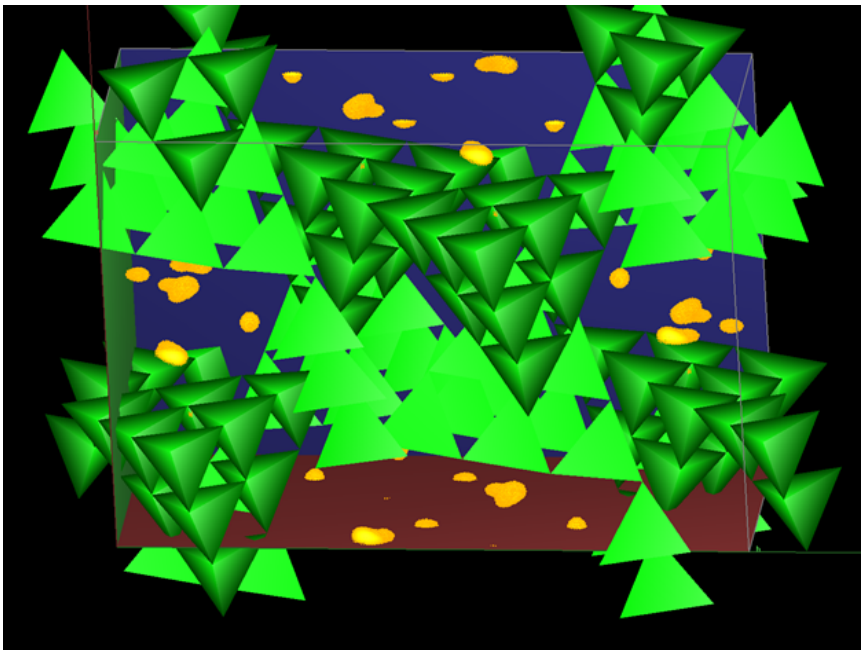

Figure D.3: Fourier difference map of $Li_{7.5}B_{10}S_{18}I_{1.5}$ from TOPAS of the empty $B_{10}S_{18}$ framework (not including any Li or iodine). Bright yellow spots are areas of missing positive density, corresponding to iodine positions in the channel with high occupancy.

D.3.3 Neutron Pair Distribution Function (PDF) Analysis

Table D.14: Crystallographic data, atomic coordinates, occupation factor, and equivalent isotropic displacement parameters of $Li_{7.5}B_{10}S_{18}Cl_{1.5}$ obtained from neutron PDF at 290 K (1-10 Å).

$C2/c$ (no. 15): a = 20.98(4) Å, b = 21.35(2) Å, c = 16.21(2) Å, β = 128.56(13) °						
Refined Compsn.: $Li_{7.5}B_{10}S_{18}Cl_{2.3}$, R_{wp} = 13.51						
Atom	**Wyck. Pos.**	**x**	**y**	**z**	**Occ.**	**B_{iso} (Å²)**
B(1-10)	8f	Fixed from single-crystal refinement			1	0.81(3)
S(1-18)	8f	Fixed from single-crystal refinement			1	0.54(3)
Li1	4e	0	0.1645	0.25	1	3.0(4)
Li2	4e	0.5	0.4368	0.25	1	3.0(4)
Li3	8f	0.1736	-0.0569	-0.0379	0.75	3.0(4)
Li4	8f	0.4711	0.2399	0.373	0.75	3.0(4)
Li5	8f	-0.0288	0.3409	0.074	0.75	3.0(4)
Li6	8f	0.342	0.3843	0.284	0.75	3.0(4)
Li7	4d	0.25	0.25	0.5	1	3.0(4)
Li8	8f	0.348	0.269	0.084	0.75	3.0(4)
Li9	8f	0.146	0.3731	0.172	0.75	3.0(4)
Li10	8f	0.4143	0.1414	0.131	0.75	3.0(4)
Li11	8f	0.1143	-0.0003	-0.0729	0.75	3.0(4)
Cl1	8f	0.0110(19)	0.3472(15)	-0.040(3)	0.77(5)	2.4(4)
Cl2	4e	0.5	0.238(3)	0.25	1.00(11)	2.4(4)
Cl4A	4e	0	0.561(2)	0.25	1.00(8)	2.4(4)
Cl5	4e	0	0.3829(18)	0.25	1.00(10)	2.4(4)

Table D.15: Crystallographic data, atomic coordinates, occupation factor, and equivalent isotropic displacement parameters of $Li_{7.5}B_{10}S_{18}Br_{1.5}$ obtained from neutron PDF at 290 K (1-10 Å).

$C2/c$ (no. 15): a = 20.97(3) Å, b = 21.49(3) Å, c = 16.23(2) Å, β = 129.30(9) °						
Refined Compsn.: $Li_7B_{10}S_{18}Br_{2.5}$, R_{wp} = 13.58						
Atom	**Wyck. Pos.**	**x**	**y**	**z**	**Occ.**	**B_{iso} (Å²)**
B(1-10)	8f	Fixed from single-crystal refinement			1	0.55(3)
S(1-18)	8f	Fixed from single-crystal refinement			1	0.54(4)
Li1	4e	0	0.1626	0.25	1	1.9(2)
Li2	8f	0.4674	0.1607	0.58	0.6875	1.9(2)
Li3	4e	0.5	0.4376	0.25	1	1.9(2)
Li4	8f	0.4685	0.2368	0.38	0.6875	1.9(2)
Li5	4d	0.25	0.25	0.5	1	1.9(2)
Li6	8f	0.351	0.271	0.086	0.6875	1.9(2)
Li7	8f	0.182	0.346	0.161	0.6875	1.9(2)
Li8	8f	0.114	0	-0.076	0.6875	1.9(2)
Li9	8f	0.1746	-0.0562	-0.037	0.6875	1.9(2)
Li10	8f	0.159	0.113	0.714	0.6875	1.9(2)
Li11	8f	0.12	0.071	0.634	0.6875	1.9(2)
Br1A	8f	0.0149(12)	0.3671(11)	0.0385(19)	1.00(7)	1.3(2)
Br2	4e	0.5	0.2458(17)	0.25	1.00(14)	1.3(2)
Br4	4e	0.5	0.0737(18)	0.25	1.00(10)	1.3(2)
Br5A	4e	0	0.3807(14)	0.25	1.00(11)	1.3(2)

Table D.16: Crystallographic data, atomic coordinates, occupation factor, and equivalent isotropic displacement parameters of $Li_{7.5}B_{10}S_{18}I_{1.5}$ obtained from neutron PDF at 290 K (1-10 Å).

$C2/c$ (no. 15): a = 21.37(4) Å, b = 21.32(3) Å, c = 16.11(2) Å, β = 128.35(12) °						
Refined Compsn.: $Li_7B_{10}S_{18}I_{2.5}$, R_{wp} = 14.02						
Atom	**Wyck. Pos.**	**x**	**y**	**z**	**Occ.**	**B_{iso} (Å²)**
B(1-10)	8f	Fixed from single-crystal refinement			1	0.84(2)
S(1-18)	8f	Fixed from single-crystal refinement			1	0.72(2)
Li1	8f	0.1737	-0.0583	-0.0377	0.55	2.9(5)
Li2	8f	0.4651	0.2291	0.392	0.55	2.9(5)
Li3	4d	0.25	0.25	0.5	1	2.9(5)
Li4	8f	0.336	0.3803	0.281	0.55	2.9(5)
Li5	8f	-0.0356	0.3429	0.083	0.55	2.9(5)
Li6	4e	0	0.167	0.25	1	2.9(5)
Li7	4e	0	0.9388	0.25	1	2.9(5)
Li8	8f	0.152	0.379	0.189	0.55	2.9(5)
Li9	8f	0.104	0.614	0.381	0.55	2.9(5)
Li10	8f	0.39	0.431	0.379	0.55	2.9(5)
Li11	8f	0.3468	0.2683	0.081	0.55	2.9(5)
Li12	8f	0.109	0.002	-0.077	0.55	2.9(5)
Li13	8f	0.444	0.208	0.446	0.55	2.9(5)
I1A	8f	0.4709(12)	0.1097(12)	0.0030(14)	1.00(7)	0.4(1)
I2	4e	0	0.7174(18)	0.25	1.00(13)	0.4(1)
I4A	4e	0	0.5233(15)	0.25	1.00(11)	0.4(1)
I5A	4e	0	0.3773(13)	0.25	1.00(14)	0.4(1)

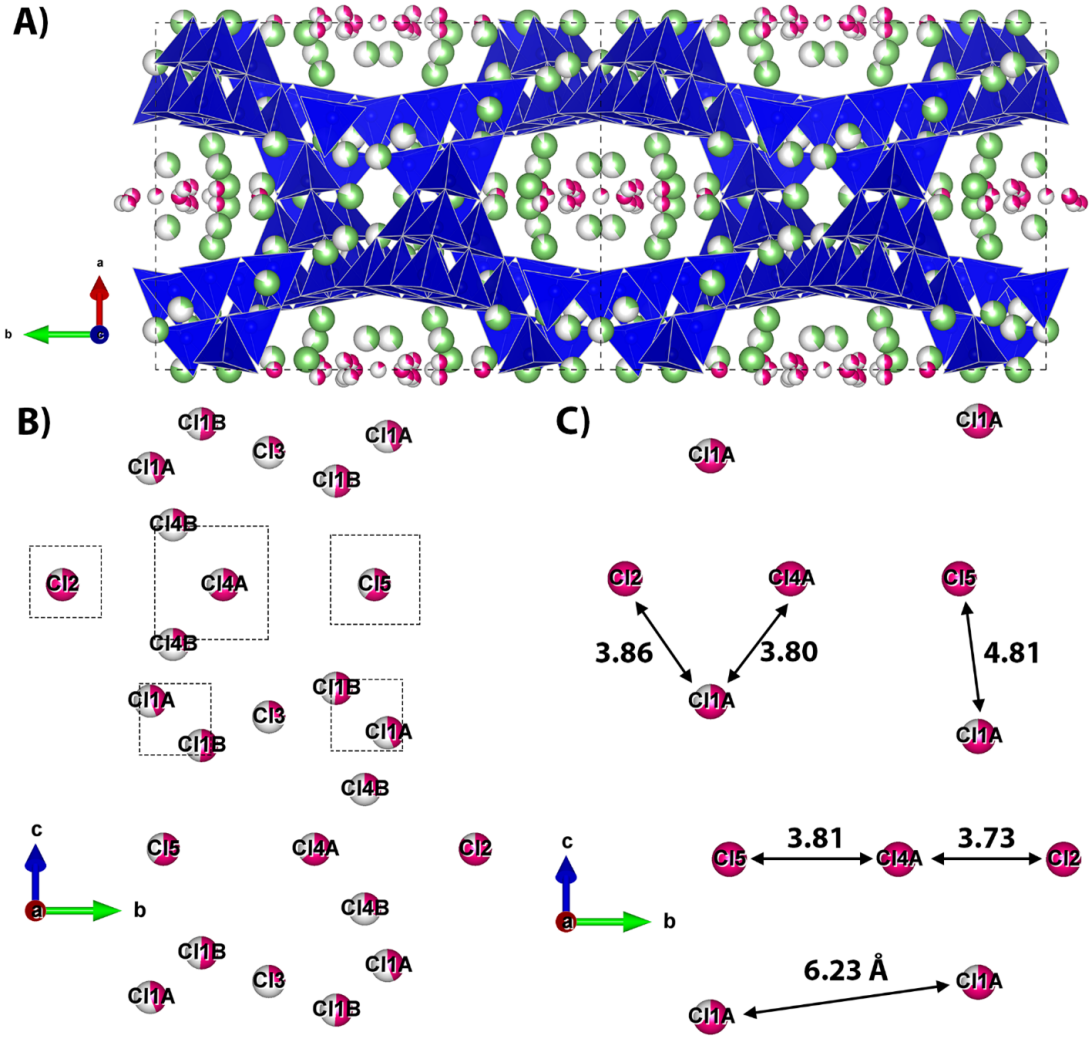

Figure D.4: A) $Li_{7.5}B_{10}S_{18}Cl_{1.5}$ structure with lithium and chlorine in the channels. B) Average structure (refined from NPD at 300 K) and C) local structure (refined from NPDF at 290 K) of chlorine in the tunnels.

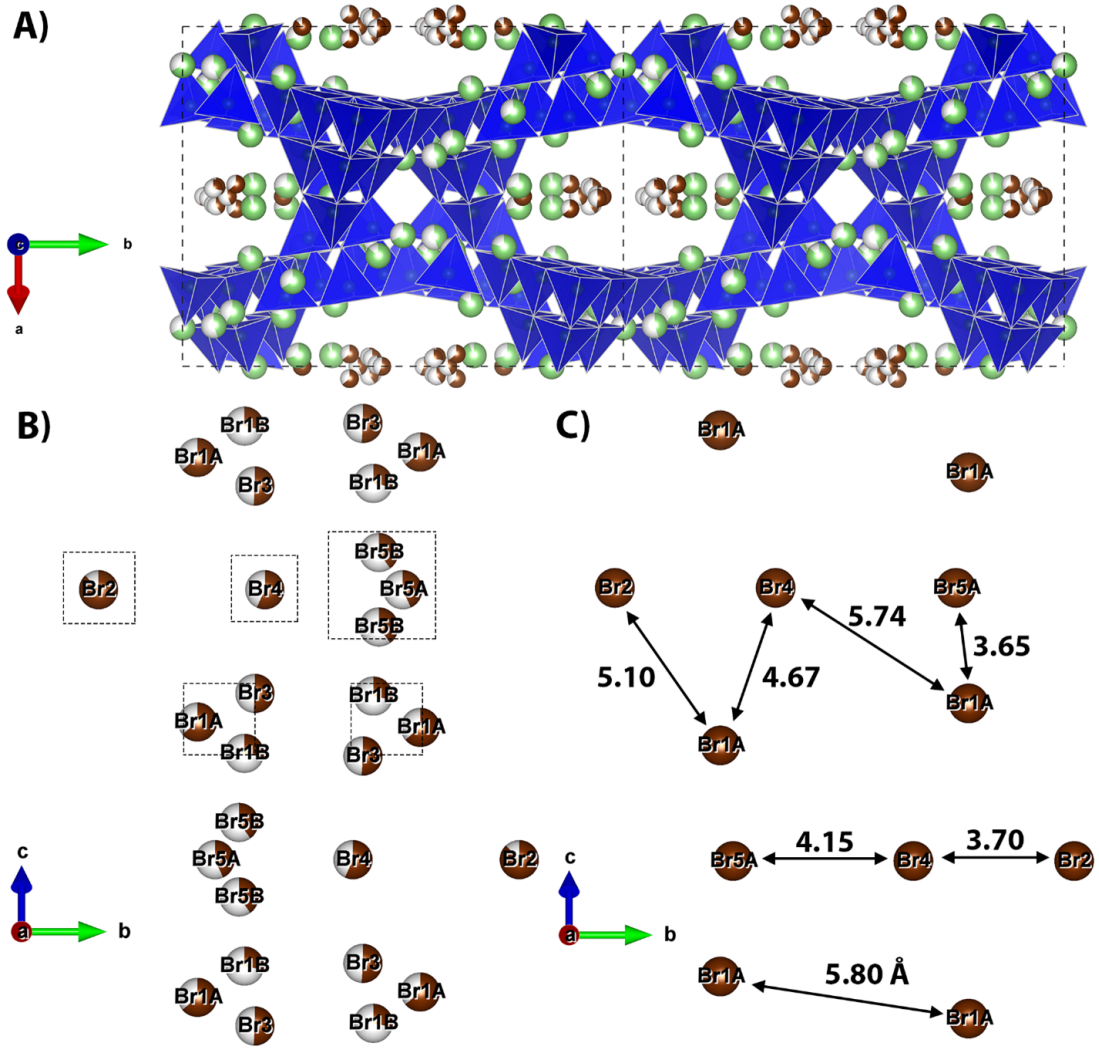

Figure D.5: A) $Li_{7.5}B_{10}S_{18}Br_{1.5}$ structure with lithium and bromine in the channels. B) Average structure (refined from NPD at 300 K) and C) local structure (refined from NPDF at 290 K) of bromine in the tunnels.

Appendix E

Supporting Information for: $Li_6B_7S_{13}I$: a fast-ion conducting thioboracite with a perovskite topology and argyrodite-like lithium substructure

E.1 Supporting Figures

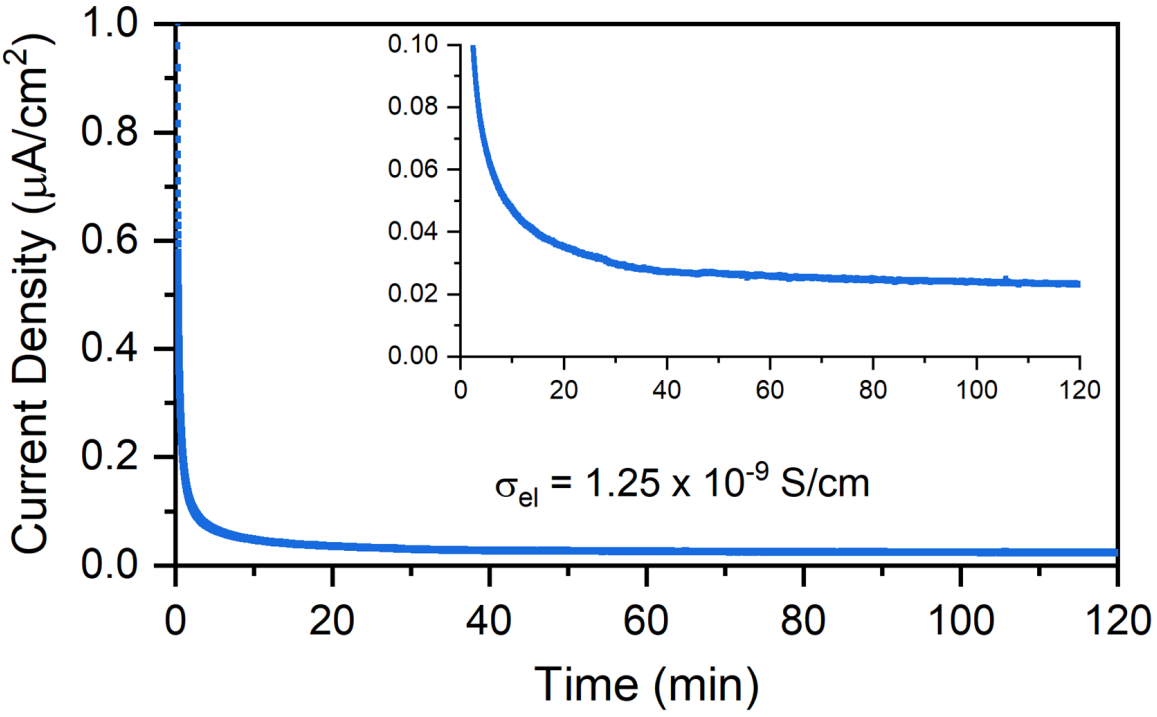

Figure E.1: DC polarization measurement for the Ti—$Li_6B_7S_{13}I$—Ti cell with an applied voltage of 500 mV.

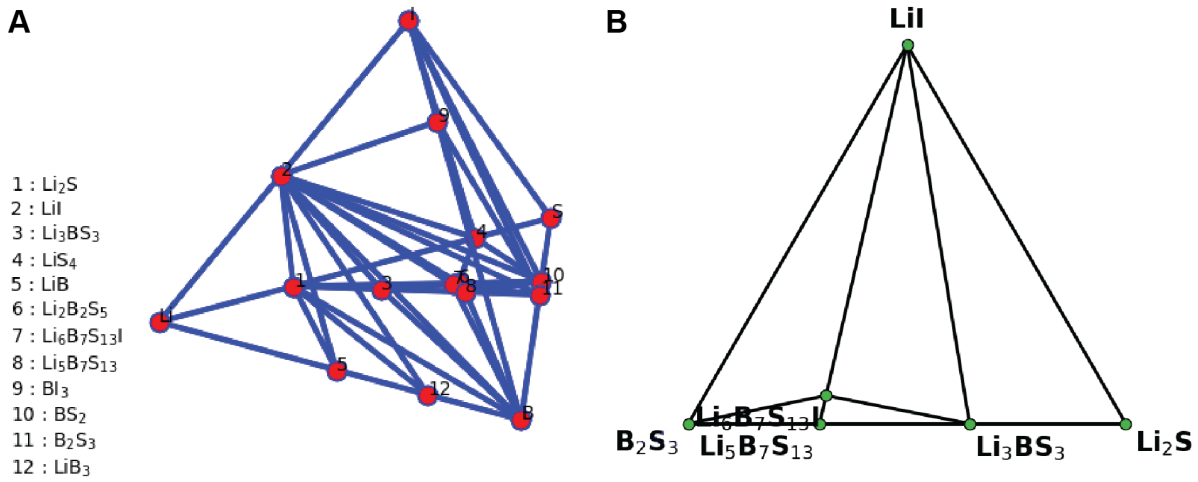

Figure E.2: A) Calculated 0 K phase diagram of Li-B-S-I showing stable phases (red nodes), including the stable $Li_6B_7S_{13}I$. B) Pseudoternary Li_2S-B_2S_3-LiI phase diagram. Green circles with labeled compositions indicate stable phases.

E.2 Supporting Tables

Table E.1: Crystallographic data for cubic-$Li_6B_7S_{13}I$ and $Li_5B_7S_{13}$ obtained from single crystal X-ray diffraction data.

Crystal Data		
Formula	$Li_{6.04}B_7S_{13}I$	$Li_5B_7S_{13}$
Formula Weight	661.27	527.15
Crystal System	Cubic	Tetragonal
Space Group	F-43c (No. 219)	$I4_1/a$ (No. 88)
a (Å)	15.245(2)	12.3120(4)
c (Å)		21.8638(7)
V (Å^3)	3543.1(14)	3314.2(2)
Z	4	8
Calc. Density (g/cm^3)	2.479	2.113
Abs. coef. μ(Mo Kα) (mm^{-1})	3.32	1.683
F(000)	2513	2064
Crystal Size (mm)	0.01 × 0.04 × 0.08	0.04 × 0.07 × 0.08
Data Collection		
Temperature (K)	280	280
Radiation (Å)	Mo Kα, 0.71073	Mo Kα, 0.71073
Theta range for data collection	2.7 – 27.9°	1.9 – 30.0°
Index ranges	-17 ≤ h ≤ 19 -20 ≤ k ≤ 12 -18 ≤ l ≤ 18	-17 ≤ h ≤ 17 -17 ≤ k ≤ 17 -30 ≤ l ≤ 30
Reflections collected	5006	22500
Independent reflections	367 (R_{int} = 0.049)	2430 (R_{int} = 0.030)
Completeness to θ = 25.242°	100%	100%
Absorption correction	Multi-scan	Multi-scan
Max. and min. transmission	0.7460, 0.6718	0.7460, 0.6960
Refinement		
Refinement method	Full-matrix least-squares on F^2	Full-matrix least-squares on F^2
Data/restraints/parameters	367/0/21	2430/0/119
Goodness of fit on F^2	1.16	1.14
Final R indices [I>2sigma(I)]	R1 = 0.0221 wR2 = 0.0481	R1 = 0.0200 wR2 = 0.053
R indices (all data)	R1 = 0.0236 wR2 = 0.0486	R1 = 0.0295 wR2 = 0.0567
Largest diff. peak and hole	-0.41 and 0.94 e·Å^{-3}	-0.53 and 0.56 e·Å^{-3}

Table E.2: Atomic coordinates, occupation factor, and equivalent isotropic displacement parameters of cubic $Li_5B_7S_{13}$ obtained from single-crystal X-ray diffraction measured at 280 K.

Atom	Wyck. Pos.	x	y	z	Occ.	U_{eq} (Å^2)
B1	16f	0.08994(15)	0.16538(15)	0.07592(8)	1	0.0096(3)
B2	16f	0.10674(15)	0.52834(15)	0.27598(8)	1	0.0102(3)
B3	16f	0.16993(14)	0.19182(15)	0.62408(9)	1	0.0099(3)
B4	8e	0	0.25	0.52375(11)	1	0.0094(5)
S1	16f	0.00463(3)	0.06579(3)	0.12475(2)	1	0.01175(9)
S2	16f	0.00698(3)	0.03724(3)	0.32521(2)	1	0.01109(9)
S3	16f	0.05702(3)	0.13136(3)	0.57259(2)	1	0.00901(8)
S4	16f	0.17570(3)	0.06820(3)	0.02561(2)	1	0.01077(9)
S5	16f	0.32723(3)	0.52481(3)	0.07654(2)	1	0.01093(9)
S6	8e	0	0.25	0.02257(3)	1	0.01244(12)
S7	16f	0.38801(3)	0.20009(3)	0.02729(2)	1	0.01249(9)
Li1	16f	0.1058(5)	0.0129(11)	0.2185(3)	1	0.154(6)
Li2	16f	0.3332(4)	0.0799(6)	0.1108(3)	1	0.073(2)
Li3	16f	0.1905(17)	0.2264(17)	0.2655(14)	0.5	0.160(11)

Table E.3: Anisotropic displacement parameters of $Li_5B_7S_{13}$ obtained from single-crystal X-ray diffraction measured at 280 K.

Atom	U_{11}	U_{22}	U_{33}	U_{23}	U_{13}	U_{12}
B1	0.0099(8)	0.0094(8)	0.0095(8)	-0.0011(6)	0.0017(6)	0.0002(6)
B2	0.0095(8)	0.0113(8)	0.0097(8)	-0.0014(6)	0.0000(6)	0.0014(6)
B3	0.0102(8)	0.0098(8)	0.0096(8)	0.0010(6)	0.0008(6)	0.0008(6)
B4	0.0092(11)	0.0110(11)	0.0080(11)	0	0	-0.0023(9)
S1	0.01271(19)	0.00917(18)	0.01337(19)	0.00013(15)	0.00402(15)	-0.00060(15)
S2	0.01143(19)	0.00964(18)	0.01219(19)	0.00259(14)	-0.00254(14)	-0.00026(14)
S3	0.00945(18)	0.00921(17)	0.00837(17)	0.00038(14)	0.00030(13)	-0.00030(14)
S4	0.01203(19)	0.00814(18)	0.01215(19)	-0.00080(14)	0.00499(14)	-0.00117(14)
S5	0.01195(18)	0.00925(18)	0.01159(19)	0.00128(14)	-0.00359(14)	-0.00168(14)
S6	0.0134(3)	0.0146(3)	0.0093(3)	0	0	0.0025(2)
S7	0.01265(19)	0.0167(2)	0.00813(18)	0.00018(15)	0.00149(14)	-0.00532(15)
Li1	0.030(3)	0.362(17)	0.071(5)	0.108(7)	0.019(3)	0.055(6)
Li2	0.038(3)	0.093(5)	0.088(4)	0.069(4)	-0.012(3)	-0.012(3)
Li3	0.136(17)	0.098(14)	0.24(3)	-0.032(16)	-0.10(2)	0.071(14)